Time Resolved Excited State Photo-Engineering

Daven Aidan Armoogum

Submitted for the degree of
Doctor of Philosophy

University of London
2004

Department of Physics and Astronomy
University College London

ProQuest LLC
789 East Eisenhower Parkway
P.O. Box 1346
Ann Arbor, MI 48106-1346

To Julie, from the boy who makes the tea

Abstract

This thesis concerns the development and application of time resolved fluorescence which yield new and detailed information on molecular order and motion in both isotropic and ordered systems.

Polarised fluorescence studies involve the photoselection of a non-equilibrium distribution of excited state probe orientations whose relaxation is monitored by time resolved fluorescence anisotropy. Chapter 1 introduces the basic concepts of probe photophysics and orientational photoselection. Chapter 2 combines photoselection with single and multiple laser pulses to provide a full description of probe alignment dynamics in the nematic phase of 5-cyanobiphenyl (5CB). In isotropic media the cylindrically symmetric and asymmetric alignment relaxation times (τ_{20} and τ_{22}) are necessarily equal. However, in 5CB, $\tau_{20} > \tau_{22}$; this was seen to correlate strongly with equilibrium order parameters, indicating the need to quantify fully the probe orientational distribution function $P(\theta,\varphi)$. In Chapter 3, single and two-photon time resolved fluorescence anisotropy measurements are used to determine the hitherto unmeasured (ground state) K=6 moment of $P(\theta,\varphi)$.

The final chapters concern the development of the next generation of photoselection techniques where an excited state population is engineered by stimulated emission depletion (STED). In Chapter 4 STED following two-photon excitation (PUMP) has been demonstrated in a range of well established single photon probes and two recently developed quadrupolar chromophores. Saturation of the DUMP transition due to excited state re-pumping was investigated, and from a two level rate equation model stimulated emission cross-sections and ground state vibrational relaxation times were determined. In Chapter 5 the polarisation properties of STED are investigated; orientation-selective depletion was shown to yield highly polarised excited state arrays. Polarisation resolved STED measurements were shown to circumvent spontaneous emission selection rules (which forbid the measurement of excited state moments of rank K>2) allowing the first measurements of hexadecapole (K=4) orientational relaxation in two fluorescent probes.

Acknowledgements

This work would not have been possible without the help of some wonderful people.

Firstly I'd like to thank my Nan for giving me the best possible start in life – I hope this makes you proud.

I'd like to express my deepest gratitude to Dr Angus Bain for all his help and support in helping me to achieve this goal. As well as being a considerate (and thorough) supervisor, Angus has been a constant drinking companion and supplier of jokes for all... thank you!

I've been fortunate enough to work with some fantastic people. Hail Dr Richard Marsh, King of the Lab – you've been awesome in the lab and a good friend too. Thanks to Jason and Bojan for their excellence in training me. Uncle Nick and Nick II, thank you, and good luck! And as for the Spaniard... Gracias, Max. I shall try to be a good person.

To everybody who has helped me (usually at no notice) at UCL: Derek; Bernard; John; Martin; Mark; Catherine; Muna; Ivan; Ted; Hilary; Brian; Tim and Ceinwen, thank you!

Special thanks to my family - Aden, Norma, Lyn, Ivor and (the amazing) Aaron, so *this* is what I've been doing for the last four years! Thank you so much for your support.

My dear friends, I'll see you in the pub very soon...

There's one more person I haven't mentioned yet who deserves her own (sparkly and *probably* pink) acknowledgements page. Thank you Julie, I'm absurdly lucky to have you in my life. Best doesn't even come close... xx

D.A. 2004

Table of contents

List of Figures

List of Tables

Chapter 1

Molecular Probe Photophysics

1.1 Introduction

This thesis involves the creation, study and manipulation of electronically excited molecular populations by their interaction with polarised laser pulses. The advent of quantum mechanics over the past one hundred years has changed the way that we understand the interaction between light and matter. In particular, the integration of quantum mechanics into existing classical theory allows scientists to describe spectroscopic phenomena.

Quantum mechanics accounts for the quantised energy level structure which describes atoms and molecules. Light induced transitions that take place between molecular states are governed by selection rules which arise from semi-classical quantum theory in which the interaction between the atom (or molecule) and the light radiation field is treated classically, but the subsequent transitions are quantised. Lasers allow significant populations of well defined molecular states to be created subject to selection rules. The relaxation of these excited state populations is also governed by well defined fluorescence, phosphorescence and non-radiant pathways. Experiments such as fluorescence lifetime and anisotropy studies can take advantage of these conditions to extract information about molecular systems. Furthermore, by developing and implementing novel fluorescence experiments applied to molecular excited states it is possible to circumvent the selection rules and extract hitherto hidden information; this is discussed in Chapter 5.

This chapter will illustrate some of the basic photophysical interactions that are relevant to this work and introduce the concepts that describe fluorescence lifetime and anisotropy studies, in particular, the photoselection of a non-equilibrium orientational distribution of excited state molecules [1]. Photoselection (the process by which molecular populations are selected using an incident light field) accesses information about the orientation and dynamics of molecular probes in a variety of environments which, in turn, yields information about the environment itself.

1.2 Basic Spectroscopic Processes

Spectroscopy is concerned with the interactions that take place between light and matter. There are many ways in which light and matter interact, and it was in the study of these interactions that quantum mechanics has developed over the past century. Quantum mechanics can describe the most basic processes that take place between light and matter: the absorption and emission of radiation [2]. These processes are illustrated in figure 1.1.

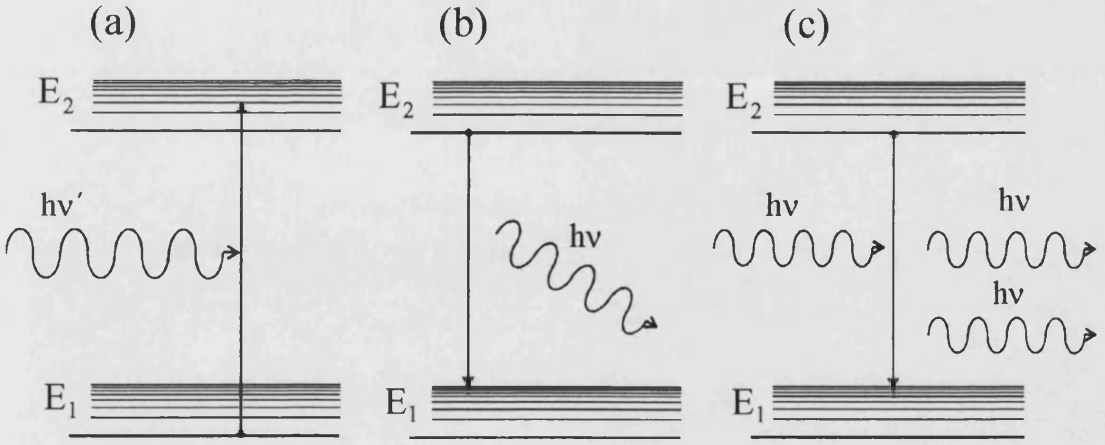

Figure 1.1: (a) absorption is the process whereby a system in energy level E_1 can be raised to energy level E_2 by the absorption of a photon whose energy hν' is equal to the difference (E_2-E_1) between the initial and final states. (b) Spontaneous emission is the mechanism in which a system in level E_2 can lose energy to level E_1 by the emission of a photon whose energy hν corresponds to the energy difference between the two levels. (c) the presence of a photon ΔE=hν can stimulate an electron to the lower energy level, resulting in the emission of a second photon with the same energy, phase and direction as the first.

1.3 The Born-Oppenheimer Approximation

The energy level structure of molecules is in general well described within the framework of the Born-Oppenheimer approximation [3]. The principle is based on the fact that the electrons in a molecule are much less massive than the nuclei and therefore can rearrange much more rapidly. A consequence of the Born-Oppenheimer approximation is that electronic energy is dependent only on the nuclear configuration and not on the kinetic energy of the nuclei; the electron energies and wavefunctions can be calculated as functions of this static nuclear framework. From this comes the concept of a potential energy surface; the rapid change in electron distribution causes a change in potential energy, resulting in a potential energy surface which determines the equilibrium positions of the nuclei [2]. This is represented schematically for the ground state and first excited state of a diatomic molecule in figure 1.2.

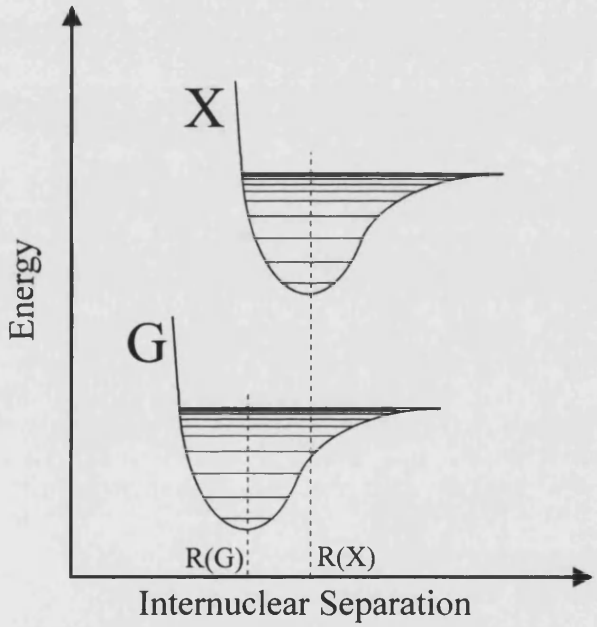

Figure 1.2: Schematic diagram of the Born-Oppenheimer potential energy surfaces for a diatomic molecule. The excited state internuclear separation R(X) is increased with respect to that of the ground state R(G).

The circumstances that describe a polyatomic molecule are analogous to the diatomic case, with a more complex vibrational and rotational level structure; the number of dimensions required to describe the potential energy surface increases with the number of nuclei present in the molecule as 3N-6, where N is the number of nuclei [2]. For a molecule with zero net charge and an even number of electrons, the lowest (i.e. ground state) energy configuration is a singlet state in which all the electrons are spin paired (consistent with the Pauli Principle) and the total electron spin is zero, and is designated

by S_0. Higher energy singlet states S_1, S_2....S_n can be accessed by electric dipole transitions typically induced by single photon absorption. Transitions via other mechanisms can occur, however, and two-photon excitation is one such mechanism that is discussed in Chapter 3. In this work, the excited state will refer to the first electronic state S_1. For molecules that absorb and emit in the visible portion of the electromagnetic spectrum, fluorescence corresponding to the $S_0 \rightarrow S_1$ transition varies between 2eV and 2.25eV (approx. 620nm to 440nm). Thermal occupation of S_1 and higher singlet states is negligible. This is due to an energetically highly unfavourable Boltzmann factor; typically, $\Delta E/kT$ varies from 80 to 90 [4].

1.4 Absorption

1.4.1 Fermi's Golden Rule

Absorption of a photon by a molecule results in a transition of the system from the ground to excited state, where certain allowed photon energies are preferred due to the quantised energy level structure of the system. However, this does not make clear why certain allowed transitions are stronger than others. This can be explained by Fermi's Golden Rule, which maintains that the transition rate in a system depends upon the coupling strength between the initial and final states and upon the density of the radiation field and density of final states. In terms of Fermi's Golden Rule, the transition probability W_{if} is given by [5]

$$W_{if} \propto \left|\langle f|E.\mu|i\rangle\right|^2 \rho_f \qquad [1.1]$$

where ρ_f is the density of final states and μ_{if} is a matrix element which represents the expectation value of the transition perturbation:

$$\mu_{fi} = \int \psi_f^* \mu \psi_i d\tau \qquad [1.2]$$

In equation 1.2 μ is the electric dipole operator for a transition between initial and final states with wavefunctions ψ_i and ψ_f respectively. The matrix element μ_{fi} is also known as the transition dipole moment. The semi-classical viewpoint of absorption, applicable

for a large number of photons interacting with a molecular population, suggests that for a molecule to be able to interact with an electromagnetic field, thereby absorbing or creating a photon of frequency ν, it should possess a dipole which oscillates at that frequency. In this way a transition comprises a re-arrangement of charge density within the molecule.

1.4.2 The Franck-Condon Principle

The $S_0 \rightarrow S_1$ transition strength is in general maximised for the excitation of higher vibrational states in S_1 than are thermally populated in S_0. This is a consequence of the sudden nature of the electronic re-arrangement with respect to nuclear motions within the molecule and the greater equilibrium internuclear separation in the excited state. This is encapsulated in the Franck-Condon Principle which states that electronic transitions take place between frozen (static) nuclear configurations in the ground and excited states of a molecule. Given that the ground and excited vibrational states are eigenfunctions of different (Born-Oppenheimer) nuclear Hamiltonians, the vibrational structure of the $S_0 \rightarrow S_1$ absorption can be described in terms of sudden transitions between eigenstates of the two (different) nuclear Hamiltonians. If $|v\rangle$ and $|v'\rangle$ are respectively the vibrational wavefunctions of the ground and excited states, the probability of the transition $P_{vv'}$, given a sudden change between the nuclear Hamiltonians, is given by the squared modulus of their overlap [6]:

$$P_{vv'} = \left|\langle v'|v\rangle\right|^2 \qquad [1.3]$$

The thermally populated ground state vibrational levels have their maxima in the vicinity of the equilibrium nuclear separation. In the excited state the average internuclear separation is generally larger given the less tightly bound nature of the excited electronic configuration. The overlap between $|v\rangle$ and $|v'\rangle$ is thus maximised for large amplitude excited vibrational states. This principle is illustrated in figure 1.3.

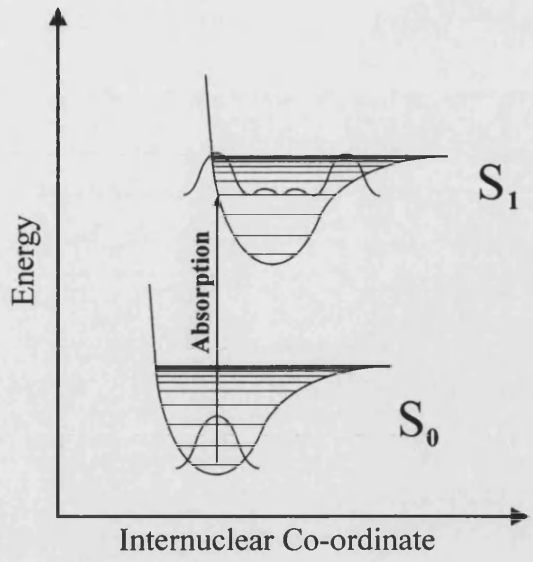

Figure 1.3: Schematic representation illustrating the Franck-Condon Principle in which the transition probability is strongest for excitation from low lying vibrational levels in S_0 to higher vibrational levels of S_1. This corresponds to the maximum overlap of ground and excited state wavefunctions $|v\rangle$ and $|v'\rangle$.

1.5 Excited State Relaxation

The $S_0 \rightarrow S_1$ transition probability is maximised for transitions to upper vibrational levels in S_1 in accordance with the Franck-Condon principle. With short pulsed excitation the initially excited population is vibrationally "hot", i.e. not in thermal equilibrium with surrounding solvent molecules. In addition, the sudden re-arrangement of electronic charge may lead to a re-organisation of solvent molecules about the solute [7]; this is accompanied by rapid sub-picosecond vibrational relaxation by collisions with "colder" surrounding solvent molecules. These processes lead to a rapidly thermalised vibrational population in S_1 and a lowering in the (free) energy of the excited state due to solvent reorganisation. As with absorption, spontaneous emission back to S_0 is governed by the Franck-Condon principle leading to the preferential population of higher vibrational levels in S_0. These in turn are rapidly depopulated due to interactions with the solvent. As a result of rapid solvent mediated relaxation in S_1 and the Franck-Condon principle governing spontaneous emission to S_0, the fluorescence spectrum is red-shifted from that of the absorption; this is illustrated in figure 1.4.

Non-radiative relaxation such as collisional quenching [7] and dipole-dipole transfer [8] (given the proximity and spectral compatibility of a suitable acceptor) are examples of processes other than fluorescence by which the population in S_1 can be relaxed.

Population can also be lost from S_1 due to electron spin change (intersystem crossing) to the lowest molecular triplet state (T_1). $S_1 \rightarrow T_1$ intersystem crossing times typically range from 10^{-8}-10^{-6} seconds [2]. Once intersystem crossing has taken place molecules are effectively trapped in T_1 as the $T_1 \rightarrow S_0$ spontaneous emission is formally forbidden. In practice this is manifested in a long (10^{-3}-10^{-1} second) triplet lifetime. "Bottle-necking" of population in T_1 can be a problem in continuous wave dye lasers [9] leading to a reduction in gain. Triplet trapping is also a considerable problem in single molecule fluorescence spectroscopy rendering a chromophore effectively dark, i.e. unable to absorb or emit photons for considerable periods of time [10].

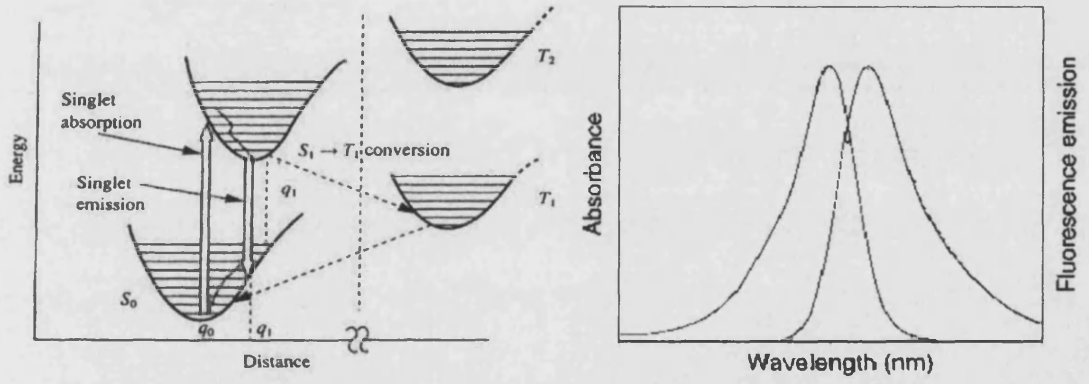

Figure 1.4: Summary of the excited state energy loss pathways, yielding an emission spectrum red-shifted from the absorption.

1.6 Fluorescent Probes

The selection of a fluorescent probe for a particular application is dependent upon the intrinsic photophysical properties of the probe and the information that is required. For polarised photoselection and time resolved fluorescence lifetime and anisotropy studies, characteristics such as a well defined (and maintained) transition dipole moment direction and a fluorescence lifetime compatible with the excited state re-orientation time are desirable. Other characteristics such as emission wavelength and the sensitivity of this to the physical environment or a particular chemical species are widely used in biophysics and life science applications [11]. Energy transfer between donor and acceptor chromophores is manifest by changes in donor lifetime and shifts in emission wavelength; these are widely used to probe conformational change in proteins [8, 12]. To this end a wide range of fluorescent chromophores have been synthesised [13].

Tryptophan in Human Serum Albumen [14] and green fluorescent protein found in the jellyfish *Aquaorae Victoriae* [15] are widely used examples of such systems.

Fluorescent dye probes are utilised throughout this work. Three of the dyes used (Rhodamine 6G, Rhodamine B and Fluorescein) belong to a family of laser dyes known as xanthenes. The molecular structures of these dyes are shown in figure 1.5. The characteristics of these dyes make them very suitable for use in tunable dye lasers [13]; they have broad band visible emission spectra; they are photochemically stable; they have quantum yields close to unity at room temperature, and they have a low probability of excited state absorption or triplet formation [13]. The high quantum yield also makes these dyes ideal for low concentration probes in fluorescence anisotropy experiments. The transition dipole for the $S_0 \rightarrow S_1$ single photon absorption is aligned parallel to the long axis of the molecules [9].

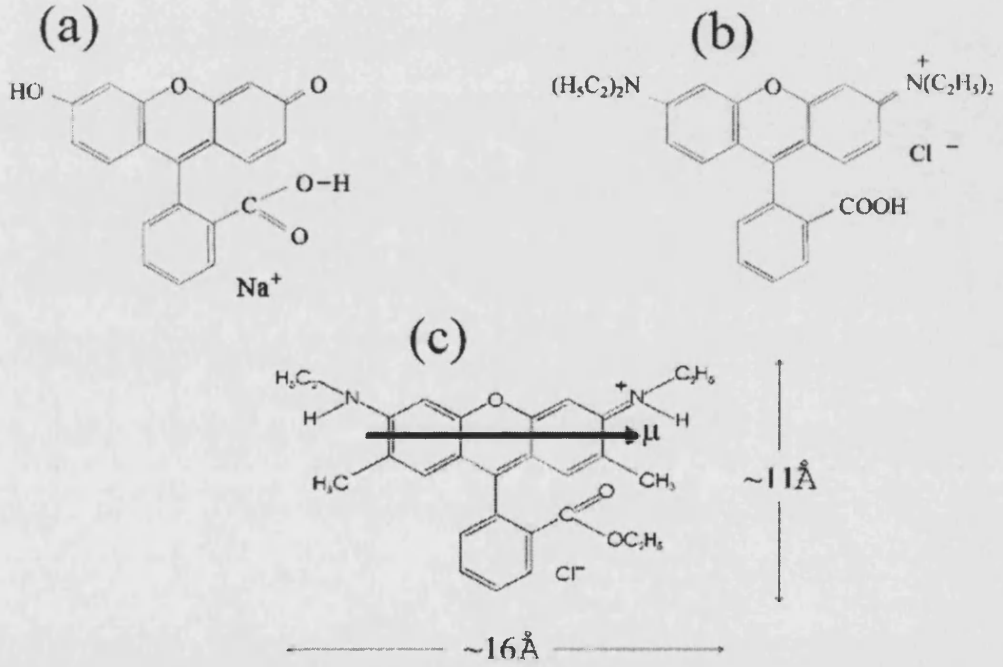

Figure 1.5: The molecular structures of (a) Fluorescein, (b) Rhodamine B and (c) Rhodamine 6G. The typical dimensions and transition dipole moment are shown for Rhodamine 6G.

The fluorescence spectra of Rhodamine 6G, Rhodamine B and Fluorescein are shown alongside their absorption spectra in figure 1.6. It is notable that the spectra are devoid of detailed structure. Like diatomic molecules, polyatomic molecules possess quantised vibrational and rotational degrees of freedom [2], but the density of these rotational and vibrational energy levels results in energy level separations of typically 0.1meV, which is sufficiently small for higher vibrational levels to be populated according to

Boltzmann statistics at ambient temperatures. Since a similarly dense energy level structure exists in the excited state there are, at any given excitation wavelength, a wide range of ground to excited state rovibronic transitions, broadened further by rapid solute-solvent collisions, giving rise to a broadband and featureless absorption spectrum. The density of states in the upper vibrational levels of the ground state is also high, allowing de-excitation to occur with a variety of different energies (as governed by the Franck-Condon factor), that is, a broad range of fluorescence photon wavelengths. The Stokes shift in emission from the absorption peak is approximately 20-30nm in these dyes [13], as illustrated in table 1.1.

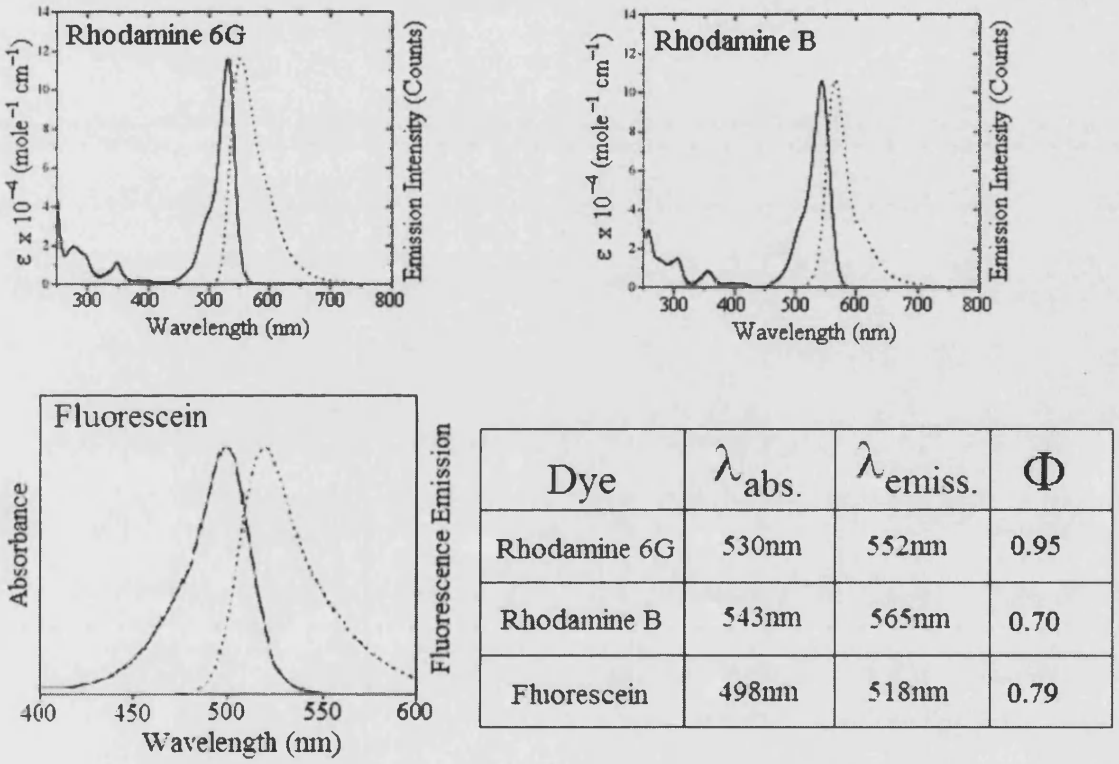

Dye	$\lambda_{abs.}$	$\lambda_{emiss.}$	Φ
Rhodamine 6G	530nm	552nm	0.95
Rhodamine B	543nm	565nm	0.70
Fluorescein	498nm	518nm	0.79

Figure 1.6: Absorption and emission spectra for Rhodamine 6G, Rhodamine B and Fluorescein {Original data from [13]}.

Table 1.1: Absorption maxima (λ_{abs}), emission maxima (λ_{emiss}) and quantum yields (Φ) for Rhodamine 6G, Rhodamine B and Fluorescein in methanol. Stokes shifts in these chromophores between absorption (λ) and emission peaks is typically 20-30nm.

Coumarin 153 has also been used in this work. Coumarins have absorption peaks towards the blue end of the visible spectrum, but the emission peaks are generally red shifted much more than the Rhodamines; the Stokes shift in Coumarin 153 is over 100nm, and Coumarin 153 has a lower quantum yield than the dyes described earlier [13]. The absorption and emission spectra for Coumarin 153 in DMF are shown in figure 1.7.

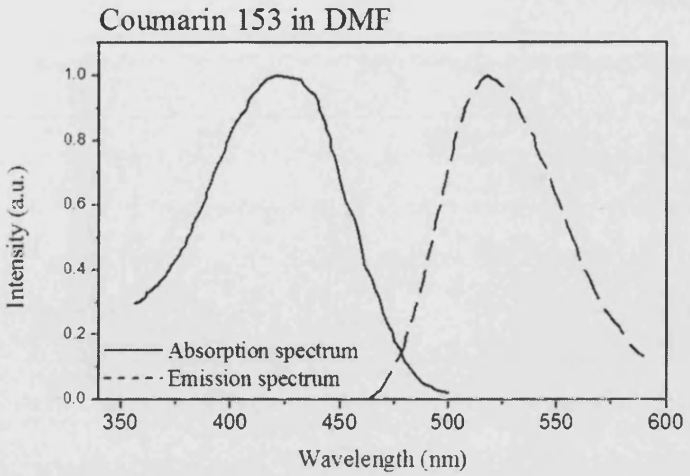

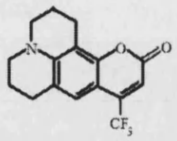

Coumarin 153	
λ_{abs}	421nm
λ_{emiss}	518nm
Φ	0.60

Figure 1.7: (Normalised) steady-state absorption and emission spectra of Coumarin 153 in DMF {original data from W C Flory & G J Blanchard, Applied Spectrscopy 52(1), 82 (1998)}; molecular structure of Coumarin 153; absorption & emission maxima, and quantum yield for Coumarin 153.

1.7 The Orientational Distribution Function

The ability of polarised photoselection experiments to provide information on probe molecular order and motion relies on the angular dependence of the excitation probability (i.e. the orientation of the molecular transition dipole moment with respect to the excitation polarisation vector). Ground state molecular orientation will thus affect both the transition probability and the order produced in the excited state. This in turn will determine the polarisation of fluorescence. To this end it is convenient to employ a formalism where molecular order and its influence on experimental observables is clearly set out. This is most easily achieved using a spherical harmonic expansion of the ground (and excited) state orientational distribution function $P(\theta,\varphi)$, which represents the probability of finding a molecule that is oriented between θ and $\theta+d\theta$ and between φ and $\varphi+d\varphi$ (figure 1.8).

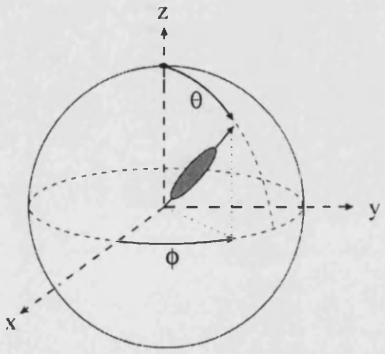

Figure 1.8: The spherical co-ordinate system used to define the orientational distribution function $P(\theta,\varphi)$

In a spherical harmonic expansion $P(\theta,\varphi)$ is given by [16]

$$P(\theta,\varphi)=\Sigma_{KQ}\langle C_{KQ}\rangle Y_{KQ}(\theta,\varphi) \qquad [1.4]$$

where $Y_{KQ}(\theta,\varphi)$ are spherical harmonics of rank K and projection Q [17] and $\langle C_{KQ}\rangle$ are the corresponding expansion coefficients which determine the explicit form of $P(\theta,\varphi)$. Spherical harmonics are constructed from Legendre Polynomials ($P_{KQ}(\cos\theta)$) as [4]:

$$Y_{KQ}(\theta,\varphi)=\sqrt{\frac{(2K+1)(K-Q)!}{4\pi(K+Q)!}}P_{KQ}(\cos\theta)e^{iQ\varphi} \qquad [1.5]$$

For each value of K there are 2K+1 possible functions with values Q which range in integer steps from +K to -K. In terms of spherical harmonics the orientational distribution function is written as

$$\int_0^{2\pi}\int_0^{\pi} Y^*_{KQ}(\theta,\varphi)Y_{KQ}(\theta,\varphi)\sin\theta d\theta d\varphi = \delta_{KK'}\delta_{QQ'} \qquad [1.6]$$

where

$$Y^*_{KQ}(\theta,\varphi)=(-1)^Q Y_{K-Q'}(\theta,\varphi) \qquad [1.7]$$

the moments of the expansion can then be found from [16]

$$\langle C_{KQ}\rangle = \int_0^{2\pi}\int_0^{\pi} Y^*_{KQ}(\theta,\varphi)P(\theta,\varphi)\sin\theta d\theta d\varphi \qquad [1.8]$$

The functional forms and graphical representations of some spherical harmonics are shown in table 1.2.

$Y_{00} = \left(\frac{1}{4\pi}\right)^{1/2}$	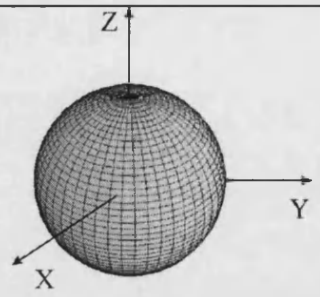
$Y_{20} = \left(\frac{5}{4\pi}\right)^{1/2} \frac{1}{2}\left(3\cos^2\theta - 1\right)$	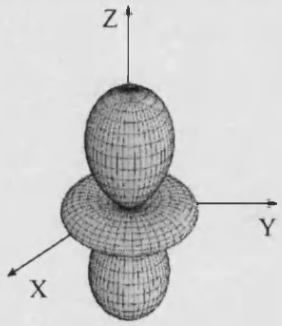
$Y_{2\pm2} = \left(\frac{15}{32\pi}\right)^{1/2} \sin^2\theta e^{\pm 2i\varphi}$	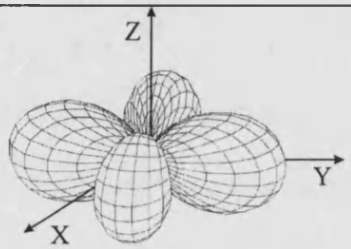
$Y_{40} = \left(\frac{1}{4\pi}\right)^{1/2} \frac{3}{8}\left(35\cos^4\theta - 30\cos^2\theta + 3\right)$	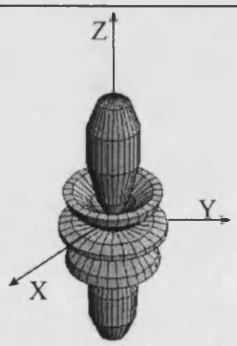
$Y_{60} = \left(\frac{13}{4\pi}\right)^{1/2} \frac{1}{16}\left(\begin{matrix}231\cos^6\theta - 315\cos^4\theta \\ +105\cos^2\theta - 5\end{matrix}\right)$	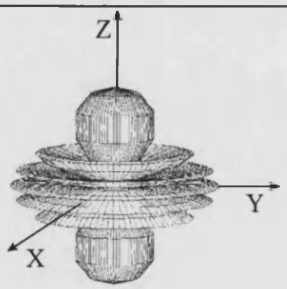

Table 1.2: Graphical representations of the axially symmetric and axially asymmetric spherical harmonics discussed in this thesis: The moments of Y_{00}, Y_{20} and $Y_{2\pm2}$ are directly measurable in polarised fluorescence experiments (fluorescence observables). Moments of higher order moments of even rank and zero projection (i.e. $K_{EVEN}>2$, $Q=0$) are employed to describe fully the ground state distribution function of dye probes in aligned nematic liquid crystals, as shown in Chapter 2.

The probability of finding a molecule on the unit sphere is unity:

$$\int_0^{2\pi}\int_0^{\pi} P(\theta,\varphi)\sin\theta d\theta d\varphi = 1 \qquad [1.9]$$

Substitution of equation 1.8 into equation 1.9 yields

$$\sum_{KQ}\langle C_{KQ}\rangle \int_0^{2\pi}\int_0^{\pi} Y_{KQ}(\theta,\varphi)\sin\theta d\theta d\varphi = 1 \qquad [1.10]$$

This can be written as [16]

$$\sum_{KQ}\langle C_{KQ}\rangle (4\pi)^{1/2} \int_0^{2\pi}\int_0^{\pi} Y_{00}^{*}(\theta,\varphi) Y_{KQ}(\theta,\varphi)\sin\theta d\theta d\varphi = 1 \qquad [1.11]$$

From equation 1.6 the only non-zero contribution is $\langle C_{00}\rangle = \left(\frac{1}{4\pi}\right)^{1/2}$.

The $\langle C_{00}\rangle$ (population) term is necessarily present in any orientational distribution function, so it is convenient to normalise the higher order expansion coefficients of the distribution function to $\langle C_{00}\rangle$. It will be seen that the normalised moments correspond to directly measurable physical quantities:

$$P(\theta,\varphi) = \langle C_{00}\rangle \sum_{KQ}\langle \alpha_{KQ}\rangle Y_{KQ}(\theta,\varphi) \qquad [1.12]$$

where $\langle \alpha_{KQ}\rangle = \langle C_{KQ}\rangle / \langle C_{00}\rangle$ [1.13]

1.8 Photoselection with Picosecond and Femtosecond Laser Pulses

1.8.1 Weak Excitation

Throughout this thesis, excited state molecular populations are prepared by pulsed excitation; a cavity dumped synchronously pumped dye laser is used in the single photon photoselection experiments of Chapter 2. A (regeneratively amplified) Ti:Sapphire laser is used for the two-photon excited fluorescence studies of Chapter 3, and as the excitation source for the stimulated emission depletion (STED) studies of Chapters 4 and 5. In all of these experiments, initial probe photoselection is achieved by polarised excitation from an isotropic ground state (in STED) and an aligned liquid crystal mesophase for the studies of Chapters 2 and 3.

The spherical polar co-ordinate system used to describe polarised photoselection in the laboratory frame of reference is illustrated in figure 1.9. The single photon transition probability for a molecule with a transition dipole moment μ oriented at an angle θ with respect to the electric field E of the excitation pulse is given by (where B is a constant of proportionality):

$$W(\theta,\varphi) = B\left|\langle f|E.\mu|i\rangle\right|^2$$

$$= B|E|^2\left|\mu_{fi}\right|^2\cos^2\theta \qquad [1.14]$$

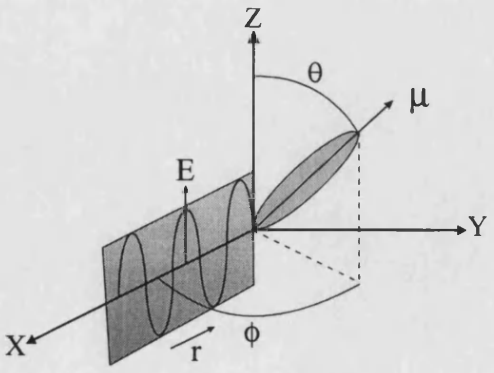

Figure 1.9: The spherical co-ordinate frame is used to define the transition dipole moment in the laboratory frame. The propagation direction $\underline{r}$ of the incident electromagnetic radiation, the polarisation plane and the direction of the electric field amplitude E are shown.

If only a small fraction of the ground state population is removed, the excited state population distribution is (assuming an isotropic ground state):

$$N_{ex}(\theta,\varphi) = N_{gs} W(\theta,\varphi) \qquad [1.15]$$

For Z-polarised excitation (as in figure 1.8)

$$N_{ex}(\theta,\varphi) \propto N_{gs} \cos^2 \theta \qquad [1.16]$$

The molecular probes used throughout this work are well described in terms of a four-level system. Pumping from lower ground state vibrational levels (level 1) to a rapidly deactivated set of excited vibrational levels (level 2) which when thermalised (level 3) emit to rapidly deactivated ground state vibrational levels (level 4 to level 1). As the transition between levels 2 and 3 is rapid and due to unfavourable Franck-Condon factors, levels 1 and 3 are not optically connected, re-pumping of the ground state (level 2 to 1) during the excitation pulse is small.

As will be seen for molecules with parallel absorption and emission transition dipole moment directions a distribution of this form results in an initial fluorescence anisotropy (R(0)) of 0.4. If, however, the transition strength were increased such that a significant fraction of the isotropic ground state population were pumped into the excited state, this distribution would be considerably less polarised and R(0) would be reduced. It is thus important to keep the degree of ground state depopulation low such that $N_{gs} >> N_{ex}$.

The rate equations for the population of level 3 assuming the rate of transfer from level 1 to level 2 is rapid is given by

$$\frac{dN_3}{dt} = \frac{I(t)\sigma}{h\nu} N_1 - N_3 \gamma_{34} \qquad [1.17]$$

where σ is the absorption cross-section (cm^2) and γ_{34} is the spontaneous decay rate of the S_1 population (level 3) to the ground state vibrational levels (level 4). For picosecond excitation, fluorescence during the pulse timescale can be neglected. Integrating over I(t) and assuming $N_1 >> N_3$,

$$N_3 = \frac{\sigma N_1}{h\nu}\int I(t)dt \qquad \left[\left(= \frac{\sigma}{h\nu A}\int \frac{dE_P(t)}{dt}dt\right)\right] \qquad [1.18]$$

$$= \frac{\sigma E_P}{h\nu A} \qquad (=S) \qquad [1.19]$$

where E_P is the pulse energy and A is the focused spot size. Equation 1.19 introduces a transition saturation parameter $S(=\sigma E_P/h\nu A)$. In the weak excitation limit $S<<1$, and the transition probability follows the $\cos^2\theta$ angular dependence introduced in equation 1.16. In the photoselection experiments described in Chapter 2, typical excitation pulse parameters are $\sigma \approx 10^{-16}cm^{-2}$, $E_p \approx 3.3x10^{-13}J$, $h \approx 6.6x10^{-34}Js$, $\nu \approx 5x10^{14}s^{-1}$ and $A \approx 10^{-5}cm^{-2}$ [18]. This yields for saturation parameter S

$$S \approx \frac{3.3}{33}\left(\frac{10^{-16}.10^{-13}}{10^{-34}.10^{14}.10^{-5}}\right) \approx 1.10^{-5}$$

1.8.2 Strong Excitation Dynamics

In a fluorescent probe the spontaneous emission resulting from the transition between levels 3 and 4 can (as will be seen in Chapters 4 and 5) be strongly perturbed by stimulated emission using an intense time-delayed laser pulse $I_D(t)$ following excitation. Under these conditions

$$\frac{dN_3}{dt} = -\frac{I_D(t)\sigma_{STIM}}{h\nu}(N_3 - N_4) - \frac{N_3}{\tau_f} \qquad [1.20]$$

$$\frac{dN_4}{dt} = \frac{I_D(t)\sigma_{STIM}}{h\nu}(N_3 - N_4) + \frac{N_3}{\tau_f} - \frac{N_4}{\tau_{vib}} \qquad [1.21]$$

where σ_{STIM} represents the stimulated emission cross-section (cm^2), τ_f the fluorescence lifetime of level 3 and τ_{vib} the vibrational lifetime of level 4. Typical timescales for τ_f and τ_{vib} are nanosecond and picosecond-sub-picosecond respectively [6]. For a pulse with width (τ_P) in the range of hundreds of femtoseconds to picoseconds, there is still sufficient time to re-pump level 3 from level 4. The saturation parameter S for the stimulated emission transition $\left(= \sigma_{STIM} E_D / h\nu A\right)$ and the ratio of laser pulsewidth to level 4 vibrational lifetime ($\tau_P/\ \tau_{vib}$) are critical factors in the investigation of stimulated emission depletion, as will be discussed in Chapter 4.

1.9 Fluorescence Anisotropy

Weak excitation from an isotropic ground state yields an excited state orientational probability distribution that has the same form as the transition probability. Expanding $\cos^2\theta$ in spherical harmonics [16]:

$$\cos^2\theta = \frac{\sqrt{4\pi}}{3}\left[Y_{00}(\theta,\varphi) + \frac{2}{\sqrt{5}}Y_{20}(\theta,\varphi)\right] \qquad [1.22]$$

In the limit of weak excitation the photoselected excited state population N_{ex} is given by

$$N_{ex}(\theta,\varphi) = N_{gs}P_{ex}(\theta,\varphi) \qquad [1.23]$$

The substitution of equations 1.22 and 1.23 into equations 1.4 and 1.16 yields for $P_{ex}(\theta,\varphi)$ and $N_{ex}(\theta,\varphi)$:

$$P_{ex}(\theta,\varphi) = C\frac{\sqrt{4\pi}}{3}\left[Y_{00}(\theta,\varphi) + \frac{2}{\sqrt{5}}Y_{20}(\theta,\varphi)\right] \qquad [1.24]$$

$$N_{ex}(\theta,\varphi) = CN_{gs}\frac{\sqrt{4\pi}}{3}\left[Y_{00}(\theta,\varphi) + \frac{2}{\sqrt{5}}Y_{20}(\theta,\varphi)\right] \qquad [1.25]$$

where C is a constant of proportionality. Integrating over all angles and normalising to unity yields total excited state population

$$N_{ex} = C\frac{\sqrt{4\pi}}{3}\int_0^{2\pi}\int_0^{\pi}\left[Y_{00}(\theta,\varphi) + \frac{2}{\sqrt{5}}Y_{20}(\theta,\varphi)\right]\sin\theta d\theta d\varphi \qquad [1.26]$$

giving

$$C = \frac{3}{\sqrt{4\pi}}N_{ex} \qquad [1.27]$$

and

$$P_{ex}(\theta,\varphi)=\frac{1}{\sqrt{4\pi}}\left[\frac{1}{\sqrt{4\pi}}Y_{00}(\theta,\varphi)+\frac{2}{\sqrt{5}}Y_{20}(\theta,\varphi)\right] \qquad [1.28]$$

In time resolved fluorescence anisotropy experiments, an excited state molecular population is photoselected by an ultrashort laser pulse which is normally linearly polarised [18]. The angle-dependent photoselection creates an ordered array of excited state molecules which corresponds to an anisotropy in the angular distribution of absorption and emission transition dipole moments, resulting in a difference in fluorescence intensity for polarisations parallel and perpendicular to the excitation field. Two experimental observables are required in order to construct the fluorescence anisotropy; these are the linearly polarised fluorescence intensities parallel ($I_{\parallel}$) and perpendicular ($I_{\perp}$) to the excitation polarisation. The subsequent fluorescence anisotropy is defined from these observables as [19]

$$R(t)=\frac{I_{\parallel}(t)-I_{\perp}(t)}{I_{\parallel}(t)+2I_{\perp}(t)} \qquad [1.29]$$

In practice the orthogonally polarised fluorescence components can be collected using either a right-angled or collinear excitation-detection geometry, shown in figure 1.10. In conventional fluorescence experiments the Z-axis of the experimental geometry is determined by the polarisation vector of the excitation pulse; the right-angle configuration and collinear configuration yield equivalent information since the photoselection process has cylindrical symmetry about the laboratory Z-axis, that is

$$R(t)=\frac{I_Z(t)-I_Y(t)}{I_Z(t)+2I_Y(t)}=\frac{I_Z(t)-I_X(t)}{I_Z(t)+2I_X(t)} \quad \text{for a Z-polarised excitation pulse.} \qquad [1.30]$$

The right-angled geometry exploits the φ-independence of the excitation process in isotropic or cylindrically symmetric media; the excited state population has cylindrical symmetry and all collection angles in the laboratory X-Y plane are equivalent. It will be shown in the next chapter that the excitation process is no longer φ-independent for variable excitation polarisation angle experiments, and earlier work [18] has shown that the collinear excitation-detection geometry is very versatile in fluorescence studies in

both isotropic and anisotropic media. Both geometries are utilised extensively throughout this work.

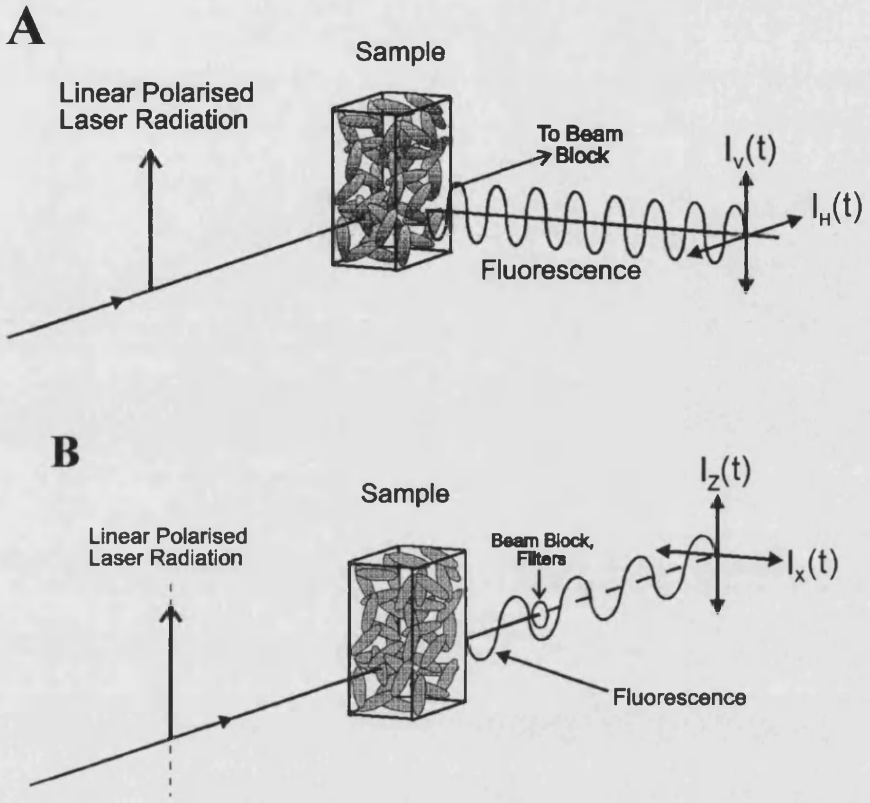

Figure 1.10: Polarised fluorescence components can be detected using (a) a 90° geometry or (b) a 180° "collinear" excitation detection geometry.

The linearly polarised fluorescence intensity of the $S_1 \rightarrow S_0$ transition with initial state $|i\rangle$ and final state $|f\rangle$ with a linear polarisation vector $\hat{e}_i$ in the laboratory frame is given by [16]

$$I_i(t) = B \int_0^{2\pi} \int_0^{\pi} |\langle f|\mu.\hat{e}_i|i\rangle| N_{ex}(\theta,\varphi,t) \sin\theta d\theta d\varphi \qquad [1.31]$$

where B is a constant of proportionality. For the vertical (V) and horizontal (H) components of fluorescence, $\hat{e}_i$ is given by

$$\begin{aligned} \hat{e}_V &= \cos\theta \\ \hat{e}_H &= \sin\theta \sin\varphi \end{aligned} \qquad [1.32]$$

The expressions in 1.31 utilise θ and φ as defined in figure 1.8. Substituting these expressions into equation 1.30 and expressing $N_{ex}(\theta,\varphi,t)$ in terms of the orientational distribution function gives the vertical and horizontal components of fluorescence intensity as

$$I_V(t) = BN_{ex}(t)\left|\mu_{fi}\right|^2 \int_0^{2\pi}\int_0^{\pi} \cos^2\theta P_{ex}(\theta,\varphi,t)\sin\theta d\theta d\varphi$$
$$I_H(t) = BN_{ex}(t)\left|\mu_{fi}\right|^2 \int_0^{2\pi}\int_0^{\pi} \sin^2\theta \sin^2\varphi P_{ex}(\theta,\varphi,t)\sin\theta d\theta d\varphi \qquad [1.33]$$

Expressing the emission probability in terms of spherical harmonics [18] and expanding the orientational distribution function, the emission intensities can be rewritten as

$$I_V(t) = BN_{ex}(t)\left|\mu_{fi}\right|^2 \frac{\sqrt{4\pi}}{3}\sum_{KQ}\left\langle C_{KQ}^{ex}(t)\right\rangle \int_0^{2\pi}\int_0^{\pi} Y_{KQ}(\theta,\varphi)\left[Y_{00}(\theta,\varphi)+\frac{2}{\sqrt{5}}Y_{20}(\theta,\varphi)\right]\sin\theta d\theta d\varphi$$
$$I_H(t) = BN_{ex}(t)\left|\mu_{fi}\right|^2 \frac{\sqrt{4\pi}}{3}\sum_{KQ}\left\langle C_{KQ}^{ex}(t)\right\rangle \int_0^{2\pi}\int_0^{\pi} Y_{KQ}(\theta,\varphi)$$
$$\left[Y_{00}(\theta,\varphi)-\frac{1}{\sqrt{5}}Y_{20}+\sqrt{\frac{3}{10}}\{Y_{22}(\theta,\varphi)+Y_{2-2}(\theta,\varphi)\}\right]\sin\theta d\theta d\varphi \qquad [1.34]$$

The solution of these integrals is given in [18] and yields

$$I_V(t) = BN_{ex}(t)\left|\mu_{fi}\right|^2 \frac{\sqrt{4\pi}}{3}\left[\left\langle C_{00}^{ex}\right\rangle+\frac{2}{\sqrt{5}}\left\langle C_{20}^{ex}(t)\right\rangle\right] \qquad [1.35]$$

$$I_H(t) = BN_{ex}(t)\left|\mu_{fi}\right|^2 \frac{\sqrt{4\pi}}{3}\left[\left\langle C_{00}^{ex}\right\rangle-\frac{1}{\sqrt{5}}\left\langle C_{20}^{ex}(t)\right\rangle+\sqrt{\frac{3}{10}}\left\{\left\langle C_{22}^{ex}(t)\right\rangle+\left\langle C_{2-2}^{ex}(t)\right\rangle\right\}\right] \qquad [1.36]$$

The time evolution of the polarised components of fluorescence intensity is expressed in terms of the invariant $\left\langle C_{00}^{ex}\right\rangle$ population term and the time dependent $\left\langle C_{20}^{ex}(t)\right\rangle$ and $\left\{\left\langle C_{22}^{ex}(t)+C_{2-2}^{ex}(t)\right\rangle\right\}$ moments. Normalising these moments to $\left\langle C_{00}^{ex}\right\rangle$ and substituting the fluorescence intensity components into the expression for the fluorescence anisotropy (equation 1.29) gives

$$R(t)=\frac{\frac{1}{\sqrt{5}}\langle\alpha_{20}^{ex}(t)\rangle-\frac{1}{\sqrt{30}}\{\langle\alpha_{22}^{ex}(t)\rangle+\langle\alpha_{2-2}^{ex}(t)\rangle\}}{1+\frac{2}{\sqrt{30}}\{\langle\alpha_{22}^{ex}(t)\rangle+\langle\alpha_{2-2}^{ex}(t)\rangle\}} \quad [1.37]$$

Thus the fluorescence anisotropy can be described in terms of the orientational distribution of the photoselected excited state. Furthermore, this expression indicates that the fluorescence anisotropy from a single photon photoselected excited state is sensitive only to the alignment (specified by K=2) of the population, and depends on a cylindrically symmetric moment (Q=0) and cylindrically asymmetric moment (Q=±2). The evolution of these moments is governed by diffusion in the liquid phase, whereby the non-equilibrium photoselected excited state order is dissipated due to randomising collisions with solvent molecules.

1.10 Diffusion

1.10.1 Debye Small Step Diffusion

In a fluid medium probe molecules are in continuous rapid interaction with their neighbours, and hence probe motion is governed by a hindering frictional force resulting from the transfer of momentum during solute-solvent collisions. The collisional timescale in a liquid is between 10^{-14}s and 10^{-13}s [20] which is rapid compared to molecular reorientation rates (10^{-12}s – 10^{-9}s). The rotational motion of molecules in a viscous medium can be expressed using Debye's small step diffusion model which describes the reorientation of a molecule as a random walk trajectory on the surface of a unit sphere [21]. The temporal evolution of the orientational distribution function of a non-equilibrium population of excited state molecules undergoing diffusion in an isotropic liquid is given by

$$\frac{\partial P_{ex}(\theta,\varphi,t)}{\partial t}=D_{rot}\nabla^2 P_{ex}(\theta,\varphi,t) \quad [1.38]$$

with

$$D_{rot}\nabla^2 = \sum_i D_i L_i^2 \qquad [1.39]$$

where D_{rot} is termed the rotational diffusion coefficient tensor, L_i^2 is the orbital angular momentum operator in the molecular frame [22] and ∇^2 is the Laplacian operator. By expressing the orientational distribution function in terms of spherical harmonics, the Debye equation becomes

$$\frac{\partial}{\partial t}\sum_{KQ}\langle C_{KQ}(t)\rangle Y_{KQ}(\theta,\varphi) = D\sum_{K'Q'}\nabla^2\langle C_{K'Q'}(t)\rangle Y_{K'Q'}(\theta,\varphi) \qquad [1.40]$$

Since the spherical harmonics $Y_{KQ}(\theta,\varphi)$ are eigenfunctions of the Laplacian operator with eigenvalues $-K(K+1)$,

$$\frac{\partial}{\partial t}\sum_{KQ}\langle C_{KQ}(t)\rangle Y_{KQ}(\theta,\varphi) = -D\sum_{K'Q'}K(K+1)\langle C_{K'Q'}(t)\rangle Y_{K'Q'}(\theta,\varphi) \qquad [1.41]$$

Multiplication by $Y^*_{KQ}(\theta,\varphi)$ and integrating over θ and φ gives

$$\begin{aligned}\frac{\partial}{\partial t}\sum_{KQ}\langle C_{KQ}(t)\rangle Y_{KQ}(\theta,\varphi) &= -D\sum_{K'Q'}K'(K'+1)\langle C_{K'Q'}(t)\rangle \int_0^{2\pi}\int_0^{\pi} Y^*_{KQ}(\theta,\varphi)Y_{K'Q'}(\theta,\varphi)\sin\theta d\theta d\varphi \\ &= -D\sum_{K'Q'}K'(K+1)\langle C_{K'Q'}(t)\rangle \delta_{KK'}\delta_{QQ'} \qquad [1.42]\end{aligned}$$

Hence

$$\frac{\partial}{\partial t}\langle C_{KQ}(t)\rangle = -DK(K+1)\langle C_{K'Q'}(t)\rangle \qquad [1.43]$$

This is a first order differential equation with solution

$$\langle C_{KQ}(t)\rangle = \langle C_{KQ}(0)\rangle \exp[-DK(K+1)t] \qquad [1.44]$$

So the rate at which each moment in the excited state orientational distribution relaxes to zero (the equilibrium isotropic distribution) is given by

$$\gamma_{KQ} = DK(K+1) \qquad [1.45]$$

The fluorescence anisotropy is sensitive to excited state moments with rank K=2, so the re-orientational lifetime $\tau_{or} = 1/\gamma_{20}$ that is directly measureable in time resolved fluorescence experiments in isotropic media is given by

$$\tau_{or} = \frac{1}{\gamma_{20}} = \frac{1}{\gamma_{2\pm2}} = \frac{1}{6D_{rot}} \qquad [1.46]$$

The re-orientational lifetime is independent of projection Q. For an isotropic medium the measured relaxation rate must be the same for any chosen co-ordinate system, so γ_{KQ} is dependent only upon rank K. It will be shown in Chapter 2 that the imposition of ground state order can break this equivalence and affect the excited state dynamics of the system.

1.10.2 Diffusion Coefficient D

The photoselection process that has been described in this chapter creates a non-equilibrium ordered population, which is manifested by an excited state anisotropy in polarised components of fluorescence emission. The angular averaging of the non-equilibrium population can be expressed using diffusion, that is, as a concentration gradient arising from a perturbation, in this case, the process of photoselection. Other examples of physical gradients include heat (temperature gradient) and electricity (electric potential gradient). Fick [23] postulated that the potential for diffusive flux J_x in an arbitrary direction x was proportional to the number density N(x,t) per unit distance dx. This is known as Fick's first law:

$$J_x = -D\frac{dN(x,t)}{dx} \qquad [1.47]$$

where D is a proportionality constant known as the diffusion coefficient. The negative sign indicates the flow of matter in the direction of decreasing concentration. The

conservation of mass applied to a restricted volume differential element formed by arbitrary area A and thickness dx can be expressed by

$$\frac{dN(x,t)}{dt} = -\frac{d(J_x)}{dx} \qquad [1.48]$$

Combining this expression with equation 1.47 and assuming D to be independent of concentration yields an expression for the time evolution of concentration; this is known as the diffusion equation:

$$\frac{dN(x,t)}{dt} = D\frac{d^2N(x,t)}{dx^2} \qquad [1.49]$$

yielding solution [4]

$$N(x,t) = \frac{N}{(4\pi Dt)^{1/2}}\exp\left(-\frac{x^2}{4Dt}\right) \qquad [1.50]$$

This describes the spatial and temporal evolution of the particle concentration with initial conditions that all particles are concentrated in the YZ plane x=0 for t=0. Since diffusion will occur in directions +x and –x, the mean displacement at any time is zero, so particle spread is measured via the mean square displacement:

$$\langle x^2 \rangle = \frac{1}{N}\int_{-\infty}^{\infty} x^2 N(x,t) \qquad [1.51]$$

yielding the Einstein-Smoluchowski equation [24]

$$\langle x^2 \rangle = \frac{1}{N}\frac{N}{(4\pi Dt)^{1/2}}\int_{-\infty}^{\infty} x^2 \exp\left(-\frac{x^2}{4Dt}\right)dx \qquad [1.52]$$

$$\langle x^2 \rangle = 2Dt \qquad [1.53]$$

From a microscopic standpoint, the diffusive mechanism experienced by pollen particles suspended in solution was first observed by Robert Brown in 1827. This series of irregular movements was subsequently named Brownian motion [25].

In his investigations of Brownian motion Einstein concluded that the random movements of a particle arose from a fluctuating pressure difference caused by the continuous bombardment on all sides by neighbouring particles [26]. The application of Newtonian mechanics to a Brownian particle of mass M and velocity v experiencing a fluctuating force B(t) yields Langevin's equation:

$$M\frac{dv}{dt} = -M\xi v + B(t) \qquad [1.54]$$

where ξ is the microscopic friction constant [27]. Multiplication by x/M gives

$$x\ddot{x} = -\xi x\dot{x} + x\frac{B(t)}{M} \qquad [1.55]$$

Upon the substitutions $\dot{x}^2 = 2x\dot{x}$ and $\ddot{x}^2 = 2(\dot{x})^2 + 2x\dot{x}$ this becomes

$$\frac{1}{2}\ddot{x}^2 - (\dot{x})^2 = -\frac{\xi}{2}\dot{x}^2 + x\frac{B(t)}{M} \qquad [1.56]$$

Using the equipartition theorem the average kinetic energy can be written as [26]

$$\frac{1}{2}M\langle\dot{x}^2\rangle = \frac{1}{2}k_B T \qquad [1.57]$$

where k_B is Boltzmann's constant, T is the absolute temperature and $\langle\ \rangle$ denotes an average in time. If the average value of the fluctuating force is zero, the substitution of $\langle\dot{x}^2\rangle$ into a time average form of equation 1.56 gives

$$\frac{d^2}{dx^2}\langle x^2\rangle - \left(\frac{2k_B T}{M}\right) = -\xi\frac{d}{dt}\langle x^2\rangle \qquad [1.58]$$

Einstein's solution to this equation is written as [26]

$$\left\langle x^2 \right\rangle = \frac{2k_B T}{M\xi}\left\{t - (\xi)^{-1}\left(1 - e^{-\xi t}\right)\right\} \qquad [1.59]$$

In the very short time regime, $t<<\xi^{-1}$ and $\left\langle x^2 \right\rangle \approx (k_B T/M)t^2$ so the particles move with thermal velocity $\sqrt{2k_B T/M}$. At longer times the dominant process is Brownian movement and

$$\left\langle x^2 \right\rangle \approx (2k_B T/M\xi)t \qquad [1.60]$$

Combining this equation with equation 1.53 allows the macroscopic diffusion coefficient D to be written in terms of the microscopic frictional force constant:

$$D = \frac{k_B T}{\xi} \qquad [1.61]$$

For a spherical molecule of radius R in a medium with viscosity η, the frictional coefficient can be expressed by applying Stokes' law [28]:

$$\xi = 6\pi\eta R \qquad [1.62]$$

and the diffusion coefficient becomes

$$D = \frac{k_B T}{6\pi\eta R} \qquad [1.63]$$

In the Brownian motion description, diffusion can be separated into translational and rotational motion, which can be considered as independent. Equation 1.53 expressed the translational diffusion coefficient in terms of the mean square displacement in time along one spatial (x) dimension. Extending this to three dimensional space yields

$$\left\langle r^2 \right\rangle_{XYZ} = 6D_{trans}t \qquad [1.64]$$

Similarly, the rotational diffusion coefficient can be expressed in terms of the mean square angular displacement $\langle\theta^2\rangle$ with time by

$$\langle\theta^2\rangle = 4D_{rot}t \qquad [1.65]$$

Furthermore, in the same way that the translational frictional coefficient for a particle with diffusion velocity v can be described by a force $f=-\xi_{trans}v$, so too can the rotational frictional coefficient be described in terms of a torque T acting on a particle with rotational velocity Ω, such that

$$T = -\xi_{rot}\Omega \qquad [1.66]$$

Applying the Langevin equation to rotational Brownian motion yields [4]

$$D_{rot} = \frac{k_B T}{\xi_{rot}} \qquad [1.67]$$

Up to this point it has been assumed that diffusing molecules can be described by an isotropic diffusion coefficient. In reality this is not the case; for non-spherical molecules, the diffusion coefficient is not a scalar quantity but a second rank tensor [16] with up to three independent components D*x*, D*y*, and D*z*. For uniaxial molecules such as nematic liquid crystals (discussed in Chapter 2), two of the three principle axes are equivalent, resulting in two independent diffusion coefficients $D_\perp$ and $D_\parallel$ which correspond to θ and φ diffusion respectively, as illustrated in figure 1.11.

$$D_\perp = D_x = D_y \qquad (\theta \text{ diffusion}) \qquad [1.68]$$

$$D_\parallel = D_z \qquad (\varphi \text{ diffusion}) \qquad [1.69]$$

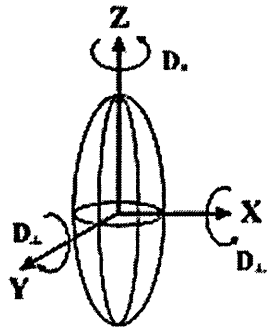

Figure 1.11: Uniaxial molecules display two independent diffusion coefficients, $D_{\parallel}$ and $D_{\perp}$, corresponding to diffusion in the Z-axis and X & Y axes respectively.

Equation 1.43 described the temporal evolution of the excited state distribution function moments with rank K and projection Q in an isotropic system:

$$\left\langle C_{KQ}^{ex}(t)\right\rangle_{isotropic} = \left\langle C_{KQ}^{ex}(0)\right\rangle \exp[-DK(K+1)t] \qquad [1.70]$$

where D is the diffusion coefficient. It should be noted that the isotropic decay rate of any moment $\left\langle C_{KQ}^{ex}(t)\right\rangle$ depends only upon its rank K. Furthermore in an isotropic medium the rotational diffusion rate must be independent of the choice of axis system, so the net alignment decay rates must be independent of Q. This result requires more consideration since moments for which Q is not equal to zero are sensitive both to θ and φ diffusion; although this is not significant for isotropic environments, this becomes relevant when dealing with ordered systems, as discussed in Chapter 2. Furthermore, in isotropic media where probe molecule motion exhibits inertial (free rotation) or co-operative behaviour, this picture of orientational relaxation (i.e. equation 1.70) does not hold [29].

The time dependent diffusion dynamics introduced in equation 1.70 can be written as:

$$\left\langle C_{KQ}^{ex}(t)\right\rangle - \left\langle C_{KQ}^{ex}(ss)\right\rangle = \left\{\left\langle C_{KQ}^{ex}(0)\right\rangle - \left\langle C_{KQ}^{ex}(ss)\right\rangle\right\}\exp(-\gamma_{KQ}t) \qquad [1.71]$$

where

$$\gamma_{KQ} = D\langle KQ|\nabla^2|KQ\rangle \qquad [1.72]$$

Expressing ∇^2 in terms of normalised angular momentum operators (in units of ħ) yields [22]

$$\nabla^2 = -\left(\hat{J}_X^2 + \hat{J}_Y^2 + \hat{J}_Z^2\right) = -\hat{J}^2 \qquad [1.73]$$

where $\hat{J}_X$, $\hat{J}_Y$ and $\hat{J}_Z$ are the generators of infinitesimal rotation about the x, y and z laboratory axes respectively. In terms of polar co-ordinates $\hat{J}_X^2 + \hat{J}_Y^2$ corresponds to θ diffusion and $\hat{J}_Z^2$ corresponds to φ diffusion. Expressing $\hat{J}_X^2 + J_Y^2$ in terms of angular momentum raising and lowering operators yields

$$\hat{J}_X^2 + J_Y^2 = \frac{1}{2}\{J_+ J_- + J_- J_+\} \qquad [1.74]$$

$D\nabla^2$ contains both θ and φ diffusion operators, which can be expressed as follows:

$$\gamma_{KQ}(\theta) = D(\theta)\langle KQ|\frac{1}{2}\{J_+ J_- + J_- J_+\}|KQ\rangle = D_\perp\left[K(K+1) - Q^2\right] \qquad [1.75]$$

$$\gamma_{KQ}(\varphi) = D(\varphi)\langle KQ|\hat{J}_Z^2|KQ\rangle = D_\parallel Q^2 \qquad [1.76]$$

Applying equations 1.75 and 1.76 to equation 1.70 yields the following diffusion rates for the fluorescence observable moments $\langle C_{20}^{ex}(t)\rangle$ and $\langle C_{2+2}^{ex}(t)\rangle + \langle C_{2-2}^{ex}(t)\rangle$ in terms of θ and φ diffusion:

$$\gamma_{20} = 2(3)D_\perp + 0D_\parallel = 6D_\perp \qquad \text{(θ diffusion only)} \qquad [1.77]$$

$$\gamma_{22} = \gamma_{2-2} = 2D_\perp + 4D_\parallel \qquad \text{(θ and φ diffusion)} \qquad [1.78]$$

In an isotropic environment θ and φ are equivalent and the re-orientation of fluorescence observable excited state moments arising from photoselection is related to the diffusion rates by $\tau_{or}^{iso} = 1/6D_{rot}$ as in equation 1.46; knowledge of γ_{20} is all that is required to determine probe motion.

1.11 Summary

The photoselection of a non-equlibrium subset of dye molecules by an ultrashort linearly polarised laser pulse gives rise to an initially ordered excited state array which is dependent upon an angular dependent excitation probability and any intrinsic ground state order if present. Fluorescence anisotropy experiments measure the alignment of the excited state population and monitor its subsequent temporal evolution, which is governed by the rotational diffusion of the dye molecules. Chapter 2 discusses the full angular relaxation (θ and φ diffusion) of dye molecules and how the presence of an ordered environment can affect that relaxation.

References for Chapter 1

1. G R Fleming, *Chemical Applications of Ultrafast Spectroscopy*, Clarendon, (1986)
2. P W Atkins, *Molecular Quantum Mechanics*, 2nd edition, Oxford University Press, Oxford, (1992)
3. M Born and J R Oppenheimer, Ann. Phys. **84**, 457, (1927)
4. J Bryant, Ph. D. Thesis, University of Essex, (2000)
5. J Wilson and J Hawkes, *Optoelectronics* (3rd Ed.) Prentice Hall (1998)
6. C Cohen-Tannoudji, *Quantum Mechanics*, Hermann, Paris (1977)
7. B Valeur, *Molecular Fluorescence*, Wiley-VCH, Weinheim (2001)
8. P Wu and L Brand, Anal. Biochem. **218**, 1 (1994)
9. F P Schäfer, *Topics in Applied Physics: Dye Lasers*, Ed. F P Schäfer, Springer-Verlag, Berlin, (1990)
10. R J Marsh, A J Bain and M A Osborne, Proc. SPIE **5222A**, (2003)
11. J R Lakowicz, *Principles of Fluorescence Spectroscopy* (2nd Ed.), Kluwer Academic, (1999)
12. V Calleja, S M Ameer-Beg, B Vojnovic, J Downward and B Larijani, Biochem. J. **372**, 33 (2003)
13. U Brackmann, *LambdaChrome® Laser Dyes* (3rd Ed.), Lambda Physik AG, Goettingen (2000)
14. N Chadborn, J Bryant, A J Bain and P O'Shea, Biophys. J. **76**, 2198 (1999)
15. R Y Tsien, Annu. Rev. Biochem. **67**, 509 (1998)
16. A J Bain, P Chandna, and J Bryant, J. Chem. Phys. **112**, 10418 (2000)
17. M L Boas, *Mathematical Methods in the Physical Sciences*, (2nd Ed.), Wiley, New York (1983)
18. A J Bain, P Chandna, G Butcher and J Bryant, J. Chem. Phys. **112**, 10435 (2000)
19. A J Bain and A J McCaffery, J. Chem. Phys. **83**, 2632 (1985)
20. G R Fleming, Ann. Rev. Phys. Chem. **37**, 81 (1986)
21. P Debye, *Polar Molecules*, Dover, New York (1929)
22. A Yariv, *An Introduction to Theory & Applications of Quantum Mechanics*, Wiley (1982)
23. A Fick, Pogg. Annin. **94**, 59 (1855)
24. A Einstein, Ann. D. Physik. **17**, 549 (1905)
25. R Brown, Philos. Mag. **4**, 161 (1828)

26. C E Hecht, *Statistical Thermodynamics and Kinetic Theory*, Freeman, New York, (1990)
27. N V Brilliantov, V P Denisoc and P L Krapivsky, Physica A, **175**, 293 (1991)
28. W P Crummett and A B Western, *University Physics*, WCB (1994)
29. D J Cook, J X Chen, E A Morlino and R M Hochstrasser, Chem. Phys. Lett. **309**, 221 (1999)

Chapter 2

Single and Three Beam Photoselection of Dye Probes in Ordered Environments

2.1 Introduction

The concept of photoselection in which an initially ordered molecular excited state distribution is created as a result of polarised laser excitation was introduced in Chapter 1. The sensitivity of fluorescence observables to molecular order and its relaxation (equation 1.36) show that time resolved fluorescence anisotropy experiments can yield information on the order and angular motion of the fluorescent probe distribution.

Polarised photoselection techniques allow the study and comparison of molecular motion in both isotropic and ordered systems. The study of ordered systems is of considerable scientific interest. The presence of order can have a profound influence on intrinsic optical [1] and photophysical properties [2], molecular motion [3] and chemical reactivity [4]. Order can be found in natural molecular environments such as cell membranes [5] and the local environments of chromophores in proteins [6].

In this chapter a variety of photoselection experiments study molecular probe order and motion in the nematic phase of the liquid crystal 5-cyanobiphenyl (5CB). Photoselection experiments within the group have traditionally relied on the use of single beam linearly polarised excitation [7-9]. Here the excitation polarisation angle (β) is varied with respect to the Z-axis of the ordered system and the corresponding fluorescence anisotropy $R(t, \beta)$ is measured using time resolved single photon counting techniques. For all excitation polarisation angles other than $\beta=0°$ both cylindrically symmetric and asymmetric degrees of excited state alignment are created. From experimental observations [7-8, 10-11] and theory [12] the equivalence of cylindrically symmetric and asymmetric rotational diffusion dynamics as set out in equations 1.77 and 1.78 is no longer valid. Z-polarised photoselection ($\beta=0°$) prepares a cylindrically symmetric excited state alignment greater than that of the equilibrium ensemble. For $\beta=90°$ an initial degree of cylindrically symmetric alignment is prepared that is below the equilibrium value, however it is accompanied by the creation of significant cylindrical asymmetry with an inherently different time evolution. It is therefore desirable to develop techniques that allow the variation in initial excited state alignment without the interference of asymmetric observables. As will be seen this can be achieved using three orthogonally polarised excitation pulses. Three pulse photoselection in isotropic media was developed by Bryant et al. [9] and the technique has recently been extended to anisotropic media [11, 13-14]. In this chapter both single and three pulse photoselection techniques are used to determine the order and full angular motion of Rhodamine 6G and Rhodamine B in the nematic phase of 5CB.

2.2 Liquid Crystals

The ordered environments that are studied in this work are liquid crystals. The term "liquid crystal" refers to the phase of matter exhibited by certain materials which is an intermediate state of matter (a mesophase) between a solid and a liquid; this is best described by considering the orientational and positional molecular ordering, as illustrated in figure 2.1 [15]:

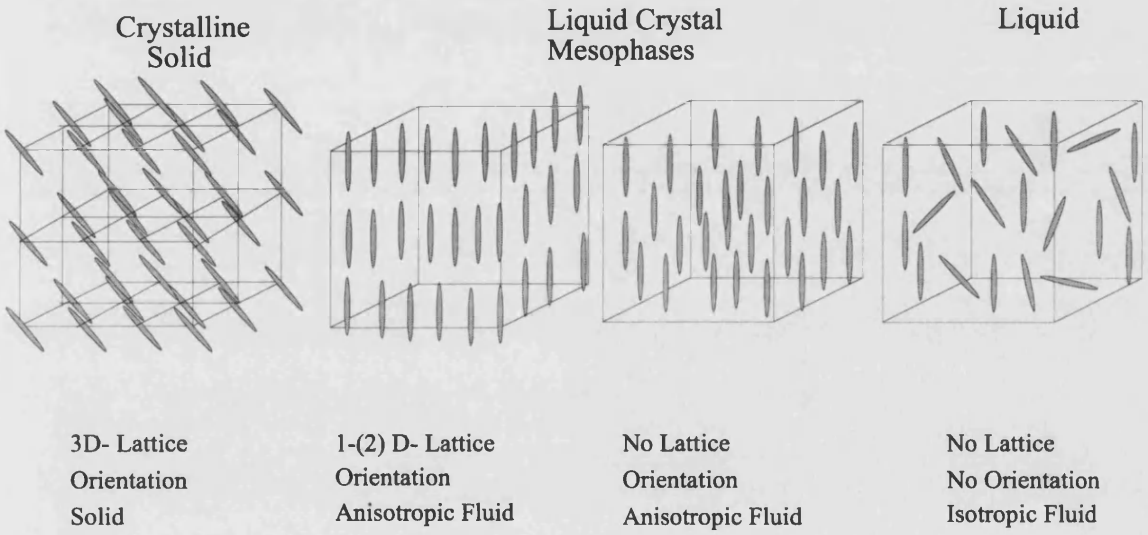

Figure 2.1: A phase of matter between solids and liquids, materials with a liquid crystal phase can display orientational and/or positional order.

Solids exhibit both long range positional order and orientational order, and molecules in the solid state tend to vibrate about fixed positions in a crystalline lattice. This structure (and subsequent resistance to change by deformation) is maintained over vast molecular scales [16] by long range forces. In contrast, liquids possess neither positional nor orientational order, and molecules in the liquid phase are free to translate and rotate randomly, with only a weak long range interaction force maintaining the liquid phase.

Liquid crystal mesophases fall between the crystalline solid and amorphous liquid states of matter. Liquid crystals possess some local orientational and positional order (i.e. over a few molecular lengths) for a finite temperature range; although they are fluid they exhibit anisotropic optical and mechanical characteristics like a solid.

Liquid crystals can be categorised in terms of the mechanisms by which transitions between their mesophases can be induced. Thermotropic liquid crystals undergo mesophase transitions by temperature change, whereas lyotropic liquid crystal phase transitions are governed by solvent concentration. The liquid crystal host used in this chapter is 4-n-pentyl-4'-cyanobiphenyl (5CB) which belongs to a family of thermotropic liquid crystals known as cyanobiphenyls. The molecular structure of 5CB is shown in figure 2.2.

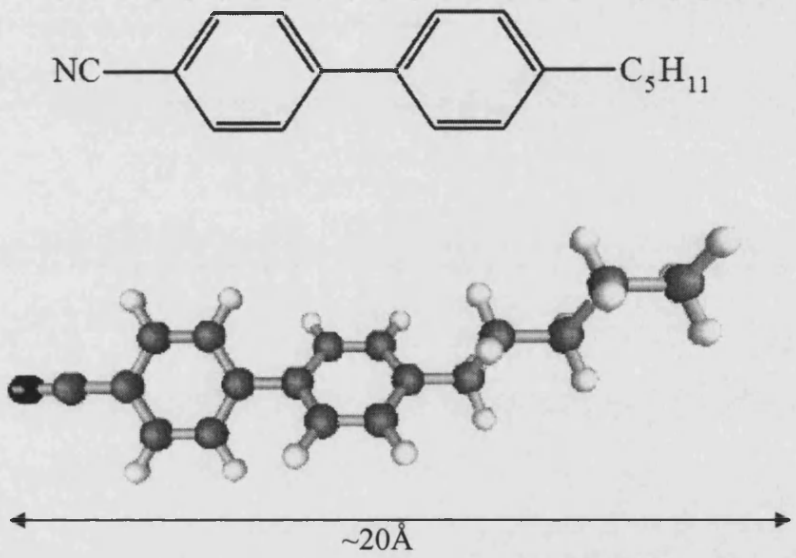

Figure 2.2: Structure of liquid crystal 5CB. The long axis of the molecule measures approximately 20Å.

2.2.1 Nematic Liquid Crystals

In addition to the solid and liquid phases, 5CB exhibits a nematic liquid crystal mesophase. The nematic phase is characterised by the liquid crystal possessing no positional order (in common with an isotropic fluid) but displaying a long range correlation between the orientation of the constituent molecules, illustrated in figure 2.3.

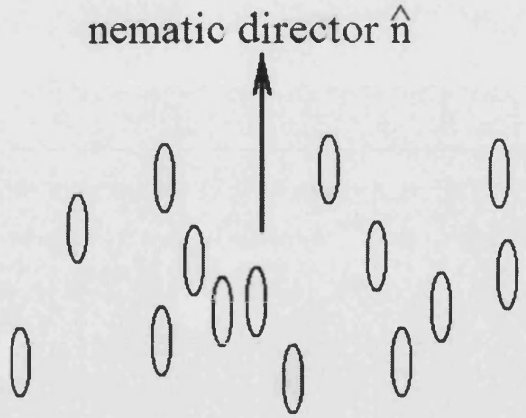

Figure 2.3: Schematic representation of nematic ordering; in the nematic phase orientational order of the molecules is maintained with respect to the nematic director n̂ whilst positional order is wholly random.

The calamatic (rod-like) shape of the 5CB molecules gives rise to a preferential alignment of the molecular long axis in the nematic phase, which is defined by a unit vector or director $\hat{n}$ as shown in figure 2.3. The anisotropic nature of the constituent molecules means that the nematic liquid crystal can be considered as an anisotropic liquid, although the ability of the molecules to diffuse whilst remaining parallel is comparable to a true isotropic liquid. The average viscosity for nematics is about the same as that for an isotropic fluid [17]; the viscosity of liquid crystals is, however, anisotropic and as will be seen probe rotational times for θ and φ diffusion with respect to $\hat{n}$ are unequal. Like the majority of nematic materials, 5CB has one axis of symmetry (i.e it is uniaxial). Furthermore, nematics are centrosymmetric with equivalent numbers of molecules aligned parallel and anti-parallel to the nematic director, as shown in figure 2.4.

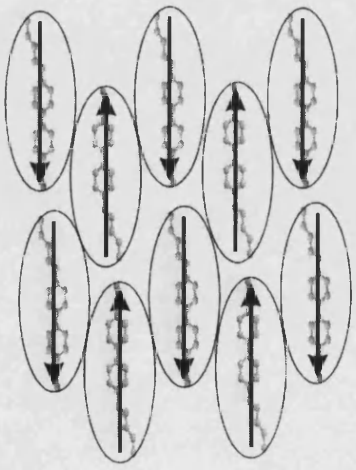

Figure 2.4: For polar nematic liquid crystal molecules such as 5CB (dipoles represented by an arrow), then there are as many dipoles oriented in the n direction as there are in the -n direction. {Original figure from [13]}

Another feature of nematic materials is that the fixed space orientations of the domains (the finite regions over which orientational molecular ordering exists) is globally random; in other words, the nematic liquid crystal is microscopically ordered and macroscopically isotropic in the absence of external boundary conditions or applied fields. In order to utilise the anisotropic properties of the liquid crystal it is necessary to establish a well-defined uniform director. In practice, homogeneous alignment can be achieved by the application of minor forces such as the guiding effect of sample walls [11]. Uniform boundary conditions can be obtained by using surfactants such as polyvinyl alcohol (PVA) [18] which can be mechanically rubbed in one direction causing the surfactant molecules to align parallel to the rubbing direction. When the liquid crystal is applied to a surface with a mechanically rubbed surfactant, homogeneous alignment of the liquid crystal molecules is established for a finite range (see Sample Preparation, section 2.7.4).

2.2.2 Orientational Distribution Function for Nematic Liquid Crystals: Order Parameters

Under normal circumstances molecules in the liquid phase are randomly orientated with an equal orientational distribution over all angles on the unit sphere. This is in contrast to nematic liquid crystals: in the homogeneously aligned nematic phase, the tendency of molecules to align along a preferred direction **n** gives rise to an orientational distribution function that is not uniform over the unit sphere.

From equation 1.12 the orientational distribution function for an arbitrary system can be expressed in terms of a sum of normalised coefficients of spherical harmonics:

$$P(\theta,\varphi)=\langle C_{00}\rangle\sum_{KQ}\langle\alpha_{KQ}\rangle Y_{KQ}(\theta,\varphi) \qquad [2.1]$$

This expression contains order parameters $<\alpha_{KQ}>$for all ranks (K) and projections (Q). However, $P(\theta,\varphi)$ can be described fully with fewer moments by considering the inherent symmetry of the environment. Nematic liquid crystals possess axial symmetry with respect to the director **n**, which defines the laboratory Z axis. This makes the molecular array invariant to rotations about Z, i.e. the system is φ-independent. The only spherical

harmonics with φ-independence have projection Q=0, so P(θ,φ) will only have non-zero moments for Q=0. Furthermore, the uniaxial property of the nematic liquid crystal means that the system is invariant to inversion of the director, and thus only the moments where K is even are present in the expansion of P(θ,φ). As a result of these symmetry considerations the orientational distribution function becomes

$$P(\theta,\varphi)=\langle C_{00}\rangle\left[Y_{00}(\theta,\varphi)+\langle\alpha_{20}\rangle Y_{20}(\theta,\varphi)+\langle\alpha_{40}\rangle Y_{40}(\theta,\varphi)+\ldots\right] \qquad [2.2]$$

$$P(\theta,\varphi)=\frac{1}{4\pi}\left[1+\sum_{K>0,EVEN}(4\pi)^{1/2}\langle\alpha_{K0}\rangle Y_{K0}(\theta,\varphi)\right] \qquad [2.3]$$

which in terms of Legendre Polynomials $P_K(\theta)$ becomes [19]

$$P(\theta,\varphi)=\frac{1}{4\pi}\left[1+\sum_{K>0,EVEN}(4\pi)^{1/2}\frac{\langle\alpha_{K0}\rangle}{(2K+1)^{1/2}}P_K(\theta)\right] \qquad [2.4]$$

And since Q=0 there is no φ dependence, giving

$$P(\theta)=\frac{1}{2}\left[1+\sum_{K>0,EVEN}(4\pi)^{1/2}\frac{\langle\alpha_{K0}\rangle}{(2K+1)^{1/2}}P_K(\theta)\right] \qquad [2.5]$$

The $\langle\alpha_{K0}\rangle/(2K+1)^{1/2}$ coefficients in the expansion are referred to as the order parameters of the system. In a fully aligned nematic, all the molecules are oriented exactly parallel to the director. From equation 1.10 (Chapter 1) this yields

$$\langle\alpha_{K0}\rangle=(4\pi)^{1/2}Y_{K0}(\theta=0^{\circ}) \qquad [2.6]$$

Therefore the degree of alignment $\langle\alpha_{20}\rangle$ of a fully ordered array is $\sqrt{5}$.

2.3 Variable Angle Photoselection

In Chapter 1 it was shown that the single photon fluorescence anisotropy R(t) of an arbitrary molecular excited state population can be expressed in terms of the cylindrically symmetric $\langle \alpha_{20}^{ex} \rangle$ and cylindrically asymmetric $\langle \alpha_{2\pm2}^{ex} \rangle$ degrees of excited state alignment:

$$R(t) = \frac{\frac{\langle \alpha_{20}^{ex}(t) \rangle}{\sqrt{5}} - \frac{\{\langle \alpha_{22}^{ex}(t) \rangle + \langle \alpha_{2-2}^{ex}(t) \rangle\}}{\sqrt{30}}}{1 + 2\frac{\{\langle \alpha_{22}^{ex}(t) \rangle + \langle \alpha_{2-2}^{ex}(t) \rangle\}}{\sqrt{30}}} \qquad [2.7]$$

The collinear excitation-detection geometry with a variable angle photoselection angle β is shown in figure 2.5. Orthogonal components of the fluorescence emission (i.e. $I_Z(t)$, $I_X(t)$) are used to construct the fluorescence anisotropy as set out in equation 1.30.

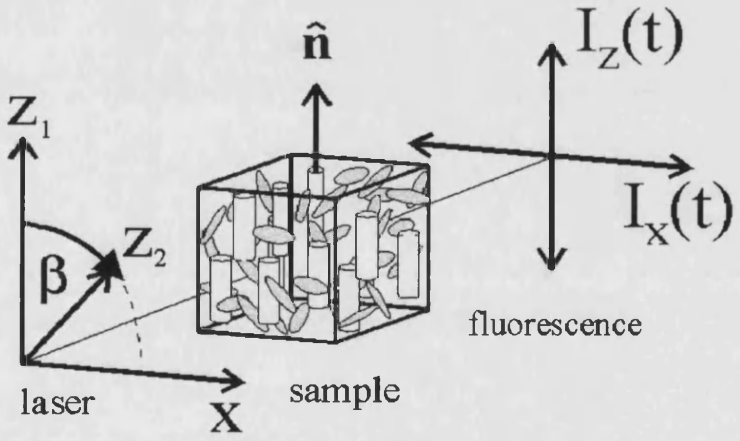

Figure 2.5: Illustration of the collinear excitation-detection geometry and variable angle photoselection, where the excitation polarisation angle β is defined with respect to the nematic director of the liquid crystal host, aligned parallel with the laboratory Z axis (Z_1).

The excitation polarisation angle can be varied between 0° and 90° with respect to the laboratory vertical fixed axis. In the axis frame defined by the polarisation vector of the excitation pulse the angle dependent excitation probability is given by

$$W(\theta',\varphi',t)_{Z_2} = BI(t)|\vec{\mu}_a|^2 \frac{\sqrt{4\pi}}{3}\left[Y_{00}(\theta',\varphi')+\frac{2}{\sqrt{5}}Y_{20}(\theta',\varphi')\right] \quad [2.8]$$

where θ' and φ' are the polar angles defining the orientation of the absorption transition dipole moment μ_a in the reference frame that is defined by the polarisation vector of the excitation pulse (Z_2). I(t) represents the pulse intensity and B is a proportionality constant [9]. However, all the fluorescence measurements are made with the fixed laboratory frame as the reference, defined by the initial polarisation of the excitation beam (Z_1); equation 2.8 must be transformed into a laboratory frame expression. This is achieved by utilising the Euler rotation D(0,-β,0) which connects the light and laboratory axis frames, where β is the angle between the polarisation vector Z_2 and the laboratory Z axis Z_1. In terms of spherical harmonics in the laboratory frame equation 2.8 becomes [7]

$$W(\theta,\varphi,t)_{Z_1} = BI(t)|\vec{\mu}_a|^2 \frac{\sqrt{4\pi}}{3}\left[Y_{00}(\theta',\varphi')+\frac{2}{\sqrt{5}}\sum_{Q=-2}^{2} d^2_{0Q}(-\beta)Y_{2Q}(\theta',\varphi')\right] \quad [2.9]$$

where $d^2_{0Q}(-\beta)$ is a reduced Euler rotation matrix element [19]

$$d^K_{QQ'}(-\beta) = \int Y^*_{KQ'}(\theta,\varphi)D(0,-\beta,0)Y_{KQ}(\theta',\varphi')d\Omega \quad [2.10]$$

The β dependence of the transition probability in Z_1 is determined by

$$d^2_{00}(\beta) = \frac{1}{2}\left(3\cos^2\beta - 1\right) \quad [2.11a]$$

$$d^2_{10}(\beta) = d^2_{-10}(\beta) = \sqrt{\frac{3}{2}}\sin\beta\cos\beta \quad [2.11b]$$

$$d^2_{20}(\beta) = d^2_{-20}(\beta) = \sqrt{\frac{3}{8}}\sin^2\beta \quad [2.11c]$$

Under weak excitation conditions (Chapter 1 section 1.8) any initial excited state distribution is given by the product of the excitation operator and the ground state orientational distribution function:

$$P_{ex}(\theta,\varphi)=P_{gs}(\theta,\varphi)W(\theta,\varphi) \qquad [2.12]$$

For an isotropic ground state only the population term in equation 2.12 exists and the excited state distribution follows the angular dependence of the excitation probability. For a nematic host the equilibrium order of a molecular probe is cylindrically symmetric about n. In this case the initial excited state distribution is given by

$$P_{ex}(\theta,\varphi,\beta,t=0)=\frac{C}{3\sqrt{4\pi}}\sum_{K'even}\left\langle C^{gs}_{K'0}\right\rangle Y_{K'0}(\theta,\varphi)\left[Y_{00}(\theta,\varphi)+\frac{2}{\sqrt{5}}\sum_{Q}d^{2}_{0Q}(\beta)Y_{2-Q}(\theta,\varphi)\right] \qquad [2.13]$$

where C is a constant of proportionality, and the moments of the excited state orientational distribution function are given by [7]

$$\left\langle C^{ex}_{KQ}(0)\right\rangle = C\frac{\sqrt{4\pi}}{3}\sum_{K'}\left\langle C^{gs}_{K'0}\right\rangle\left\langle KQ\left|\left[Y_{00}(\theta,\varphi)+\frac{2}{\sqrt{5}}\sum_{Q'}d^{2}_{0Q'}(-\beta)Y_{2Q'}(\theta,\varphi)\right]\right|K'0\right\rangle \qquad [2.14]$$

Yielding for $P_{ex}(\theta,\varphi)$ [7]

$$P_{ex}(\theta,\varphi)=C\frac{\sqrt{4\pi}}{3}\sum_{K=2,4,6..}\left(\left\langle C_{K0}\right\rangle Y_{K0}(\theta,\varphi)\right)\left[Y_{00}(\theta,\varphi)+\frac{2}{\sqrt{5}}\sum_{K=2}^{-2}d^{2}_{0K}(\beta)Y_{2K}(\theta,\varphi)\right] \qquad [2.15]$$

The excited state moments observable in fluorescence measurements are given by [12]

$$\frac{\left\langle\alpha^{ex}_{20}(0,\beta)\right\rangle}{\sqrt{5}}=\frac{\frac{1}{5}\left(3\cos^2\beta-1\right)+\frac{\left\langle\alpha^{gs}_{20}\right\rangle}{\sqrt{5}}\left(1+\frac{2}{7}\left\{3\cos^2\beta-1\right\}\right)+\frac{6\left\langle\alpha^{gs}_{40}\right\rangle}{35}\left(3\cos^2\beta-1\right)}{1+\frac{\left\langle\alpha^{gs}_{20}\right\rangle}{\sqrt{5}}\left(3\cos^2\beta-1\right)} \qquad [2.16]$$

$$\frac{\left\langle\alpha^{ex}_{22}(0,\beta)\right\rangle+\left\langle\alpha^{ex}_{2-2}(0,\beta)\right\rangle}{\sqrt{30}}=\frac{\frac{1}{5}\sin^2\beta\left(1-\frac{10\left\langle\alpha^{20}_{gs}\right\rangle}{7\sqrt{5}}+\frac{\left\langle\alpha^{gs}_{40}\right\rangle}{7}\right)}{1+\frac{\left\langle\alpha^{gs}_{20}\right\rangle}{\sqrt{5}}\left(3\cos^2\beta-1\right)} \qquad [2.17]$$

The dependence of the fluorescence observables on excitation polarisation angle β for aligned and isotropic ground state distributions is shown in figure 2.6.

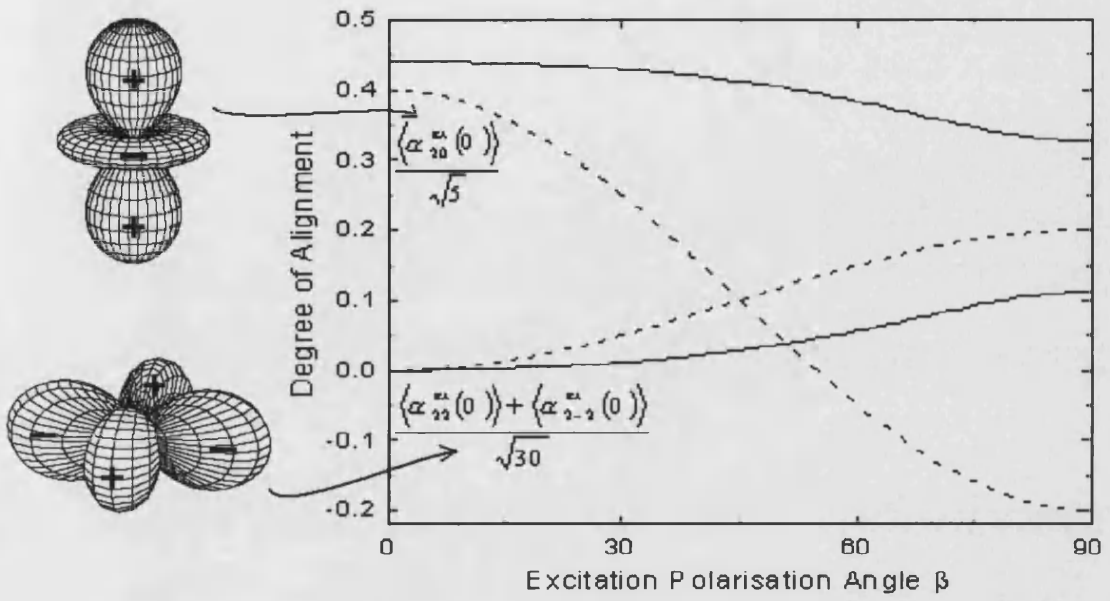

Figure 2.6: Contributions of fluorescence observables to the initial excited state anisotropy as a function of excitation polarisation angle β for excitation from an isotropic ground state (dashed lines) and from a ground state with positive net alignment (solid lines).

Combining equations 2.16 and 2.17 yields the initial fluorescence anisotropy:

$$R(0,\beta)=\frac{\frac{2}{5}\left(\cos^2\beta-\sin^2\beta\right)+\frac{\left\langle\alpha_{20}^{gs}\right\rangle}{\sqrt{5}}\left[1+\frac{4}{7}\cos^2\beta\right]+\frac{\left\langle\alpha_{40}^{gs}\right\rangle}{35}\left(19\cos^2\beta-7\right)}{1+\frac{2}{5}\sin^2\beta+\frac{\left\langle\alpha_{20}^{gs}\right\rangle}{\sqrt{5}}\left[\frac{25\cos^2\beta-11}{7}\right]+\frac{\left\langle\alpha_{40}^{gs}\right\rangle}{35}2\sin^2\beta} \qquad [2.18]$$

For β=0° the contribution to the fluorescence anisotropy from the cylindrically asymmetric moment $\left\langle\alpha_{22}^{ex}(t,\beta)\right\rangle+\left\langle\alpha_{2-2}^{ex}(t,\beta)\right\rangle$ is zero and the fluorescence anisotropy can be defined purely in terms of the cylindrically symmetric moment $\left\langle\alpha_{20}^{ex}(t,\beta)\right\rangle$; the angular diffusion can be expressed purely in terms of the decay rate γ_{20}. For any other excitation polarisation the asymmetric moment makes a contribution to the fluorescence anisotropy and the excited state relaxation is dependent upon γ_{20} and γ_{22}.

2.4 Relaxation Dynamics in Ordered Systems

If the collisions that take place between probe and host molecules in a fluid are extremely rapid [20], only a small angular variation is allowed between successive collision events. In this case the molecular motion can be described by the Debye small step diffusion model introduced in Chapter 1 [21]. If the fluid is anisotropic, the theory must be modified and can be considered as a static perturbation H′ in the isotropic excited state order according to [12]

$$\frac{d}{dt}P_{ex}(\theta,\varphi,t)=\left[D\nabla^2+H'\right]P_{ex}(\theta,\varphi,t) \qquad [2.19]$$

In a first order approximation $D\nabla^2$ must be much greater than H′ for H′ to be considered a perturbation and H′ has to retain the initial symmetry of the unperturbed state. In terms of moments of the orientational distribution, equation 2.19 becomes

$$\begin{aligned}\frac{d}{dt}\left\{\left\langle C_{KQ}^{ex}(t)\right\rangle-\left\langle C_{KQ}^{ex}(ss)\right\rangle\right\}&=\left\langle KQ\left|D\nabla^2+H'\right|KQ\right\rangle\left\{\left\langle C_{KQ}^{ex}(t)\right\rangle-\left\langle C_{KQ}^{ex}(ss)\right\rangle\right\}\\&+\sum_{\substack{K'\neq K\\Q'\neq Q}}\left\langle KQ\left|H'\right|K'Q'\right\rangle\left\{\left\langle C_{K'Q'}^{ex}(t)\right\rangle-\left\langle C_{K'Q'}^{ex}(ss)\right\rangle\right\}\end{aligned} \qquad [2.20]$$

A first order perturbation treatment of equation 2.20 has proved successful in calculating the form of the orientational relaxation dynamics based purely on symmetry considerations [22] giving

$$\begin{aligned}&\left\langle C_{KQ}^{ex}(t)\right\rangle-\left\langle C_{KQ}^{ex}(ss)\right\rangle=\left\{\left\langle C_{KQ}^{ex}(0)\right\rangle-\left\langle C_{KQ}^{ex}(ss)\right\rangle\right\}\exp\left(-\gamma_{KQ}t\right)\\&+\sum_{\substack{K'\neq K\\Q'\neq Q}}\int_0\left[\begin{array}{c}\left\{\left\langle C_{K'Q'}^{ex}(0)\right\rangle-\left\langle C_{K'Q'}^{ex}(ss)\right\rangle\right\}\exp\left(-\gamma_{K'Q'}t'\right)\exp\left(-\gamma_{KQ}(t'-t)\right)\\\times\left\langle \mathrm{KQ}\left|H'\right|K'Q'\right\rangle\end{array}\right]dt'\end{aligned} \qquad [2.21]$$

where $\gamma_{KQ}=-\left\langle \mathrm{KQ}\left|\mathrm{D}\nabla^2+\mathrm{H}'\right|\mathrm{KQ}\right\rangle$. It is not necessary to know the explicit form of H′ in equation 2.29 to simplify the matrix element. By applying symmetry considerations the matrix elements $\left\langle KQ\left|H'\right|K'Q'\right\rangle$ vanish for Q≠Q′, yielding

$$\left\langle C_{KQ}^{ex}(t)\right\rangle - \left\langle C_{KQ}^{ex}(ss)\right\rangle = \left[\left\langle C_{KQ}^{ex}(0)\right\rangle - \left\langle C_{KQ}^{ex}(ss)\right\rangle\right]\exp\left(-\gamma_{KQ}t\right)$$
$$+\sum_{K'\neq K}\int_0^t\left[\begin{array}{c}\left[\left\langle C_{K'Q}^{ex}(0)\right\rangle - \left\langle C_{K'Q}^{ex}(ss)\right\rangle\right]\exp\left(-\gamma_{K'Q}t'\right)\exp\left(-\gamma_{KQ}(t'-t)\right)\\ \times\left\langle KQ\left|H'\right|K'Q\right\rangle\end{array}\right]dt' \qquad [2.22]$$

The normalisation of orientational probability (Chapter 1, section 1.7) requires that $\left\langle C_{00}^{ex}\right\rangle$ is independent of time, and that the orientational relaxation of the other distribution moments is linear and diagonal (that is, there is no cross-relaxation between excited state moments):

$$\begin{aligned}\left\langle C_{K0}^{ex}(t)\right\rangle - \left\langle C_{K0}^{ex}(ss)\right\rangle &= \left[\left\langle C_{K0}^{ex}(0)\right\rangle - \left\langle C_{K0}^{ex}(ss)\right\rangle\right]\exp(-\gamma_{K0}t)\\ \left\langle C_{KQ}^{ex}(t)\right\rangle &= \left\langle C_{KQ}^{ex}(0)\right\rangle\exp\left(-\gamma_{KQ}t\right)\end{aligned} \qquad [2.23]$$

In axially symmetric systems the diffusion tensor in the laboratory frame of reference is diagonal with $D_{XX} = D_{YY} \neq D_{ZZ}$ ($D_{||}$ and $D_{\perp}$, respectively). Under this circumstances the γ_{KQ} decay rates are given by [12],

$$\gamma_{KQ} = D_{\perp}\left[K(K+1) - Q^2\right] + D_{||}Q^2 + \left\langle KQ\left|H'\right|KQ\right\rangle \qquad [2.24]$$

H′ must possess the same symmetry as the medium and can be expressed in terms of spherical operators (H_0^L), to rank order L=2 [12]. Application of the Wigner-Eckart theorem [19] yields

$$\gamma_{KQ} = \left[\begin{array}{l}D_{\perp}\left[K(K+1) - Q^2\right]\\ +D_{||}Q^2\end{array}\right] - \left[\begin{array}{l}\left\langle a_{00}\right\rangle\left\langle K\left\|H^0\right\|K\right\rangle\\ +\left\langle a_{20}\right\rangle\dfrac{3Q^2 - K(K+1)}{\sqrt{K(K+1)(2K+3)(2K-1)}}\left\langle K\left\|H^2\right\|K\right\rangle\end{array}\right] \qquad [2.25]$$

where $\left\langle a_{K0}\right\rangle$ are the coefficients of H′ expansion.

The evolution of the excited state fluorescence anisotropy is dependent on the $\left\langle \alpha_{20}^{ex}\right\rangle$ and $\left\langle \alpha_{22}^{ex}\right\rangle + \left\langle \alpha_{2-2}^{ex}\right\rangle$ moments (equation 2.7). From equation 2.25 the cylindrically symmetric and asymmetric alignment relaxation rates are given by:

$$\gamma_{20} = 6D_{\perp} - \left[\langle a_{00}\rangle\langle 2\|H^0\|2\rangle - \langle a_{20}\rangle\sqrt{\frac{2}{7}}\langle K\|H^2\|K\rangle\right]$$
$$\gamma_{22} = 2D_{\perp} + 4D_{\|} - \left[\langle a_{00}\rangle\langle 2\|H^0\|2\rangle + \langle a_{20}\rangle\sqrt{\frac{2}{7}}\langle K\|H^2\|K\rangle\right] \quad [2.26]$$

In the first order approximation the perturbation is small, and the dominant mechanism in orientational relaxation is due to anisotropic viscosity (i.e. unequal values of $D_{\|}$ and $D_{\perp}$) yielding the decay rates introduced in Chapter 1 (equations 1.77 and 1.78):

$$\gamma_{20} = 6D_{\perp} \quad [2.27]$$

$$\gamma_{22} = 2D_{\perp} + 4D_{\|} \quad [2.28]$$

2.5 Time Dependent Fluorescence Anisotropy

In section 2.4 it has been shown [22] that the rate of change of displacement of a particular excited state moment from its equilibrium (steady state) value obeys first order kinetics:

$$\frac{d}{dt}\left[\langle\alpha^{ex}_{KQ}(t)\rangle - \langle\alpha^{ex}_{KQ}(ss)\rangle\right] = -\gamma_{KQ}\left[\langle\alpha^{ex}_{KQ}(t)\rangle - \langle\alpha^{ex}_{KQ}(ss)\rangle\right] \quad [2.29]$$

where (ss) denotes the steady state value of the moment. Equation 2.29 has a solution of

$$\langle\alpha^{ex}_{KQ}(t)\rangle = \left\{\langle\alpha^{ex}_{KQ}(0)\rangle - \langle\alpha^{ex}_{KQ}(ss)\rangle\right\}\exp(-\gamma_{KQ}t) + \langle\alpha^{ex}_{KQ}(ss)\rangle \quad [2.30]$$

Equation 2.7 showed that the fluorescence anisotropy is dependent only upon the $\langle\alpha^{ex}_{20}\rangle$ and $\langle\alpha^{ex}_{22}\rangle + \langle\alpha^{ex}_{2-2}\rangle$ moments, and from equation 2.5 for an axially symmetric medium, the steady state distribution function is characterised by moments of even rank K and projection Q of zero, that is, $\langle\alpha^{ex}_{2\pm2}(ss)\rangle$ =0. For the time dependent fluorescence anisotropy this yields:

$$R(t)=\frac{\frac{1}{\sqrt{5}}\left[\left\langle\alpha_{20}^{ex}(0)\right\rangle-\left\langle\alpha_{20}^{ex}(ss)\right\rangle\right]e^{(-\gamma_{20}t)}+\left\langle\alpha_{20}^{ex}(ss)\right\rangle\Big]-\frac{1}{\sqrt{30}}\left[\left\langle\alpha_{22}^{ex}(0)\right\rangle+\left\langle\alpha_{2-2}^{ex}(0)\right\rangle\right]e^{(-\gamma_{22}t)}}{1+\frac{2}{\sqrt{30}}\left[\left\langle\alpha_{22}^{ex}(0)\right\rangle+\left\langle\alpha_{2-2}^{ex}(0)\right\rangle\right]e^{(-\gamma_{22}t)}}$$

[2.31]

which upon substitution of equations 2.24 and 2.25 and $R_{SS}=\left\langle\alpha_{20}^{ex}\right\rangle/\sqrt{5}$ leads to

$$R(t,\beta)=\frac{\left[\frac{\left(3\cos^2\beta-1\right)}{35}\{7+6b\}+\frac{a}{7}\left(6\cos^2\beta+5\right)-R_{ss}\left(1+a\left(3\cos^2\beta-1\right)\right)\right]\exp(-\gamma_{20}t)}{-\frac{1}{5}\sin^2\beta\left(1-\frac{10}{7}a+\frac{b}{7}\right)\exp(-\gamma_{22}t)+R_{ss}\left(1+a\left(3\cos^2\beta-1\right)\right)}$$
$$\left(1+a\left(3\cos^2\beta-1\right)\right)+\frac{2}{5}\sin^2\beta\left(1-\frac{10}{7}a+\frac{b}{7}\right)\exp(-\gamma_{22}t)$$

[2.32]

where $a=\left\langle\alpha_{20}^{gs}\right\rangle/\sqrt{5}$ and $b=\left\langle\alpha_{40}^{gs}\right\rangle$.

2.6 Time Correlated Single Photon Counting

The technique used to measure fluorescence intensity and fluorescence anisotropy decays in this chapter is known as picosecond Time Correlated Single Photon Counting (TCSPC). TCSPC is a well established technique which makes repeated measurements of the coincidence time between an excitation pulse and the first detected fluorescence photon. Over time a histogram of excitation-emission intervals is built up; since fluorescence emission is a purely statistical process a large number of coincidence times will yield a distribution that is a convolution of the fluorescence decay and the excitation instrument response. The coincidence time frequency histogram H(t) generated by TCSPC measurements is given by [24]

$$H(t)=\int_{-\infty}^{t}G(t')F(t-t')dt' \qquad [2.33]$$

where F(t-t') is the fluorescence response function corresponding to the fluorescence emission from a molecular population excited by an ultrashort laser pulse, proportional to $\exp[(t-t')/\tau_F]$. G(t') corresponds to the instrument response signal from the excitation pulse. The technique is illustrated in figure 2.7.

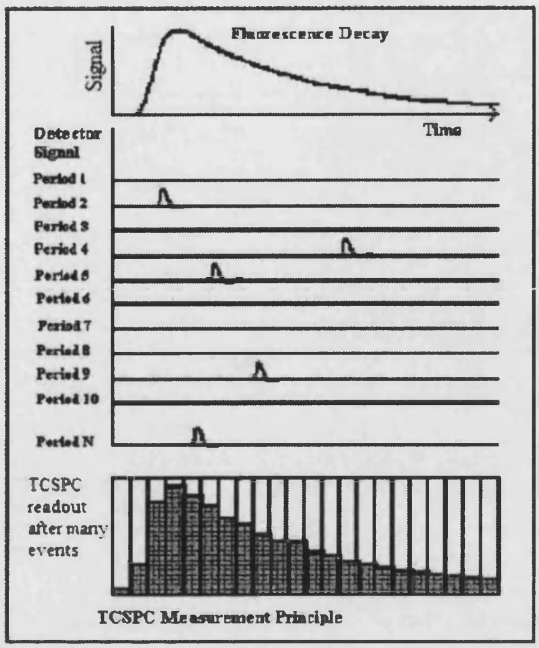

Figure 2.7: Following excitation from a short laser pulse, a single fluorescence event is recorded. After many repetitions of the excitation-event detection cycle, a histogram of the correlation between the laser pulse and fluorescence is built up. Approximating the laser pulse as a delta function at the time of excitation, the histogram returns the original fluorescence decay.

The histogram function is effectively the correlation between the instrument response function and the fluorescence emission for all delays t'. If the excitation pulse is sufficiently short (i.e. ultrashort) it may be treated effectively as a delta function and its correlation with the fluorescence emission simply returns the fluorescence signal itself. In practice, the instrumental response function is defined by the measurement of the scattered (and highly attenuated) excitation source. The source contribution to the response is at most a few picoseconds [25]; the determining factor lies predominately in the detection electronics, in particular the spread in transit times of photoelectrons generated in the detection photomultiplier (see detection apparatus, section 2.6.2). The overall response of the picosecond TCSPC system used in this work is approximately 50ps [11]. Since the fluorescence and re-orientational lifetimes of the Rhodamine dye probe molecules used in the experiments described in this chapter are in the order of 3-8 nanoseconds, the instrument response function is sufficiently short that analysis of the TCSPC signal can be undertaken without the de-convolution of equation 2.33.

An important consideration of TCSPC is that for the measured histogram to be a true representation, it is necessary to ensure that each coincidence that is detected corresponds to a single event. For high fluorescence count rates there is an increased

probability that more than one photon will be detected per excitation, which favours shorter coincidence intervals disproportionately. To avoid this, the fluorescence count rate must be capped at a level such that the probability of detecting a fluorescent photon is much less than unity [25]. Experimentally this corresponds to a maximum count rate of 1% of the excitation source repetition rate [24].

2.7 Experimental Apparatus

The laser system and detection apparatus used in the experiments described in this chapter is shown in figure 2.8.

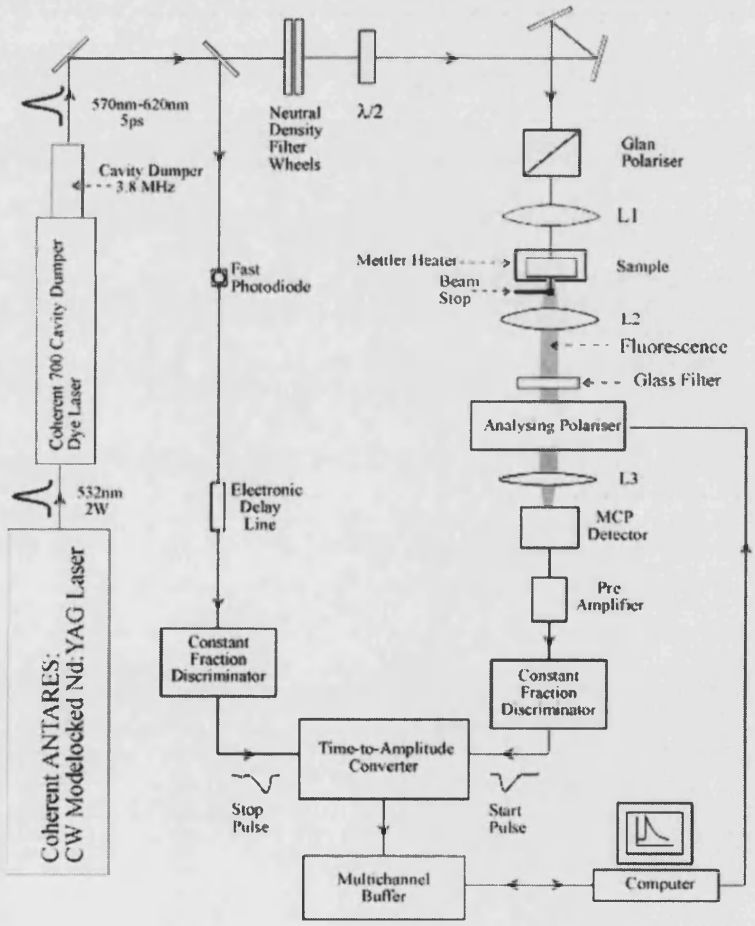

Figure 2.8: Excitation Source and TCSPC equipment used for single & three beam photoselection. The excitation-detection geometry for three beam photoselection is illustrated in figure 2.12.

2.7.1. Excitation Source

The laser source was a cavity dumped dye laser (Coherent 702) synchronously pumped by the frequency doubled output of a 76MHz mode-locked Nd:YAG laser (Coherent Antares 76-S).

The output stability of the dye laser is critically dependent upon the modelocked pump beam; amplitude and spatial fluctuations of the Nd:YAG beam were reduced using an Active Amplitude Stabilisation (AAS) system (Coherent 7670). The AAS monitors the beam pointing stability using a quadrant detector placed in front of the laser head. This provides feedback signals to piezoelectric transducers placed on the vertical and horizontal controls of the Nd:YAG cavity end mirror. Amplitude fluctuations are reduced using an acousto optic modulator mounted on the laser head that diffracts a small portion (6%-10%) of the beam to provide a constant preset output power. A typical output for the frequency doubled portion of the Nd:YAG laser used to pump the dye laser was 2W at 532nm with 26nJ pulse energy.

The Coherent 702 dye laser was operated with Rhodamine 6G in Ethylene Glycol. The high quantum yield and broad emission in the visible region of the electromagnetic spectrum make Rhodamine 6G ideal for these experiments [26]. The dye laser is tunable from 560nm to 620nm; the output wavelength could be chosen by the adjustment of a birefringent filter (BRF) in the dye laser cavity (effectively altering the cavity length). The initial repetition rate of the dye laser was synchronised to be equal to the pump source at 76MHz. By using an acousto-optic cavity dumper a repetition rate of 3.8MHz was chosen as a convenient value for the measurement of lifetimes from approx. 80ps to several hundred nanoseconds. Output power varied between 20mW and 100mW depending on the chosen wavelength and cavity optimization. Typically, the dye laser pulse train consisted of 30nJ pulses with a width of 8-10 picoseconds.

2.7.2 Detection Apparatus

Photons from an excitation pulse and the first detected subsequent fluorescence photon were measured using two photodetectors. A fast photodiode (Hamamatsu S2381) was used to detect a photon from the excitation pulse, and a microchannel plate photomultiplier (MCP) (Hamamatsu R3809U) detected sample fluorescence. The time interval between these two signals was measured using a time–to–amplitude converter (TAC) (EG&G Ortec 475). A linear voltage ramp at the TAC was initiated by the "start" signal received from the MCP on the detection of a fluorescence photon; the subsequent "stop" signal originated from the fast photodiode response to an incident photon from the excitation pulse. The time interval between the excitation pulse and the first detected fluorescence photon is proportional to the final ramp voltage generated at the TAC. This value was digitised and stored into a channel address corresponding to the measured interval by a multichannel buffer (MCB) (EG&G Ortec ADCAM &MCB Model 918A).

The signal from the MCB was relayed to a PC (Viglen 486 DX) for each coincidence event which also controlled resetting the TCSPC apparatus for the next interval. Over the course of recording many excitation-fluorescence pairs, a histogram of intervals built up showing a proportional representation of the fluorescence decay. Proper statistical sampling was ensured by restricting the photon detection rate at the MCP to a maximum of 1% of the repetition rate of the laser to minimise the probability of multiphoton events at the MCP.

Since the amplitudes of the signals from the photodetectors varied from event to event, the "start" and "stop" signals were routed through constant fraction discriminators (CFD) (Tennelec Model TC454 quad CFD) which produced an output signal representing a constant fraction of the pulse amplitude. The CFD output signals had very little associated timing jitter, making TAC timing more reliable by ensuring that the CFD output is generated at the same point on each pulse. By adjusting the level of discrimination at the CFD it was possible to separate with more certainty the photodetector signals arising from an excitation or emission photon and that from inherent noise in the system.

2.7.3 Optical Layout

A small fraction (4%-6%) of the laser output beam was split from the main path and focussed into the fast photodiode that provided the "stop" signal for the TCSPC measurements. The photodiode was protected by a set of neutral density filters. The remainder of the beam was passed through a half wave plate and neutral density wheel filters ($0 \leq$ Optical Density ≤ 3.5) to provide intensity control at the selected excitation polarisation angle (β), which was controlled using a high quality Glan Taylor polariser cube (extinction ratio 10^6:1) mounted in a precision rotation stage (Photon Control RM100). A 10cm focal length quartz lens was used to focus the polarised beam onto the thin sample (section 2.6.4).

A collinear "straight-through" excitation-detection geometry was employed when using thin samples. This geometry necessitated the use of apparatus that would allow fluorescence to be detected whilst blocking the excitation beam which would otherwise be incident upon the photosensitive MCP. The majority of the laser beam was blocked using a physical beam block which was larger than the excitation beam diameter but small enough to allow the passage of fluorescence photons through to the detector. It comprised a matt black allen key covered with black tape and was placed immediately after the collection lens. Further protection was provided using glass cut-off filters (Schott RG610, RG630, RG645), the selection of which depended on the excitation and emission wavelengths of the sample.

Sample fluorescence was collected and collimated using quartz lenses with focal lengths of 6.3cm and 25cm respectively. A polaroid sheet was used to isolate detection of the vertically or horizontally polarised components of the fluorescence that had passed the laser beam block and cut-off filters. The fluorescence image was incident on the detection area (~1cm diameter) of the MCP. In addition to the beam block and filters, a mechanical shutter was placed directly in front of the MCP, and the detector was housed in a matt black wooden enclosure.

2.7.4 Sample Preparation

Studies of molecular dye probes in liquid crystals were carried out in thin sample cells rather than a fluorescence cuvette. Homeotropically aligned cells for studies in the nematic phase consisted of two microscope cover slips coated with a rubbed surfactant separated by a film of known thickness, and were prepared using the following procedure.

The $1cm^2$ quartz cover slips were cleaned thoroughly using spectroscopic grade methanol and bathed in deionised water before being dried at 50°C. The slips were then spin coated with a solution of the surfactant polyvinyl alcohol (PVA). The surfactant solution consisted of a mixture of 0.25g of PVA in 100ml of deionised water and 25ml of methanol heated to 60°C.

The PVA surfactant was aligned by mechanically rubbing the coated surface of the cover slips in a single direction. The slips were then brought together with a separating layer comprising two strips of Mylar film with a thickness of 100μm, as illustrated in figure 2.9. The 100μm path length was chosen because it falls within the 300μm range over which homeotropic alignment persists [27]. The Mylar spacers were glued to the cover slips using an ultra-violet curing adhesive (Norland). A hypodermic syringe was used to insert the dye-doped liquid crystal into the cell, before sealing the ends using the aforementioned adhesive.

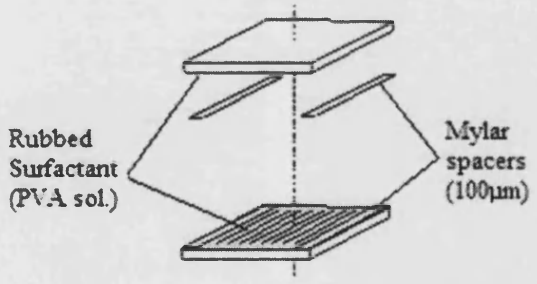

Figure 2.9: Schematic diagram of the construction of an aligned cell used to fix the nematic director to the laboratory Z-axis.

The preparation of isotropic cells (used in Chapter 5) followed the same procedure except that the cover slips were not coated with surfactant or rubbed prior to formation.

2.8 Single Beam Photoselection: Experimental Procedure

In order to carry out a variable photoselection experiment, there were some initial preparatory procedures described below.

2.8.1 Optical Alignment

All of the optical elements were carefully aligned such that any back reflections were steered along the original laser beam path. Optical alignment was carried out with the minimum laser power required to carry out the procedure by eye; the neutral density wheels were adjusted for this power level. The MCP aperture was then aligned with the laser beam, with power to the detector switched off and mechanical shutter in place. The excitation polariser was inserted into the optical path and the Polaroid sheet was adjusted such that beam extinction was achieved with the elements crossed. The lenses and beam block were then inserted and aligned.

Following optical alignment an instrument response function (IRF) was recorded to check the response of the MCP and to verify the absence of secondary reflections in the optical path. The IRF was obtained by using low intensity laser light from a scattering sample (a thin cell containing undoped liquid crystal is suited to this purpose). To avoid damage to the MCP the beam intensity was raised from its minimum value until a satisfactory count rate was achieved (section 2.7.2). An IRF with a FWHM greater than 100ps was discarded, and optical alignment was repeated. Similarly, if unwanted reflection artefacts were observed in the IRF (this was best achieved using a logarithmic plot), alignment was repeated until no reflections were present. Following the IRF the system was calibrated; this was achieved by repeating the IRF with the inclusion of a known electronic delay, resulting in a response function with two peaks. A typical calibration is shown in figure 2.10.

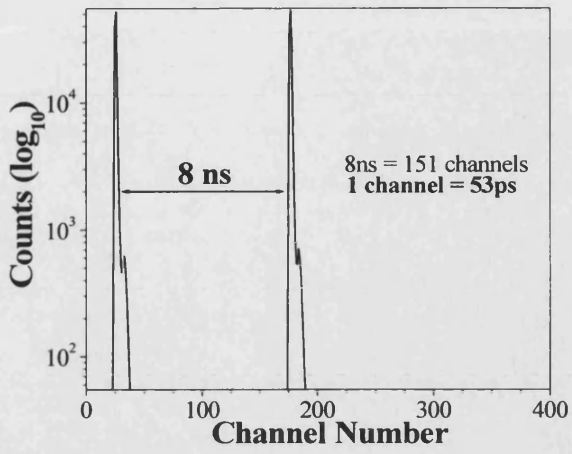

2.10: Logarithmic plot of the calibration for TCSPC bin numbers (channels) to time. The instrument response functions, separated by 8ns and 151 channels, yield a calibration of 53ps / bin.

2.8.2 G-Factor

The next experimental check, known as the G-Factor test, was to ensure that there was no polarisation bias arising from the optical elements. In conventional fluorescence experiments on isotropic systems, any polarisation bias between the vertical (I_V) and horizontal (I_H) components of fluorescence can be corrected for in analysis by matching the tails of the fluorescence decays [24] as the anisotropy tends to zero. This is not the case in an aligned environment and so it is necessary to ensure that there is no polarisation bias. This was achieved by substituting the aligned thin cell for an isotropic sample (typically an isotropic solvent such as ethylene glycol doped with the experimental dye) and measuring the fluorescence arising from a laser excitation polarisation angle of 45°. If no polarisation bias exists in the set up then the I_V and I_H components should yield identical decays at all times; if necessary the optical elements were adjusted and the G-Factor test was repeated until this condition had been met.

In the experiments described in this chapter the vertical and horizontal components of fluorescence emission were collected alternately for periods of 10 seconds over the course of several minutes, with an identical total collection time for each component. The two components of fluorescence were not measured consecutively since any slow drift in the laser output would distort the anisotropy. Alternate components (i.e vertical and horizontal) of fluorescence emission were collected by attaching the polaroid sheet to a stepper motor which could be controlled by the PC with a synchronous change in the MCB memory address. A non-commercial program written by Dr Gary Holtom

(Pacific North Western Research Laboratory) was used to stop and start the experiment; a polarisation data collection program was developed by W.J.Noad (formerly of RAL) which was run in conjunction with the Holtom program.

2.8.3 Data Collection

Vertical and horizontal components of fluorescence emission of Rhodamine 6G and Rhodamine B following single photon excitation at 560-575nm were collected for excitation polarisation angles of 0° and 90° and shown in figures 2.11a and 2.11b respectively.

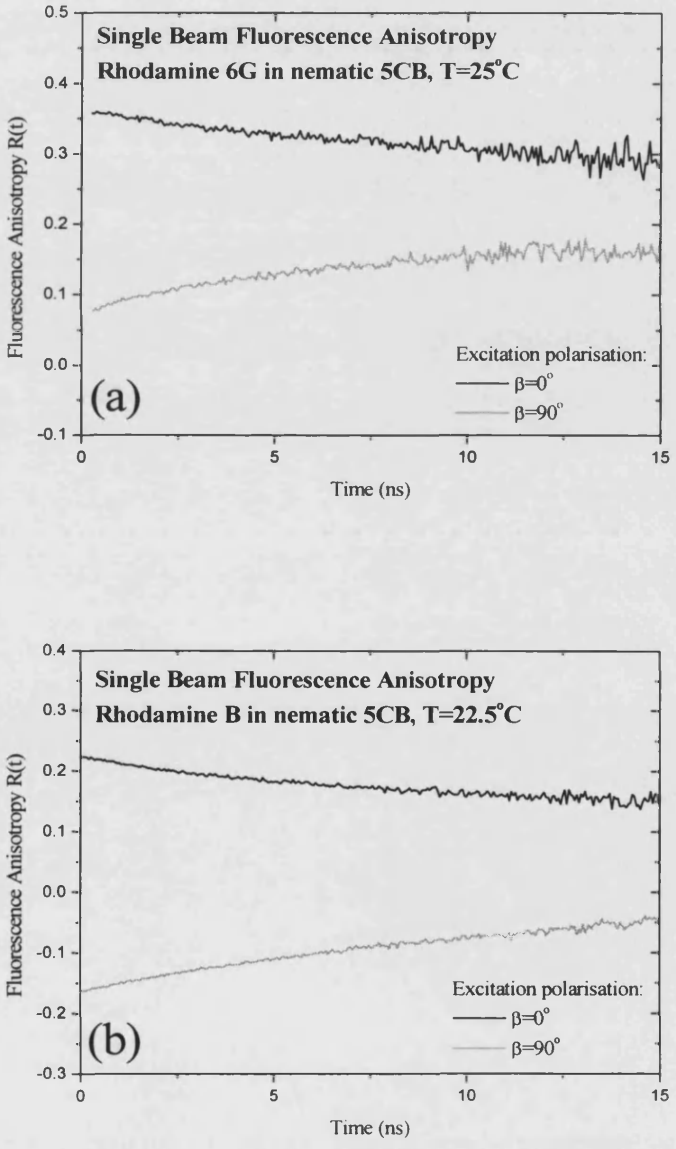

Figure 2.11: Fluorescence anisotropy decays for excitation polarisation angles of 0° and 90° for (a) Rhodamine 6G and (b) Rhodamine B in nematic 5CB.

2.8.4 Correction Factors

It is necessary to consider the effects of birefringence from the liquid crystal and depolarisation from the optics and local field effects [28] before fitting the experimental data.

2.8.4.1 Reflection Losses and Local Field Effects

The effect of the sample birefringence gives rise to differential reflection losses for ordinary (o) and extraordinary rays (e) at the boundary between the aligned sample and the cell walls (refractive index n_g). The transmission of light (T) through a boundary between two media with different refractive indices can be expressed in terms of a Fresnel coefficient [29].

$$T_e = 4n_e n_g / \left(n_e + n_g\right)^2 \qquad [2.34]$$

$$T_o = 4n_o n_g / \left(n_o + n_g\right)^2 \qquad [2.35]$$

Moreover, in an anisotropic dielectric, the ordinary and extraordinary polarised components of fluorescence emission are modified due to local field effects, yielding modified intensities as [30]

$$I_Z(\text{observed}) \propto I_Z(\text{i})\left(n_e^2 + 2\right) \qquad [2.36]$$

$$I_X(\text{observed}) \propto I_X(\text{i})\left(n_o^2 + 2\right) \qquad [2.37]$$

where (i) denotes the intensity for the emission in an anisotropic dielectric of unit refractive index.

The total modification of the Z and X polarised components of the fluorescence anisotropy is thus,

$$I_z(\text{observed}) \propto I_z(\text{i}) \frac{\left(n_e^2 + 2\right) 4n_e n_g}{\left(n_e + n_g\right)^2} \equiv I_z(\text{i}) \cdot a \qquad [2.38]$$

$$I_x(\text{observed}) \propto I_x(\text{i}) \frac{\left(n_o^2 + 2\right) 4n_o n_g}{\left(n_o + n_g\right)^2} \equiv I_x(\text{i}) \cdot b \qquad [2.39]$$

Defining a parameter k=a/b the measured fluorescence anisotropy can be written as,

$$R = \frac{kI_Z(i) - I_X(i)}{kI_Z(i) + 2I_X(i)} \qquad [2.40]$$

where the parameter k is given by

$$k = \frac{\left(n_e^2 + 2\right)n_e\left(n_o + n_g\right)^2}{\left(n_o^2 + 2\right)n_o\left(n_e + n_g\right)^2} \qquad [2.41]$$

The measured fluorescence anisotropy for anisotropic rotational diffusion in a cylindrically symmetric medium is calculated by substitution of equations 2.40 and 2.41 into equation 1.30, yielding

$$R(t) = \frac{(k-1) + \frac{\langle \alpha_{20}^{ex}(t) \rangle}{\sqrt{5}}(2k+1) - \sqrt{\frac{3}{10}}\left\{\alpha_{2+2}^{ex}(t) + \alpha_{2-2}^{ex}(t)\right\}}{(k+2) - \frac{\langle \alpha_{20}^{ex}(t) \rangle}{\sqrt{5}}(2k-2) + 2\sqrt{\frac{3}{10}}\left\{\alpha_{2+2}^{ex}(t) + \alpha_{2-2}^{ex}(t)\right\}} \qquad [2.42]$$

Published data for n_e and n_o for 5CB [31] yield the value of the correction factor k for the excitation wavelengths and temperatures used in the photoselection experiments. Values of the k correction factor of 1.14015 and 1.13287 were determined for Rhodamine 6G and Rhodamine B respectively.

Recent work within the group has shown that k can be determined from an analysis of the Z and X polarised emission intensities [32], allowing studies of probe order and motion to be extended to media where detailed refractive index data is unavailable [14].

2.8.4.2 Depolarisation Effects

The initial fluorescence anisotropy of a single photon excited state distribution in an isotropic medium has a maximum value of 0.4, but there are reasons why this may not be observed in a polarised fluorescence experiment [33]. If the absorption and emission dipole moments of the fluorophore are not parallel, then the initial fluorescence anisotropy would be given by [34]

$$R(0) = 0.4\frac{1}{2}\left[3(\hat{\mu}_{abs}\cdot\hat{\mu}_{em})^2 - 1\right] \qquad [2.43]$$

Additional depolarisation of fluorescence can arise from self-absorption [35], scattering [36] and depolarisation in the collection optics [37]. The net effect of these depolarising influences is to modify the excited state alignment by a correction factor $\bar{A}$ less than unity such that [9]

$$R(t) = \frac{\frac{(k-1)}{\bar{A}} + \frac{\langle\alpha_{20}^{ex}(t)\rangle}{\sqrt{5}}(2k+1) - \sqrt{\frac{3}{10}}\{\alpha_{2+2}^{ex}(t) + \alpha_{2-2}^{ex}(t)\}}{\frac{(k+2)}{\bar{A}} - \frac{\langle\alpha_{20}^{ex}(t)\rangle}{\sqrt{5}}(2k-2) + 2\sqrt{\frac{3}{10}}\{\alpha_{2+2}^{ex}(t) + \alpha_{2-2}^{ex}(t)\}} \qquad [2.44]$$

The $\bar{A}$ correction factor was determined for each dye probe in 5CB by a fit to the variation in initial anisotropy values with excitation polarisation in the isotropic phase of the liquid crystal [9] according to equation 2.45:

$$R(0,\beta) = \frac{\frac{2}{5}(\cos^2\beta - \sin^2\beta)}{\frac{1}{\bar{A}} + \frac{2}{5}\sin^2\beta} \qquad [2.45]$$

The isotropic phase of 5CB was reached by raising the temperature of the sample above the nematic-isotropic phase transition temperature (~35°C) [38]. This was achieved by placing the sample into a ±0.1°C precision temperature controlled oven (Mettler FP 82 Hot Stage). Fits to R(0,β) data yielded $\bar{A}$ values of 0.9 and 0.917 for Rhodamine 6G and Rhodamine B respectively, a depolarising effect of 5-10%.

2.9 Single Beam Photoselection Results

With k and Ā known, it was possible to fit the single beam fluorescence anisotropy data from section 2.7.3 with five variables, namely $a = \langle \alpha_{20}^{gs} \rangle / \sqrt{5}$, $b = \langle \alpha_{40}^{gs} \rangle$, R_{ss}, τ_{20} and τ_{22}. Variables a and b could be determined by solving the simultaneous equations generated by entering the initial anisotropies from $\beta=0°$ and $\beta=90°$ excitation into equations 2.16 and 2.17 and substituting equations 2.16 and 2.17 into equation 2.18. The evaluation of equation 2.18 was achieved using mathematical software "MathCad". Fixing the values of a and b, the $R(t,\beta=0°)$ was fitted allowing τ_{20} and $R_{SS}(\beta=0°)$ to be determined. Finally, fixing the values of a, b and τ_{20} allowed τ_{22} to be determined from a fit to $R(t, \beta=90°)$. Values of a, b, τ_{20} and τ_{22} for Rhodamine 6G and Rhodamine B from fits to the experimental data are shown in table 2.1.

Parameter	Rhodamine 6G	Rhodamine B
$\frac{\langle \alpha_{20}^{gs} \rangle}{\sqrt{5}}$	0.246	0.006
$\langle \alpha_{40}^{gs} \rangle$	-0.774	-0.583
τ_{20}	10.7±1.0	9.4±0.5
τ_{22}	5.83±0.01	9.75±0.03

Table 2.1: Ground state parameters and re-orientational lifetimes for Rhodamine 6G and Rhodamine B in the nematic phase of 5CB.

In the linear relaxation model described in section 2.5 anisotropic viscosity is taken to be the dominant mechanism which causes differences in τ_{20} and τ_{22}. Observation of the alignment dynamics for an excitation polarisation angle of $\beta=0°$ has shown the θ diffusion dynamics of probe molecules are aligned predominantly along the laboratory Z-axis. For single beam photoselection (in a positively aligned medium) the observation of θ diffusion for probe molecules aligned orthogonally to Z is invariably convoluted with the asymmetric alignment dynamics. In a highly ordered environment such as nematic 5CB it is possible that the diffusion dynamics may not be linear and the simple picture of alignment relaxation described in section 2.5 will not hold. In these circumstances an experimentally unambiguous picture of the full alignment dynamics is advantageous. To this end, the ability to control the initial photoselected excited state

alignment whilst retaining an axis of cylindrical symmetry is highly desirable, as this would allow a range of excited state distributions to be created which should only contain information on the evolution of the $\langle \alpha_{20}^{ex}(t) \rangle / \sqrt{5}$ moment. If the cylindrically symmetric relaxation rate was found to vary with alignment, it would indicate that cross-relaxation between distribution moments had taken place and the first order perturbation linear relaxation model would no longer be valid.

2.10 Three Beam Photoselection

The experimental scheme for the single-photon photoselection of a sample by three temporally coincident picosecond pulses with mutually orthogonal polarisation vectors is shown in figure 2.12.

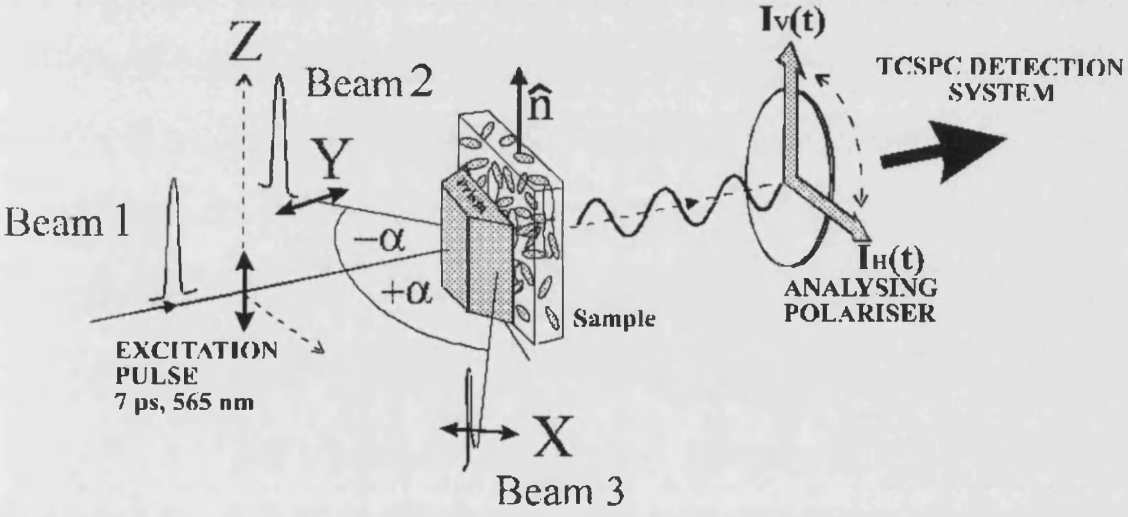

Figure 2.12: Schematic of the excitation-detection geometry utilised for three beam photoselection

Two horizontally (H) polarised laser beams are propagated at ±45° respectively, with a vertically (V) polarised beam directed at normal incidence to the sample. If the two H-polarised beams are introduced to the sample and are of equal intensity the net result of photoselection is a transition probability that, whilst peaked for transition dipole moments oriented in the XY plane is ϕ independent. The combination of this $\sin^2\theta$ transition probability and the $\cos^2\theta$ photoselection from the vertically polarised (Z) pulse is an excited state order that is characterised wholly by the cylindrically symmetric moment. The net degree of excited state alignment can be varied simply by controlling the ratio of intensities of the vertically polarised beam to that of the (equal) horizontally polarised beams whilst retaining cylindrical symmetry as shown in figure 2.13.

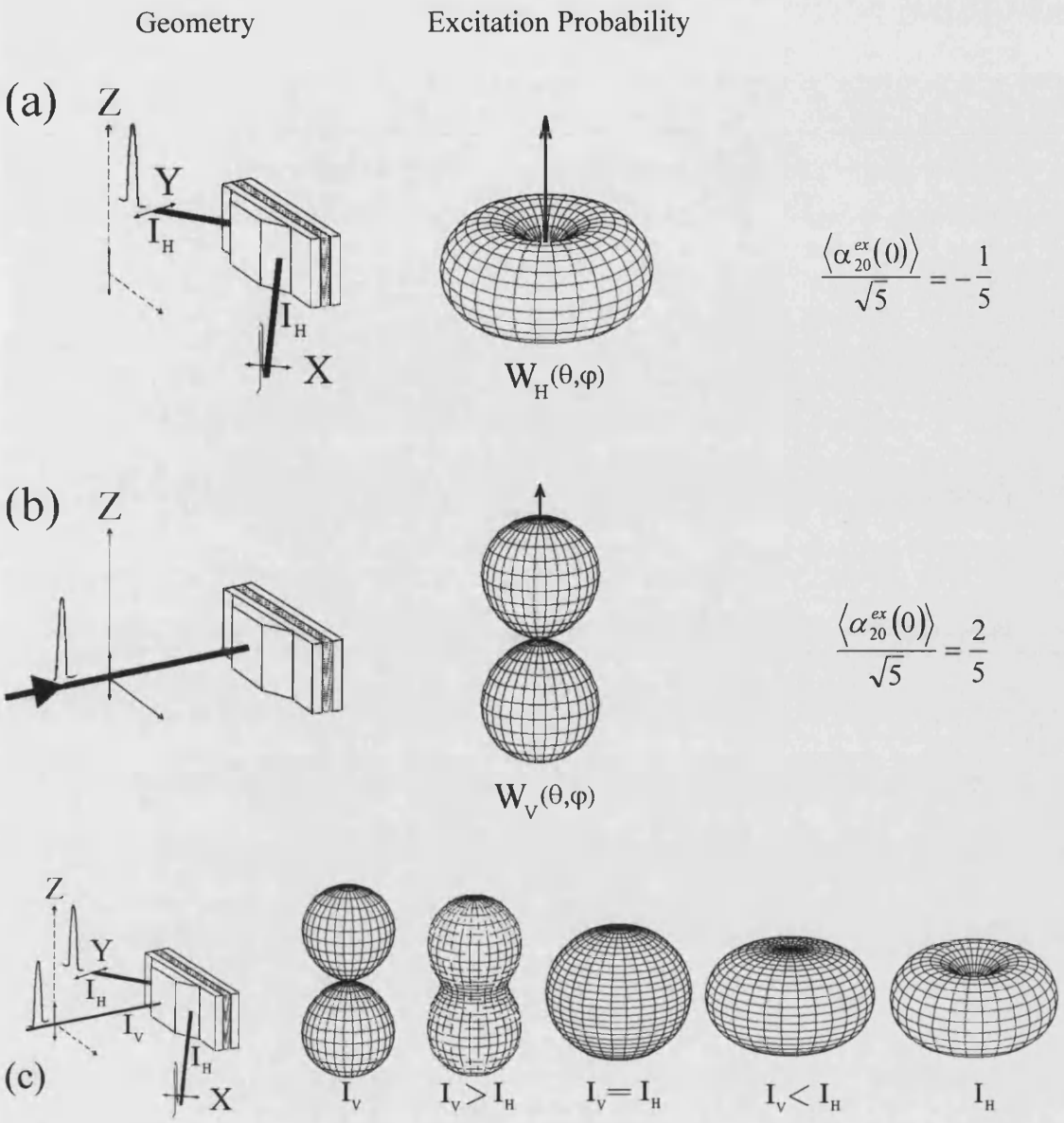

Figure 2.13: Illustration of the 3 beam photoselection technique in which the degree of cylindrical alignment $\langle \alpha_{20}^{ex} \rangle / \sqrt{5}$ in isotropic media can be varied from a minimum value of (-1/5) as shown in figure (a) produced by horizontally polarised beams propagating at ± 45^0 or a maximum value of (2/5) as shown in figure (b) or intermediate values between by the use of all three beams (c).

2.10.1 Initial Fluorescence Anisotropy for 3-Beam Photoselection

Following the approach in section 2.4, the excitation operator for a normally incident laser with polarisation angle β is given by;

$$W_1(\theta,\phi) = BI_1(t)|\mu_a|^2 \frac{(4\pi)^{\frac{1}{2}}}{3}\begin{bmatrix} Y_{00}(\theta,\phi) + \frac{2}{\sqrt{5}} d^2_{02}(\beta) Y_{22}(\theta,\phi) \\ + \frac{2}{\sqrt{5}} d^2_{01}(\beta) Y_{21}(\theta,\phi) \\ + \frac{2}{\sqrt{5}} d^2_{00}(\beta) Y_{20}(\theta,\phi) \\ + \frac{2}{\sqrt{5}} d^2_{0-1}(\beta) Y_{2-1}(\theta,\phi) \\ + \frac{2}{\sqrt{5}} d^2_{0-2}(\beta) Y_{2-2}(\theta,\phi) \end{bmatrix} \quad [2.46]$$

where $d^2_{0Q}(\beta)$ are the reduced rotation matrix elements introduced in section 2.4. Rotation of the angle of incidence through α in the XY plane modifies each spherical harmonic by [11]

$$D(\alpha,0,0)Y_{KQ}(\theta,\phi) = e^{-i\alpha Q} Y_{KQ}(\theta,\phi) \quad [2.47]$$

For non-normal incidence, the excitation operator becomes

$$W_2(\theta,\phi) = BI_1(t)|\mu_a|^2 \frac{(4\pi)^{\frac{1}{2}}}{3}\begin{bmatrix} Y_{00}(\theta,\phi) + \frac{2}{\sqrt{5}} d^2_{00}(\beta) Y_{20}(\theta,\phi) \\ + \frac{2}{\sqrt{5}} d^2_{02}(\beta) Y_{22}(\theta,\phi)\{\cos 2\alpha - i\sin 2\alpha\} \\ + \frac{2}{\sqrt{5}} d^2_{01}(\beta) Y_{21}(\theta,\phi)\{\cos \alpha - i\sin \alpha\} \\ + \frac{2}{\sqrt{5}} d^2_{0-1}(\beta) Y_{2-1}(\theta,\phi)\{\cos \alpha + i\sin \alpha\} \\ + \frac{2}{\sqrt{5}} d^2_{02}(\beta) Y_{2-2}(\theta,\phi)\{\cos 2\alpha + i\sin 2\alpha\} \end{bmatrix} \quad [2.48]$$

rearranging equation 2.48 yields

$$W_2(\theta,\phi) = BI_1(t)|\mu_a|^2 \frac{(4\pi)^{\frac{1}{2}}}{3}\begin{bmatrix} Y_{00} + \frac{2}{\sqrt{5}} d^2_{00}(\beta) Y_{20}(\theta,\phi) \\ + \frac{2}{\sqrt{5}} d^2_{02}(\beta)\cos 2\alpha\left(Y_{22}(\theta,\phi) + Y_{2-2}(\theta,\phi)\right) \\ + \frac{2}{\sqrt{5}} d^2_{01}(\beta)\cos \alpha\left(Y_{21}(\theta,\phi) + Y_{2-1}(\theta,\phi)\right) \\ + \frac{2}{\sqrt{5}} d^2_{0-1}(\beta) i\sin \alpha\left(Y_{2-1}(\theta,\phi) - Y_{21}(\theta,\phi)\right) \\ + \frac{2}{\sqrt{5}} d^2_{02}(\beta) i\sin 2\alpha\left(Y_{2-2}(\theta,\phi) - Y_{22}(\theta,\phi)\right) \end{bmatrix} \quad [2.49]$$

For a horizontally polarised beam (β=90°) and with a propagation angle of α=45°, the excitation operator becomes

$$W_2(\theta,\phi) = BI_1(t)|\mu_a|^2 \frac{(4\pi)^{\frac{1}{2}}}{3}\left[\begin{array}{l} Y_{00}(\theta,\phi) - \frac{1}{\sqrt{5}} Y_{20}(\theta,\phi) \\ + i\sqrt{\frac{3}{10}}\{Y_{22}(\theta,\phi) - Y_{2-2}(\theta,\phi)\} \end{array}\right] \quad [2.50]$$

For a second beam of intensity I_3 propagating at α=-45°, the excitation operator is similarly

$$W_3(\theta,\phi) = BI_3(t)|\mu_a|^2 \frac{(4\pi)^{\frac{1}{2}}}{3}\left[\begin{array}{l} Y_{00}(\theta,\phi) - \frac{1}{\sqrt{5}} Y_{20}(\theta,\phi) \\ - i\sqrt{\frac{3}{10}}\{Y_{22}(\theta,\phi) - Y_{2-2}(\theta,\phi)\} \end{array}\right] \quad [2.51]$$

Combining the two horizontally polarised beams with a third vertically polarised (β=0°) beam of intensity I_2 propagating at normal incidence to the sample (α=0), the net excitation operator $W_{1,2,3}(\theta,\varphi)$ becomes

$$W_{1,2,3}(\theta,\phi) = B(t)|\mu_a|^2 \frac{(4\pi)^{\frac{1}{2}}}{3}\left[\begin{array}{l} Y_{00}(\theta,\phi)\{I_1 + I_2 + I_3\} \\ + \frac{1}{\sqrt{5}} Y_{20}(\theta,\phi)\{2I_2 - (I_1 + I_3)\} \\ - i\sqrt{\frac{3}{10}}\{Y_{22}(\theta,\phi) - Y_{2-2}(\theta,\phi)\}\{I_3 - I_1\} \end{array}\right] \quad [2.52]$$

Equation 2.52 reveals for horizontally polarised beams of equal intensity (I_1=I_3), the cylindrically asymmetric $\{Y_{22}(\theta,\varphi) - Y_{2-2}(\theta,\varphi)\}$ contribution the excitation operator vanishes. With this arrangement, photoselection from an axially ordered ground state yields an excited state distribution with the following moments [9]

$$\langle C_{00}^{ex}(0)\rangle = \langle C_{00}^{gs}\rangle\{I_1 + I_2 + I_3\} + \frac{\langle C_{20}^{gs}\rangle}{\sqrt{5}}\{2I_1 - (I_2 + I_3)\} \quad [2.53]$$

$$\left\langle C_{20}^{ex}(0)\right\rangle = \frac{\left\langle C_{00}^{gs}\right\rangle}{\sqrt{5}}\{2I_1-(I_2+I_3)\}+\frac{\left\langle C_{20}^{gs}\right\rangle}{7}\{11I_1+5(I_2+I_3)\}+\frac{6\left\langle C_{40}^{gs}\right\rangle}{7\sqrt{5}}\{2I_1-(I_2+I_3)\} \qquad [2.54]$$

The initial fluorescence anisotropy $R(0)\sqrt{5} = \left\langle C_{20}^{ex}(0)\right\rangle / \left\langle C_{00}^{ex}(0)\right\rangle$ is thus

$$R(0) = \frac{[2I_1-(I_2+I_3)]\left(\frac{1}{5}+\frac{6\left\langle \alpha_{40}^{gs}\right\rangle}{35}\right)+[11I_1+5(I_2+I_3)]\frac{\left\langle \alpha_{20}^{gs}\right\rangle}{7\sqrt{5}}}{[I_1+I_2+I_3]+[2I_1-(I_2+I_3)]\frac{\left\langle \alpha_{20}^{gs}\right\rangle}{\sqrt{5}}} \qquad [2.55]$$

If a dimensionless ratio of intensities B(I) is given by

$$B(I) = \frac{I_1-\frac{1}{2}[I_2+I_3]}{I_1+I_2+I_3} \qquad [2.56]$$

Equation 2.56 can be simplified to

$$R(0) = \frac{\frac{\left\langle \alpha_{20}^{gs}\right\rangle}{\sqrt{5}}+B(I)\left[\frac{2}{5}+\frac{4}{7}\frac{\left\langle \alpha_{20}^{gs}\right\rangle}{\sqrt{5}}+\frac{12}{35}\left\langle \alpha_{40}^{gs}\right\rangle\right]}{1+2B(I)\frac{\left\langle \alpha_{20}^{gs}\right\rangle}{\sqrt{5}}} \qquad [2.57]$$

This anisotropy contains only cylindrically symmetric terms if the horizontally polarised beams can be made to propagate with equal intensity at ±45° to the collinear vertically polarised beam.

2.11 Experimental Procedure for Three Beam Photoselection

With correction factors k and Ā known (section 2.8.4), the experimental procedure for three beam photoselection of Rhodamine dyes in nematic 5CB was as follows:

Step 1: Single (collinear) beam excitation of the sample, with excitation polarisation angles of 0° and 90°. This step established values for the ground state moments $\langle \alpha_{20}^{gs} \rangle / \sqrt{5}$ and $b = \langle \alpha_{40}^{gs} \rangle$, as described in section 2.8.

Step 2: The X and Y polarised beams (beams 2 and 3) were set up to propagate at 45° to the collinear beam (beam 1). This was achieved using prism coupling and a prediction of the initial anisotropy that would be obtained using horizontally polarised light (section 2.11.2).

Step 3: All beams were spatially and temporally overlapped (section 2.11.3).

Step 4: Fluorescence anisotropy measurements were made for varying values of beam intensity ratio B(I) from 1 (Z-polarised excitation) to –0.5 (X and Y polarised excitation).

2.11.1 Experimental Setup

The experimental setup for three beam photoselection is illustrated in figure 2.14; it remains the same as for the single beam experiments (figure 2.8), with the exception of two additional beams (Beams 2 and 3 in figure 2.12) which propagate at ±45° with respect to the collinear beam (Beam 1, figure 2.12). Half-wave plates and neutral density wheels were employed to provide polarisation and intensity control for all beams.

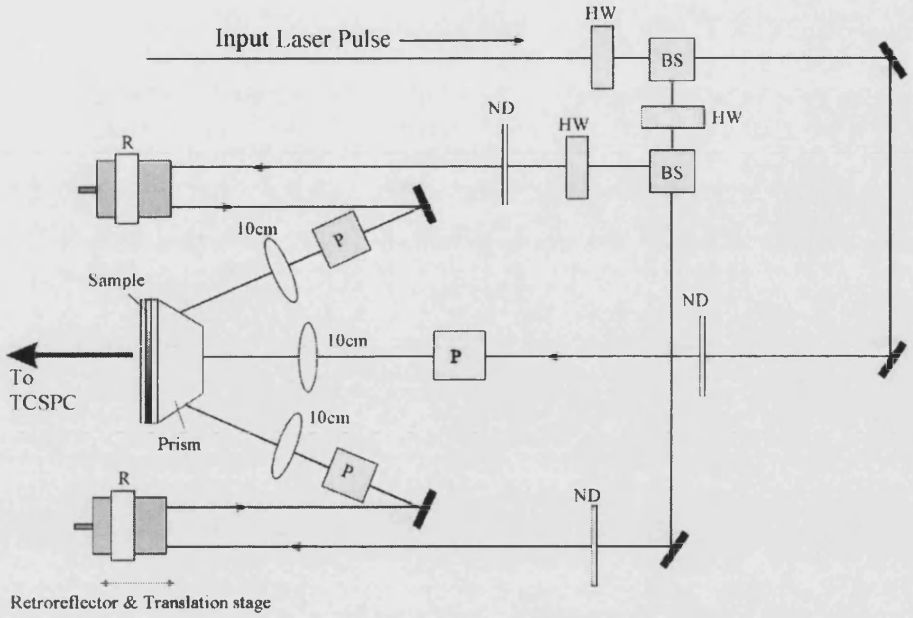

Figure 2.14: experimental setup for three beam photoselection. The excitation laser source was split into three paths using half-wave plates (HW) and polarising beamsplitters (BS). The path lengths of the 45° propagating beams was matched to the collinear beam using cube retro-reflectors (R) mounted on precision translation stages with 10cm (0.67ns) travel. All beams were focused into the sample using 10cm focal length lenses.

2.11.2 Beam Alignment

In order to achieve the conditions whereby net cylindrical symmetry is maintained by three pulse photoselection, it is necessary for the horizontally polarised beams to propagate through the sample at ±45° to the Z polarised excitation pulse. From Snell's Law for propagation at 45° to the normal the incident light angle ξ_{air} at the air-glass interface for a sample must satisfy [14]

$$\sin \xi_{air} = n_{sample} / \sqrt{2} \qquad [2.58]$$

It is clear therefore that n_{sample} must not exceed $\sqrt{2}$, however in 5CB n_{sample} is greater than $\sqrt{2}$ [38], so prism coupling is necessary to achieve 45° sample propagation [11].

The correct propagation angle of 45° for the X and Y polarised beams could be established from measurements of the initial anisotropy relation for horizontally polarised excitation (i.e. β =90°) (R_H) with varying external propagation angle ξ. The variation of R_H with ξ is given by [14],

$$R_H(0,\xi)=\frac{\frac{k-1}{A}\left[1-\frac{\langle\alpha_{20}^{gs}\rangle}{\sqrt{5}}\right]+(2k+1)\left[-\frac{1}{5}+\left(\frac{5}{7}\right)\frac{\langle\alpha_{20}^{gs}\rangle}{\sqrt{5}}-\frac{6}{35}\langle\alpha_{40}^{gs}\rangle\right]-\frac{3}{5}\cos(2\xi)\left[1-\frac{10}{7\sqrt{5}}\langle\alpha_{20}^{gs}\rangle-\frac{\langle\alpha_{40}^{gs}\rangle}{7}\right]}{\frac{k+2}{A}\left[1-\frac{\langle\alpha_{20}^{gs}\rangle}{\sqrt{5}}\right]+2(k-1)\left[\frac{-1}{5}+\left(\frac{5}{7}\right)\frac{\langle\alpha_{20}^{gs}\rangle}{\sqrt{5}}-\frac{6}{35}\langle\alpha_{40}^{gs}\rangle\right]+\frac{6}{5}\cos(2\xi)\left[1-\frac{10}{7\sqrt{5}}\langle\alpha_{20}^{gs}\rangle-\frac{\langle\alpha_{40}^{gs}\rangle}{7}\right]}$$

[2.59]

The predicted variation in R_H with propagation angle ξ for Rhodamine 6G in 5CB is shown in figure 2.15. For Rhodamine 6G, 45°propagation in the sample corresponds to an initial anisotropy of 0.177. The angle of incidence of one horizontally polarised beam was varied until the target anisotropy of 0.177 was reached. The second horizontally polarised beam was similarly aligned.

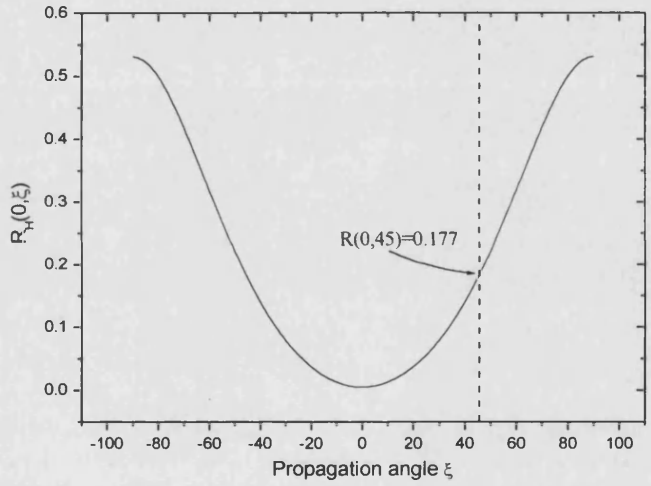

Figure 2.15: Variation of initial anisotropy from horizontally polarised light as a function of external propagation angle for Rhodamine 6G in 5CB. In this system, 45° propagation would yield an initial anisotropy of 0.177.

2.11.3 Beam Overlap

Spatial matching was achieved by overlapping the fluorescence spots from each beam at the sample. Temporal overlap was achieved by translation of the retro-reflectors in the 45° propagating beams to match the path length of the collinear beam. To ensure that cylindrical symmetry was retained in the overall photoselection process, the three pulses should not add together coherently (i.e. exact temporal overlap). The relative delays of the three beams were adjusted to within 1 channel (±53ps) by measuring the individual fluorescence signals.

2.12 Three Beam Photoselection Results

The fluorescence anisotropy data for three beam photoselection of Rhodamine 6G and Rhodamine B in nematic 5CB are shown in figures 2.16 and 2.17 respectively.

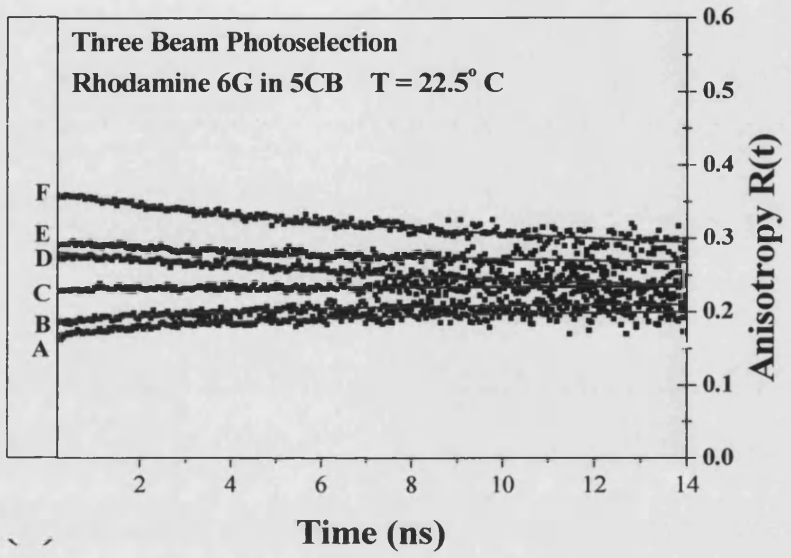

Figure 2.16: Three beam photoselection of Rhodamine 6G in nematic 5CB. Anisotropy decays A-F correspond to values of beam ratio B(I) in table 2.2.

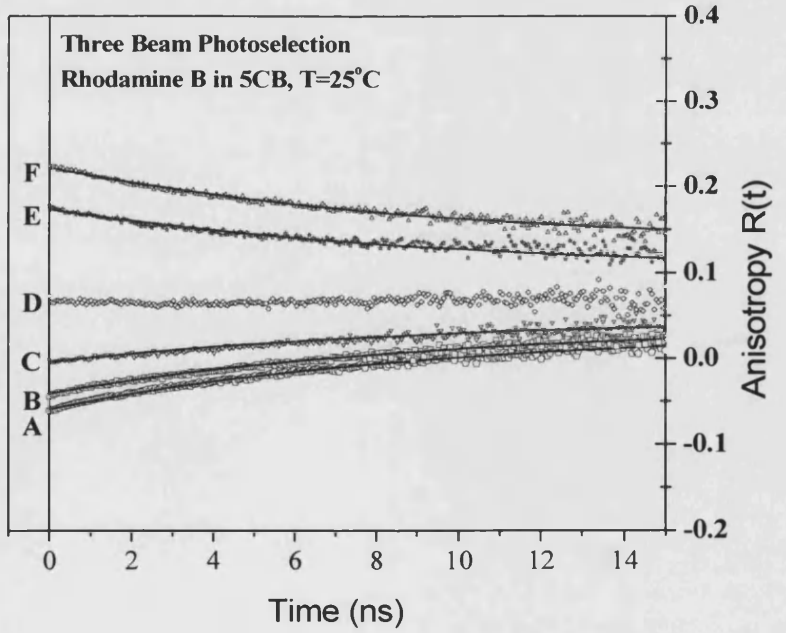

Figure 2.17: Three beam photoselection of Rhodamine B in nematic 5CB. Anisotropy decays A-F correspond to values of beam ratio B(I) in table 2.3.

All the fluorescence anisotropy decays were fitted to a single exponential lifetime in accordance with the linear relaxation model described in section 2.5. The values for re-orientational lifetime from best fits to experimental data are shown in table 2.2 and table 2.3 for Rhodamine 6G and Rhodamine B respectively.

Rhodamine 6G

Beam	Beam Ratio	Lifetime (ns)
A	1	10.7±1.0
B	-0.500	10.6±1.1
C	-0.143	10.7±1.0
D	0.330	11.0±2.4
E	0.600	10.3±2.4
F	0.610	10.8±1.9

Table 2.2: Lifetime fits to the three beam photoselection data for Rhodamine 6G in nematic 5CB

Rhodamine B

Beam	Beam Ratio	Lifetime (ns)
A	1	10.73±1.00
B	-0.500	9.2±0.2
C	-0.182	9.3±0.1
D	0.091	R(0)≈R(ss)
E	0.538	9.8±0.2
F	0.801	9.4±0.2

Table 2.3: Lifetime fits to the three beam photoselection data for Rhodamine B in nematic 5CB

The lifetime fits from three beam excitation are in excellent agreement (within experimental uncertainties) with the lifetime obtained for a single beam photoselection experiment using vertically polarised light in section 2.8.

The predicted maximum and minimum degrees of initial alignment can be determined from equation 2.57 where B(I) is 1 and –0.5 respectively, yielding:

$$R(0,\max)=\left[\frac{k-1}{A}+(2k+1)\left[\langle P_2\rangle+\left(\frac{2}{5}+\frac{4}{7}\langle P_2\rangle+\frac{36}{35}\langle P_4\rangle\right)\right]\right]\Big/\left[\frac{k+2}{A}+2(k-1)\langle P_2\rangle\right] \qquad [2.60]$$

$$R(0,\min)=\left[\frac{k-1}{A}+(2k+1)\left[\langle P_2\rangle-\left(\frac{1}{5}+\frac{2}{7}\langle P_2\rangle+\frac{18}{35}\langle P_4\rangle\right)\right]\right]\Big/\left[\frac{k+2}{A}-(k-1)\langle P_2\rangle\right] \qquad [2.61]$$

where $\langle P_2\rangle$ and $\langle P_4\rangle$ are the more commonly used 2nd and 4th rank order parameters used to describe cylindrically symmetric samples [14] these are related to the alignment moments through

$$\langle P_K\rangle=\langle\alpha_{K0}\rangle/\sqrt{2K+1} \qquad [2.62]$$

The tuning range of initial anisotropy measured for Rhodamine 6G and Rhodamine B in excellent accordance (i.e. within experimental error) with the predicted maximum and minimum initial anisotropy values, as shown in table 2.4.

Rhodamine 6G, T=22.5°C	B(I)	$R_{predicted}$	$R_{observed}$
$\langle P_2\rangle = 0.246$ $\langle P_4\rangle = -0.774$ k = 1.14015 A = 0.9	1	0.371	0.36 ± 0.01
	-0.5	-0.177	-0.18 ± 0.01

Rhodamine B, T=25°C	B(I)	$R_{predicted}$	$R_{observed}$
$\langle P_2\rangle = -0.006$ $\langle P_4\rangle = -0.583$ k = 1.13287 A = 0.917	1	0.224	0.22 ± 0.01
	-0.5	-0.057	-0.06 ± 0.01

Table 2.4: Comparison of predicted initial anisotropies using three beam photoselection with experimental values for Rhodamine 6G and Rhodamine B in nematic 5CB; the ground state parameters obtained from the single beam β=0° and 90° curves predict the initial anisotropy tuning range that should be possible using three beam photoselection.

It is also possible to make a comparison between cylindrically symmetric and cylindrically asymmetric reorientation. By varying the excitation polarisation angle β using a single beam such that the initial anisotropy created matches that obtained by the three beam photoselection with beam ratio B(I)=-0.5, a dynamic comparison of angular

averaging from pure θ diffusion and both θ and φ diffusion can be made; this is shown for Rhodamine 6G in figure 2.18.

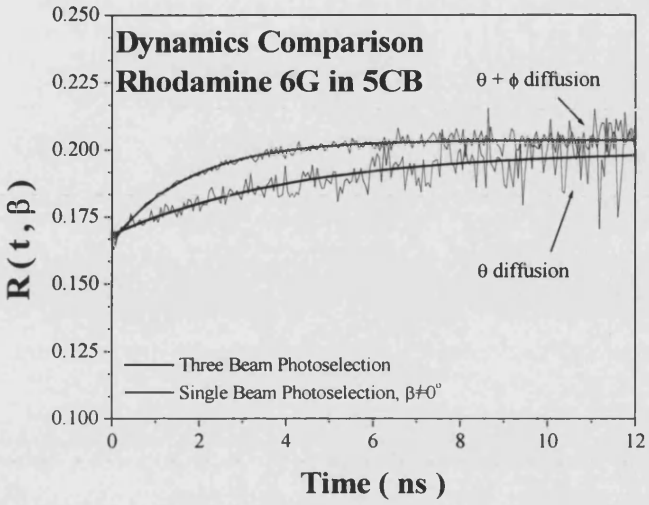

Figure 2.18: Dynamics Comparison of excited state distributions with the same initial anisotropy but different cylindrically symmetric and asymmetric contributions highlights the anisotropic viscosity present for Rhodamine 6G in nematic 5CB.

Using the single beam photoselection data with β=0° and β=90°, it is possible to determine the difference in θ and φ diffusion rates. From equations 2.27 and 2.28,

$$\tau_{20} = \frac{1}{\gamma_{20}} = \frac{1}{6D_\theta} \qquad [2.63]$$

$$\tau_{22} = \frac{1}{\gamma_{22}} = \frac{1}{4D_\varphi + 2D_\theta} \qquad [2.64]$$

The values of γ_θ and γ_φ are shown for Rhodamine 6G in nematic 5CB in table 2.5.

τ_{20} (ns)	τ_{22} (ns)	$\gamma_\theta \equiv D_\perp^{LAB}$ ($\times 10^7 s^{-1}$)	$\gamma_\phi \equiv D_\parallel^{LAB}$ ($\times 10^7 s^{-1}$)	$\gamma_\phi / \gamma_\theta$
10.7±1.0	5.83±0.01	1.55±0.08	3.51±0.08	2.26±0.10

Table 2.5: Values for the cylindrically symmetric and asymmetric relaxation times for Rhodamine 6G in 5CB together with the corresponding θ and φ diffusion rates relative to the nematic director (laboratory Z axis).

The anisotropy in the intrinsic θ and φ diffusion rates in Rhodamine 6G is marked with $\gamma_\phi \cong 2.26\gamma_\theta$. The relative reduction in the θ diffusion rate would suggest that the probe is allowed to adopt only a restricted range of θ orientations in the nematic host. This is investigated further in the next chapter.

2.13 Conclusions

The comparison between single and three pulse photoselection has proven to be a powerful tool in providing an unambiguous picture of excited state orientational dynamics. In the Rhodamine 6G-5CB system in spite of the high degree of intrinsic probe order ($\langle P_2^{EX} \rangle$ approx. 0.246) the alignment dynamics are seen to be wholly independent of the initial molecular orientation and conform well to first order relaxation processes as predicted by perturbation theory and simple symmetry considerations.

It is clear that in the nematic phase of 5CB, Rhodamine 6G motion is highly anisotropic, whereas the differences between τ_{20} and τ_{22} for Rhodamine B in table 2.1 are much less marked. It is also clear that the ground state order parameters for the two dyes are different.

Equilibrium order within the nematic host seems to be an important factor in determining θ and φ diffusion dynamics; in this light, knowledge of $P(\theta,\varphi)$ is important. In liquid crystals this requires the measurement of higher order parameters (K>4) for the probe. The measurement of ground state order parameters up to K=6 can be achieved by a combination of single and two-photon fluorescence anisotropy measurements as presented in Chapter 3.

References for Chapter 2

1. W R Thomkins, M S Malcut, R W Boyd and J E Sipe, J. Opt. Soc. Am. **6**, 757 (1990)
2. D L Andrews and D Juzelinas, J. Chem. Phys. **95,** 5513 (1995)
3. P A Anfinrud, D E Hart and W S Struve, J. Phys. Chem. **92,** 4067 (1988)
4. H J Loesch, E Stenzel and B Wustenecker, J. Chem. Phys. **95,** 3841 (1991)
5. W M Yu, P T C So, T French and E Gratton, Biophys. J. **70**, 626 (1996)
6. N Chadborn, J Bryant, A J Bain and P O'Shea, Biophys. J. **76**, 2198 (1999)
7. A J Bain, P Chandna, G Butcher and J Bryant, J. Chem. Phys. **112**, 10435 (2000)
8. A J Bain, G Butcher-Taylor and P Chandna, Chem. Phys. Lett. **260**, 441 (1996)
9. J Bryant and A J Bain, Chem. Phys. Lett. **286**, 121 (1998)
10. P Chandna, Ph.D. Thesis, University of Essex (1995)
11. J Bryant, Ph.D. Thesis, University of Essex (2000)
12. A J Bain, P Chandna, G Butcher and J Bryant, J. Chem. Phys. **112**, 10418 (2000)
13. E M Monge, Ph.D. Thesis, University of London (2003)
14. D A Armoogum, J Bryant, E M Monge and A J Bain, Proc. SPIE **4799**, 63 (2002)
15. P G de Gennes and P Prost, "*The Physics of Liquid Crystals*" (2nd Ed.), Clarendon Press, (1993)
16. W D Callister Jr, "*Materials Science and Engineering*" (5th Ed.), Wiley, (2000)
17. G Vertogen and W H de Jeu,"*Thermotropic Liquid Crystals*", Springer-Verlag, (1988)
18. F J Kahn, G N Taylor and H Schonhorn, Proc. IEEE, **61**, 823, (1973)
19. D M Brink and G R Satchler, "Angular Momentum" (2nd Ed.), Clarendon Press, (1968)
20. G R Fleming and M Cho, Ann. Rev. Phys. Chem. **47**, 109 (1996)
21. T J Chang and K B Eisenthal, J. Chem. Phys. **57**, 5094, (1972)
22. A J Bain, "*Time Resolved Polarised Fluorescence Studies of Ordered Molecular Systems*", (Eds. D L Andrews and A Demidov), Kluwer, (2002)
23. D A Varshalovich, A N Moskalev and V K Khersonskii, *Quantum Theory of Angular Momentum*, Ed. World Scientific (1989)
24. D V O'Connor and D V Phillips, *Time Correlated Single Photon Counting*, Academic Press (1984)
25. G R Fleming, "*Chemical Applications of Ultrafast Spectroscopy*", Clarendon Press, Oxford (1986)

26. U Brackmann, *LambdaChrome® Laser Dyes* (3rd Ed.), Lambda Physik AG, Goettingen (2000)
27. I Dozov, N Kirov, M P Fontana, M Manfredi, B Rosi and R Cywinski, Liq. Cryst. **4**(3), 241 (1989)
28. I Dozov, S Temkin and N Kirov, Liq. Cryst. **8**(5), 727 (1990)
29. S G Lipson and H Lipson, *Optical Physics* (2nd Ed.), Cambridge University Press (1981)
30. S D Durbin and Y R Shen, Phys. Rev. A **30**, 1419, (1984)
31. S T Wu and C S Wu, Opt. Eng. **32**(8), 1775 (1993)
32. E M Monge, A Harsono, J Bryant, B Obradovic and A J Bain, Proc. SPIE **4797**, 264 (2003)
33. D S Kliger, J W Lewis and C E Randall, *Polarised light in Optics and Spectroscopy*, Academic Press, San Diego, (1990)
34. J R Lakowicz, *Principles of Fluorescence Spectroscopy* (2nd Ed.), Kluwer Academic, (1999)
35. A D Stein and M D Fayer, Chem. Phys. Lett. **176**, 159, (1991)
36. J Karolin, C D Geddes, K Wynne and D J S Birch, Meas. Sci. Technol. **13**, 21, (2002)
37. A Sharma, "*Introduction to Fluorescence Spectroscopy*", Wiley, New York, (1999)
38. Liquid Crystal Group Hamburg, URL: http://liqcryst.chemie.uni-hamburg.de/

Chapter 3

Two-Photon Excitation of Dye Probes in Ordered Environments

3.1 Introduction

It was shown in Chapter 2 that single photon time resolved fluorescence anisotropy experiments could yield information on the excited state dynamics of fluorescent probe molecules in isotropic and ordered environments and also upon the K=2 and K=4 ground state moments. From single photon electric dipole selection rules, fluorescence emission following single photon excitation was seen to be sensitive only to the alignment (K=2, Q=±2, 0) moments of the excited state array irrespective of the full orientational distribution [1,2]. The ability of polarised single photon fluorescence to yield information on ground state moments with rank K=2 and K=4 lies in the coupling between these moments and the quadrupolar (i.e. $Y_{2q}(\theta,\varphi)$) terms in the single photon transition excitation operator. In Chapter 2, the second and fourth order moments of the ground state distribution of dye probe molecules in ordered nematic liquid crystal environments were determined by measurements of the initial fluorescence anisotropy as a function of excitation polarisation.

The measurement of higher degrees of molecular order is critical to obtaining a correct picture of the true order of a molecular probe and its motion within the local environment. Neglect of higher moments can lead to significant errors in the determination of probe orientation within liquid crystal hosts [3]. The direct measurement of moments higher than K=4 in the ground state distribution function is only possible if the ground state population experiences a higher order interaction with the light field. This is possible using multi-photon techniques; in this chapter polarised excited probe fluorescence anisotropy measurements are applied to isotropic and ordered environments. In addition to the second order rank moment present in single photon interactions, the two-photon excitation operator contains a fourth order rank moment in the transition tensor [4]. There is now a direct coupling between the initial excited state fluorescence anisotropy and the K=2, 4, and 6 moments of the ground state distribution function. In this chapter, single and two-photon fluorescence anisotropy measurements are used to investigate the ground state order and excited state motion of Rhodamine B and Rhodamine 6G in the nematic phase of 5CB. With this approach measurements of the hitherto "hidden" K=6 ground state order parameter can be made.

Photoselection of a molecular population via two-photon absorption yields a more highly polarised excited state array due to the $\cos^4\theta$ dependence of the interaction between the polarisation of the radiation field and the molecular transition moment, yielding a narrower angular spread in the photoselected molecules about the excitation polarisation angle β [5]. Two-photon excitation leads to a greater displacement of initial molecular alignment from steady state values. The three beam photoselection experiments discussed in Chapter 2 investigated θ diffusion for $\langle\alpha_{20}(0)\rangle$ below $\langle\alpha_{20}(ss)\rangle$; two-photon excitation yields alignments such that $\langle\alpha_{20}(0)\rangle$ is greater than $\langle\alpha_{20}(ss)\rangle$. By investigating the angular averaging of a highly polarised array of probe molecules in a nematic liquid crystal host following two-photon excitation, a further test of the symmetry based linear relaxation model in ordered systems is provided.

The advent of two-photon excitation as a widespread tool in the life sciences [6] and microscopy [7, 8] has led to the development of molecular probes designed specifically for their two-photon absorption properties [9]; two such molecular probes are introduced in this chapter.

3.2 Two-Photon Absorption

Molecular two-photon absorption describes the photophysical process whereby two-photons with frequency ν are simultaneously absorbed by a molecule in a transition between an initial (ground) state and an (allowed) excited state that is raised from the ground state by energy 2hν [10]. The transition can be thought of as taking place via a set of "virtual" intermediate levels at energy hν, with lifetimes governed by the uncertainty principle, and is of the order of $(2\pi\nu)^{-1}$ or approximately one optical cycle; the transition probability for a given molecule is inversely proportional to the optical pulse width [11]. It is therefore necessary for two photons to interact simultaneously with the molecule and the transition to be quantum mechanically allowed. Two-photon excitation is illustrated in figure 3.1.

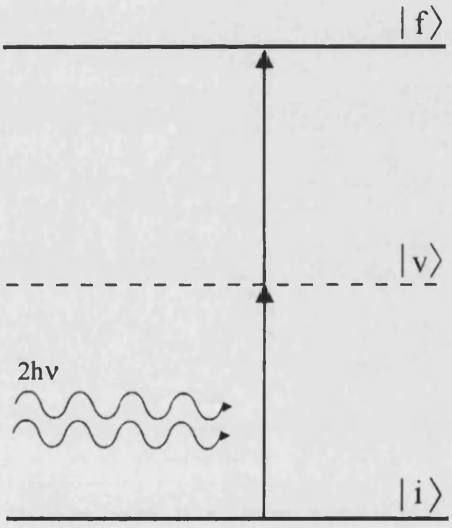

Figure 3.1: An illustration of two-photon excitation from a system in initial level $|i\rangle$ to final level $|f\rangle$, which can be considered as having taken place via virtual levels $|v\rangle$ with a lifetime governed by the uncertainty principle.

The theoretical groundwork for two-photon excitation was developed by Maria Goppert-Mayer in 1929 [12], but due to the fundamental physical restrictions described above it was not until the invention of pulsed lasers in the 1960s with nanosecond pulse widths and energies in the millijoule regime and higher that molecular two-photon absorption was observed in the laboratory. The development of the femtosecond Titanium:Sapphire laser allowed two-photon excitation to be achieved with low energy (nanojoule) pulses at high repetition rates [13]. The advent of this laser technology has advanced two-photon spectroscopy to applications in the life sciences [11] and photophysics [14].

A molecule emitting fluorescence following two-photon absorption follows an energetic pathway as illustrated in figure 3.2. Initially, a molecular population in ground state S_0 is raised to an excited state S_n. The thermodynamically unfavourable population can then dissipate energy non-radiatively, where vibronic coupling results in internal conversion to upper vibrational levels in S_1, which are subsequently depopulated by solvent collisions. A fluorescence photon provides the energy loss mechanism for the transition from the excited state S_1 to upper vibrational levels in S_0; this process and the subsequent ground state vibrational relaxation occurs in the same manner as described for the single photon absorption-emission cycle in Chapter 1. The excited state can also be depopulated by intersystem crossing to a low lying triplet state from which a radiative energy loss mechanism is forbidden by electric dipole selection rules (leading to phosphorescence), which is also the case following single photon excitation described in Chapter 1.

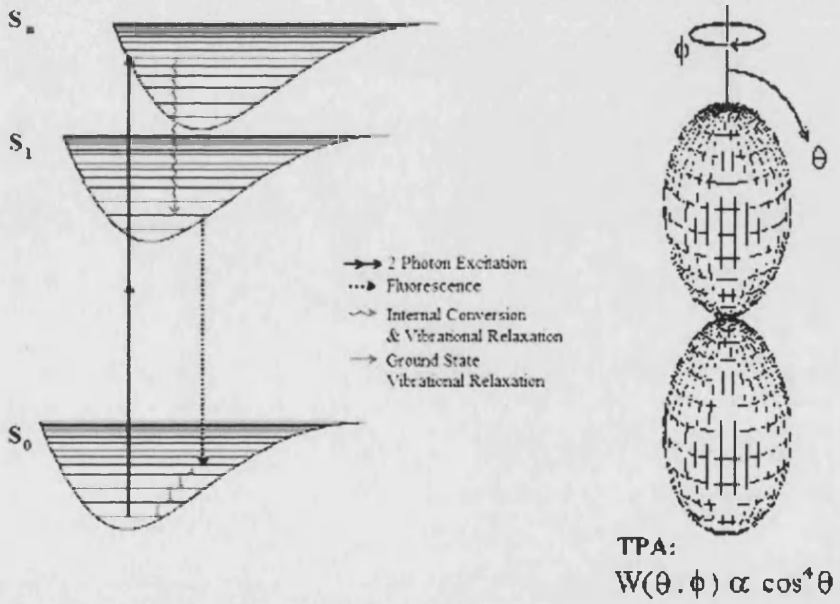

Figure 3.2: A schematic illustration of the radiative pathways used in the two-photon excitation-fluorescence emission cycle. Orientational photoselection via two-photon excitation yields an initial $\cos^4\theta$ distribution in the excited state as opposed to a $\cos^2\theta$ dependence with single photon excitation.

Since two-photon absorption can be described as a two step process from initial level $|i\rangle$ to virtual level $|v\rangle$ to final state $|f\rangle$, third order perturbation theory constructs the transition probability for two-photon absorption from the product of single photon transition moments between $|i\rangle \rightarrow |v\rangle$ and $|v\rangle \rightarrow |f\rangle$ [15]. In this way, $|v\rangle$ is represented

by a linear combination of all the real molecular levels $|k_n\rangle$ that combine with $|i\rangle$ by allowed single photon transitions, and the probability amplitude for $|i\rangle \rightarrow |v\rangle$ is the sum of the amplitudes of the allowed (off-resonance) $|i\rangle \rightarrow |k\rangle$ transitions; the same argument applies to $|v\rangle \rightarrow |f\rangle$. As a result of this, the symmetry of the initially excited state differs from that from single photon excitation. However, the energy dissipation of the two-photon excited state population described above occurs on a sub-picosecond timescale and steady state fluorescence emission originates from the same low lying vibrational levels in S_1. This can be seen in figure 3.3 which compares steady state emission spectra of Fluorescein in two isotropic solvents following single photon and two-photon absorption.

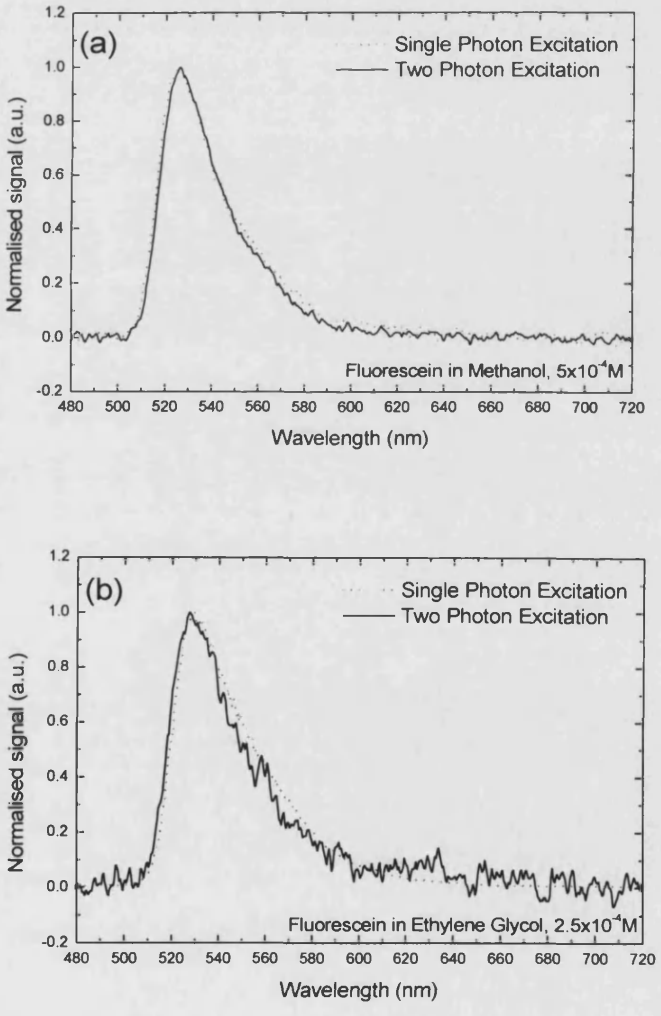

Figure 3.3: a) Emission spectra of a solution of Fluorescein in methanol ($5x10^{-4}$M). Single photon excitation was achieved using 490±3nm laser radiation; two-photon excitation was achieved using 800±7nm radiation. (b) Emission spectra of Fluorescein in ethylene glycol ($2.5x10^{-4}$M). The wavelengths used for single and two-photon excitation were 500±4nm and 800±7nm respectively.

Upon the application of a laser pulse with intensity I(t) at frequency ν on a ground state population N_{gs}, the rate of change of the excited state population N_{ex} (neglecting losses due to spontaneous emission) due to two-photon excitation is given by

$$\frac{dN_{ex}}{dt} = \frac{\sigma^{(2)} I^2(t) G^{(2)}}{(h\nu)^2}\left[N_{gs} - N_{ex}\right] \qquad [3.1]$$

where $\sigma^{(2)}$ is the two-photon absorption cross-section and $G^{(2)}$ is the degree of second order coherence of the laser pulse [16]. For a system in thermodynamic equilibrium and in the limit of weak excitation N_{ex} is negligible compared to N_{gs}:

$$\frac{dN_{ex}}{dt} = \frac{N_{gs}\sigma^{(2)} I^2(t) G^{(2)}}{(h\nu)^2} \qquad [3.2]$$

Assuming a Gaussian laser pulse of width τ with energy E_P illuminating an area A, $G^{(2)}$ is unity, and integrating equation 3.2 yields

$$N_{ex} = \frac{N_{gs}\sigma^{(2)}}{(h\nu)^2}\left(\frac{E_P}{A}\right)^2 \times \frac{0.664}{\tau} \qquad [3.3]$$

Typical two-photon cross-sections for molecular dyes lie in the range 10^{-48}-10^{-51}cm^{4}s/photon [17], requiring the use of short laser pulses (i.e. sub-picosecond) with energies in the region of 10^{-11}-10^{-9}J to achieve a significant excited state population.

3.3 Angular Dependence of Two-Photon Excitation

Photoselection via two-photon absorption has a narrower angular dependence than that for single photon absorption. Since two-photon absorption can be considered as a product of two single photon transitions (section 3.1), the transition probability $W_{2photon}(\theta,\varphi)$ for two-photon absorption given a diagonal transition tensor [18] for a linearly polarised excitation source with intensity I at frequency ν can be expressed as

$$W_{2photon}(\theta,\varphi) \propto \sigma^{(2)}\left(\frac{I}{h\nu}\right)^2 \cos^4\theta \qquad [3.4]$$

where θ is defined as the angle between the excitation polarisation and the two parallel single photon transition moments of the molecule. Expanding $\cos^4\theta$ in terms of spherical harmonics yields:

$$\cos^4\theta = \frac{\sqrt{4\pi}}{5}\left[Y_{00}(\theta,\varphi)+\frac{20}{7\sqrt{5}}Y_{20}(\theta,\varphi)+\frac{8}{21}Y_{40}(\theta,\varphi)\right] \qquad [3.5]$$

Substituting equation 3.5 into equation 3.4 gives

$$W_{2photon}(\theta,\varphi,t) \propto \sigma^{(2)}\left(\frac{I(t)}{h\nu}\right)^2 \frac{\sqrt{4\pi}}{5}\left[Y_{00}(\theta,\varphi)+\frac{20}{7\sqrt{5}}Y_{20}(\theta,\varphi)+\frac{8}{21}Y_{40}(\theta,\varphi)\right] \qquad [3.6]$$

Equation 3.6 represents the angular dependent transition probability for two-photon excitation in the laboratory frame for a Z-polarised pulse. If the excitation polarisation is rotated by an angle β from the lab Z-axis, the laboratory frame transition probability becomes

$$W_{2photon}(\theta,\varphi) \propto \sigma^{(2)}\left(\frac{I(t)}{h\nu}\right)^2 \frac{\sqrt{4\pi}}{5}\left[Y_{00}(\theta,\varphi)+\frac{20}{7\sqrt{5}}\sum_Q d^2_{0Q}(\beta)Y_{20}(\theta,\varphi)+\frac{8}{21}\sum_Q d^4_{0Q}(\beta)Y_{40}(\theta,\varphi)\right] \qquad [3.7]$$

From Chapter 1, in the weak excitation regime the initial excited state distribution is given by the product of the ground state distribution function and the excitation

probability; under these circumstances the initial moments of the excited state distribution are given by [19],

$$\left\langle C_{KQ}^{ex}(0)\right\rangle = \int_0^{2\pi}\int_0^{\pi} Y_{KQ}^{*}(\theta,\varphi) W_{2\,photon}(\theta,\varphi) P_{gs}(\theta,\varphi)\sin\theta d\theta d\varphi \qquad [3.8]$$

Substituting equation 3.7 allows the moments of the distribution to be calculated as

$$\left\langle C_{KQ}^{ex}(0)\right\rangle = B'\frac{\sqrt{4\pi}}{5}\sum_{K'}\left\langle C_{K'0}^{gs}(ss)\right\rangle\left\langle KQ\left|\begin{bmatrix} Y_{00}(\theta,\varphi)+\frac{20}{7\sqrt{5}}\sum_q d_{q0}^{2}(-\beta)Y_{2q}(\theta,\varphi) \\ +\frac{8}{21}\sum_q d_{q0}^{4}(-\beta)Y_{4q}(\theta,\varphi)\end{bmatrix}\right|K'0\right\rangle \qquad [3.9]$$

where B' is a constant of proportionality.

Chapter 2 showed that fluorescence anisotropy measurements are sensitive to the cylindrically symmetric and cylindrically asymmetric normalised excited state moments $\left\langle \alpha_{20}^{ex}(t)\right\rangle$ and $\left\{\left\langle \alpha_{22}^{ex}(t)\right\rangle + \left\langle \alpha_{2-2}^{ex}(t)\right\rangle\right\}$ respectively. The more highly polarised excited state array created by two-photon excitation is illustrated by comparison of the value of these moments to those created by single photon excitation, as can be seen in figure 3.4.

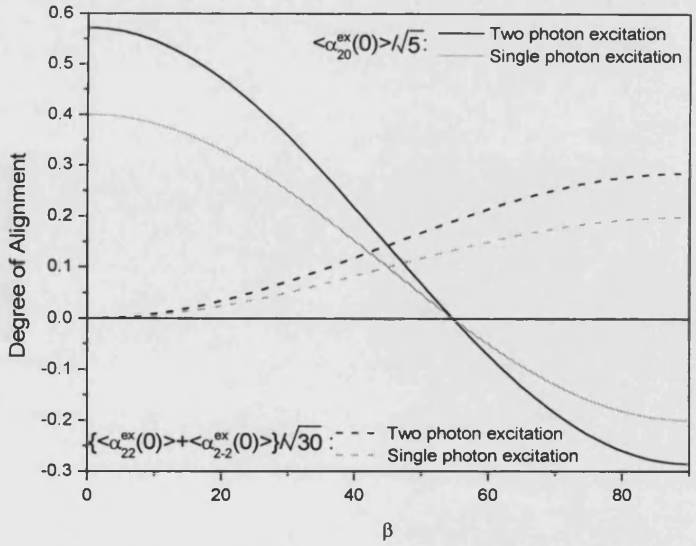

Figure 3.4: β-dependence of the initial degrees of cylindrically symmetric and asymmetric degrees of excited state alignment ($\left\langle \alpha_{20}^{ex}(0)\right\rangle/\sqrt{5}$ and $\left\{\left\langle \alpha_{22}^{ex}(0)\right\rangle + \left\langle \alpha_{2-2}^{ex}(0)\right\rangle\right\}/\sqrt{30}$) obtained for single and two-photon excitation from an isotropic ground state.

The increased degree of angular photoselection afforded by two-photon excitation is reflected in an initial anisotropy that is significantly greater than that for single photon transitions. Theoretically, R(0) values for two and single photon excitation are 4/7 and 2/5 respectively. In practice, the measured R(0) values are lower, due to a variety of depolarising effects (Chapter 2, section 2.7.4.2). These effects are accounted for in single photon fluorescence by the parameter $\bar{A}$ (equation 2.49). Measurements of anisotropy R(t, β=0°) for Rhodamine B for single and two-photon excitation in Ethylene Glycol are shown in figure 3.5.

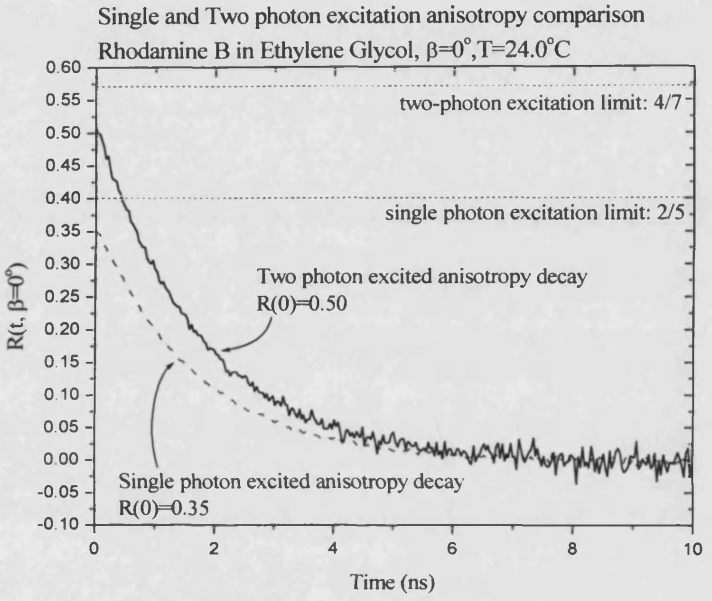

Figure 3.5: Anisotropy comparison graph showing the greater alignment afforded by two-photon excitation relative to single photon excitation for an excitation polarisation angle of β=0° for Rhodamine B in ethylene glycol. The initial anisotropies (0.35 for single photon excitation, 0.50 for two-photon excitation) are lower than theoretical limits (2/5 and 4/7) due to de-polarisation effects described in Chapter 2.

The previous chapters have shown that in the case of single photon absorption, the interaction of the light field upon the ground state distribution function involved coupling of spherical harmonics up to rank K=2, and the initial fluorescence anisotropy contains information on the population, second and fourth rank order parameters in the ground state, that is, $\langle C_{00}^{gs}(ss)\rangle$, $\langle C_{20}^{gs}(ss)\rangle$ and $\langle C_{40}^{gs}(ss)\rangle$. In the case of two-photon excitation the field interaction allows coupling of ground state spherical harmonics up to rank K=4 to be present in the initial excited state order. The contribution of these ground state moments as a function of the excitation polarisation angle β can be calculated by evaluation of the matrix elements in equation 3.9. Expressions for $d_{Q0}^{4}(\beta)$ are evaluated using standard angular momentum rules:

$$d^4_{00}(\beta)=\frac{1}{8}\left(35\cos^4\beta-30\cos^2\beta+3\right) \qquad [3.10a]$$

$$d^4_{01}(\beta)=-d^4_{0-1}(\beta)=\frac{\sqrt{5}}{4}\sin\beta\cos\beta\left(3-7\cos^2\beta\right) \qquad [3.10b]$$

$$d^4_{02}(\beta)=d^4_{0-2}(\beta)=\frac{\sqrt{10}}{8}\sin^2\beta\left(7\cos^2\beta-1\right) \qquad [3.10c]$$

$$d^4_{03}(\beta)=-d^4_{0-3}(\beta)=\frac{\sqrt{35}}{4}\sin^3\beta\cos\beta \qquad [3.10d]$$

$$d^4_{04}(\beta)=d^4_{0-4}(\beta)=\frac{\sqrt{35}}{8}\sin^4\beta \qquad [3.10e]$$

For weak excitation, the excited state moments which make up the excited state distribution function $P_{ex}(\theta,\varphi)$ are formed by the product of the ground state distribution function and the angle dependent transition probability:

$$P_{ex}(\theta,\varphi)=\sum_{KQ}\left\langle C^{ex}_{KQ}(\theta,\varphi)\right\rangle Y_{KQ}(\theta,\varphi)=W(\theta,\varphi)P_{gs}(\theta,\varphi) \qquad [3.11]$$

For two-photon excitation this yields

$$P_{ex}(\theta,\varphi)=A\frac{\sqrt{4\pi}}{5}\left[Y_{00}(\theta,\varphi)+\frac{20}{7\sqrt{5}}\sum_{Q=2}^{-2}d^2_{Q0}(\beta)Y_{2q}(\theta,\varphi)+\frac{8}{21}\sum_{Q=4}^{-4}d^4_{Q0}(\beta)Y_{4Q}(\theta,\varphi)\right]$$
$$\times\left[\sum_{K'=0,EVEN}\left\langle C^{gs}_{K'0}\right\rangle Y_{K'0}(\theta,\varphi)\right] \qquad [3.12]$$

where A is a constant of proportionality. Applying the Wigner-Eckhart theorem [20] to equation 3.9 gives

$$\left\langle C_{KQ}^{ex}(0)\right\rangle = \frac{B}{5}\sum_{K'}\left\langle C_{K'0}^{gs}(ss)\right\rangle \left[\begin{array}{l} \delta_{KK'}\delta_{Q0} + \frac{20}{7}\sum_{q} d_{q0}^{2}(\beta)\begin{pmatrix} K & 2 & K' \\ -Q & q & 0 \end{pmatrix}\begin{pmatrix} K & 2 & K' \\ 0 & 0 & 0 \end{pmatrix}\hat{K}\hat{K}'\delta_{Qq} \\ + \frac{8}{7}\sum_{q} d_{q0}^{4}(\beta)\begin{pmatrix} K & 4 & K' \\ -Q & q & 0 \end{pmatrix}\begin{pmatrix} K & 4 & K' \\ 0 & 0 & 0 \end{pmatrix}\hat{K}\hat{K}'\delta_{Qq} \end{array}\right] \qquad [3.13]$$

Evaluating the 3-j symbols in equation 3.13 yields

$$\left\langle C_{00}^{ex}(0)\right\rangle = C\left[\left\langle C_{00}^{gs}(ss)\right\rangle + \frac{20}{7\sqrt{5}} d_{00}^{2}(\beta)\left\langle C_{20}^{gs}(ss)\right\rangle + \frac{8}{21}\delta_{q0}^{4}(\beta)\left\langle C_{40}^{gs}(ss)\right\rangle\right] \qquad [3.14]$$

$$\left\langle C_{20}^{ex}(0)\right\rangle = C\left[\begin{array}{l} \frac{10}{7\sqrt{5}}\left(3\cos^2\beta - 1\right)\left\langle C_{00}^{gs}(ss)\right\rangle + \\ \left\{1 + \frac{20}{49}\left(3\cos^2\beta - 1\right) + \frac{2}{49}\left(35\cos^4\beta - 30\cos^2\beta + 3\right)\right\}\left\langle C_{20}^{gs}(ss)\right\rangle + \\ \left\{\frac{60}{49\sqrt{5}}\left(3\cos^2\beta - 1\right) + \frac{20\sqrt{5}}{1617}\left(35\cos^4\beta - 30\cos^2\beta + 3\right)\right\}\left\langle C_{40}^{gs}(ss)\right\rangle + \\ \frac{5}{77}\sqrt{\frac{5}{13}}\left(35\cos^4\beta - 30\cos^2\beta + 3\right)\left\langle C_{60}^{gs}(ss)\right\rangle \end{array}\right] \qquad [3.15]$$

$$\left\langle C_{2\pm2}^{ex}(0)\right\rangle = C\left[\begin{array}{l} \frac{10}{7}\sqrt{\frac{3}{10}}\sin^2\beta\left\langle C_{00}^{gs}(ss)\right\rangle + \\ \left\{-\frac{20}{49}\sqrt{\frac{3}{2}}\sin^2\beta + \frac{1}{49}\sqrt{\frac{50}{3}}\sin^2\beta\left(7\cos^2\beta - 1\right)\right\}\left\langle C_{20}^{gs}(ss)\right\rangle + \\ \left\{\frac{10}{49}\sqrt{\frac{3}{10}}\sin^2\beta - \frac{8\sqrt{30}}{539}\sin^2\beta\left(7\cos^2\beta - 1\right)\right\}\left\langle C_{40}^{gs}(ss)\right\rangle + \\ \frac{5}{231}\sqrt{\frac{30}{13}}\sin^2\beta\left(7\cos^2\beta - 1\right)\left\langle C_{60}^{gs}(ss)\right\rangle \end{array}\right] \qquad [3.16]$$

Recalling that the normalised excited state moments $\left\langle \alpha_{KQ}^{ex}\right\rangle$ are formed by division by the population $\left\langle C_{00}^{ex}\right\rangle$ term, and that the fluorescence anisotropy is expressed (including correction factors for local field effects and reflection losses discussed in Chapter 2) as

$$R(0)=\frac{\frac{k-1}{\bar{A}}+\frac{\langle\alpha_{20}^{ex}(0)\rangle}{\sqrt{5}}(2k+1)-\sqrt{\frac{3}{10}}\{\alpha_{2+2}^{ex}(0)+\alpha_{2-2}^{ex}(0)\}}{\frac{k+2}{\bar{A}}-\frac{\langle\alpha_{20}^{ex}(0)\rangle}{\sqrt{5}}(2k-2)-2\sqrt{\frac{3}{10}}\{\alpha_{2+2}^{ex}(0)+\alpha_{2-2}^{ex}(0)\}} \qquad [3.17]$$

The initial fluorescence anisotropy is thus sensitive to $\langle C_{00}^{gs}(ss)\rangle$, $\langle C_{20}^{gs}(ss)\rangle$, $\langle C_{40}^{gs}(ss)\rangle$ and $\langle C_{60}^{gs}(ss)\rangle$. Higher moments are created in the excited state but do not contribute to the initial fluorescence anisotropy. The evolution of the fluorescence anisotropy in an ordered environment is governed by the orientational dynamics imposed by the nematic host. For a given rank K, cross relaxation between different projections Q is not permitted in a cylindrically symmetric medium [21]. A comparison between the fluorescence anisotropy decays created by single photon and two-photon excitation for dye probes in liquid crystals should be beneficial as a test of the theoretical framework that governs the interpretation of fluorescent probe experiments; being able to determine directly the $\langle C_{60}^{gs}(ss)\rangle$ moment in an aligned environment will investigate the methods of Durbin and Shen [22] for the estimation of higher order ground state moments (section 3.8).

3.4 Experimental Apparatus

The time resolved fluorescence anisotropy experiments described in this chapter were carried out using time correlated single photon counting as described in chapter 2. Two-photon excitation of Rhodamine 6G and Rhodamine B in 5CB was achieved using the Titanium:Sapphire laser system described in section 3.4.2.

3.4.1 Molecular Probes

The molecular probes chosen for the experiments described in this chapter were Rhodamine 6G and Rhodamine B. At the excitation wavelength of 800nm, both probes have two-photon cross-sections greater than $1x10^{-49}cm^4s$/photon [17, 21].

3.4.2 Laser Source

Two-photon excitation of the rhodamine dyes was achieved using the partial output of a regeneratively amplified Titanium sapphire oscillator. The oscillator (Coherent Mira 900-F) is illustrated schematically in figure 3.6. The laser uses sapphire doped with titanium ions as the active gain medium ($Ti^{3+}:Al_2O_3$). Since its conception in the 1980s [13] use of the Ti:Sapphire solid state laser has become widespread because of its ability to generate ultrashort pulses over a continuously tuneable broad spectral region (680nm to 1100nm) with a high gain and negligible excited state absorption. The gain medium is pumped by a solid state, diode pumped, frequency-doubled Neodynium:Vanadate ($Nd:YVO_4$) laser (Coherent Verdi V-5) that provides 5W of continuous wave single mode laser radiation at 532nm.

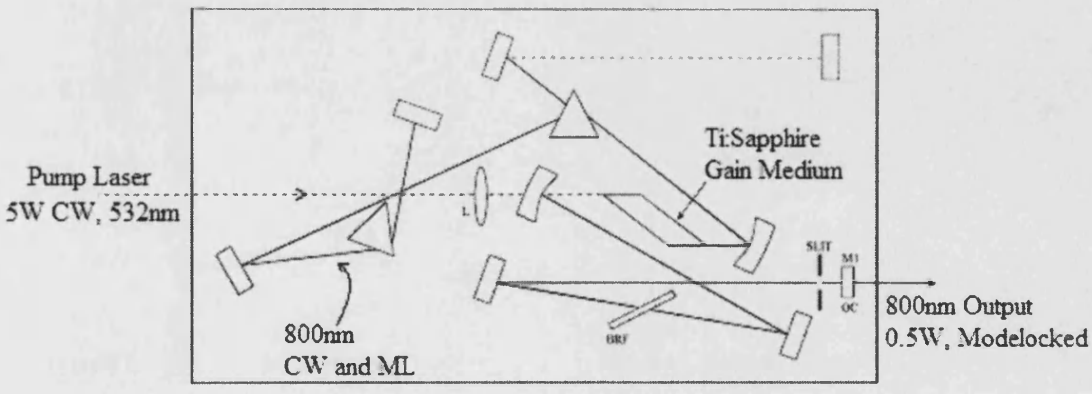

Figure 3.6: Schematic diagram of the femtosecond Titanium:Sapphire oscillator used in the two-photon excitation experiments

Due to the broadband nature of the Ti:Sapphire gain medium [24], there are many longitudinal modes which could be free to oscillate in the laser cavity. In principle this would result in a laser output consisting of a random train of Gaussian noise with an average spike width of approximately $\Delta\nu^{-1}$, where $\Delta\nu$ is the bandwidth of the gain medium. The laser output is controlled by a technique known as Kerr Lens Modelocking [25] in which the refractive index (n) of the Ti:Sapphire crystal is modified according to the intensity I(t) of the passing radiation by

$$n = n_0 + n_2 I(t) \qquad [3.18]$$

where n_0 is the nominal refractive index of the medium and n_2 is the intensity dependent refractive index. For a TEM_{00} (Gaussian) transverse mode the refractive index has a radial dependence of the form

$$n(r) = n_0 + n_2 I_0(t) e^{(-a^2/r^2)} \qquad [3.19]$$

where $I_0(t)$ is the intensity at the centre of the beam, r is a radial distance unit and a is a length unit associated with the fundamental mode of the cavity. If n_2 is positive then greater intensities are refracted towards the centre of the beam (this is known as a Kerr Lens). Since this only occurs for very high intensities, only the intense modelocked pulse will form the lens; the weak intensity continuous wave lasing action is not sufficient to cause this effect. This results in a high intensity modelocked pulse with a lower beam radius than the low intensity continuous wave beam. By placing a slit in the cavity at the appropriate width the gain is reduced for modes with a more extensive radial distribution. A birefringent filter (BRF) is used to control the output wavelength – typically this was set to 800nm, which is near the gain maximum. Self phase modulation and the group velocity dispersion (GVD) caused by the Kerr modelocking and dispersive optical elements in the cavity are compensated by a prism pair leading to a laser output consisting of a near transform limited (minimum time-frequency uncertainty) laser pulse train at a repetition rate of 76MHz with 140fs pulse width (measured using an autocorrelator (APE)) and pulse energies of approximately 10nJ.

Amplification of the oscillator output was achieved using a regenerative amplifier (Coherent RegA 9000). This is illustrated in figure 3.7. The amplifier consists of a

Ti:Sapphire cavity which is pumped by the frequency doubled output of a $Nd:YV0_4$ solid state laser (Coherent Verdi V-10) providing 10W of continuous wave radiation at 532nm. A pulse from the Mira oscillator is introduced into the amplifier via a Faraday Isolator by a Tellerium oxide (TeO_2) cavity dumper. The seed pulse is stretched before amplification to avoid damaging the optical components and causing saturation of the gain medium; this is achieved by passage through a TeO_2 Q-switch which is switched on in the absence of a seed pulse to prevent lasing before injection. Amplification occurs over 20-30 cavity round trips, during which the pulse is stretched via GVD to 30ps. The pulse, now several μJ in energy, is ejected from the cavity using the cavity dumper and recompressed via multiple passes off a diffraction grating. The final output of the amplifier is a pulse train with a repetition rate controllable between 100kHz-250kHz with 3-4μJ pulse energy, a typical pulse width of 200fs and a tuning range of approx. 780-840nm [24].

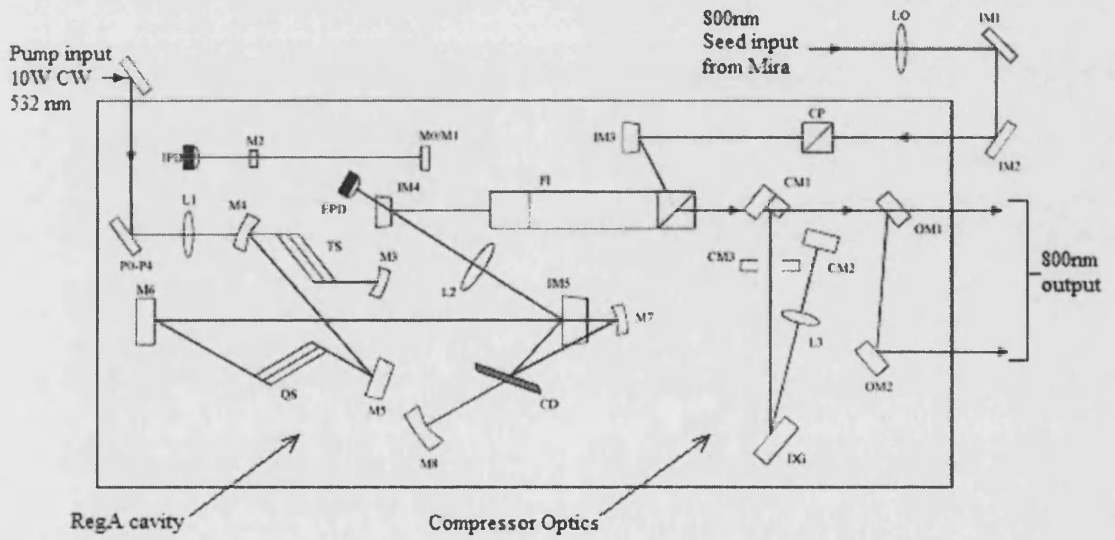

Figure 3.7: Schematic diagram of the regenerative amplifier used in conjunction with the Ti:Sapphire laser to provide microjoule pulse energies with a repetition rate in the kilohertz regime.

3.5 Optical Layout

In order to design and construct a successful TCSPC experiment using two-photon excitation, it is instructive to make an approximate quantitative comparison between the input requirements for single photon (1) and two-photon (2) excited fluorescence. For the two methods of excitation, the transition probabilities in the weak excitation regime with an ultrashort modelocked laser pulse ($G^{(2)}=1$) are

$$P_1 = \frac{\sigma E_p}{h\nu A} \qquad [3.20]$$

$$P_2 = \frac{1}{\tau}\frac{\sigma^{(2)}(E_p)^2}{(h\nu A)^2} \qquad [3.21]$$

Equation 3.21 assumes a square pulse approximation, that is, a pulse of constant intensity and width τ. For single photon excitation of a molecular probe such as Rhodamine 6G the cross section is typically of the order of $10^{-16}cm^2$, for a typical excitation wavelength of 575nm and photon energy of $3.4x10^{-19}J$. For a probe concentration of $5x10^{-4}M$, spot diameter of 70μm a path length of 100μm, an excitation pulse energy of $2.6x10^{-13}J$ gives rise to an excited state population of $2.3x10^5$.

For two-photon excitation of the same Rhodamine 6G sample, the cross section at 800nm is approx. $2.4x10^{-48}cm^4s$/photon [21]. A typical pulse energy is $8x10^{-10}J$ with a beam area measured at $1.77x10^{-6}cm^2$ and a pulse width of 200fs. This yields an excited state population of $2.1x10^5$.

In both cases there are many more laser photons than fluorescence photons travelling towards the photodetector, requiring the use of a beam block and filters to obtain a minimum acceptable signal to background count rate of approx. 5000:1. In the single photon excitation estimate there are $7.6x10^5$ laser photons per second at 575nm superimposed on $1.15x10^5$ fluorescence events per second before filtering and beam blocking.

For the case of two-photon excitation, there are $8x10^{10}$ laser photons at 800nm superimposed on approximately $1.15x10^4$ fluorescence events in the forward collection direction, assuming a quantum yield of near unity. The solid angle of detection does not cover all forward facing fluorescence events (figure 3.8), and other losses in the detection process result in an optical collection efficiency of approx. 1-5%.

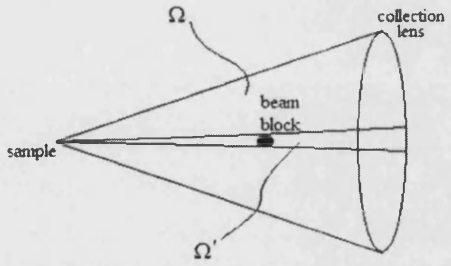

Figure 3.8: The solid angle of collection reduces the number of detectable fluorescence photons. The beam block reduces the collection angle, such that $\Omega_{collection} = (\Omega - \Omega')/4\pi$

As in experiments using single photon excitation, a beam block was utilised to block the vast majority of the laser photons (confined to a low solid angle distribution) without significantly impairing the number of detectable fluorescence photons (emitted over all solid angles). A circular block of width 2a placed on the axis of a fundamental Gaussian beam of width w yields an attenuation A (neglecting diffraction effects) of [10]

$$A = e^{-2a^2/w^2} \qquad [3.22]$$

For a block of width a=2w the attenuation is of the order of $3\text{x}10^{-4}$. Applying this attenuation factor, the collection efficiency of the apparatus yields estimates of laser photons and fluorescence photons of $4.8\text{x}10^{5}$ and $4.8\text{x}10^{2}$ respectively; there are still too many laser photons by several orders of magnitude for TCSPC. Further reduction of the 800nm laser signal was achieved by using two 1mm thick band pass colour filters (Schott BG39). The transmittance per millimetre of 800nm and 560nm radiation (560nm being near the emission peak of Rhodamine 6G) is $2\text{x}10^{-5}$ and 0.8 respectively [26]. With this optical layout an acceptable signal to background rate was achieved.

3.6 Experimental Procedure

Apart from the different optical set up, the experimental procedure for two-photon excitation of Rhodamine 6G and Rhodamine B was the same as for the single photon experiments described in Chapter 2. The ambient laboratory temperature was maintained at 22-23°C. Typical on-sample powers were between 100 and 400μW (0.4-1.6nJ pulse energies); neutral density wheels were used to control the incident laser power and obtain a signal count rate of 2500s^{-1}. Anisotropy measurements of Rhodamine 6G and Rhodamine B fluorescence in aligned nematic 5CB were then made using single and two-photon excitation with an excitation polarisation angle β=0°, 90°.

The fluorescence anisotropy measurements of Rhodamine 6G and Rhodamine B in ethylene glycol for varying excitation angle β are shown in figure 3.9a and figure 3.9b respectively. The range of initial anisotropy values which can be achieved using two-photon excitation (4/7 to -4/11) exceeds the range for single photon excitation (2/5 to -2/7). The range of initial anisotropies is, like the single photon case, limited by depolarising effects inherent in the experiment. Plots of the measured initial anisotropy as a function of excitation polarisation angle β are shown for Rhodamine 6G and Rhodamine B in figures 3.9c and 3.9d respectively.

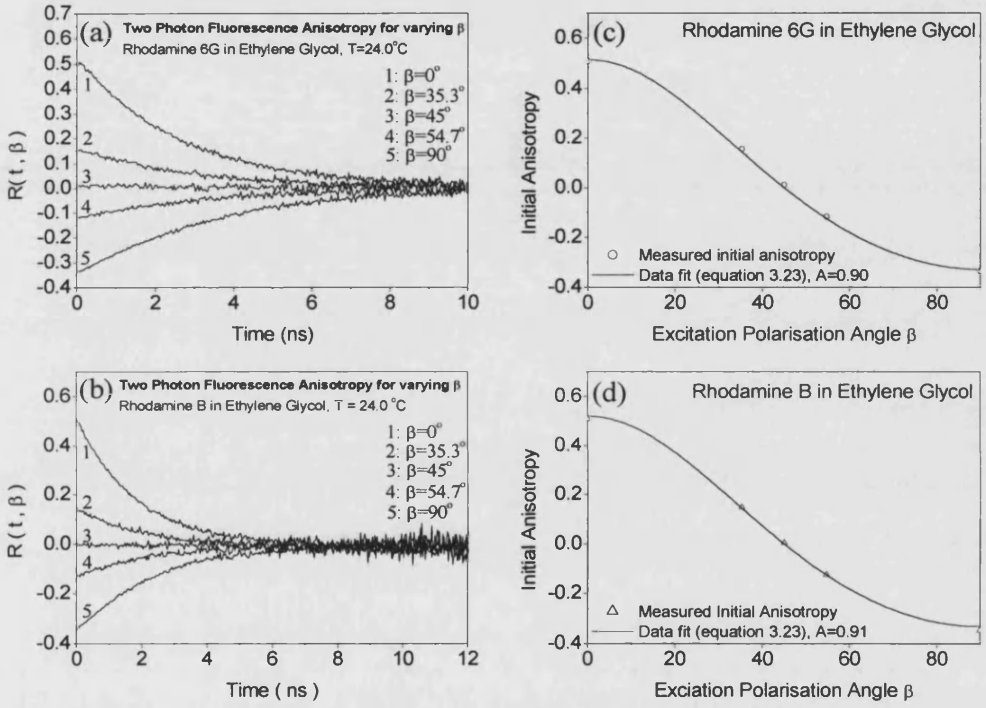

Figure 3.9: Fluorescence anisotropy decays for varying excitation polarisation angle β for (a) Rhodamine 6G and (b) Rhodamine B in ethylene glycol. The initial anisotropy values can be plotted against β and fitted to yield a value for the depolarisation correction factor Ã for (c) Rhodamine 6G and (d) Rhodamine B in this system.

Single and two-photon fluorescence anisotropy decays for Rhodamine 6G and Rhodamine B in nematic 5CB are shown in figure 3.10 for excitation polarisation angles of 0° and 90°. It is clear that the initial R(0,β=0°) values for two-photon fall significantly short of the two-photon anisotropy limit despite the presence of a positive alignment in the liquid crystal host. This indicates a negative contribution from a higher order parameter to the ground state distribution function which reduces the initial degree of alignment, as was observed in the single photon excitation case. Nevertheless, the initial anisotropy values arising from two-photon excitation for both β=0° and β=90°

display a greater displacement from the steady state anisotropy (R_{ss}) for both Rhodamine 6G and Rhodamine B, which is a consequence of the narrower angular sensitivity afforded by this method of photoselection.

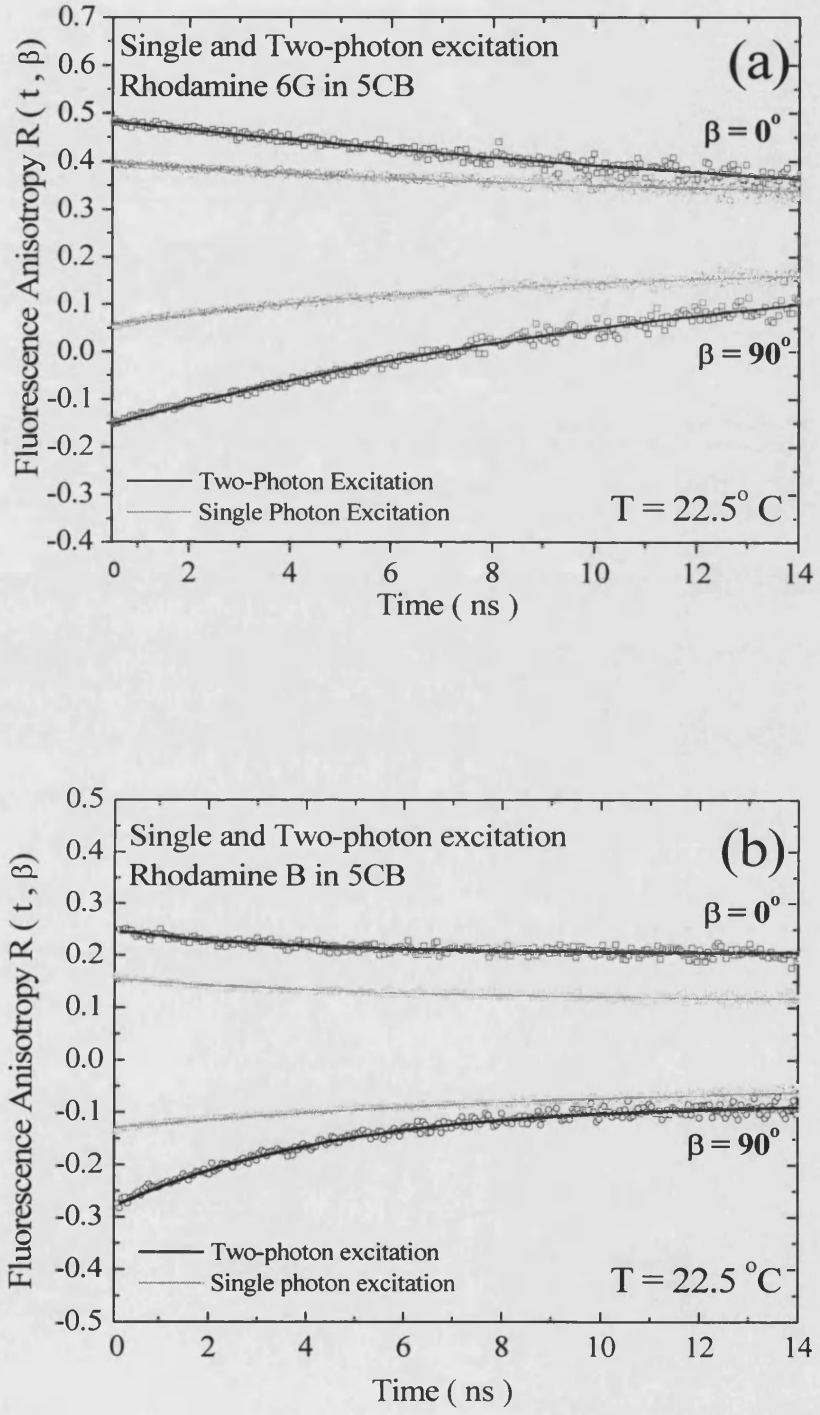

Figure 3.10: Fluorescence anisotropy decays of (a) Rhodamine 6G and (b) Rhodamine B arising from single and two-photon excitation in nematic 5CB for excitation polarisation angles of β=0° and β=90°. The range of R(0,β) for two-photon excitation (0.49 to -0.15 for Rhodamine 6G, 0.25 to -0.27 for Rhodamine B) is greater than that for single photon excitation (0.40 to 0.05 for Rhodamine 6G, 0.16 to -0.13 for Rhodamine B)

3.7 Fitting Procedure

The first step in analysis of the experimental data was the determination of the correction factors k and Ā as described in Chapter 2. The correction factor k was the same for both the single and two-photon cases since both excitation methods were carried out at the same temperature in the same liquid crystal host doped with the same dyes. Determination of Ā was achieved by a fit to the initial anisotropy values for varying β in an isotropic solvent, as described in Chapter 2. In the case of two-photon excitation Ā can be determined by a fit to the initial anisotropy values measured according to [5]

$$R(0,\beta)=\frac{\frac{4}{7}\left(\cos^2\beta-\sin^2\beta\right)}{\frac{1}{\bar{A}}+\frac{4}{7}\sin^2\beta} \qquad [3.23]$$

Fits to the initial anisotropy values measured for Rhodamine 6G and Rhodamine B yielded values of Ā of 0.9 and 0.92 respectively, as shown in figure 3.9c and figure 3.9d respectively. The correction factor k was found to be 1.13 in both systems.

The analysis of the single photon anisotropy decays proceeded as described in the previous chapter, and the two-photon analysis can be achieved in a similar manner [4]. The alignment relaxation dynamics follow the same basic form as in equations 2.31 and 2.32, with differences in the initial anisotropy values arising from a contribution from the $\langle \alpha_{60}^{gs}(ss) \rangle$ moment of the ground state distribution function. This is a consequence of the difference in the coupling between the experimental system and the light field allowing higher order ground state moments to contribute to the excited state alignment. The analysis can be broken down as follows:

Step 1

The initial anisotropy values were obtained by averaging the first 3 channels (approx. 125ps) of the R(t, β=0°) and R(t, β=90°) decays. For single photon excitation the values of the ground state order parameters $a = \langle \alpha_{20}^{gs} \rangle / \sqrt{5}$ and $b = \langle \alpha_{40}^{gs} \rangle$ could be determined by substitution of the correction factors k and Ā. In terms of the ground state moments (a and b) the initial anisotropies for β=0° and β=90° arising from single photon photoselection are

$$R(0, \beta = 0^\circ) = \frac{\frac{2}{5} + \frac{11}{7}a + \frac{12}{35}b}{1 + 2a} \qquad [3.24]$$

$$R(0, \beta = 90^\circ) = \frac{-2 + 5a - b}{7 - \frac{55}{7}a + \frac{2}{7}b} \qquad [3.25]$$

The initial anisotropies arising from two-photon photoselection are given by

$$R(0, \beta = 0^\circ) = \frac{4 + 15a + \frac{136}{33}b + \frac{40}{11\sqrt{13}}c}{7 + 20a + \frac{8}{3}c} \qquad [3.26]$$

$$R(0, \beta = 90^\circ) = \frac{-4 + \frac{155}{21}a + \frac{10}{7}b + \frac{10}{3\sqrt{13}}c}{11 - \frac{50}{3}a + \frac{15}{11}b + \frac{20}{33\sqrt{13}}c} \qquad [3.27]$$

where $c = \langle \alpha_{60}^{gs}(ss) \rangle$.

Values for a and b were calculated using a MathCad program (Chapter 2, section 2.9) by the solutions of the simultaneous equations 3.24 and 3.25 using the initial single photon anisotropy values retrieved from the experimental data. Substitution of these values into equations 3.26 or 3.27 with the appropriate two-photon initial anisotropy value yielded a value for c.

Step 2

The single (R_1) and two-photon (R_2) anisotropy decays for excitation polarisation $\beta=0°$ can be described by

$$R_1(t,\beta=0°)=\frac{(1+2a)\frac{(k-1)}{\bar{A}}+(2k+1)\left[\left\{\left(\frac{2}{5}+\frac{11}{7}a+\frac{36}{35}b\right)-R_{SS}\right\}e^{-t/\tau_{20}}+R_{SS}\right]}{(1+2a)\frac{(k+2)}{\bar{A}}+2(k-1)\left[\left\{\left(\frac{2}{5}+\frac{11}{7}a+\frac{36}{35}b\right)-R_{SS}\right\}e^{-t/\tau_{20}}+R_{SS}\right]} \quad [3.28]$$

$$R_2(t,\beta=0°)=\frac{\left(\frac{k-1}{\bar{A}}\right)\left(7+20a+\frac{8b}{3}\right)+(2k+1)\left[\left\{4+15a+\frac{136b}{33}+\frac{40c}{11\sqrt{13}}-R_{SS}\right\}e^{-t/\tau_{20}}+R_{SS}\right]}{\left(\frac{k+2}{\bar{A}}\right)\left(7+20a+\frac{8b}{3}\right)+(2k-2)\left[\left\{4+15a+\frac{136b}{33}+\frac{40c}{11\sqrt{13}}-R_{SS}\right\}e^{-t/\tau_{20}}+R_{SS}\right]} \quad [3.29]$$

Having obtained the values of the order parameters a and b as well as the correction factors k and $\bar{A}$, the re-orientational lifetime τ_{20} and $R_{SS}(\beta=0°)$ could be determined by a fit to the single photon $R_1(t,\beta=0°)$ data using equation 3.28. The same parameters for two-photon excitation could be determined with the additional order parameter c and a fit to the two-photon $R_2(t,\beta=0°)$ experimental data using equation 3.29.

Step 3

With an excitation polarisation angle of β=90° the single and two-photon anisotropy decays are given by

$$R_1(t,\beta=90^\circ)=\frac{(1-a)\frac{(k-1)}{\bar{A}}+(2k+1)\left[\left\{-\frac{1}{5}+\frac{5}{7}a-\frac{18}{35}b-R_{SS}\right\}e^{-t/\tau_{20}}+R_{SS}\right]-\frac{1}{5}\left(1-\frac{10}{7}a-\frac{3}{7}b\right)e^{-t/\tau_{22}}}{(1-2a)\frac{(k+2)}{\bar{A}}+2(k-1)\left[\left\{-\frac{1}{5}+\frac{5}{7}a-\frac{18}{35}b-R_{SS}\right\}e^{-t/\tau_{20}}+R_{SS}\right]-\frac{2}{5}\left(1-\frac{10}{7}a-\frac{3}{7}b\right)e^{-t/\tau_{22}}} \quad [3.30]$$

$$R_2(t,\beta=90^\circ)=\frac{(7-10a+b)\left(\frac{k-1}{\bar{A}}\right)+(2k+1)\left[\left\{-2+\frac{23a}{7}+\frac{16b}{11}+\frac{40c}{11\sqrt{13}}-R_{SS}\right\}e^{-t/\tau_{20}}+R_{SS}\right]-\left(2-\frac{10}{21}a+\frac{6}{11}b-\frac{10}{33\sqrt{13}}c\right)e^{-t/\tau_{22}}}{(7-10a+b)\left(\frac{k+2}{\bar{A}}\right)+2(k-1)\left[\left\{-2+\frac{23a}{7}+\frac{16b}{11}+\frac{40c}{11\sqrt{13}}-R_{SS}\right\}e^{-t/\tau_{20}}+R_{SS}\right]+2\left(2-\frac{10}{21}a+\frac{6}{11}b-\frac{10}{33\sqrt{13}}c\right)e^{-t/\tau_{22}}} \quad [3.31]$$

With a, b, k, $\bar{A}$ and τ_{20} known from previous steps it was possible to extract values for R_{SS} and τ_{22} by fitting the single photon $R_1(t,\beta=90^\circ)$ data using equation 3.30. Similarly, knowledge of c meant that the values of R_{SS} and τ_{22} could be obtained by applying a nonlinear least squares fit (MicroCal Origin) to the two-photon $R_2(t,\beta=90^\circ)$ data using equation 3.31.

The order parameters, alignment relaxation times and diffusion rates for Rhodamine 6G and Rhodamine B in aligned nematic 5CB are detailed in table 3.1.

	Rhodamine 6G		Rhodamine B	
	One Photon	Two-photon	One Photon	Two-photon
$\tau_{20}=\tau_{\theta}(x10^{-9}s)$	10.62±1.5	10.7±0.2	9.27±0.93	9.36±1.36
τ_{22} $(x10^{-9}s)$	5.8±0.7	6.1±0.9	8.04±0.98	8.37±1.04
τ_{φ} $(x10^{-9}s)$	4.70±0.65	4.97±0.84	7.54±0.92	7.94±0.98
$D\perp$ $(x10^{7}s^{-1})$	1.57±0.23	1.56±0.03	1.80±0.18	1.78±0.26
$D_{\parallel}$ $(x10^{7}s^{-1})$	3.54±0.44	3.35±0.61	2.21±0.29	2.10±0.24
$D_{\parallel}/D\perp=\gamma_{\varphi}/\gamma_{\theta}$	2.26±0.05	2.14±0.35	1.23±0.04	1.18±0.04
$R_{SS}=\langle\alpha_{20}^{ex}(ss)\rangle/\sqrt{5}$	0.31±0.06	0.34±0.05	0.096±0.001	0.181±0.003
$\langle\alpha_{20}^{gs}(ss)\rangle/\sqrt{5}\equiv\langle P_2\rangle$	0.24±0.06	0.30±0.03	-0.0015±0.0007	0.0053+0.0002
$\langle\alpha_{40}^{gs}(ss)\rangle\equiv 3\langle P_4\rangle$	-0.55±0.07	-0.53±0.08	-0.78±0.93	-0.857±0.065
$\langle\alpha_{60}^{gs}(ss)\rangle\equiv\sqrt{13}\langle P_6\rangle$	n/a	-0.51±0.09	n/a	0.292±0.032

Table 3.1: Summary of molecular motion and order parameters for Rhodamine 6G and Rhodamine B in nematic 5CB

3.8 Ground State Distribution Function

The values of the ground state order parameters obtained using the methods described in the previous section can be substituted into the expansion of the ground state orientational distribution function:

$$P_{gs}(\theta,\varphi)=\frac{1}{4\pi}\left[1+\sum_{K>0,EVEN}\langle\alpha_{K0}^{gs}(ss)\rangle Y_{K0}(\theta,\varphi)\right] \qquad [3.32]$$

This yields a first approximation to the ground state orientational distribution function shown for the cases of Rhodamine 6G and Rhodamine B in nematic 5CB in figure 3.11a and 3.11b respectively. Both the single photon and the two-photon distributions are seen to peak in the region of θ_{peak}=35°-45° for Rhodamine 6G, and in the region of θ_{peak}=45°-55° for Rhodamine B. (The equivalent maxima at (180-θ) arising from the even parity of the distribution function are not displayed in the figures.)

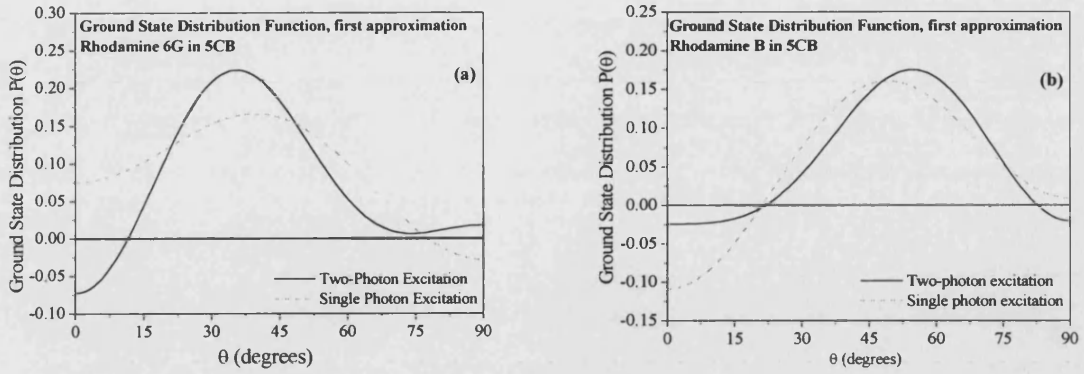

Figure 3.11: First approximation ground state distributions for (a) Rhodamine 6G and (b) Rhodamine B in nematic 5CB from single & two-photon excitation. Physically unreal distributions confirm the presence of higher order ground state moments in the distribution function.

In both cases, the approximate orientational distribution functions are physically unreal, yielding regions of negative probability near 0° and 90°; this indicates that higher terms must be present in the expansion of P(θ), not directly measurable using single or two-photon excitation. It is, however, possible to make physically reasonable "estimates" for the higher order moments (equation 2.2) by the method first described by Durbin and Shen [22]; with the sole constraint that the distribution retains a single maximum between 0° and 90°, trial values for the higher rank moments (i.e. K=6,8,10...) are added sequentially and in decreasing magnitude in order to obtain a physically real distribution; order parameters up to and including K=12 are necessary to achieve a meaningful distribution function. This approach yielded the orientational distribution functions shown in figures 3.12a and 3.12b.

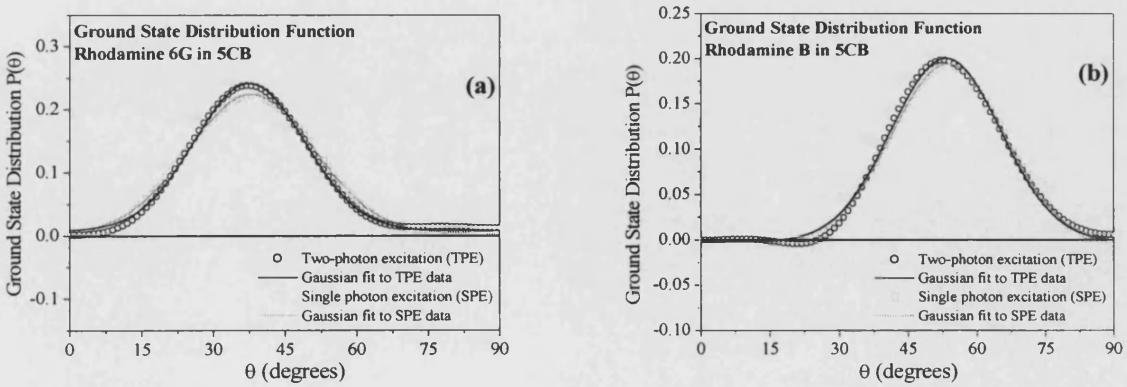

Figure 3.12: Physically real ground state distributions for (a) Rhodamine 6G and (b) Rhodamine B in nematic 5CB, achieved by including estimates for the values of higher order moments than those directly measurable using single and two-photon excitation according to the methods of Durbin and Shen [22].

Table 3.2 shows values of the directly measured and extrapolated ground state moments.

	Rhodamine 6G		Rhodamine B	
	Single Photon	Two-photon	Single Photon	Two-photon
$\langle\alpha_{20}^{gs}(ss)\rangle/\sqrt{5} \equiv \langle P_2\rangle$	0.242	0.297	-0.0015	-0.0053
$\langle\alpha_{40}^{gs}(ss)\rangle \equiv 3\langle P_4\rangle$	-0.545	-0.528	-0.789	-0.819
$\langle\alpha_{60}^{gs}(ss)\rangle \equiv \sqrt{13}\langle P_6\rangle$	-0.461*	-0.513	0.340*	0.306
$\langle\alpha_{80}^{gs}(ss)\rangle \equiv \sqrt{17}\langle P_8\rangle$	0.096*	0.149*	0.143*	0.197*
$\langle\alpha_{100}^{gs}(ss)\rangle \equiv \sqrt{21}\langle P_{10}\rangle$	0.059*	0.056*	-0.095*	-0.095*
$\langle\alpha_{120}^{gs}(ss)\rangle \equiv 5\langle P_{12}\rangle$	-0.004*	-0.004*	-0.001*	-0.001*

Table 3.2: Comparison of ground state distribution moments from single and two-photon excitation - moments marked with an asterisk are extrapolated values using the method of Durbin et al [22].

These results make possible a direct comparison between measured and extrapolated values of the $\langle\alpha_{60}^{gs}(ss)\rangle$ moment of the ground state distribution function for both dyes. In both cases the values are close: for Rhodamine 6G the measured value of $\langle\alpha_{60}^{gs}(ss)\rangle$ of -0.513 compares favourably with the extrapolated value of -0.461; Rhodamine B yields measured and extrapolated $\langle\alpha_{60}^{gs}(ss)\rangle$ values of 0.306 and 0.340 respectively. Irrespective of the dye probe used, ground state moments higher than the $\langle\alpha_{60}^{gs}(ss)\rangle$ moment are extrapolated in both photoselection methods, whereas the lower moments are both directly measurable. The two methods of excitation yield comparable values for all moments and the subsequent distribution functions are similar.

Although the ground state distributions for both dyes are well described by Gaussian fits, they are substantially different. The sign of the $\langle\alpha_{60}^{gs}(ss)\rangle$ moment changes between the Rhodamine 6G and Rhodamine B (-0.513 and 0.306 respectively), and the low magnitude of $\langle\alpha_{20}^{gs}(ss)\rangle/\sqrt{5}$ in Rhodamine B (-0.0053) is also noteworthy. These observations lend support to the conclusion that Rhodamine 6G and Rhodamine B occupy significantly different positions within the liquid crystal host environment.

Whereas the difference between the ground state ordering between the two dyes is substantial, the Gaussian fits to the ground state distribution functions obtained by single and two-photon excitation yield similar maxima (θ_{max}) and widths. For Rhodamine 6G θ_{max} lies at 38° which is very similar to θ_{alkyl} (the angle made by the alkyl tail of the liquid crystal with respect to the nematic director); in the case of Rhodamine B θ_{max} lies at 53°, significantly greater than θ_{alkyl}. The widths of the distributions for both dyes are comparable (approx. 24°). It is noteworthy that the low fluorescence anisotropy of Rhodamine B does not arise from a lack of ground state local order, but from the global ordering of the dye domains in the laboratory frame.

3.9 Orientational Dynamics

There are marked differences in the cylindrically symmetric and asymmetric alignment dynamics for the Rhodamine dyes in the restricted geometry of the nematic liquid crystal. Whereas τ_θ and τ_φ must necessarily be equal in an isotropic environment, the rate of φ diffusion is more than double the rate of θ diffusion for Rhodamine 6G whereas they are similar for Rhodamine B.

The single and two-photon measurements yield similar values for τ_{20} and τ_{22} for both dyes. The creation of moments of rank K=4 in the excited state distribution function by two-photon excitation would maximise the possibility of cross relaxation [18] allowed on symmetry grounds between moments of different rank and equal projection. However, the observation of equivalent relaxation dynamics is a good indication that cross relaxation does not take place; the single and two-photon photoselection experiments of Rhodamine dyes in nematic 5CB provides further verification (along with the three beam photoselection experiments) that the assumption of linear relaxation dynamics is valid for cylindrically symmetric and asymmetric degrees of probe alignment.

3.10 Quadrupolar Two-Photon Chromophores

Rhodamine 6G and Rhodamine B have been used successfully as two-photon fluorescent probes to study molecular motion and order in liquid crystals. The use of these probes in applications such as two-photon fluorescence microscopy may be limited in terms of the detectable concentration, and many place an unacceptable photon flux on (possibly living) samples. The development of chromophores which permit two-photon fluorescence with considerably reduced average powers is thus highly desirable.

Simple quantum models of two-photon absorption [27-30] predict that an elongated conjugated system combined with strong electro-active endgroups (electron donating or withdrawing) will lead to a significant enhancement of the two-photon cross-section. In this respect two-photon quadrupolar systems have proved most successful. The design utilises a centro-symmetric system of donor and acceptor groups connected by a conjugated π-electron system. This strategy has been successfully developed by the CNRS group of Dr Mireille Blanchard-Desce (Synthèse et Electrosynthèse Organiques, University of Rennes). Compounds based on photostable fluorescent cores such as biphenyl and fluorene have been synthesised and their cross-sections measured [31-33].

Two fluorene-based donor-acceptor acceptor-donor molecules (LP79 and OM62, figure 3.13) were supplied as potential fluorophores for two-photon stimulated emission depletion studies (see Chapter 4) The photophysical properties of these chromophores are set out in table 3.3.

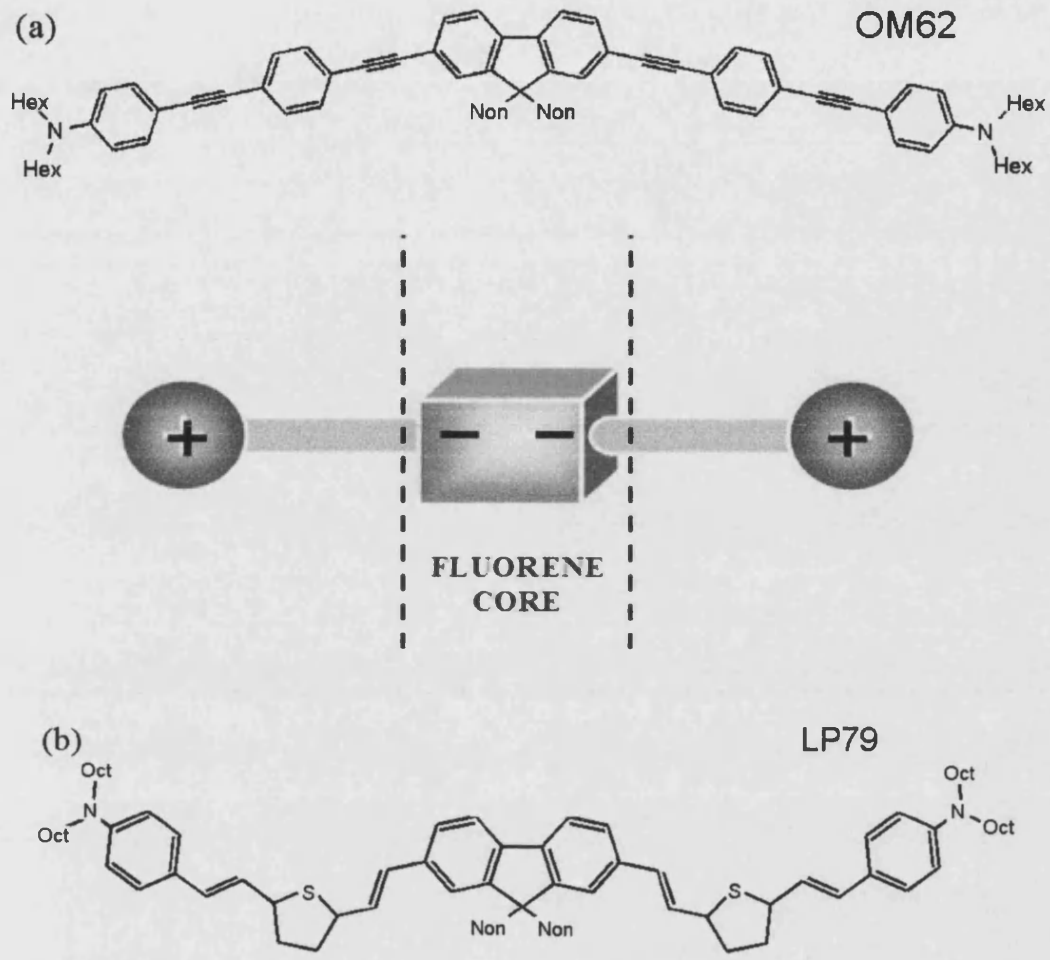

Figure 3.13: The two-photon fluorophores (a) OM62 and (b) LP79 synthesised at *Université de Rennes*.

Fluorophore	OM62	LP79	Fluorescein
Molecular Weight	1185.876	1318.208	332.32
Absorption Maximum	387nm	470nm	491nm
ε ($10^4 M^{-1}.cm^{-1}$)	12.8	12.3	7.6
Emission Maxima (nm)	433, 456	524, 563	515
Quantum Yield	0.82	0.53	0.90
Fluorescence Lifetime (ns)	0.60 (in toluene)	0.79 (in toluene)	2.58 (in E.G.*)
TPA Maximum (nm)	735	740	780
$\sigma^{(2)}$ at TPA Maximum (cm^4s/photon)	8.2×10^{-48}	37.1×10^{-48}	0.37×10^{-48}
$\sigma^{(2)}$ at 800nm (cm^4s/photon)	4.39×10^{-48}	17.73×10^{-48}	0.36×10^{-48}

Table 3.3: Some of the photophysical properties of OM62 and LP79 compared with Fluorescein. *Ethylene Glycol

These visible emitting molecules have two-photon absorption cross-sections greatly in excess of conventional dye probes. The emission spectra and two-photon absorption spectra of these dyes are shown in figure 3.14, shown with Fluorescein for comparison.

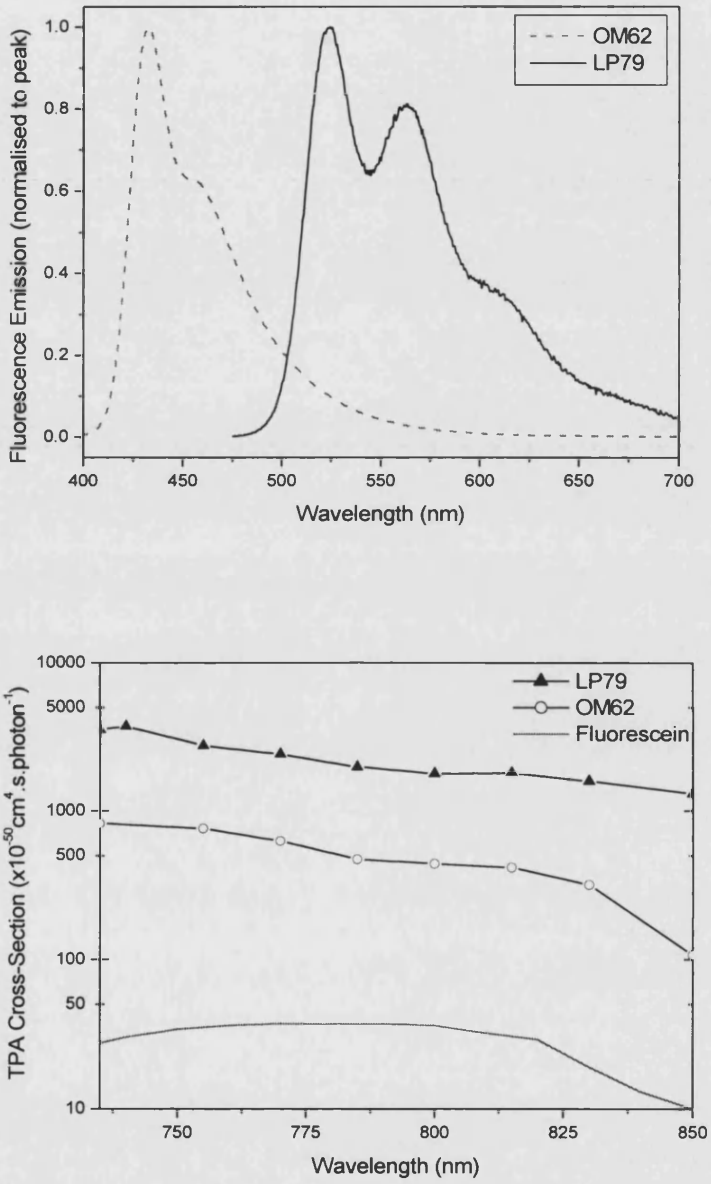

Figure 3.14: This figure shows the visible-region emission spectra and near infra-red two-photon absorption cross-section spectra of OM62 in Toluene and LP79 in Toluene. The two-photon absorption cross section spectrum of Fluorescein in H_20 is shown for comparison. (All spectra taken at room temperature with 10^{-4} molarity)

Figure 3.15 shows preliminary TCSPC fluorescence lifetime and anisotropy data for LP79 in methylcyclohexane.

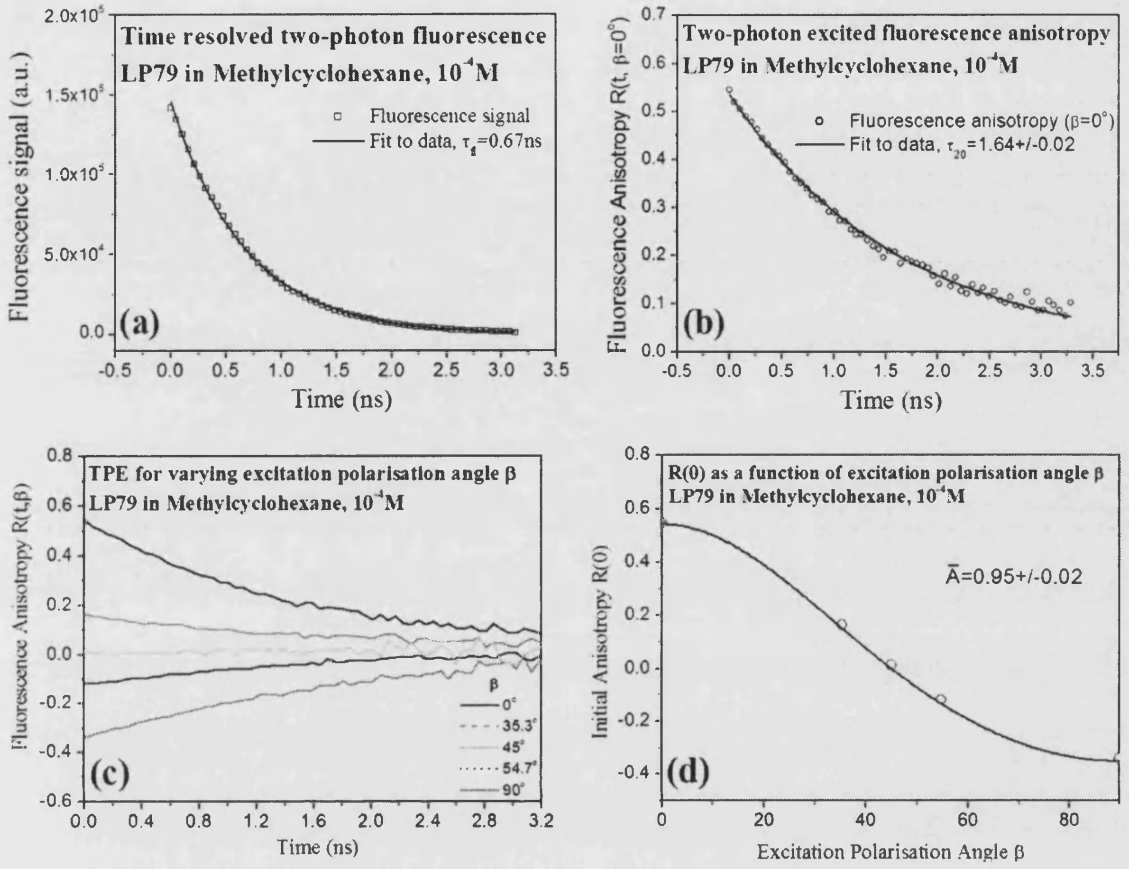

Figure 3.15: Preliminary TCSPC fluorescence lifetime (a) and anisotropy (b), (c), (d) data for push-push chromophore LP79 in Methylcyclohexane.

Analysis of the lifetime and anisotropy data yield a fluorescence lifetime of 0.67ns and re-orientational lifetime of 1.64ns. Fitting the initial anisotropy for varying excitation polarisation yields a correction factor Ā of 0.95, suggesting that the absorption and emission dipole moments are nearly parallel.

The enhanced two-photon cross-section afforded by the quadrupolar chromophores means that lower excitation energy is required to achieve a comparable excited state population. In section 3.5 it was shown that an 800nm, 200fs pulse with an energy of $8x10^{-10}$J was required to create an excited state population of $2.1x10^{5}$ in Rhodamine 6G. For LP79 with the same pump characteristics, a pulse energy of $3x10^{-10}$J is sufficient to create the same excited state population.

3.11 Conclusions

This chapter has shown that the combination of single and two-photon fluorescence anisotropy studies can provide new information about molecular probe order in the restricted environment of an aligned nematic liquid crystal. Single and two-photon fluorescence anisotropy decays yield the same relaxation times (within experimental error) for Rhodamine 6G and Rhodamine B in 5CB.

The increased order of the excited state population arising from two-photon photoselection does not lead to cross relaxation and the orientational dynamics are seen to remain linear, providing further evidence to justify the linear relaxation model in addition to the single and three pulse photoselection methods used in Chapter 2.

The ground state order parameter $\langle \alpha_{60}^{gs}(ss) \rangle$ has now been directly measured using the fluorescence anisotropy measurements obtained from two-photon excitation of Rhodamine 6G and Rhodamine B. In both cases the empirically determined values of $\langle \alpha_{60}^{gs}(ss) \rangle$ were found to be in agreement with the values extrapolated from single photon excitation experiments using the methods of Durbin and Shen, thus validating the approach. It is still necessary however to adopt these methods with two-photon excitation, since estimates for the values of ground state moments higher than $\langle \alpha_{60}^{gs}(ss) \rangle$ are necessary to form a physically real distribution function.

The advances in two-photon spectroscopy have led to the synthesis of molecular probes specifically designed for an enhanced two-photon absorption cross-section at wavelengths achievable using the popular Titanium:Sapphire oscillator. Two such dyes have been introduced in this chapter; along with established molecular probes, the photophysical properties of these synthesised fluorophores make them suitable candidates for the excited state photo-engineering experiments developed in Chapter 4.

References for Chapter 3

1. A J Bain and A J McCaffery, J. Chem. Phys. **83**, 2627 (1985)
2. A J Bain, P Chandna, G Butcher and J Bryant, J. Chem. Phys. **112**, 10435 (2000)
3. D A Armoogum, R J Marsh and A J Bain, Proc. SPIE **5222A** (2003)
4. R R Birge, J A Bennett, B M Pierce and T M Thomas, J. Am. Chem. Soc. **100**, 1533 (1978)
5. E M Monge, D A Armoogum and A J Bain, Proc. SPIE **4797**, 264 (2002)
6. K Konig, J. Microsc. **200** 83 (2000)
7. A Volkmer, V Subramaniam, T M Jovin and D J Birch, Biophys. J. **78** 1589 (2000)
8. W Denk, J H Strickler and W W Webb, Science **248**, 73 (1990)
9. O Mongin, L Porres, L Moreaux, J Mertz and M Blanchard-Desce, Org. Lett. **4**, 719-722 (2002)
10. W Demtröder, "*Laser Spectroscopy: Basic Concepts and Instrumentation*", Springer, Berlin (1996)
11. C Xu, W Zipfel, J B Shear, R M Williams and W W Webb, Proc. Natl. Acad. Sci USA, **93**, 10763 (1996)
12. M Goppert, Naturwissenschaften **17**, 932 (1929)
    (later M. Goppert-Mayer, Ann. Phys., **5**, 273 (1931))
13. P F Moulton, J. Opt. Soc. Am. B **3**, 125 (1986)
14. A Volkmer, D A Hatrick and D J Birch, Meas. Sci. Technol. **8**, 1339, (1997)
15. H Mahr in *Quantum Electronics* Vol.1, (Part A), Eds. H. Rabin and C. L. Tang, Academic Press, New York (1975)
16. R Loudon, "*The Quantum Theory of Light*", Clarendon Press, Oxford, (1973)
17. M A Albota, C Xu and W W Webb, App. Opt. **37**(31), 7352 (1998)
18. M A Bopp, Y Jia, G Haran, E A Morelino and R M Hochstrasser, Appl. Phys. Lett. **77**, 7 (1998)
19. A J Bain, P Chandna and J Bryant, J. Chem. Phys. **112**, 10418 (2000)
20. W J Thompson in *Angular Momentum: an illustrated guide to rotational symmetries for physical systems*, Wiley, New York (1994)
21. A J Bain and A J McCaffery, J. Chem. Phys. **80**, 5893 (1984)
22. S D Durbin and Y R Shen, Phys. Rev. A **30**(3), 1419 (1984)
23. A Fischer, C Cremer and E H K Stelzer, App. Opt. **34** (12), 1989 (1995)
24. M K Reed, M K Steiner-Shepard and D K Negus, Opt. Lett. **19**(22), 1855 (1994)

25. M K Reed, M K Steiner-Shepard, M S Armas and D K Negus, J. Opt. Soc. Am. B **12**, 2229 (1995)
26. *Schott Filter Glass Datasheet*, Schott Glas, Hattenbergstr. 10, 55122 Mainz, Germany (2004)
27. M Barzoukas and M Blanchard-Desce, J. Chem. Phys. **113**, 3951 (2000)
28. M Barzoukas and M Blanchard-Desce, Mol. Cryst. Liq. Cryst. Sci. Tech. **27**, 209 (2001)
29. M Barzoukas and M Blanchard-Desce, Proc. SPIE **4461**, 78 (2001)
30. W H Lee, M Cho, S-J Leon and B R Cho, J. Phys. Chem. A **104**, 11033 (2000)
31. L Ventelon, L Moreaux, J Mertz and M Blanchard-Desce, Chem. Commun. 2055 (1999)
32. L Ventelon, S Charier, L Moreaux, J Mertz and M Blanchard-Desce, Angew. Chem. Int. Ed. **40**, 2098 (2001)
33. L Ventelon, L Moreaux, J Mertz and M Blanchard-Desce, Synth. Methods **127**, 17 (2002)

Chapter 4

Excited State Photo-Engineering I:
Stimulated Emission Depletion of Two-Photon Excited Fluorescence

4.1 Introduction – Conventional photoselection experiments and the need for control of excited state populations.

The experiments described so far in this work have used variable photoselection to prepare a range of non-equilibrium excited state orientational distributions in the ordered environment of nematic liquid crystals. Variation of the linear excitation polarisation with respect to the nematic director creates both cylindrically symmetric and asymmetric degrees of excited state alignment; their relaxation dynamics are seen to be markedly different reflecting an anisotropy in θ and φ diffusive motions that is not present in isotropic media. Single beam photoselection experiments were augmented by two-photon and three pulse photoselection schemes allowing the creation of a wider range of cylindrically symmetric excited state distributions. However in all of these approaches the excited state observables are, by the constraints of single photon electric dipole selection rules, restricted to the K=2 (alignment) moments of the excited state distribution. Measurement of higher moments (e.g. $\langle \alpha_{40} \rangle$) for the probe ground state were found to be crucial in determining the correct orientational distribution; with single photon correlations (polarisation measurements) this information cannot be accessed for the excited state.

Irrespective of the nature of the excitation process, fluorescence experiments are essentially passive. The initial excited state order is determined by the interaction between the excitation probability (which has intrinsic cylindrical symmetry about the polarisation vector) and the ground state distribution. The fluorescence observables are constrained by single-photon selection rules to a combination of moments of rank K=2. If more information on excited state dynamics is to be obtained it will be necessary to develop preparation and observation techniques which circumvent these restrictions.

The experiments described here and in Chapter 5 involve active control of the excited state population and alignment using two laser pulses. Two-photon excitation (PUMP pulse) is used to prepare the excited state; this is followed by time-delayed polarisation selective de-population using stimulated emission (DUMP pulse). This approach allows the creation of order in excited states that is not possible using single laser pulses and, when coupled with time resolved fluorescence polarisation measurements, excited state moments of rank K=4 can be accessed.

4.2 Stimulated Emission Depletion

In this work, the active method of exerting control on the population and alignment of an excited state array is based on stimulated emission depletion or STED. In the absence of external influences, the excited state population prepared by short pulsed laser excitations (the PUMP) will firstly undergo rapid (sub-picosecond→picosecond) non-radiative deactivation mediated by interactions (reorganisation and/or vibrational energy transfer) with surrounding solvent molecules leading to a thermal distribution of vibrational energy levels within S_1. Spontaneous emission from this relaxed distribution takes place over several nanoseconds, populating upper vibrational levels of S_0 in accordance with the Franck-Condon principle. These levels are in turn rapidly de-activated by solvent-solute interactions leading to a wholly thermalised ground state.

Stimulated emission depletion affects the absorption-emission process by the introduction of a second time-delayed laser pulse (hereafter referred to as the DUMP). Provided that there is an overlap between the DUMP wavelength range and the spontaneous emission spectrum, transitions to the ground state are induced with the gain of photons (stimulated emission) in the DUMP pulse. A schematic representation of the PUMP-DUMP process is shown in figure 4.1.

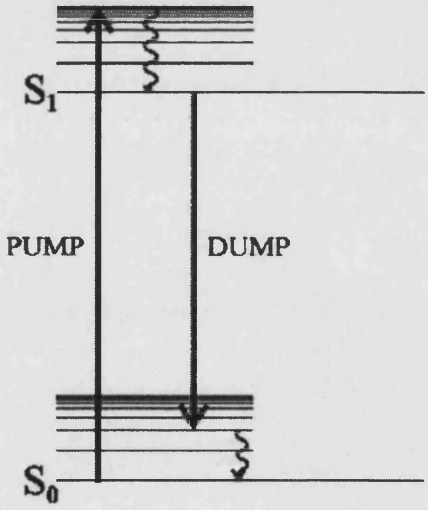

Figure 4.1: Following excitation to S_1 by a PUMP pulse, the system can be returned to S_0 by a DUMP pulse with the emission of a photon via stimulated emission.

STED (then referred to as Stimulated Emission Pumping) was first developed by Dai et al [1] as a high resolution tool in gas phase spectroscopy of vibrationally excited ground states. The first application of STED to condensed phase fluorescent probes (then

termed Light Quenching) was achieved by Lakowicz and co-workers [2,3]. PUMP-DUMP delay measurements were subsequently shown to yield information on excited state relaxation dynamics [4] and fast solvation effects [5]. STED has also shown considerable promise as a technique for time-resolved microscopy as exemplified by the work of Gratton et al [6]. Recent developments by Hell and co-workers have shown that sub-wavelength spatial resolution can be achieved by STED from single photon excited states [7].

4.3 Two-Photon STED

With the advent of widely tuneable femtosecond lasers, two-photon excitation has become a useful adjunct to single photon techniques. In the field of fluorescent microscopy two-photon excitation affords increased spatial resolution in that the intensity dependent transition probability is maximised in the waist region of a focussed laser beam [8,9]. Fluorescence occurs from a highly localised region in a sample and there is the highly desirable reduction (or elimination) of unwanted effects such as sample heating and background fluorescence from molecules outside the immediate observation area. This has important applications for medical physics, where the two-photon excitation process has been shown to reduce specimen damage and enhance penetration depth for non-invasive three-dimensional studies of biological specimens [10].

Since both two-photon excitation and STED have been shown to yield increased spatial resolution in fluorescence microscopy, the development of two-photon STED would be an attractive goal for this end alone. The single and two-photon polarised photoselection techniques developed and applied in Chapters 2 and 3, whilst yielding useful information on ground state order and excited state orientational relaxation, are however restricted through spontaneous emission selection rules to (K=2) excited state alignment dynamics.

The imposition of molecular order has been shown to break the equivalence of θ and φ probe diffusion dynamics manifested in unequal τ_{20} and τ_{22} diffusion times and their temperature dependence [11]. It is not possible, however, to investigate the influence of an ordered environment on K=4 relaxation dynamics using unperturbed spontaneous emission, as although K=4 moments may be present in the excited state they do not

contribute to spontaneous fluorescence observables as shown in Chapter 2. As will be seen, these constraints can be lifted by observing polarised fluorescence changes brought on by STED from an excited state. It is this property, together with the possibility of creating degrees of order and excited state symmetries not accessible by conventional (single *and* two-photon) excitation routes, that sets STED aside as a truly active means of *photo-engineering* the properties of excited state ensembles.

The work on STED in this thesis falls into two distinct categories. Firstly, STED depletion dynamics are investigated following two-photon excitation in two widely used fluorescent chromophores (Fluorescein and Rhodamine 6G). These studies are extended to molecules specifically designed for enhanced two-photon fluorescence in collaboration with the CNRS research group of Dr Mireille Blanchard-Desce at Rennes. This work allows us to investigate the conditions necessary to optimise the STED process and to draw conclusions as to the feasibility of implementing two-photon STED with unamplified high repetition rate (e.g. 76 MHz) laser systems. The second category, discussed in Chapter 5, will show how polarised STED in conjunction with time-resolved fluorescence anisotropy measurements can be used to access information on K=4 relaxation dynamics in the excited state, thereby breaking a fundamental restriction imposed by single photon emission.

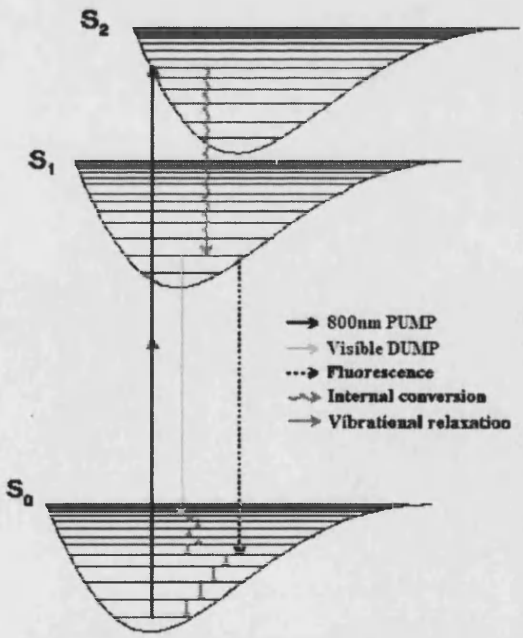

Figure 4.2: Excitation and relaxation pathways for two-photon excitation and stimulated emission depletion

The energy levels, radiative and non-radiative relaxation processes pertaining to STED in two-photon excited states are shown in figure 4.2. As in the two-photon excitation experiments described in Chapter 3 the PUMP pulse was derived from the partial output of a regeneratively amplified Ti:Sapphire laser (Coherent RegA 9000) which initially accesses a state in the singlet manifold above S_1. This is followed by rapid internal conversion and solvent mediated relaxation leading to emission from lower vibrational levels of S_1. As with single photon excitation, fluorescence from S_1 occurs on a nanosecond timescale to the upper vibrational levels of S_0. In the STED experiments this process is altered by the application of a time-delayed visible laser pulse generated from an optical parametric amplifier (Coherent OPA 9400). The laser sources and experimental set-up are described in detail in section 4.6. The disposition of PUMP, DUMP and observed fluorescence wavelengths are set out in figure 4.3. The DUMP wavelength is red-shifted from the absorption maximum of the fluorescence to minimise the contribution of DUMP induced excitation from $S_0 \rightarrow S_1$. The DUMP pulse energies necessary for significant excited state depletion can, at the appropriate wavelengths, lead to a measurable background fluorescence signal. Observation of STED (i.e. fluorescence depletion) depends not only on the choice of DUMP pulse wavelength but also the time over which it is applied. Re-pumping of S_1 can be a significant factor in reducing STED efficiency if the DUMP pulsewidth is comparable to, or shorter than, the relaxation times of the vibrationally excited levels in S_0 that are initially populated as a result of stimulated emission. Optimisation of STED and the tailoring of the DUMP pulse to meet this objective are discussed in detail later in this chapter.

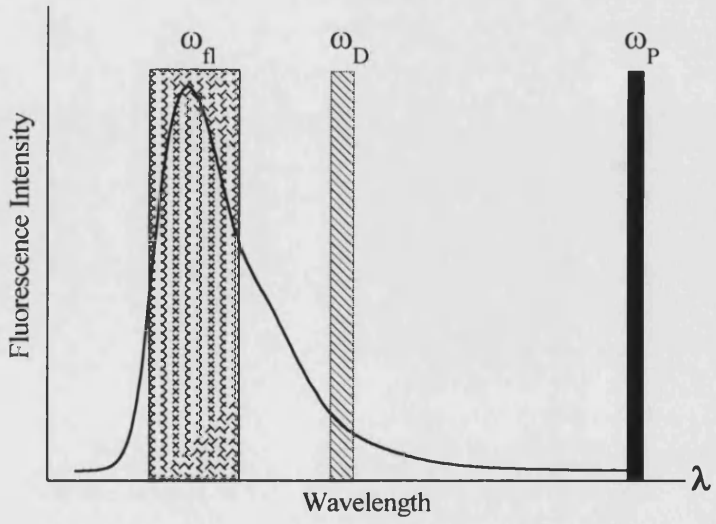

Figure 4.3: Following two-photon excitation at 800nm, the wavelength of the DUMP field must lie within the spontaneous emission region of a chromophore. Fluorescence is observed at frequencies to the blue of ω_D.

4.4 Orientational Photoselection in STED using parallel PUMP and DUMP fields

The rate of change in an excited state population due to stimulated emission to a lower and rapidly depleting set of ground state vibrational levels by a DUMP pulse of intensity $I_D(t)$ and photon energy hν is, neglecting spontaneous emission and orientational relaxation which are assumed to take place over longer timescales, described by

$$\frac{dN_{EX}(\theta,\phi,t)}{dt} = -\frac{I_D(t)\sigma}{h\nu} W_D(\theta,\phi) N_{EX}(\theta,\phi,t) \qquad [4.1]$$

where $N_{EX}(\theta,\varphi,t)$ is the excited state population at time t found between θ and θ+dθ, φ and φ+dφ in the laboratory axis system, and σ is the cross-section for stimulated emission. Integrating over the pulse duration yields (assuming a constant intensity between t=0 and $t=t_D$)

$$N_{EX}(\theta,\phi,t_D) = N_{EX}(\theta,\phi,t=0)\exp\left[-\left(\frac{E_D\sigma}{Ah\nu}\right)W_D(\theta,\phi)\right] \qquad [4.2]$$

where E_D is the pulse energy and A is the area over which the DUMP pulse is focussed. Here the form of the angular dependence of the transition probability $W_D(\theta,\varphi)$ can be varied in an exactly analogous manner to the single and three beam photoselection work described in Chapters 2 and 3 (i.e. by the use of single or multiple X, Y and Z polarised dump pulses) but there is an additional degree of control arising from the saturation parameter $S=E_D\sigma/Ah\nu$ for the transition.

The excited state distributions immediately before and after STED can be expressed in terms of the total population and an orientational probability:

$$\begin{aligned} N_{EX}(\theta,\varphi,t_D) &= N_{EX}(D)P_D(\theta,\varphi) \\ N_{EX}(\theta,\varphi,t=0) &= N_{EX}(U)P_U(\theta,\varphi) \end{aligned} \qquad [4.3]$$

where (U) and (D) denote the undumped and dumped distributions respectively. Substitution into equation 4.2 and rearranging yields

$$P_D(\theta,\phi) = \frac{N_{EX}(U)}{N_{EX}(D)} P_U(\theta,\phi)\exp[-SW_D(\theta,\phi)] \qquad [4.4]$$

Both initial and modified orientational distribution functions can be expressed as expansions in terms of spherical harmonics [12]:

$$P_U(\theta,\varphi) = \sum_{K'Q'} \left\langle C^{EX}_{K'Q'}(U) \right\rangle Y_{K'Q'}(\theta,\varphi) \qquad [4.5a]$$

$$P_D(\theta,\varphi) = \sum_{KQ} \left\langle C^{EX}_{KQ}(D) \right\rangle Y_{KQ}(\theta,\varphi) \qquad [4.5b]$$

Substituting equation 4.5a into equation 4.4 yields

$$P_D(\theta,\varphi) = \frac{N_{EX}(U)}{N_{EX}(D)} \sum_{K'Q'} \left\langle C^{EX}_{K'Q'}(U) \right\rangle Y_{K'Q'}(\theta,\varphi)\exp[-SW_D(\theta,\varphi)] \qquad [4.6]$$

The moments of $P_D(\theta,\varphi)$ are given by

$$\left\langle C^{EX}_{KQ}(D) \right\rangle = \int_0^{2\pi}\int_0^{\pi} Y^*_{KQ}(\theta,\varphi) P_D(\theta,\varphi)\sin\theta d\theta d\varphi \qquad [4.7]$$

Substituting equation 4.6 into equation 4.7 yields

$$\left\langle C^{EX}_{KQ}(D) \right\rangle = \frac{N_{EX}(U)}{N_{EX}(D)} \sum_{K'Q'} \left\langle C^{EX}_{K'Q'}(U) \right\rangle \left\langle KQ \middle| \exp[-SW_D(\theta,\phi)] \middle| K'Q' \right\rangle \qquad [4.8]$$

In the limit of weak STED (i.e. S<<1) equation 4.8 becomes

$$\left\langle C^{EX}_{KQ}(D) \right\rangle = \frac{N_{EX}(U)}{N_{EX}(D)} \sum_{K'Q'} \left\langle C^{EX}_{K'Q'}(U) \right\rangle \left\langle KQ \middle| 1 - SW_D(\theta,\phi) \middle| K'Q' \right\rangle \qquad [4.9]$$

For Z polarised PUMP and DUMP pulses this becomes

$$\left\langle C^{EX}_{KQ}(D) \right\rangle = \frac{N_{EX}(U)}{N_{EX}(D)} \sum_{K'Q'} \left\langle C^{EX}_{K'Q'}(U) \right\rangle \left\langle KQ \middle| 1 - S\frac{\sqrt{4\pi}}{3}\left(Y_{00}(\theta,\phi) + \frac{2}{\sqrt{5}} Y_{20}(\theta,\phi) \right) \middle| K'Q' \right\rangle \qquad [4.10]$$

Rearrangement yields

$$\left\langle C_{KQ}^{EX}(D)\right\rangle = \frac{N_{EX}(U)\sqrt{4\pi}}{3N_{EX}(D)} \sum_{K'Q'} \left\langle C_{K'Q'}^{EX}(U)\right\rangle \left\langle KQ \left| \left(3-S\right)Y_{00}(\theta,\phi) + \frac{2}{\sqrt{5}} S Y_{20}(\theta,\phi) \right| K'Q' \right\rangle \qquad [4.11]$$

Evaluation of the matrix elements gives [12]

$$\left\langle C_{KQ}^{EX}(D)\right\rangle = \frac{N_{EX}(U)}{3N_{EX}(D)} \sum_{K'Q'} \left\langle C_{K'Q'}^{EX}(U)\right\rangle \begin{bmatrix} (3-S)\begin{pmatrix} K & 0 & K' \\ -Q & 0 & Q' \end{pmatrix}\begin{pmatrix} K & 0 & K' \\ 0 & 0 & 0 \end{pmatrix}\hat{K}\hat{K}' \\ -\frac{2}{\sqrt{5}} S \begin{pmatrix} K & 2 & K' \\ -Q & 0 & Q' \end{pmatrix}\begin{pmatrix} K & 2 & K' \\ 0 & 0 & 0 \end{pmatrix}\hat{K}\hat{K}'\sqrt{5} \end{bmatrix} \qquad [4.12]$$

The fluorescence observables for the modified array are

$$\left\langle C_{00}^{EX}(D)\right\rangle = \frac{N_{EX}(U)}{3N_{EX}(D)} \left[\left(3-S\right)\left\langle C_{00}^{EX}(U)\right\rangle - \frac{2}{\sqrt{5}} S \left\langle C_{20}^{EX}(U)\right\rangle \right] \qquad [4.13]$$

$$\frac{\left\langle C_{20}^{EX}(D)\right\rangle}{\sqrt{5}} = \frac{N_{EX}(U)}{3N_{EX}(D)} \left[\left(3-S\right)\frac{\left\langle C_{20}^{EX}(U)\right\rangle}{\sqrt{5}} - \frac{2}{5} S \left\langle C_{00}^{EX}(U)\right\rangle - \frac{4}{7}\frac{\left\langle C_{20}^{EX}(U)\right\rangle}{\sqrt{5}} + \frac{12}{35}\left\langle C_{40}^{EX}(U)\right\rangle \right] \qquad [4.14]$$

In terms of normalised moments $\left\langle \alpha_{K0}^{EX}(U)\right\rangle$ of the initial distribution equations [4.13] and [4.14] become

$$\left\langle C_{00}^{EX}(D)\right\rangle = \frac{N_{EX}(U)}{3N_{EX}(D)} \left\langle C_{00}^{EX}(U)\right\rangle \left[\left(3-S\right) - \frac{2}{\sqrt{5}} S \left\langle \alpha_{20}^{EX}(U)\right\rangle \right] \qquad [4.15]$$

$$\frac{\left\langle C_{20}^{EX}(D)\right\rangle}{\sqrt{5}} = \frac{N_{EX}(U)}{3N_{EX}(D)} \left\langle C_{00}^{EX}(U)\right\rangle \left[\left(3-S\right)\frac{\left\langle \alpha_{20}^{EX}(U)\right\rangle}{\sqrt{5}} - \frac{2}{5} S - \frac{4}{7} S \frac{\left\langle \alpha_{20}^{EX}(U)\right\rangle}{\sqrt{5}} + \frac{12}{35} S \left\langle \alpha_{40}^{EX}(U)\right\rangle \right] \qquad [4.16]$$

It was shown in Chapter 1 that by conservation of orientational probability $\langle C_{00}\rangle$ is necessarily $\sqrt{4\pi}$ for any distribution function; from equation 4.15, the relationship between the initial and altered excited state populations is then:

$$N_{EX}(D) = \frac{N_{EX}(U)}{3}\left[(3-S) - \frac{2}{\sqrt{5}} S\left\langle \alpha_{20}^{EX}(U)\right\rangle\right] \qquad [4.17]$$

This can be re-written as:

$$N_{EX}(D) = \frac{N_{EX}(U)}{3}[(3-S) - 2R(U)S] \qquad [4.18]$$

since $\left\langle \alpha_{20}^{EX}(U)\right\rangle / \sqrt{5}$ corresponds to the fluorescence anisotropy R(U) prior to excited state depletion. The fraction of the initial population remaining after application of the dump pulse, F_R, is thus,

$$F_R = \frac{N_{EX}(D)}{N_{EX}(U)} = 1 - \frac{(1+2R(U))S}{3} \qquad [4.19]$$

The fluorescence anisotropy after the dump pulse is applied is given by

$$R(D) = \frac{\left[\left(3 - \frac{11}{7}S\right)R(U) - \frac{2}{5}S - \frac{12}{35}\left\langle \alpha_{40}^{EX}(U)\right\rangle S\right]}{(3-(1+2R(U))S)} \qquad [4.20]$$

In two-photon excitation, given a diagonal transition tensor and a parallel emission transition dipole moment, the fluorescence anisotropy is significantly higher than in single photon excitation [13,14] (4/7 vs. 2/5 respectively). Moreover, unlike single photon excitation a K=4 moment $\left\langle \alpha_{40}^{EX}\right\rangle$ is created [15] and will make a direct contribution to R_D as can be seen from equation 4.20.

With parallel PUMP and DUMP polarisations the more highly ordered initial distribution produced by two-photon excitation intuitively would be expected to lead to an increased degree of depletion over single photon excitation provided the PUMP-DUMP delay time is short compared to τ_{20}. This is indeed born out by the simple analysis above; from equations 4.19 and 4.20 the population depletion and depolarisation of single and two-photon excited states can be predicted. Expressions for F_R following STED from single and two-photon excited state populations (for short PUMP-DUMP delays) are compared in table 4.1; plots of F_R for values of S from 0 to

0.3 for single and two-photon prepared states are plotted in figure 4.4 where a 16% increase in depletion efficiency is predicted.

Excitation	R(0)	F_R
Single photon STED	$2/5$	$F_R = 1 - \frac{3}{5}S$
Two-photon STED	$4/7$	$F_R = 1 - \frac{5}{7}S$

Table 4.1: Comparison of excited state population removal following single and two-photon excitation

The simple analysis presented here shows that, in principle, STED measurements can access information on K=4 moments in the excited state distribution (equation 4.20); this unique feature of STED is exploited in Chapter 5 where time-delayed PUMP-DUMP anisotropy measurements are used to determine the τ_{40} diffusion times of Fluorescein and Rhodamine 6G. It should be stressed that STED takes place in molecules where the ground state vibrational relaxation times, although fast, take place on finite timescales (10^{-13}-10^{-12}s) and the effects of re-pumping S_1 during the DUMP pulse passage cannot be ignored. These issues are addressed in section 4.5.

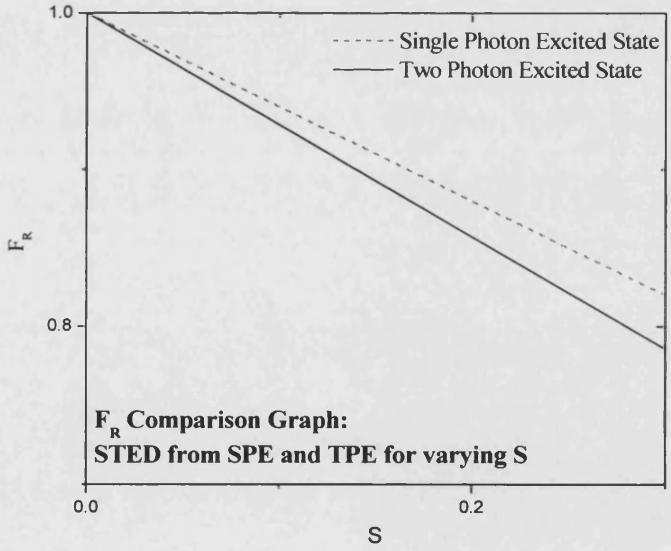

Figure 4.4: Relative efficiencies of STED from single and two-photon excited states.

4.5 Saturation Dynamics in STED

The preceding analysis assumed a saturation parameter S significantly less than unity and neglected re-pumping of S_1 by the DUMP pulse. To achieve significant population (and anisotropy) changes it is clear from equation 4.19 that values of S close to unity are required. Moreover, the DUMP pulse is derived from an optical parametric amplifier with a characteristic output pulsewidth of approx. 200fs (section 4.6); this is comparable to or shorter than typical ground state vibrational relaxation times [16]. At present, the DUMP pulses can be stretched between 700fs and 3.2ps; on these timescales vibrational de-population of target levels in the ground state is unlikely to be complete [17]. The rate equations for STED on a timescale that is fast compared to spontaneous emission (nanosecond to sub-nanosecond) and orientational relaxation (nanosecond) become:

$$\frac{dN_{EX}(\theta,t)}{dt} = -\frac{I_D(t)\sigma W_D(\theta,t)}{h\nu}\left(N_{EX}(\theta,t) - N_{GS}(\theta,t)\right) \qquad [4.21]$$

$$\frac{dN_{GS}(\theta,t)}{dt} = \frac{I_D(t)\sigma W_D(\theta,t)}{h\nu}\left(N_{EX}(\theta,t) - N_{GS}(\theta,t)\right) - \frac{N_{GS}(\theta,t)}{\tau_R} \qquad [4.22]$$

It is possible to obtain analytic solutions to the rate equations 4.21 and 4.22 by assuming a rectangular DUMP pulse with width τ_P, which yield the fractional remaining population F_R as a function of $E_P\sigma/h\nu A$ for given ratios of τ_P/τ_R. By assuming that the initial population distribution in the upper ground state vibrational levels is negligible, the excited state population evaluated at $t=\tau_P$ is:

$$N_{EX}(\theta,\tau_P) = \frac{N_{EX}(\theta,0)}{2d}\left[\exp\left(-\frac{1}{2}\left\{\frac{\tau_P}{\tau_R} + 2S\cos^2\theta + d\right\}\right)\right]\left\{\frac{\tau_P}{\tau_R}\left(e^d - 1\right) + d\left(e^d + 1\right)\right\} \qquad [4.23]$$

where the parameter d is

$$d = \sqrt{\left(\frac{\tau_P}{\tau_R}\right)^2 + 4S^2\cos^4\theta} \qquad [4.24]$$

With the moments of the altered excited state distribution function calculated from

$$\left\langle C_{KQ}^{EX}(\tau_P)\right\rangle \equiv \left\langle C_{K0}^{EX}(D)\right\rangle = \frac{\int_0^{2\pi}\int_0^{\pi} N_{EX}(\theta,\tau_P)Y_{KQ}^{*}(\theta,\varphi)\sin\theta d\theta d\varphi}{\int_0^{2\pi}\int_0^{\pi} N_{EX}(\theta,\tau_P)\sin\theta d\theta d\varphi} \qquad [4.25]$$

The fractional depletion of the excited state population can be calculated using

$$1-F_R = \frac{\int_0^{2\pi}\int_0^{\pi}[N_{EX}(\theta,\tau_P)-N_{EX}(\theta,0)]\sin\theta d\theta d\varphi}{\int_0^{2\pi}\int_0^{\pi} N_{EX}(\theta,0)\sin\theta d\theta d\varphi} \qquad [4.26]$$

where $N_{EX}(\theta,0)$ represents the excited state population immediately prior to STED.

The evaluation of equation 4.26 was performed using a Mathematica program developed in our group by Dr Richard Marsh [18]. This yields numerical solutions for the population removal from a two-photon excited state immediately following STED (i.e. before the onset of significant orientational relaxation) for varying S and ratios of DUMP pulse width to ground state vibrational relaxation time τ_P/τ_R. A set of numerical solutions for F_R for different values of τ_P/τ_R is shown in figure 4.5. This shows that as the DUMP pulse is applied for longer times in comparison to τ_R (i.e. as the DUMP pulsewidth is stretched), so re-pumping of S_1 by the DUMP is reduced and higher levels of excited state depletion can be achieved.

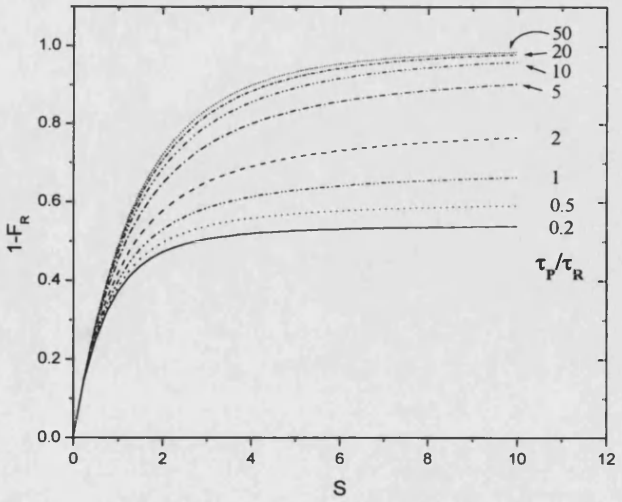

Figure 4.5: Numerical solutions to the rate equations generate a family of "saturation" curves for the population removal by STED for different values of τ_P/τ_R. In this example, τ_P/τ_R is varied from 0.2 to 50 and values of S from 0 to 12.

By fitting numerical solutions such as in figure 4.5 to experimental data, it was possible to obtain values for the stimulated emission cross-section and ground state vibrational relaxation time for a range of molecular probes in isotropic solvents.

4.6 Experimental Apparatus and Realisation

4.6.1 Laser Sources

The 800nm PUMP radiation was provided by the partial output of the Regenerative Amplifier (RegA 9000) as described in Chapter 3. The visible region DUMP pulses were generated by an Optical Parametric Amplifier (OPA) (Coherent 9400); an optical schematic of the OPA is shown in figure 4.6.

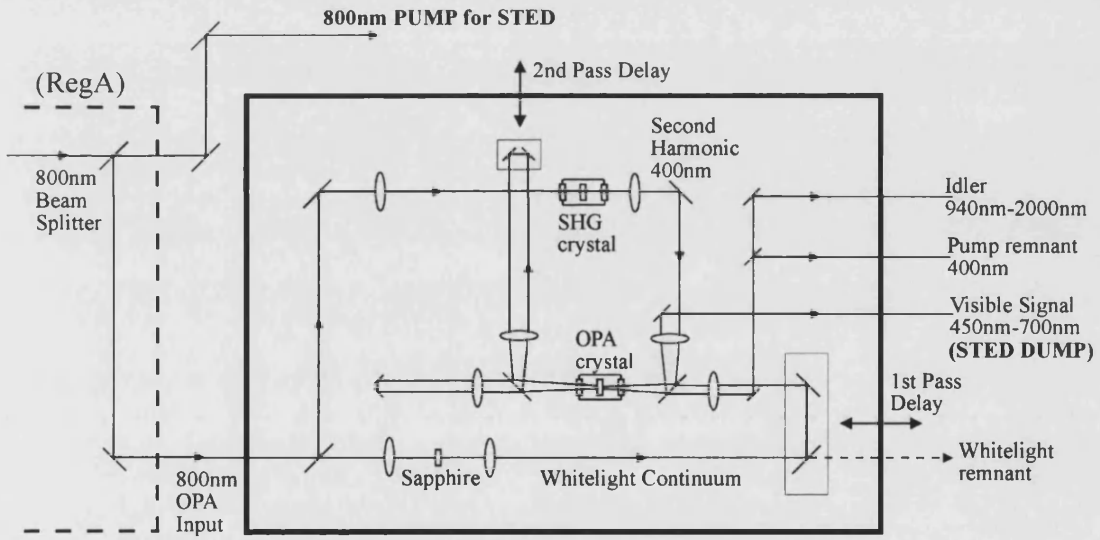

Figure 4.6: Schematic diagram of the Optical Parametric Amplifier used to generate the visible DUMP wavelengths in the excited state photo-engineering experiments.

The OPA is used in conjunction with the femtosecond Titanium:Sapphire oscillator-amplifier system described in the previous chapter to provide laser pulses at multiple wavelengths. It uses as an input the remaining portion of the 800nm radiation from the regenerative amplifier. Upon arrival at the OPA, the RegA 800nm beam (μJ energies with 140fs pulse width) is split further into two portions. About 25% of the beam is used to generate a white-light continuum using self phase modulation in a sapphire crystal, and the remaining 75% is frequency doubled to create pulses at 400nm which provide the pump energy for optical parametric amplification [19].

Optical Parametric Amplification is achieved by non-linear mixing of the 400nm pump wave with the continuum. By varying the angle of incidence of the BBO crystal (figure 4.6), a specific wavelength component of the continuum for which the phase matching condition [19,20] is met is amplified, along with the corresponding idler wavelength ($\omega_{idler}=\omega_{pump}-\omega_{signal}$) at the expense of the pump.

Rotation of the OPA crystal yields a signal wavelength tuning range of 450nm to 700nm whilst the idler scans from over 2μm to 933nm. For extra efficiency the continuum and SHG beams make two passes through the OPA crystal. After optical parametric amplification has occurred, the visible "signal" beam, idler beam, the remnant white continuum and 400nm beams are split using coated optics and exit the OPA from different apertures, allowing unwanted components (i.e. all beams except the visible "signal") to be blocked.

The wavelength conversion properties of the OPA allow access to visible laser light across the visible spectrum. Figure 4.7 shows typical OPA outputs from 453nm to over 700nm. The PUMP and DUMP wavelengths were measured using a laser spectrum analyser (IST-Rees), and the pulse widths monitored using a scanning autocorrelator (APE).

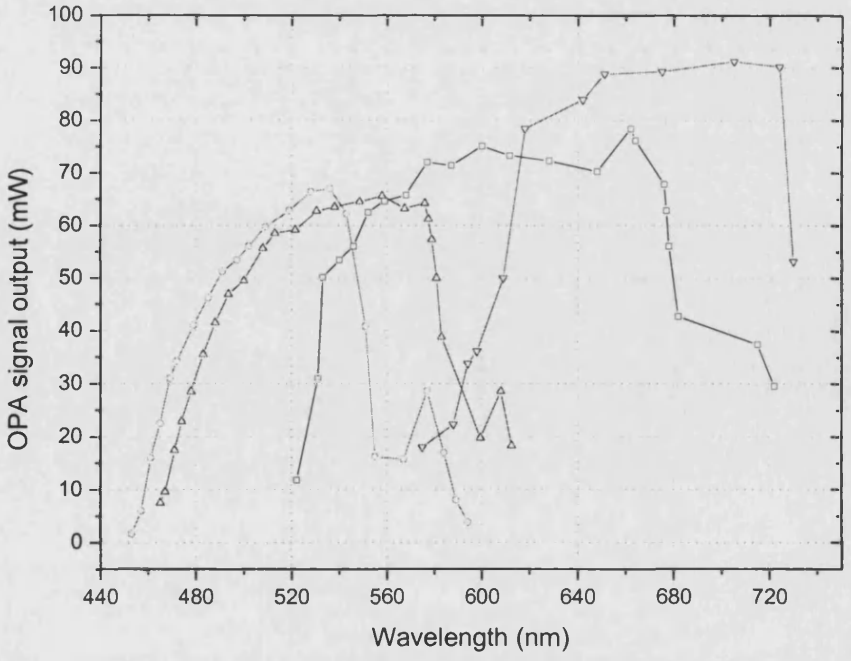

Figure 4.7: OPA output across the visible spectrum. The four lines represent the four output couplers required to span the entire visible spectral region.

4.6.2 Photodetector – Streak Camera

The photodetector used in the experiments described in this chapter was a streak camera (Hamamatsu C4334). The imaging properties and temporal resolution afforded by the streak camera have found widespread applications in photochemistry [21], medical physics [22] and semiconductor research [23].

The basic principle of streak camera operation is depicted in figure 4.8. The fluorescence signal with time profile I(t) passes through a slit and is focussed onto a photocathode, producing a pulse of photoelectrons $N_{PE}(t)$ such that $N_{PE}(t) \propto I(t)$ [24]. The photoelectrons are accelerated further into the camera by an electric potential towards a pair of deflection electrodes. An optical trigger initiates a rapid (increasing) voltage sweep across the electrodes resulting in a linear (vertical) displacement of photoelectrons with time. This vertical spread of photoelectrons is incident upon a microchannel plate (MCP) detector, amplified and transferred to a phosphor screen; the resultant phosphorescent signal is recorded by a video camera. If the fluorescence signal is spectrally dispersed across the entrance slit of the streak camera a two-dimensional wavelength-time image of the fluorescence is recorded. This feature is not used in the current setup; integration over the vertical axis of the streak camera signal allows total intensity measurements to be made. The horizontal axis is employed for imaging the STED process (section 4.6.3.9).

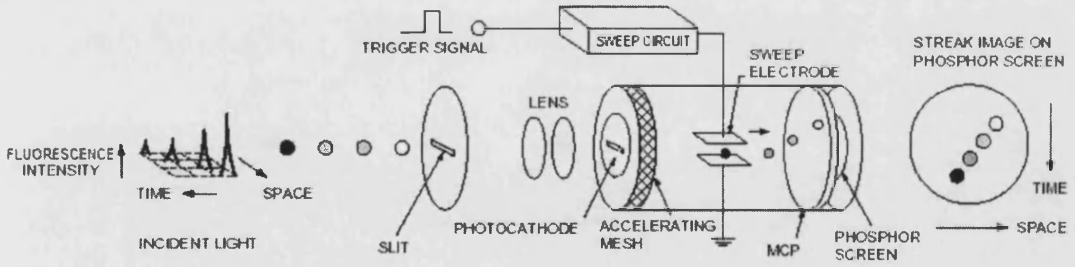

Figure 4.8: Operating principle of the streak camera. Fluorescence photons incident upon the photocathode produce photoelectron signals which are deflected by differing amounts by a rapid voltage sweep onto a phosphor screen which is recorded by a video camera, resulting in a two-dimensional streak image. {Original illustration from "Guide to Streak Cameras", *Hamamatsu Photonics K.K.*, (2002)}

For the experiments described in this chapter, a split was taken from the 800nm PUMP beam into a fast photodiode (Hamamatsu C1808); the photodiode signal was electronically delayed to provide the trigger input to initiate the voltage sweep at the streak camera.

4.6.3 Experimental Setup

In order to investigate STED from two-photon excited states it is first necessary to overlap the PUMP and DUMP beams in space at the sample and then introduce a known time delay between the two beams. The next section describes the steps necessary to achieve spatial and temporal beam overlap.

4.6.3.1 Spatial Overlap (I)

Spatial beam overlap was achieved using a coated optical element that would yield one output beam from the two inputs, as illustrated in figure 4.9.

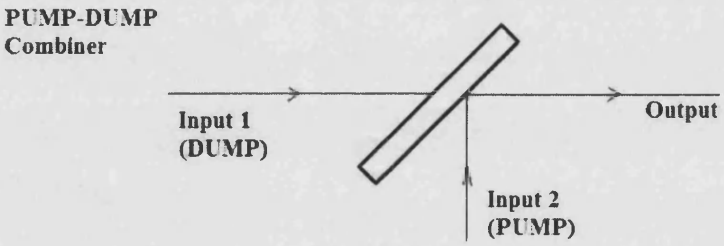

Figure 4.9: A PUMP-DUMP combiner would have to reflect and transmit a two-colour signal for successful combination prior to arrival at the sample.

It was preferable for the combining optic to reflect the 800nm PUMP, since transmission through the element would cause unwanted stretching of the pulse. By contrast, any increase in the DUMP pulse width by transmission through the optic was favourable in minimising re-pumping of S_1 following STED (section 4.6.3.4).

A coated optical element from CVI Optics provided the necessary conditions for beam combination. The element was a broadband dichroic beam combiner reflective in the wavelength range 750-850nm and transparent from 400-700nm, optimised for use at 45°. The broad transparency range allowed for the necessary variation in DUMP wavelength between different chromophores.

Beam overlap was first approximated by eye (using an IR viewing card for the PUMP) at the beam combiner; the PUMP and DUMP beams were then overlapped in the far field by reflection to a point several metres away. By making alternate and successive iterative beam alignments at the combiner and in the far field, the PUMP and DUMP beams were matched for collinear propagation.

4.6.3.2 Temporal Overlap (I)

In order to observe significant STED from the two-photon prepared excited state it is necessary to introduce the DUMP pulse to the sample when there is still a significant excited state population to deplete. This sets some conditions for the arrival of the DUMP pulse in time relative to two-photon excitation by the PUMP:

Condition 1: The DUMP pulse must arrive at the sample after the PUMP for STED to occur.

Condition 2: For optimal excited state population removal, the DUMP pulse should arrive within ~1 fluorescence lifetime of the experimental sample. At one fluorescence lifetime after excitation the excited state population will have reduced in number to 1/e of its original value (i.e. approximately 37% of the original population available for depletion). If the DUMP pulse arrived later than this there may be insufficient excited state molecules to make initial observations of STED even if the beams are overlapped spatially.

The fluorescence lifetimes of the chromophores used in this experiment vary between 0.6 and 3.2ns (table 4.2). The boundary conditions stated above therefore give a temporal "window of incidence" for the DUMP pulse to arrive, that is, within a fluorescence lifetime of the PUMP pulse. The temporal "window of incidence" can be transformed into a spatial window (or path length difference) between the two beams. For example, for a sample with a fluorescence lifetime of 1.7ns the allowed path length difference between splitting (at the RegA beamsplitter) and recombination (at the beam combiner) that satisfies the boundary conditions above is 51cm.

Chromophore	Solvent	Typical Fluorescence Lifetime (ns)
Fluorescein Sodium Salt	Ethylene Glycol	1.7±0.1
Rhodamine 6G	Ethylene Glycol	2.2±0.1
Coumarin 153	Ethylene Glycol	3.2±0.1
OM62	Toluene	0.6±0.1
LP79	Toluene	0.8±0.1

Table 4.2: Typical fluorescence lifetimes at room temperature of the chromophores used in this chapter

It was also necessary to take into account the extra path length taken by the DUMP pulse through the OPA, measured at 1.8m. This allowed a first approximation path length match to be estimated but in order to make fine adjustments to the path lengths it was necessary to utilise a delay line. To this end the DUMP beam path incorporated a retro-reflector positioned on a variable 1.08m delay line (Time and Precision).

Another factor which must be taken into consideration when attempting a temporal overlap of the beams is the effect of the pulse stretcher.

4.6.3.3 Stretching the DUMP Pulse

The importance of having a DUMP pulse long enough to allow ground state vibrational relaxation to occur following STED was discussed in section 4.3. The effect of wavelength conversion by optical parametric amplification is not insignificant, with typical visible OPA pulsewidths in the region of 300fs compared to the 800nm compressed RegA output pulse widths of approx. 140fs. However in order to increase the efficiency of STED it is necessary to stretch the DUMP pulses still further; to this end a pulse stretcher was constructed and placed in the DUMP beam path.

The pulse stretcher consisted of a 20cm cylindrical cell filled with distilled water with optically transparent quartz end faces. Upon passage through the cell the DUMP pulse width was increased from 300fs-850fs (the exact pulse widths depend upon the DUMP wavelength chosen).

The pulse stretcher utilises the group velocity dispersion (GVD) property of light travelling through a medium [25]. The group velocity (v_g) of a light pulse is given by

$$v_g = \frac{d\omega}{dk} \qquad [4.27]$$

where ω and k are the angular frequency and wave number respectively of the light. When an optical pulse with a spectral amplitude distribution $E(\omega)$ propagates through a medium with refractive index $n(\omega)$, its temporal profile will change because its group velocity shows a dispersion as

$$\frac{dv_g}{d\omega} = \frac{dv_g}{dk} \Big/ \frac{d\omega}{dk} = \frac{1}{v_g} \frac{d^2\omega}{dk^2} \qquad [4.28]$$

For $d^2\omega/dk^2 \neq 0$, the velocity of the different frequency components varies with frequency. This means that different parts of the pulse experience different refractive indices and therefore the temporal envelope of the pulse changes with propagation. For the case of the water cell, the pulse becomes broader and chirped, with the red parts of the pulse propagating more quickly than the blue parts [26].

An additional effect of the pulse stretcher is to increase the effective path length of the DUMP beam. As a rough approximation, a 20cm passage through the water cell (n_{WATER}=1.33) [27] is equivalent to a passage through air of $n_{WATER}/n_{AIR}.20cm \approx 27cm$ (where $n_{AIR} \approx 1$). Although this extra distance is not significant compared with the 75cm initial error margin, the effects of the cell (both in terms of stretching and beam length) become more important when multiple passes are made.

4.6.3.4 Selection of the DUMP Wavelength

For effective two-photon STED, it is necessary to select DUMP wavelengths within the emission region of the fluorescent molecule for which there is a low cross-section for single and two-photon absorption. For example, Rhodamine 6G has a broad emission spectrum with detectable fluorescence spanning approx. 540-700nm. Although the peak of the emission spectrum in ethylene glycol was measured at 552nm, there is still considerable single-photon absorption at this wavelength (approx. 16% of the extinction at the 530nm absorption maximum [28]). Rhodamine 6G also possesses a significant two-photon absorption cross-section at wavelengths close to the near infra-red region (approx. 1.5×10^{-48} $(cm^4 s)$/photon at 700nm [29]). To minimise the effects of single and two-photon background fluorescence, the DUMP pulse is therefore restricted to a region between these two extremes, as illustrated in figure 4.10. In the case of Rhodamine 6G, a DUMP wavelength range of 614nm to 663.5nm was chosen; at 614nm the fluorescence intensity is 28% of the peak at 552nm, but the single-photon extinction coefficient at this wavelength is less than 0.1% of the maximum value.

By choosing a DUMP field region at the "red" end of the emission spectrum, it is necessary to utilise short-pass interference filters to block scattered DUMP laser light rather than conventional long-pass glass filters. Fluorescence was measured towards the blue end of the emission spectrum.

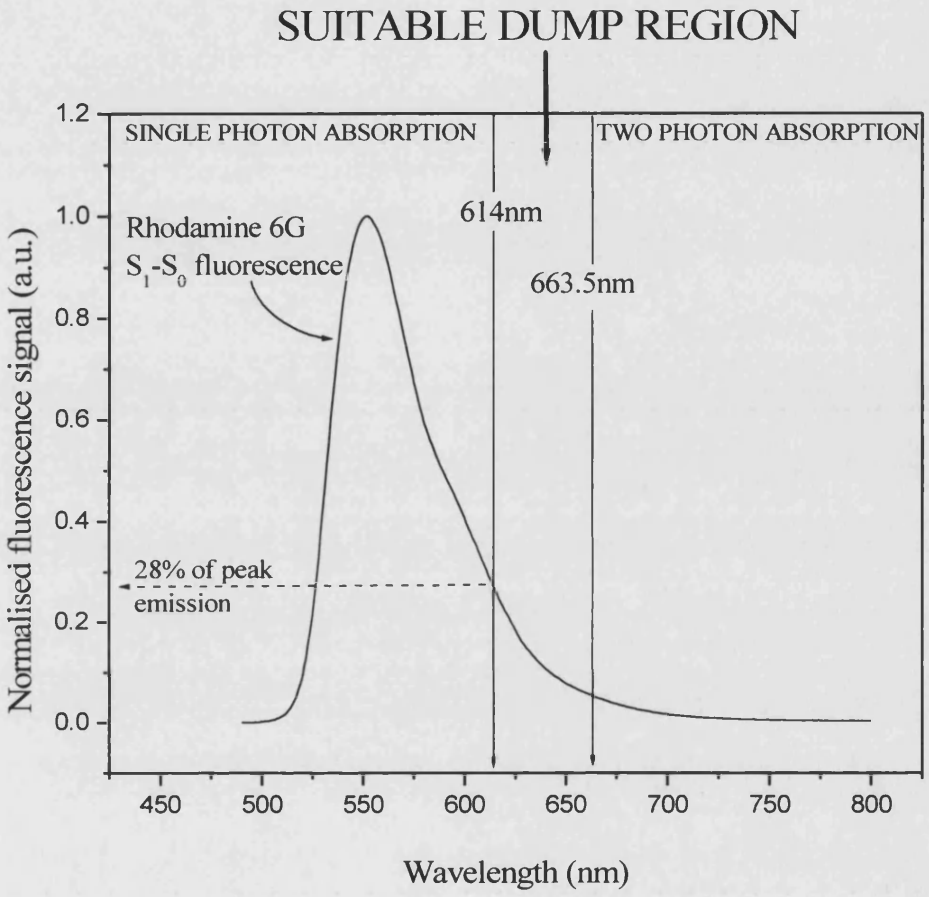

Figure 4.10: The DUMP wavelength was selected to avoid unwanted single photon or two-photon absorption of the DUMP pulse. For Rhodamine 6G, this restricts the DUMP to the spectral region spanning 614-663.5nm.

4.6.3.5 Optical Layout

The optical layout for the PUMP and DUMP to the experimental sample is illustrated in figure 4.11. By varying the number of passes made through the pulse stretcher (i.e. zero, 1, 3 or 5 passes) the DUMP pulse width could be spanned between 300fs and 3.2ps. For each extra pass through the pulse stretcher the PUMP path length was adjusted accordingly to match the additional propagation.

PUMP and DUMP polarisations were controlled using broadband half wave plates and cube polarisers (Melles Griot). PUMP and DUMP powers were controlled by neutral density wheels (Melles Griot, NDW in figure 4.12) and measured by a precision power meter (Anritsu). Mechanical shutters were placed in the PUMP and DUMP beam paths to allow experimental control of the excitation and depleting fields; the ability to toggle the fields off and on is particularly useful for initial observations of STED (section 4.6.3.7) and necessary for background measurements of DUMP-induced fluorescence.

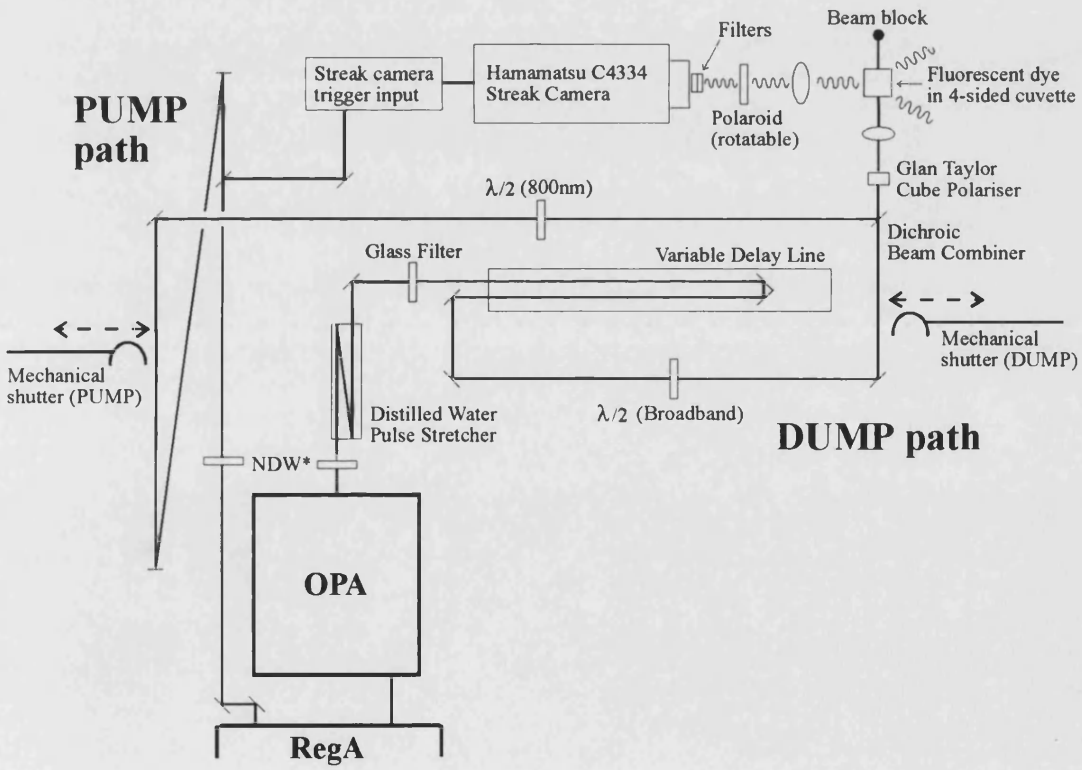

Figure 4.11: Schematic diagram of the PUMP and DUMP beam paths.

In order to ensure that no white light or blue edge remnants remained in the DUMP pulses, a long pass glass filter (Schott) was placed in the DUMP beam prior to recombination with the PUMP.

4.6.3.6 Excitation-Detection Geometry

Determination of the stimulated emission cross-sections and ground state relaxation times using STED was carried out using an orthogonal excitation-detection geometry, as illustrated in figure 4.12.

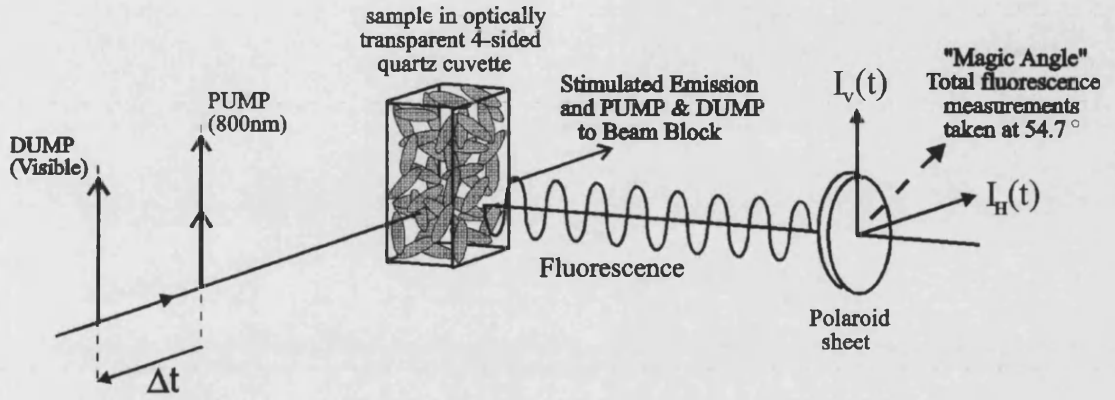

Figure 4.12: A right-angle excitation-detection geometry was used, with fluorescence measurements taken at polarisation angles of 0°, 90° and 54.7°.

The photons produced by stimulated emission are necessarily identical to those of the DUMP pulse. Measurements of STED spectra via polarisation gain in the DUMP field in a collinear geometry have been made for gas phase molecules [1]; such techniques require a crossed polarisation geometry and, whilst yielding high resolution spectral information, are not suited to measurements of STED cross-sections and ground state relaxation times.

The detection of STED and the measurement of population change in the excited state are best undertaken using fluorescence depletion measurements. A 90° excitation-fluorescence detection geometry is well suited to this purpose; contamination of the signal from the PUMP and DUMP fields is minimised and unlike the collinear excitation-detection experiments described in Chapter 3, there is no need to introduce a beam block into the fluorescence path.

4.6.3.7 Temporal overlap (II)

With the beams temporally and spatially overlapped, the sample was introduced into the experimental setup. The sample consisted of the dye in solution (approx. 10^{-4}M) stored in a fluorescence cuvette with four optically clear faces (Hellma). Fluorescence was collected and focussed into the streak camera detector using a 5cm focal length lens. A Polaroid sheet mounted in a precision rotation stage (Melles Griot) was situated before the streak camera to allow polarisation control of the detected fluorescence.

Two-photon fluorescence was observed as a vertical streak as shown in figure 4.13a. The DUMP field was then introduced by opening the mechanical shutter and scanned using the delay line in steps of 1ns; when the DUMP pulse was scanned to arrive after excitation by the PUMP, an abrupt reduction in the fluorescence signal was observed, as shown in figure 4.13b.

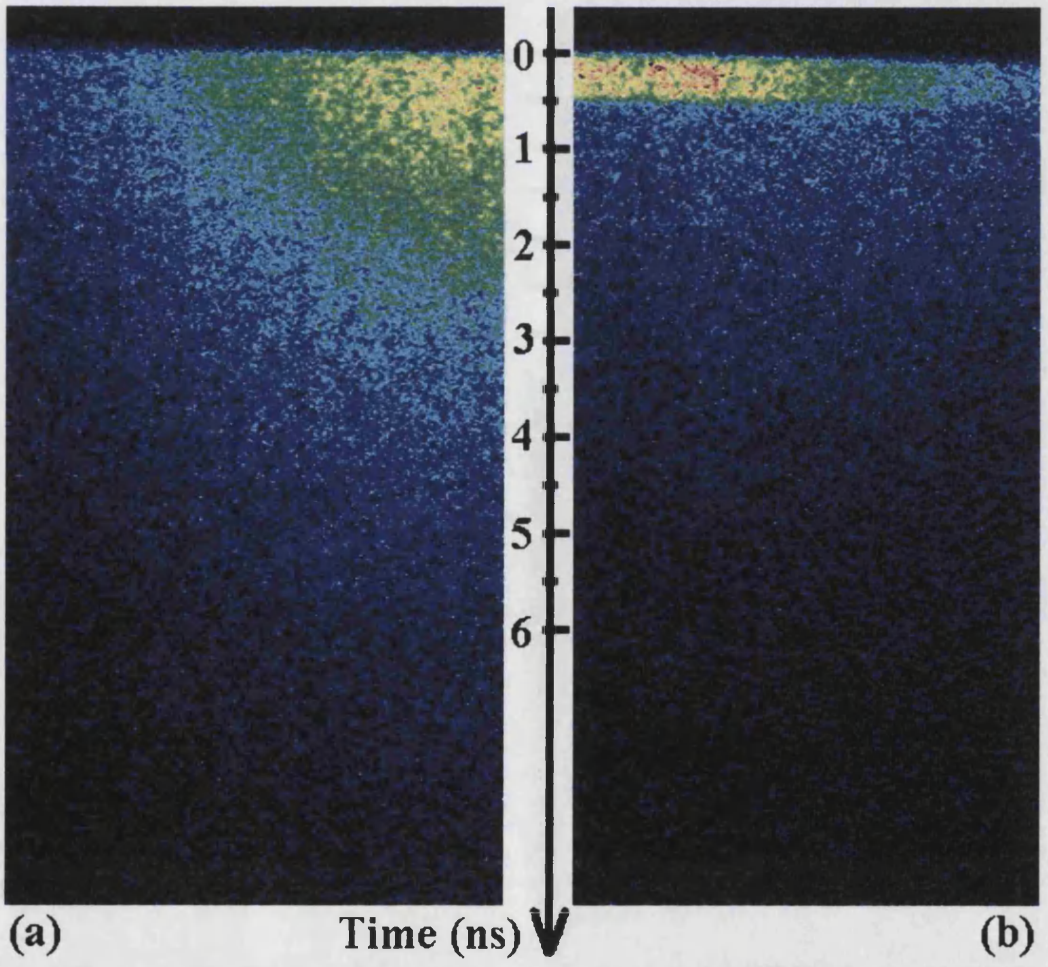

Figure 4.13: Composite diagram of the streak camera signal for (a) DUMP off and (b) DUMP on. Fluorescence strength is indicated by colour, with the highest intensities shaded red and lowest intensities by blue or black. The vertical axis represents time. The presence of STED is manifested by an abrupt reduction in the fluorescence signal. In figure (b), the DUMP pulse arrives approximately 500ps after excitation by the PUMP.

Fluorescence depletion by stimulated emission was used to obtain a more accurate temporal overlap between the PUMP and DUMP beams. The precision of the temporal overlap was improved by scanning the delay line back and forth over the region of zero path difference (thereby observing the abrupt increase or decrease in fluorescence) in progressively smaller scan steps; the smallest scan step corresponds to a 3.4fs time difference, over two orders of magnitude shorter than the DUMP pulse.

The effect of the depleting field can be demonstrated in more detail by scanning the DUMP pulse through the region of zero path difference with respect to the PUMP in small scan steps, as illustrated in figure 4.14. In this example the signal strength from fluorescence has been measured as a function of the PUMP-DUMP delay for fluorescein in methanol: the DUMP field, with a pulse width of 1.75ps (assuming a Gaussian temporal profile), was scanned 5ps either side of the PUMP excitation.

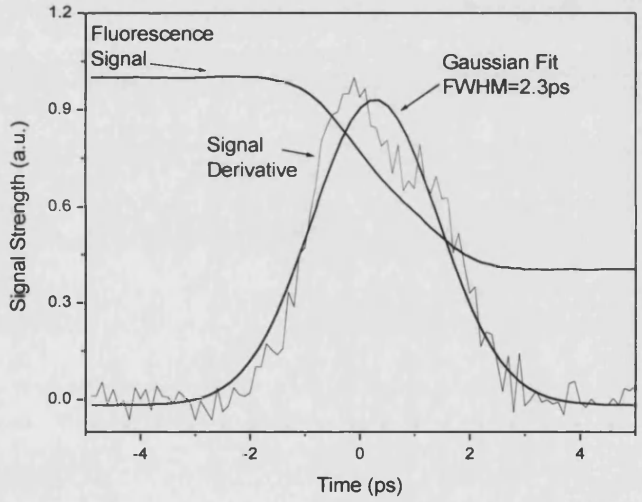

Figure 4.14: Variation in the total fluorescence emission from fluorescein in methanol as a function of PUMP-DUMP delay. The "rise time" of the depletion is compatible with the DUMP pulse width; differentiation of the signal yields an approximate Gaussian whose width is compatible with that of the DUMP pulse autocorrelation.

In this example, the DUMP is scanned through the region of zero path difference initiating STED, and the total fluorescence signal is seen to drop to approximately 50% of the undumped value sharply over 2ps. Differentiation of the transient can be approximated by a Gaussian function of comparable width to the 1.75ps dump pulse.

At longer dump delays than displayed in the figure above, the depletion efficiency was seen to decrease on a timescale compatible with nanosecond spontaneous emission losses and orientational relaxation within S_1.

Optimisation of temporal overlap was carried out using parallel vertically polarised PUMP and DUMP beams ("V-V" configuration) with the Polaroid sheet rotated to allow the maximum fluorescence signal (and hence maximum depletion) to the streak camera.

4.6.3.8 Spatial Overlap (II)

The spatial overlap between the PUMP and DUMP beams could also be adjusted for maximum depletion using the imaging properties of the streak camera. With the DUMP path closed, the PUMP power was set to maximum value (approx. 8mW). This corresponds to a peak power at the beam waist of approx. $1.3 \times 10^{11} Wcm^{-2}$, which is sufficient to initiate multi-photon processes such as excited state absorption and/or photobleaching to occur at the beam waist [13] and a reduction in $S_1 \rightarrow S_0$ fluorescence. This is manifested by a dark central spot on the streak image, as illustrated in figure 4.15. By adjusting the distance of the focussing lens from the sample, the dark central area could be translated across the imaging region. Scanning the waist across the entire streak image could be achieved by adjusting the focal point of the focussing lens using a precision translation stage (Melles Griot); this yielded a total imaging region of approx. 400μm. Centralising the "dark" area verified that the streak camera was imaging the beam waist.

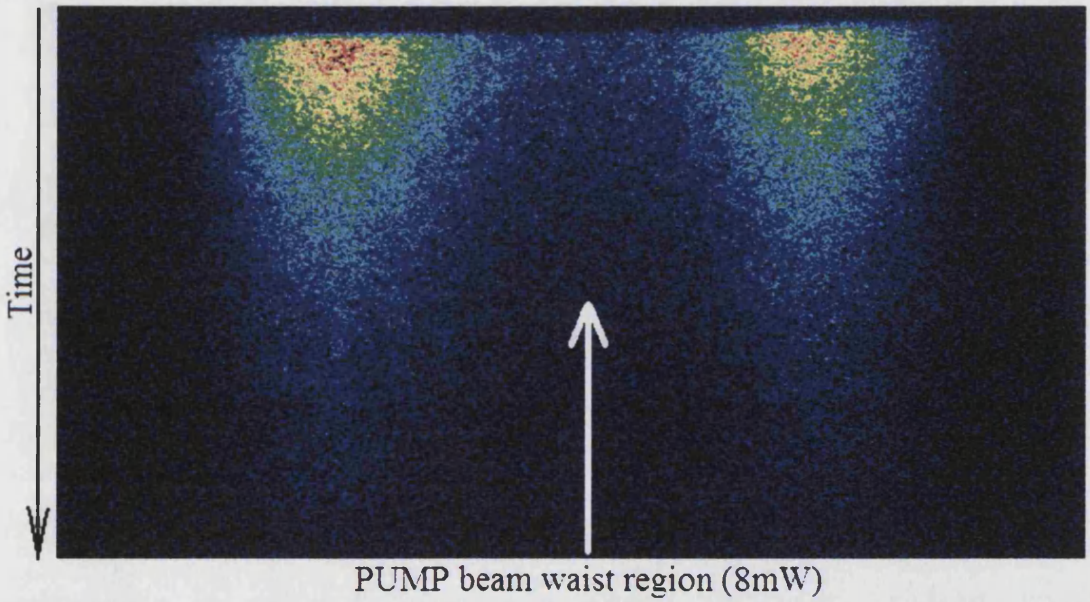

Figure 4.15: Streak camera image of PUMP-excited two-photon fluorescence for a PUMP power of 8mW. The non-radiative energy loss at the beam focus results in a dark central area, ideal for locating the beam waist.

Having identified and imaged the PUMP beam waist, the 800nm signal was reduced to a value below the threshold for non-radiative energy loss to yield a Gaussian spatial distribution with no dark central region. The next step was to ensure that the DUMP focus overlapped the PUMP waist for maximum depletion.

Obtaining a spatial overlap of the PUMP and DUMP beams by reflection to the far field yields a first approximation to the beam overlap. However the PUMP and DUMP wavelengths were sometimes spectrally over 200nm apart. Despite using a 2.5cm achromatic doublet to focus the beams into the sample, such a PUMP-DUMP separation may have caused some chromatic aberration; that is, the DUMP waist may not correspond spatially to the 800nm waist. If the PUMP and DUMP beams had slightly different divergences, this may also result in different foci. By adjusting the final mirror in the DUMP path (prior to combination with the PUMP), the level of depletion at the PUMP beam waist could be maximised. This way, any difference in beam divergence or chromatic aberration at the focussing lens could be compensated using spherical aberration and/or astigmatism.

4.6.3.9 τ_{20} Determination

The fluorescence depletion efficiency is dependent upon the orientation of the excited state molecules (section 4.4, equation 4.19). Since the STED experiments described in this chapter are concerned with depletion from distributions after any solvent relaxation, the PUMP-DUMP delays for the STED experiments described in this chapter were set to lie in the range of 33-650ps to ensure complete solvent relaxation to equilibrium following solute excitation (sub-picosecond to picosecond timescales), and in doing so, the effect of orientational relaxation of dye molecules within S_1 upon STED could not be ignored. It was therefore necessary to establish a value for the re-orientational lifetime of the experimental chromophore; this could be achieved by using the streak camera as a time resolved detector. By blocking the DUMP beam with the mechanical shutter, the apparatus could be used for "conventional" polarised two-photon excitation. The re-orientational lifetimes of the samples were determined by two-photon excitation by a vertically polarised PUMP: fluorescence was detected at 0° ($I_V(t)$) and 90° ($I_H(t)$) and as discussed in Chapter 1, the fluorescence anisotropy $R(t)$ was constructed from

$$R(t) = \frac{I_V(t) - I_H(t)}{I_V(t) + 2I_H(t)} \qquad [4.29]$$

Determination of τ_{20} was achieved by fitting R(t) to a single exponential.

4.7 Experimental Procedure

The experiments described in this chapter explore how STED from a two-photon excited molecular population is affected by a visible depleting field, and how the level of STED depends upon DUMP energy for various DUMP wavelengths and pulse widths. The DUMP pulse energy was controlled and varied using a neutral density wheel. The other experimental variables were controlled as follows:

i) **PUMP power** was controlled using a neutral density wheel in the 800nm beam path. Before each experiment began, the PUMP power was reduced to yield an even Gaussian spatial excitation region. Typically PUMP powers below 30nJ yielded a sufficient S_1 population without inducing unwanted multi-photon processes [13]

ii) The **DUMP pulse width** was controlled by the number of passes made through the distilled water pulse stretcher cell. For a given number of passes and constant DUMP wavelength, the DUMP pulse width was kept constant.

iii) The **DUMP wavelength** was kept constant for each individual experiment, but could be adjusted at the OPA for wavelength dependence studies.

iv) The **PUMP-DUMP delay** was controlled at the delay line and was kept constant during each experiment but kept sufficiently long to be outside the temporal region over which solvent reorganisation could take place [30].

All of the measurements utilised the "V-V configuration" vertically polarised PUMP and DUMP beams. Having established a value for τ_{20}, "magic angle" total fluorescence intensity measurements were made by setting the Polaroid sheet to 54.7° with respect to the laboratory Z-axis.

Since the fluorescence lifetimes of the chromophores were in the region of 0.6-3.2ns, a streak camera temporal window of 10ns or 20ns was typically employed. A spatial window (region of interest, or ROI) was chosen such that the ROI enclosed the beam waist where STED had been maximised (preparatory procedure II). The level of depletion would be averaged spatially over the ROI; it was found that an ROI of 150-200 pixels (approx. 120-160μm) represented the optimum window for averaging, over which a constant level of excitation and depletion was observed. This compares favourably with the Rayleigh range of the PUMP beam of approx. 200μm (for a beam area measured at $1.77 \times 10^{-6} cm^2$ and 800nm wavelength).

Using just the PUMP, spatial averaging over the ROI yielded a temporal profile of the fluorescence decay without STED (the "undumped" decay). Using both PUMP and DUMP, several temporal profiles of fluorescence with varying amounts of depletion were obtained for varying DUMP energies. For each DUMP energy it was also necessary to obtain a "background" two-photon excitation (TPE) signal from the DUMP only. In summary, the profiles taken to conduct an experiment are outlined in table 4.3:

Beams ON (energy)		Polaroid setting	Purpose
PUMP	-	0°, (vertical)	Two preliminary readings used to establish τ_{20}
PUMP	-	90°, (horizontal)	
PUMP	DUMP (1)	54.7° ("magic angle")	Highest DUMP energy & corresponding DUMP TPE background signal
-	DUMP (1)	54.7° ("magic angle")	
PUMP	DUMP (2)	54.7° ("magic angle")	As above, DUMP energy reduced to 2/3 of previous setting
-	DUMP (2)	54.7° ("magic angle")	
Process repeated for progressively lower DUMP energies until			
PUMP	DUMP (N)	54.7° ("magic angle")	Lowest DUMP energy, yielding N dumped traces and background signals
-	DUMP (N)	54.7° ("magic angle")	
PUMP	-	54.7° ("magic angle")	"undumped" fluorescence, no STED

Table 4.3: Experimental procedure summary for the STED DUMP energy dependence studies

4.8 Data Processing

An experiment using N DUMP energies yielded a maximum of (2N+1) temporal "magic angle" fluorescence profiles: N dumped signals, N background signals of TPE from the DUMP beam and one undumped fluorescence decay from the PUMP only. The first step in profile analysis was the subtraction of background DUMP-induced two-photon fluorescence, as illustrated in figure 4.16.

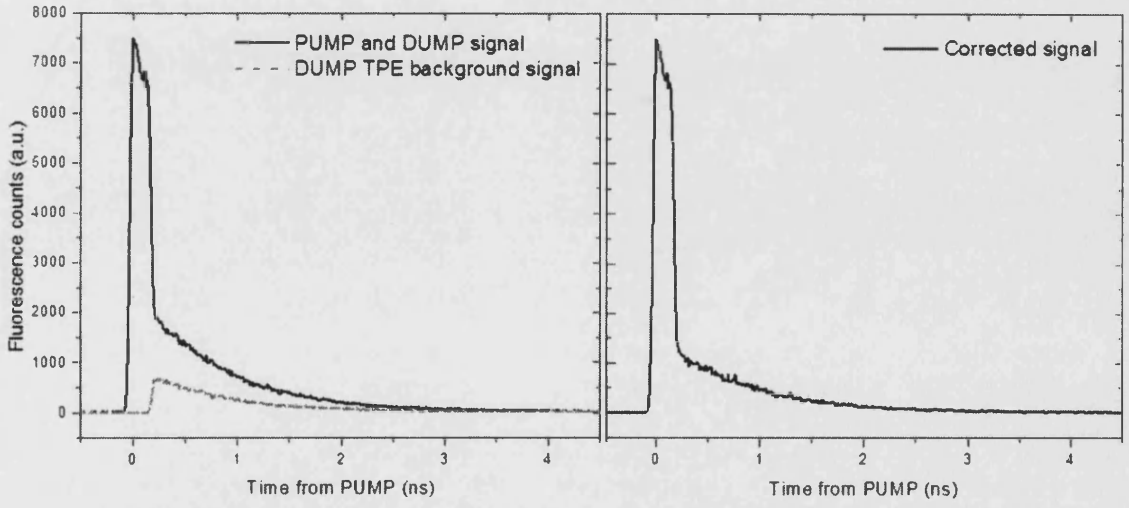

Figure 4.16: (a) Depletion in OM62 fluorescence from a 3.2ps, 10.5nJ DUMP pulse arriving 200ps after excitation from the PUMP and the corresponding background two-photon excitation signal from the DUMP. (b) Background signal subtraction yields the corrected STED fluorescence signal.

Subtraction of the DUMP-induced two-photon fluorescence yields a set of temporal profiles with varying excited state population removal corresponding to varying DUMP energies. Figure 4.17 shows corrected profiles for STED in Coumarin 153 in Ethylene Glycol, with DUMP energies varying from 0nJ (i.e. undumped) to 28.8nJ.

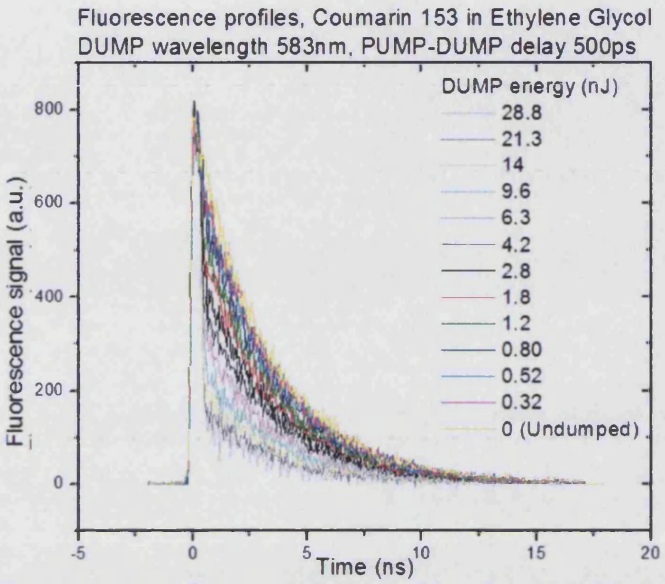

Figure 4.17: STED fluorescence profiles for Coumarin 153 in Ethylene Glycol. The depletion level increases with DUMP energy; the onset of transition saturation is seen for higher DUMP energies.

In order to find the fractional excited state population removed ($1-F_R(t)$) by a DUMP pulse with energy N, the intensity profile $I_N(t)$ was adjusted according to

$$1 - F_R = \frac{I_0(t) - I_N(t)}{I_0(t)} \equiv F_D \qquad [4.30]$$

where $I_0(t)$ refers to the undumped fluorescence profile. A set of ($1-F_R(t)$) profiles for five different DUMP energies in the Coumarin 153 data is shown in figure 4.18.

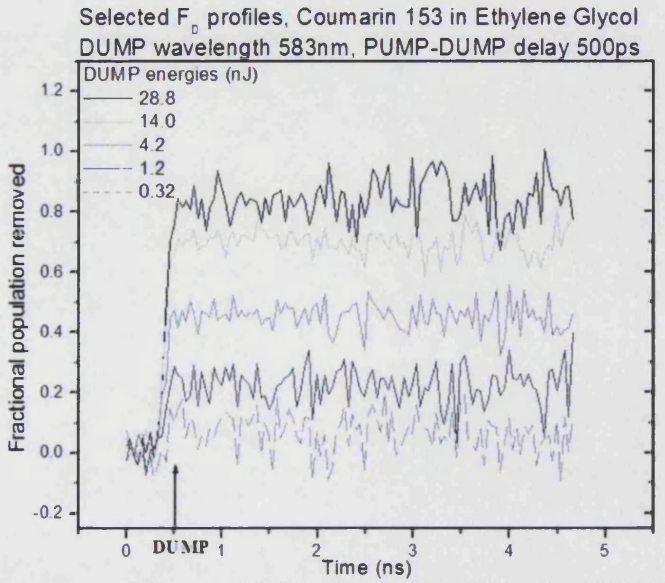

Figure 4.18: Time dependent profiles of STED in Coumarin 153 for five DUMP energies.

By averaging (1-F_R) over several nanoseconds a value for the fractional removal of excited state molecules for a given DUMP energy could be obtained. A plot of the values of (1-F_R) against DUMP energy for the Coumarin 153 example is shown in figure 4.19.

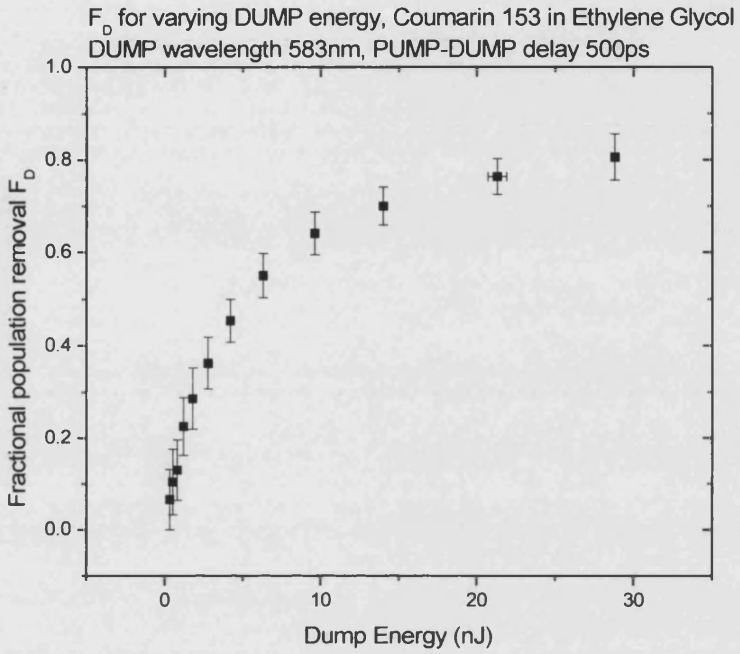

Figure 4.19: Fractional population removal 1-F_R as a function of DUMP energy in Coumarin 153.

4.9 Data Analysis

Having obtained an experimental saturation curve for the population removal from STED for a molecular probe, it was possible to fit the empirical data to numerical solutions to the coupled rate equations illustrated in figure 4.5.

Although the simulations predict the behaviour of 1-F_R for varying S, the experimental data describes 1-F_R in terms of the DUMP energy E; it was therefore necessary to calibrate the simulations in terms of $E = Sh\nu A/\sigma$ rather than S.

Step 1

The first step in the data analysis was to generate a family of simulated curves with wide ranging values of ratio τ_P/τ_R. Continuing the example from the section 4.8, figure 4.20a shows the experimental data showing $1\text{-}F_R$ in Coumarin 153 in Ethylene Glycol for varying DUMP energy E. Overlaid on this data is a family of numerical solutions for $1\text{-}F_R$ with S varying from 0 to 12; each curve has a different ratio τ_P/τ_R, with values ranging from τ_P/τ_R=0.25 to τ_P/τ_R=50.

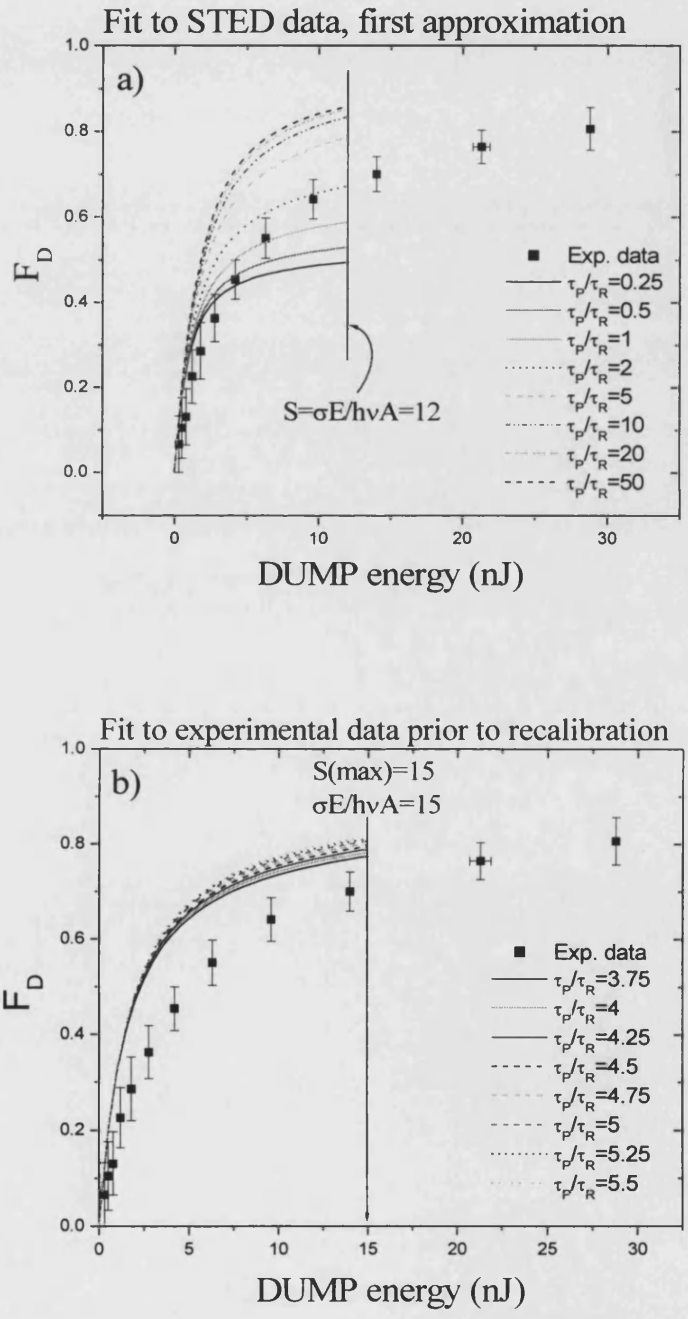

Figure 4.20: (a) The first approximation to a numerical solution to fit the experimental data used a wide range of values of τ_P/τ_R. From this, a second set of numerical solutions with a narrower range of τ_P/τ_R could be generated. (b) S could be calibrated to DUMP energy E.

This first approximation shows that the true value of τ_P/τ_R is in the region of 1-5, and that the current calibration between S and E is not correct, since the simulations do not fit the linear part of the data curve.

Step 2

Figure 4.20b shows a new family of simulations for S varying from 0 to 15, with τ_P/τ_R ratios of 3.75, 4, 4.25, 4.5, 4.75, 5, 5.25 and 5.5. Knowing that the final point on the simulations corresponds to a value for S of 15, the curves can be re-calibrated with respect to DUMP energy (x-axis in figure 4.20) until one of the curves fits the linear part of the experimental data. This is shown in figure 4.21, where a τ_P/τ_R ratio of 4.75 and an S of 15 corresponding to a DUMP energy of 32.23nJ matches the data.

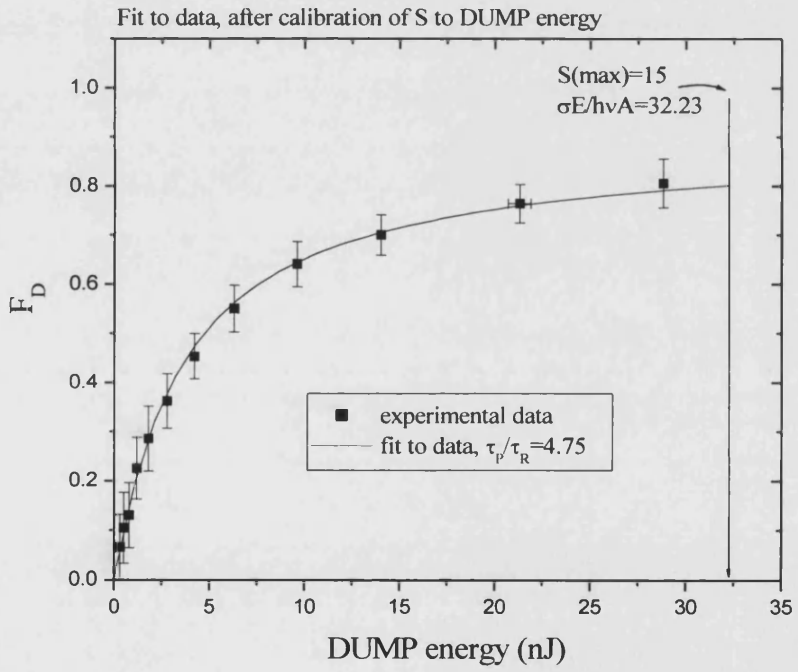

Figure 4.21: A numerical solution to the coupled rate equations shows a good fit to the Coumarin 153 experimental data with τ_P/τ_R equal to 4.75 and an S of 15 corresponding to a DUMP energy of 32.23nJ. The linear part of the fit can be used to establish a value for the stimulated emission cross-section, while the non-linear portion is used to gain information on the ground state vibrational relaxation lifetime.

Step 3

Re-arranging the relationship between S and DUMP energy described in section 4.4 means that the stimulated emission cross-section for a chromophore can be found from

$$\sigma = \frac{Sh\nu A}{E} \qquad [4.31]$$

In the Coumarin 153 example, a DUMP wavelength of 583nm was chosen, yielding a stimulated emission cross-section as follows:

S=15,
$h\nu=34.14\times10^{-20}$J,
$A=1.77\times10^{-6}cm^2$ and
$E=32.23\times10^{-9}$J yields → $\mathbf{\sigma_{STIM}(Coumarin\ 153)=2.81\times10^{-16}cm^2}$.

For the Coumarin data, a simulation with a pulse width to relaxation time ratio of $\tau_P/\tau_R=4.75$ provided the best fit. In this case, the pulse width was measured as 1.2ps, yielding the ground state vibrational relaxation time for Coumarin 153 in Ethylene Glycol:

$$\mathbf{\tau_R(Coumarin\ 153) = 1.2/4.75 = 254fs}.$$

4.10 Results

In addition to the Coumarin 153 data described in the previous section, total fluorescence intensity measurements following STED were made for Fluorescein in ethylene glycol, Rhodamine 6G in ethylene glycol, OM62 in toluene and LP79 in toluene. DUMP energy dependence measurements were made for varying DUMP pulse widths and DUMP wavelengths.

4.10.1 DUMP Pulsewidth Dependence

The chromophores studied in the STED DUMP pulsewidth dependence experiments are summarised in table 4.4.

Chromophore	DUMP pulse widths	DUMP wavelength (nm)	P-D delay (ps)
Fluorescein	0.71ps, 1.45ps, 2.5ps	580	33ps
OM62C	1.15ps, 3.2ps	535	200ps
LP79	1.23ps, 3.2ps	595	200ps

Table 4.4: Summary of the DUMP pulsewidth dependence experiments

Figures 4.22-4.24 show fits to experimental data for the population removal from STED in Fluorescein, OM62 and LP79 for different DUMP pulse widths.

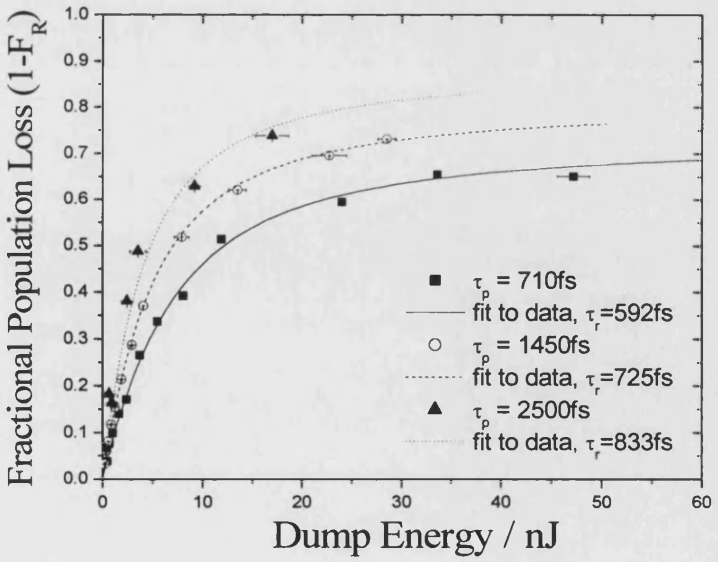

Figure 4.22: Fractional population removal for fluorescein in ethylene glycol as a function of DUMP energy for DUMP pulse widths of 700fs, 1.45ps and 2.50ps.

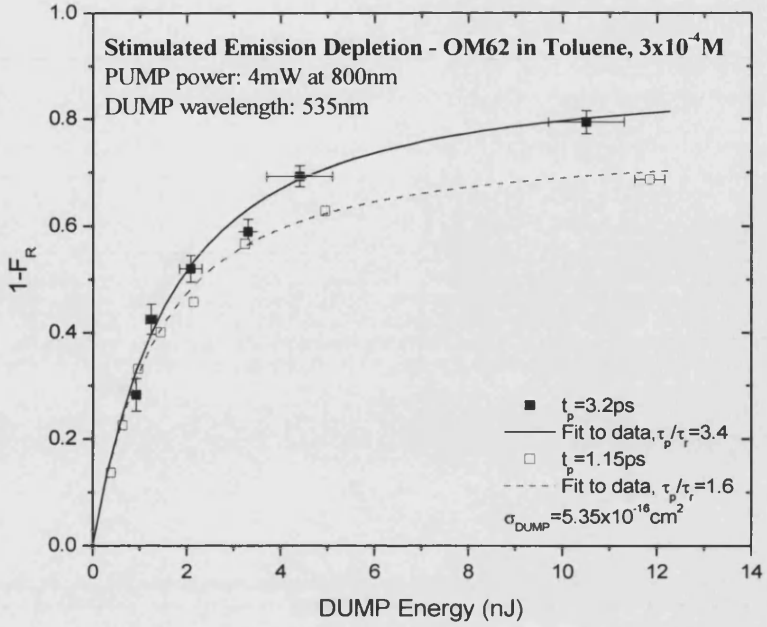

Figure 4.23: Fractional population removal for OM62 in toluene as a function of DUMP energy for DUMP pulse widths of 1.15ps and 3.20ps.

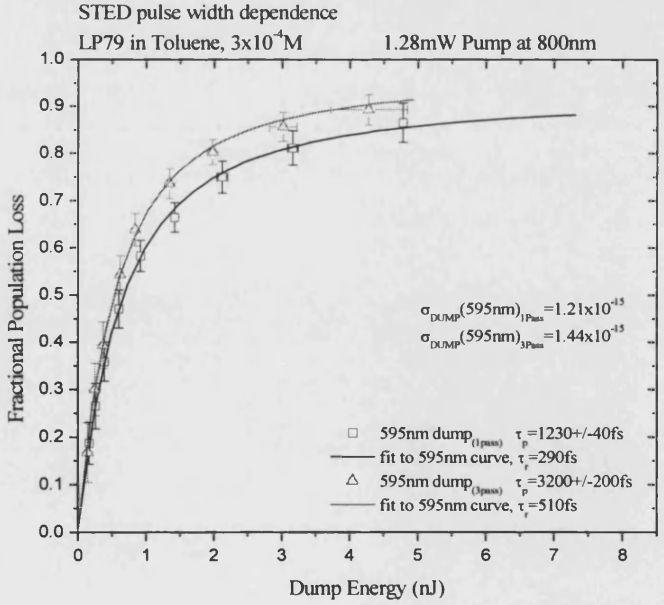

Figure 4.24: Fractional population removal for LP79 in toluene as a function of DUMP energy for DUMP pulse widths of 1.23ps and 3.20ps.

The best fits of the experimental data yield values to the stimulated emission cross-section for the DUMP transition (σ) and the ground state vibrational relaxation time (τ_R). The values of σ and τ_R are summarised for the three chromophores in table 4.5.

OM62 in Toluene

DUMP Pulse Width (ps)	Stimulated Emission Cross-Section ($x10^{-16}cm^2$)	Ground State Vibrational Relaxation Lifetime (fs)
1.15	5.35	719
3.20	5.35	941

LP79 in Toluene

DUMP Pulse Width (ps)	Stimulated Emission Cross-Section ($x10^{-16}cm^2$)	Ground State Vibrational Relaxation Lifetime (fs)
1.23	12.1	290
3.20	14.4	510

Fluorescein in Ethylene Glycol

DUMP Pulse Width (ps)	Stimulated Emission Cross-Section ($x10^{-16}cm^2$)	Ground State Vibrational Relaxation Lifetime (fs)
0.71	2.32	592
1.45	3.55	725
2.50	5.10	833

AVERAGE VALUES

OM62	**LP79**	**Fluorescein**
$\sigma = 5.35 \times 10^{-16}cm^2$ **$\tau_R = 830\pm160fs$**	**$\sigma = 1.33\pm0.16 \times 10^{-15}cm^2$** **$\tau_R = 400\pm160fs$**	**$\sigma = 3.65\pm1.14 \times 10^{-16}cm^2$** **$\tau_R = 717\pm99fs$**

Table 4.5: Summary of the values of σ_{STIM} and τ_R obtained by the best numerical fits to experimental data for OM62, LP79 and Fluorescein.

Simulated fits show good agreement with experimental data for all three chromophores. The average stimulated emission cross-sections for Fluorescein and OM62 are respectively $3.65x10^{-16}cm^2$ and $5.35x10^{-16}cm^2$; both dyes display a characteristic ground state vibrational relaxation lifetime in the sub-picosecond range (717fs and 830fs average values respectively). LP79 displays a higher stimulated emission cross-section ($1.33x10^{-15}cm^2$ average value) and a faster ground state vibrational relaxation time (400fs average) than the other chromophores.

With the exception of the OM62 cross-section (which yields the same value for both pulse widths) there is an apparent increase in both σ and τ_R with τ_P. The model does not consider the effects of the positive frequency sweep (up-chirp) across the DUMP pulse arising from group velocity dispersion upon passage through the distilled water pulse stretcher [26], nor fast spectral changes due to vibrational and solvent relaxation within S_0 and S_1 [30]. Relaxation of the dumped population in S_0 will lead to a time-dependent blue shift for the re-pumping to S_1, as illustrated in figure 4.25. If both time dependent spectral shifts are well matched there would be a decrease in the expected depletion efficiency with increasing τ_P, which would be interpreted in the current model as an increase in τ_R.

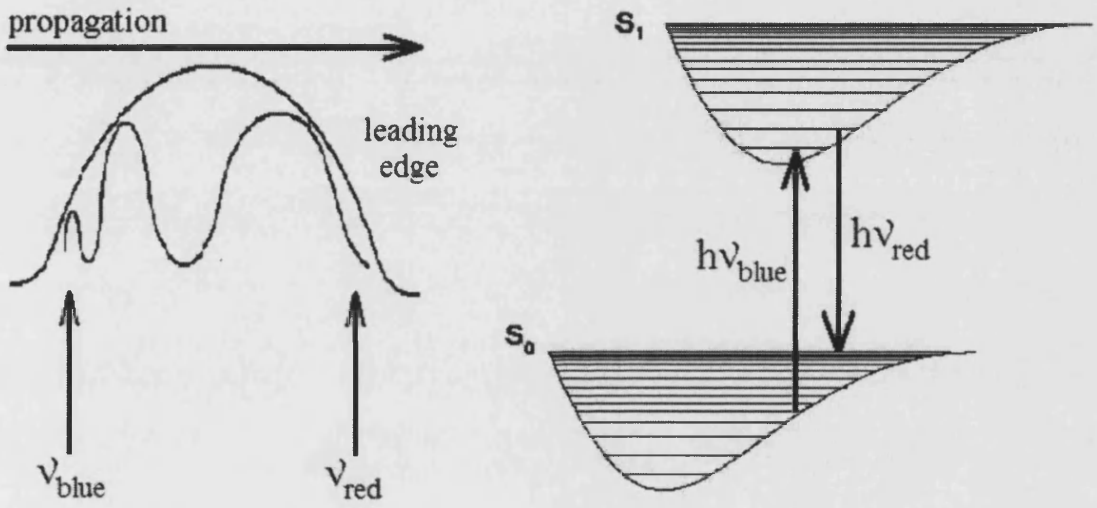

Figure 4.25: If the frequency shift across the DUMP pulse corresponds to the vibrational relaxation of the target levels within S_1, it may be possible to deplete the system with the "red" leading edge and re-excite the system with the "blue" trailing edge of the DUMP pulse.

One way to eliminate the DUMP up-chirp from the pulse stretcher would be the implementation of a diffraction grating pair similar to the RegA compressor. These have the disadvantage of increasing DUMP energy loss [31].

4.10.2 DUMP Wavelength Dependence

The dependence of STED on DUMP pulse energy and wavelength was investigated for LP79, OM62 and Rhodamine 6G. The experimental conditions for these studies are summarised in table 4.6. Population depletion measurements were made using the experimental techniques developed in section 4.6; fitting of the experimental data to simulated saturation curves was undertaken using the methods discussed in section 4.9 and displayed in figures 4.26-4.28.

Chromophore	LP79	OM62	Rhodamine 6G
DUMP wavelengths investigated (nm)	580, 595, 610	525, 535, 546	614, 622, 634, 644.5, 663.5
DUMP pulsewidth	1.23ps	3.2ps	848-933fs
PUMP-DUMP delay (ps)	200	200	650
PUMP energy (nJ)	<5nJ	<16nJ	<25nJ
DUMP energy range (nJ)	0-6nJ	0-11nJ	0-32nJ

Table 4.6: Summary of the DUMP wavelength dependence experiments

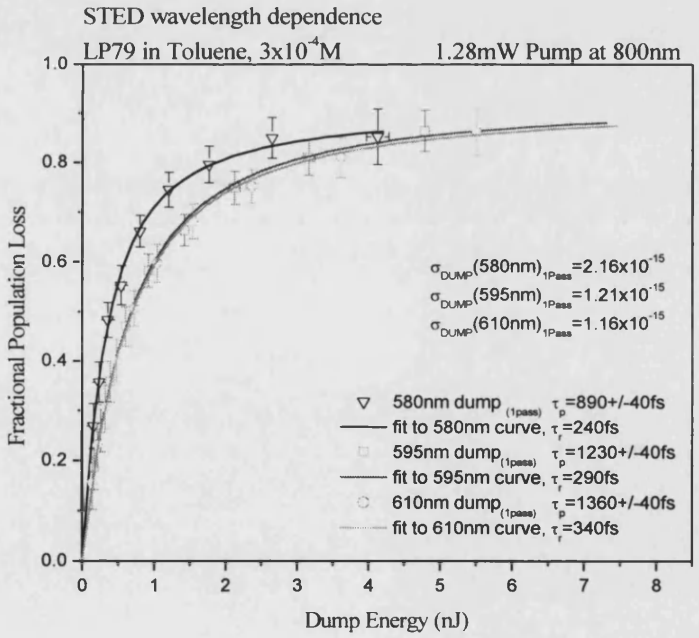

Figure 4.26: Fractional population removal for LP79 in toluene as a function of DUMP energy for DUMP wavelengths of 580nm, 595nm and 610nm.

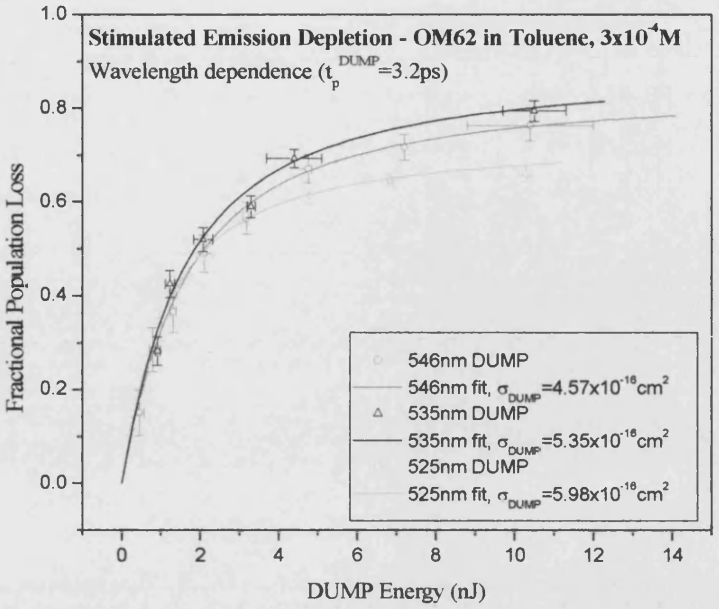

Figure 4.27: Fractional population removal for OM62 in toluene as a function of DUMP energy for DUMP wavelengths of 525nm, 535nm and 546nm.

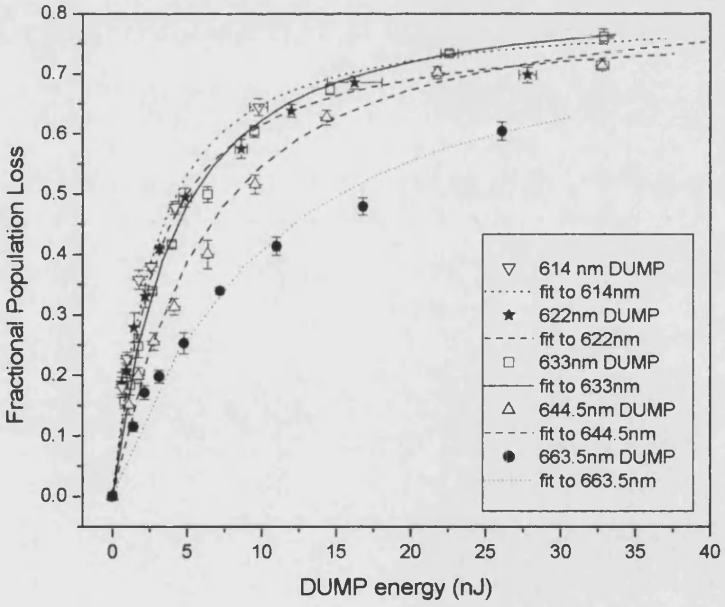

Figure 4.28: Fractional population removal for Rhodamine 6G in Ethylene Glycol as a function of DUMP energy for DUMP wavelengths of 614nm, 622nm, 633nm, 644.5nm and 663.5nm.

From the "raw" depletion data it is clear that STED is most efficient in LP79. This is highlighted by a consideration of the DUMP pulse energy required to achieve 70% depletion in the three dyes. For LP79 a DUMP energy of 1-2nJ is required whilst the corresponding energies for OM62 and Rhodamine 6G are respectively 5nJ and 25nJ.

It is also notable that for LP79 and (to a lesser degree) OM62 these energies are close to the linear region of the depletion curve whilst for Rhodamine 6G 70% depletion is only obtained when the transition is strongly saturated. A more quantitive picture of the STED efficiency is provided by the simulations which yield stimulated emission cross-sections and vibrational relaxation times for the three dyes. These values are shown in tables 4.7-4.9. A comparison between the wavelength variation in the stimulated emission cross-sections and the fluorescence spectra of the three probes is displayed in figures 4.29-4.31.

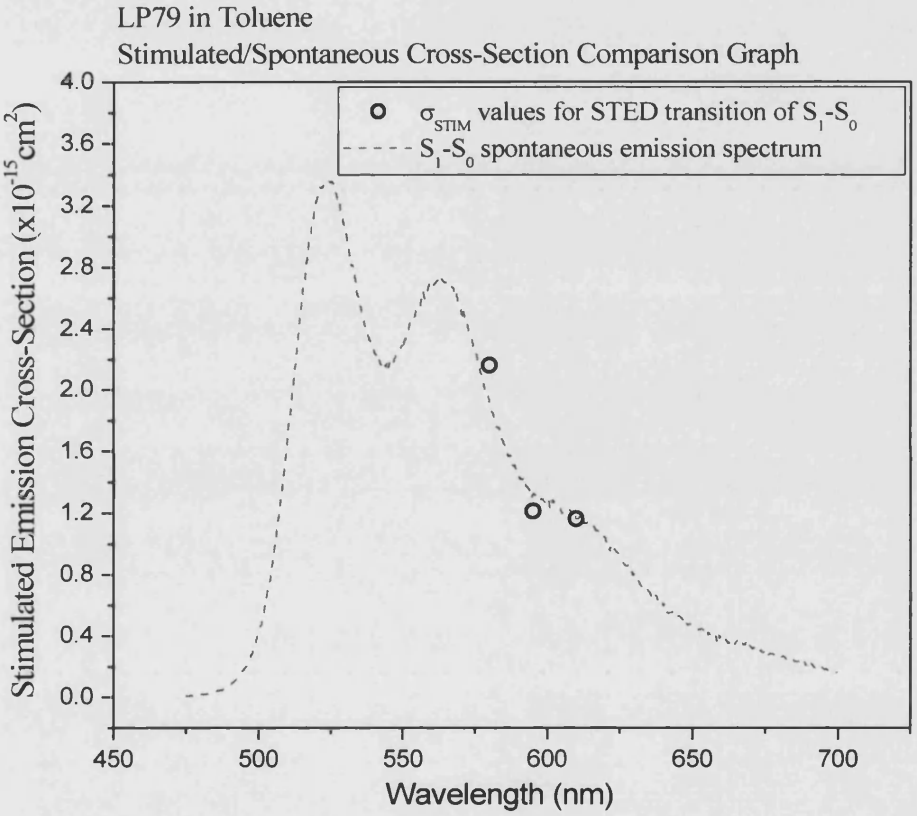

Figure 4.29: Values obtained for the stimulated emission cross-section of LP79 between 580nm and 610nm, superimposed upon the spontaneous emission spectrum.

LP79 in Toluene		
DUMP Wavelength (nm)	Stimulated Emission Cross-Section (10^{-16}cm^2)	Ground State Vibrational Relaxation Lifetime (fs)
580	21.6	240
595	12.1	290
610	11.6	340

Table 4.7: Summary of the values for the stimulated emission cross-section and ground state vibrational relaxation lifetime for LP79 for varying DUMP wavelength, obtained by the best numerical fits to experimental data.

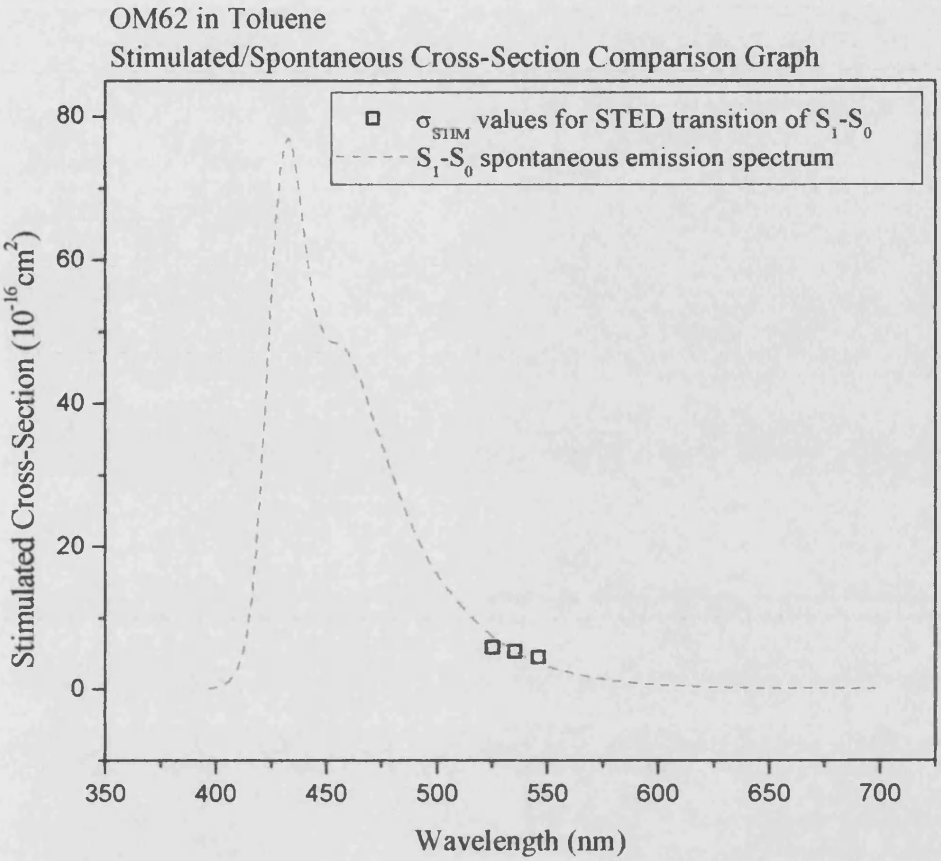

Figure 4.30: Values obtained for the stimulated emission cross-section of OM62 between 525nm and 546nm, superimposed upon the spontaneous emission spectrum.

OM62 in Toluene		
DUMP Wavelength (nm)	Stimulated Emission Cross-Section (10^{-16}cm^2)	Ground State Vibrational Relaxation Lifetime (fs)
525	5.98	892
535	5.35	941
546	4.57	979

Table 4.8: Summary of the values for the stimulated emission cross-section and ground state vibrational relaxation lifetime for OM62 for varying DUMP wavelength, obtained by the best numerical fits to experimental data.

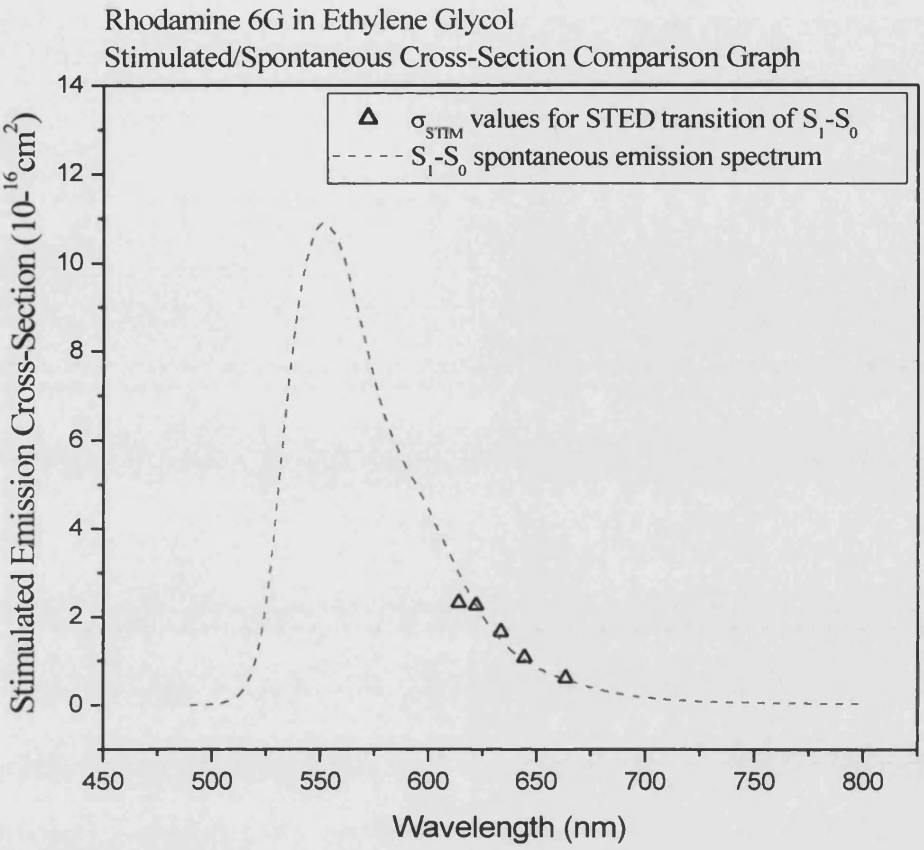

Figure 4.31: Values obtained for the stimulated emission cross-section of Rhodamine 6G between 614nm and 663.5nm, superimposed upon the spontaneous emission spectrum.

Rhodamine 6G in Ethylene Glycol		
DUMP Wavelength (nm)	Stimulated Emission Cross-Section (10^{-16}cm^2)	Ground State Vibrational Relaxation Lifetime (fs)
614	2.32	424
622	2.26	445
634	1.65	365
644.5	1.07	314
663.5	0.61	467

Table 4.9: A summary of the values for the stimulated emission cross-section and ground state vibrational relaxation lifetime for Rhodamine 6G for varying DUMP wavelength, obtained by the best numerical fits to experimental data.

LP79 is characterised by a stimulated emission cross-section that is an order of magnitude larger than that for Rhodamine 6G ($2.16x10^{-15}cm^2$ vs $2.32x10^{-16}cm^2$). This is accompanied by rapid ground state vibrational relaxation on a timescale of approx. 300fs; the corresponding vibrational relaxation times for Rhodamine 6G and OM62 are on the order of 400fs and 900fs respectively. OM62 displays a stimulated emission cross-section that is significantly higher than Rhodamine 6G, however its STED efficiency is reduced due to its relatively slow ground state relaxation time. The wavelength dependence of the STED cross-sections is seen to follow closely the steady state (spontaneous) fluorescence for each fluorophore. For LP79 it would appear that a maximum STED cross-section of $3.4x10^{-15}cm^2$ is possible, leading to significant sub-nanojoule excited state depletion at $10^{-6}cm^2$ spot sizes. However, the range of STED wavelengths that could be accessed for each of the three fluorophores is subject to the constraints of the probes' intrinsic photophysics such as the onset of DUMP induced single or two-photon fluorescence (as discussed in section 4.6.3.4) together with limitations in the apparatus arising from wavelength restrictions imposed by the OPA tuning range and losses in the DUMP pulse energy in the pulse stretcher. For LP79 the DUMP tuning range of 580-610nm is imposed by DUMP induced single photon fluorescence at wavelengths below 580nm and the onset of DUMP induced two-photon fluorescence at wavelengths beyond 610nm.

4.11 Discussion

It is clear that push-push chromophores such as LP79 offer significantly better performance in two-photon STED compared to conventional fluorophorees such as Fluorescein or Rhodamine 6G. An obvious application of such molecules would be in two-photon STED microscopy; to date this technique has not been implemented due in part to a lack of suitable instrumentation and the limitations of conventional fluorescent probes. Single photon STED microscopy has been demonstrated by Hell and co-workers [7]; these studies utilise a 76MHz Ti:Sapphire oscillator and an optical parametric oscillator (OPO) in conjunction with established visible emitting molecules. Here the OPO provides the PUMP field (558nm) and the DUMP is derived from a 20ps (stretched) portion of the 800nm Ti:Sapphire output. These wavelengths are conveniently compatible with molecules such as Styryl 8, which displays a very large Stokes shift (approx. 180nm) [28] between absorption and emission maxima. Milliwatt

range DUMP powers (approx. 10^{-11}J pulse energies) were required to achieve significant (70%) excited state depletion at spot sizes on the order of 10^{-8}cm^2.

For two-photon STED an equivalent experimental set up would involve the same apparatus but with Ti:Sapphire and OPO roles reversed: the two-photon PUMP would be derived from a portion of the Ti:Sapphire output, the remainder of which would pump the OPO to provide the DUMP pulse train. It is therefore desirable to minimise the "split" from the Ti:Sapphire oscillator and thus maximise the OPO output.

For efficient two-photon excitation, the transition probabilities equivalent to those obtainable for single photon excitation need to be achieved using low (milliwatt range) PUMP powers. Equating single photon and two-photon transition probabilities (equations 3.20 and 3.21) yields

$$\frac{\sigma^{(2)}}{2}\left(\frac{E_2}{h\nu A}\right)^2 \frac{1}{\tau_P} \times 0.664 = \frac{E_1 \sigma}{h\nu A} \qquad [4.32]$$

In single photon microscopy milliwatt PUMP powers (at 76MHz) are used to excite fluorescence in chromophores with absorption cross-sections on the order of 10^{-16}cm^2. This is equivalent to a transition probability of 0.4 for a spot size of 10^{-8}cm^2 at 600nm. For LP79 at an excitation wavelength of 800nm ($\sigma^{(2)}$=1.775x10^{-47}cm^2) and a pulse width of 140fs this yields a pulse energy E_2 of 2.42x10^{-10}J, which corresponds to an average excitation power (at 76MHz) of 18 milliwatts. A reduction in the PUMP pulsewidth to 30fs (achievable in Ti:Sapphire oscillators [32]) would reduce E_2 by a factor of 2.16 leading to an average excitation power of 8.5 milliwatts (1.12x10^{-10}J). These powers are well within the output of conventional Ti:Sapphire oscillators (approx. 1W at 76MHz).

To achieve efficient STED in LP79 with a spot size of 10^{-6}cm^2 a DUMP energy of approx. 1nJ was required. A reduction in DUMP area by two orders of magnitude requires 10^{-11}J pulses which correspond to on-sample powers of approximately 800 microwatts; these are obtainable with the milliwatt output available from a synchronously pumped OPO.

4.12 Conclusions

This chapter has investigated the possibility of photoselection within two-photon excited state populations using stimulated emission depletion. STED from two-photon excited states is in principle more efficient due to the greater degree of angular photoselection that can be afforded by two-photon absorption (in molecules with a diagonal transition tensor).

Two-photon STED was demonstrated for three conventional chromophores; Rhodamine 6G, Fluorescein and Coumarin 153. From DUMP energy, pulsewidth and wavelength dependence measurements upon depletion efficiency, STED cross-sections and vibrational relaxation times could be determined using simulations based upon an analytical two-level model. STED in chromophores specifically designed for efficient two-photon absorption and fluorescence was also investigated. Push-push chromophores LP79 and OM62, synthesised at the CNRS laboratory by Dr Mireille Blanchard-Desce et al. at Rennes, were found to outperform conventional (single photon) fluorophores such as Rhodamine 6G. STED in LP79 was extremely efficient with a stimulated emission cross-section an order of magnitude greater than those found in Rhodamine 6G, Fluorescein and Coumarin 153 and a fast vibrational relaxation from target levels in the ground state.

Population control in excited states is directly applicable to imaging and time-resolved microscopy as demonstrated by the work of Gratton and Hell [6,7]. The possibility of employing two-photon STED using unamplified laser systems (i.e. milliwatt PUMP and DUMP powers) appears to be feasible using chromophores such as LP79. The alteration of excited state populations is also accompanied by orientational photo-(de)selection as can be seen from the simple analysis of section 4.4. Polarisation effects in STED and the use of polarised depletion to investigate molecular order and orientational relaxation phenomena inaccessible to conventional spectroscopic techniques is explored in Chapter 5.

References for Chapter 4

1. D E Reisner, R W Field, J L Kinsey and H-L Dai, J. Chem. Phys. **80**, 5968 (1984)
2. I Gryczynski, J Kusba and J R Lackowicz, Biophys. J. **67**, 2024 (1994)
3. J Kusba, V Bogdanov, I Gryczynski and J R Lackowicz, J. Phys. Chem. **98**, 8886 (1994)
4. S A Kovalenko, J Ruthmann and N P Ernsting, J. Chem. Phys. **109,** 1894 (1998)
5. P Changenet-Barret, C T Choma, E F Gooding, W F DeGrado and R M Hochstrasser, J. Phys. Chem. B **104**(39), 9322 (2000)
6. P T C So, T French and E Gratton, Biophys. J. **70**, 626 (1996)
7. T A Klar, S Jakobs, M Byba, A Egner and S W Hell, Proc. Nat. Acad. Sci. (USA) **97**, 8206 (2000)
8. W Denk, J H Strickler and W W Webb, Science **248**, 73 (1990)
9. W Denk, W W Webb and J H Strickler, "Two Photon Laser Scanning Microscopy", US Patent 5,034,613 (1991)
10. P T So, C Y Dong, B R Masters and K M Berland, Annu. Rev. Biomed. Eng. **2**, 399 (2000)
11. A J Bain, P Chandna, G Butcher and J Bryant, J. Chem. Phys. **112**, 10435 (2000)
12. A J Bain, R J Marsh and D A Armoogum, UK patent application 0211781.0. (2002)
13. A Volkmer, D A Hatrick and D J Birch, Meas. Sci. Technol. **8**, 1339, (1997)
14. C Wan and C K Johnson, J. Chem. Phys. **101**, 10283 (1994)
15. A J Bain in "Introduction to Laser Spectroscopy" (2nd Ed.) Kluwer, London (2002)
16. B Valeur, "Molecular Fluorescence", Wiley, Weinheim (2002)
17. T-S Yang, M-S Chang, R Chang, M Hayashi, S H Lin, P Vöhringer, W Dietz and N F Scherer, J. Chem. Phys. **110**(24), 12070 (1999)
18. D A Armoogum, A J Bain and R J Marsh, Proc. SPIE **4812**, 45 (2002)
19. M K Reed, M K Steiner-Shepard and D K Negus, Opt. Lett. **19**(22), 1855 (1994)
20. G C Baldwin, "An Introduction to Nonlinear Optics" (2nd Ed.), Kluwer Academic (1974)
21. L M Davis and C Parigger, Meas. Sci. Technol. **3**, 85 (1992)
22. D T Delpy, M Cope and P van der Zee, Phys. Med. Biol. **33**, 1433 (1988)
23. K Ogawa, T Katsuyama and H Nakamura, Appl. Phys. Lett. **53**, 1357 (1988)
24. W Demtröder, "*Laser Spectroscopy: Basic Concepts and Instrumentation*", Springer, Berlin (1996)

25. F G Smith and J H Thomson, "Optics" (2nd Ed.), Wiley (1996)
26. G P Agrawal, "Nonlinear Fiber Optics", Academic Press, London (1989)
27. G W C Kaye and T H Laby, "Tables of Physical and Chemical Constants" (16th Ed.), Longman (1995)
28. U Brackmann, *LambdaChrome® Laser Dyes* (3rd Ed.), Lambda Physik AG, Goettingen (2000)
29. M A Albota, C Xu and W W Webb, App. Opt. **37**(31), 7352 (1998)
30. M L Horng, J A Gardecki, A Papazyan and M Maroncelli, J. Phys. Chem. **99**, 17311 (1995)
31. *Optometrics* Holographic Diffraction Grating Datasheet, URL: http://www.optometrics.com/prod/spectro/gratings/Graph-B6.pdf
32. A Stingl, M Lenzner, C Spielmann, F Krausz and R Szipöcs, Opt. Lett. **20**(6), 602 (1995)

Chapter 5

Excited State Photo-Engineering II:

Polarised Studies of Two-Photon Excited Stimulated Emission Depletion

5.1 Introduction

In Chapter 4, STED from two-photon excited states was shown to be potentially more efficient than from those created by single photon excitation due to the higher degree of molecular alignment created by the excitation process. Molecules with transition dipole moments aligned parallel to the polarization of the DUMP field are preferentially removed leading to a lower degree of excited state alignment for the remaining population. This can clearly be seen from an initial two-photon STED experiment using Fluorescein in Ethylene Glycol, as illustrated in figure 5.1. With a PUMP-DUMP delay of 636 picoseconds a 50% excited state population depletion is accompanied by an abrupt change in the fluorescence anisotropy from 0.38 to 0.20. Fluorescence de-polarisation can be achieved by rotation of a transition dipole moment [1], angular averaging due to rotational diffusion [2] or by energy transfer [3]. For a change in transition dipole moment by an angle γ the change in fluorescence anisotropy from R to R' is given by

$$\frac{R'}{R} = \frac{1}{2}\left(3\cos^2\gamma - 1\right) \qquad [5.1]$$

Application of this analysis (though not really appropriate to STED) yields a value for γ of 34° for the excited state transition dipole distribution in figure 5.1. The change in anisotropy takes place over the DUMP pulsewidth of 1.7 picoseconds, which would correspond to isotropic rotational diffusion with a re-orientational time τ_{20} of 2.65ps.

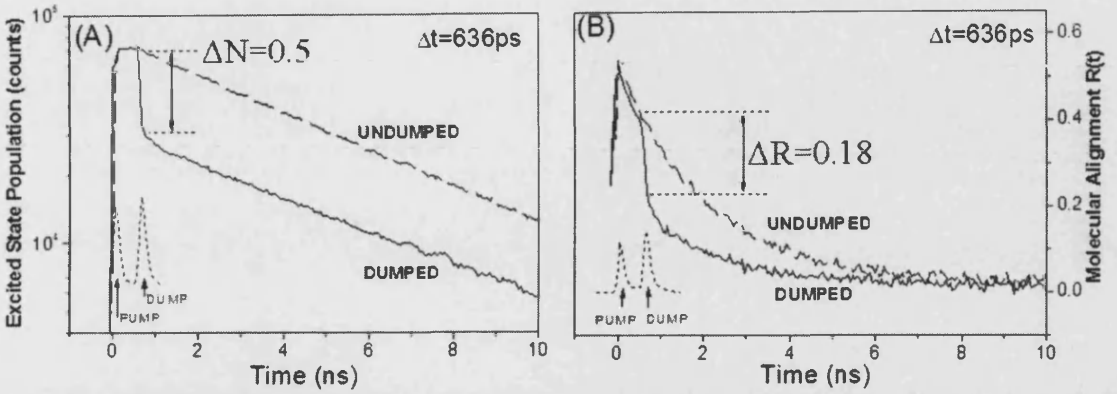

Figure 5.1: Preliminary time-resolved two-photon STED results for Fluorescein in Ethylene Glycol. (A) Following two-photon excitation by the PUMP (61nJ at 800nm), with a 636ps delay 50% of the excited state population is removed by the dump pulse (16nJ at 580 nm). (B) The selective removal of molecules oriented parallel to the DUMP polarization results in an abrupt change (approx. 0.18) in the fluorescence anisotropy.

From a simple analysis of STED in the weak depletion fast-relaxation limit (section 4.4) it was seen that a measurement of the fluorescence anisotropy before and after application of the DUMP pulse (R_U and R_D respectively) together with the fraction of excited state population remaining (F_R) and determination of the saturation parameter S for the transition ($\sigma E/h\nu A$) for a given PUMP-DUMP delay will yield the K=4 hexadecapole excited state alignment moment prior to dumping. Measurement of these parameters for a range of PUMP-DUMP delays will allow $\langle \alpha_{40}^{EX}(t) \rangle$ to be measured, a task that is impossible using unperturbed emission spectroscopy. These considerations will be developed in detail later. In addition to the determination of higher order moments from fluorescence depolarization it is possible to use STED to both increase the fluorescence anisotropy and to "write" different symmetry components into the excited state. These approaches allowing novel types of photoselection not accessible to conventional (unperturbed) time resolved fluorescence techniques are explored in this chapter.

5.2 STED Alignment modification

5.2.1 Case I - Parallel PUMP and DUMP fields

It was shown in Chapter 4 that in the limit of weak depletion (S<<1) and fast ground state relaxation (i.e. negligible re-pumping of S_1 by the DUMP field), the fraction of the initial excited state population F_R remaining after dumping is given by

$$F_R = 1 - \frac{(1+2R_U)S}{3} \qquad [5.2]$$

where $R_U = \langle \alpha^{EX}_{20\,U} \rangle / \sqrt{5}$ is the fluorescence anisotropy immediately prior to excited state depletion. The simple (weak depletion limit) analysis also showed that the anisotropy after dumping R_D, given an initial anisotropy R_U, is given by

$$R_D = \frac{\left[\left(3 - \frac{11}{7}S\right)R_U - \frac{2}{5}S - \frac{12}{35}\langle \alpha^{EX}_{40\,U} \rangle S\right]}{(3-(1+2R_U)S)} \qquad [5.3]$$

Immediately following two-photon excitation, R_U(=R(0)) and $\langle \alpha^{EX}_{40\,U} \rangle = \langle \alpha^{EX}_{40}(t=0) \rangle$ take values of 4/7 and 8/21 respectively. Substitution of these values into equation 5.3 yields the dumped anisotropy following two-photon excitation as a function of S:

$$R_D = \frac{4}{7}\left(1 - \frac{5}{6}S\right) \Big/ \left(1 - \frac{5}{7}S\right) \qquad [5.4]$$

A plot of R_D for values of S from 0 to 0.5 is shown in figure 5.2.

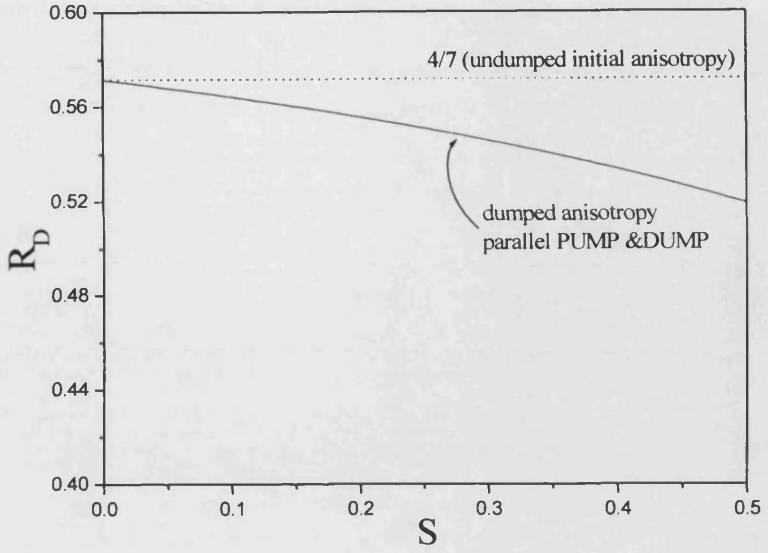

Figure 5.2: Variation in the fluorescence anisotropy with saturation parameter S for parallel PUMP and DUMP polarisations for excited state depletion immediately following two-photon excitation.

As can be seen, the dumped anisotropy shows an approximately linear decrease with S as an increasing proportion of molecules aligned parallel to the laboratory Z-axis are removed by STED. Depletion of population aligned in the X-Y plane would be expected to lead to an increase in R_D with respect to R_U. This would require an orthogonal DUMP polarisation to that of the PUMP. STED under these conditions is considered below.

5.2.2 Case II - Perpendicular PUMP and DUMP fields

In the limit of weak depletion and fast ground state relaxation, the moments of the excited state distribution after application of the DUMP pulse are given by (Chapter 4, section 4.4):

$$\left\langle C_{KQ}^{EX}(D)\right\rangle = \frac{N_{EX}(U)}{N_{EX}(D)}\sum_{K'Q'}\left\langle C_{K'Q'}^{EX}(U)\right\rangle\left\langle KQ\left|1-SW_D(\theta,\phi)\right|K'Q'\right\rangle \qquad [5.5]$$

Consider STED in which the angle β between the PUMP polarisation (Z) and that of the DUMP is varied between 0° and 90°. The PUMP and DUMP frames are connected by

an Euler rotation D(0,β,0) in the PUMP axis system; the angular dependence of the transition probability and the moments of the altered distribution are then given by

$$\left\langle C_{KQ}^{EX}(D)\right\rangle = \frac{N_{EX}(U)\sqrt{4\pi}}{3N_{EX}(D)}\sum_{K'Q'}\left\langle C_{K'Q'}^{EX}(U)\right\rangle\left\langle KQ\left|\left(3-S\right)Y_{00}(\theta,\phi)+\frac{2}{\sqrt{5}}\sum_{q}d_{0q}^{2}(-\beta)Y_{2q}(\theta,\phi)\right|K'Q'\right\rangle \qquad [5.6]$$

where $d_{0q}^{2}(-\beta)$ is the reduced Euler rotation matrix for the transformation between the DUMP and PUMP axes. For orthogonal fields β=90° and equation [5.6] becomes

$$\left\langle C_{KQ}^{EX}(D)\right\rangle = \frac{N_{EX}(U)\sqrt{4\pi}}{3N_{EX}(D)}\sum_{K'Q'}\left\langle C_{K'Q'}^{EX}(U)\right\rangle\left\langle KQ\left|\begin{bmatrix}(3-S)Y_{00}(\theta,\phi)\\ -\frac{2S}{\sqrt{5}}\left[-\frac{1}{2}Y_{20}(\theta,\phi)+\sqrt{\frac{3}{8}}\left[Y_{22}(\theta,\phi)+Y_{2-2}(\theta,\phi)\right]\right]\end{bmatrix}\right|K'Q'\right\rangle \qquad [5.7]$$

Evaluating the matrix elements yields [4]

$$\left\langle C_{KQ}^{EX}(D)\right\rangle = \frac{N_{EX}(U)}{3N_{EX}(D)}\sum_{K'Q'}\left\langle C_{K'Q'}^{EX}(U)\right\rangle\begin{bmatrix}(3-S)\begin{pmatrix}K' & 0 & K\\ -Q' & 0 & Q\end{pmatrix}\begin{pmatrix}K' & 0 & K\\ 0 & 0 & 0\end{pmatrix}\hat{K}'\hat{K}\\ -\frac{2S}{\sqrt{5}}\left[-\frac{1}{2}\begin{pmatrix}K' & 2 & K\\ -Q' & 0 & Q\end{pmatrix}\begin{pmatrix}K' & 2 & K\\ 0 & 0 & 0\end{pmatrix}\hat{K}'\hat{K}\sqrt{5}\right.\\ \left.+\sqrt{\frac{3}{8}}\left[\begin{pmatrix}K' & 2 & K\\ -Q' & 2 & Q\end{pmatrix}+\begin{pmatrix}K' & 2 & K\\ -Q' & -2 & Q\end{pmatrix}\right]\begin{pmatrix}K' & 2 & K\\ 0 & 0 & 0\end{pmatrix}\hat{K}'\hat{K}\sqrt{5}\right]\end{bmatrix} \qquad [5.8]$$

From equation 5.8 the fluorescence observables are

$$\left\langle C_{00}^{EX}(D)\right\rangle = \frac{N_{EX}(U)}{3N_{EX}(D)}\left\langle C_{00}^{EX}(U)\right\rangle\left[\left(3-S\right)+\frac{1}{\sqrt{5}}S\left\langle\alpha_{20}^{EX}(U)\right\rangle\right] \qquad [5.9]$$

$$\frac{\left\langle C_{20}^{EX}(D)\right\rangle}{\sqrt{5}} = \frac{N_{EX}(U)}{3N_{EX}(D)}\left\langle C_{00}^{EX}(U)\right\rangle\left[\left(3-\frac{5S}{7}\right)\frac{\left\langle\alpha_{20}^{EX}(U)\right\rangle}{\sqrt{5}}+\frac{S}{5}+\frac{6S}{35}\left\langle\alpha_{40}^{EX}(U)\right\rangle\right] \qquad [5.10]$$

$$\frac{\left\{\left\langle C_{22}^{EX}(D)\right\rangle+\left\langle C_{2-2}^{EX}(D)\right\rangle\right\}}{\sqrt{30}} = \frac{N_{EX}(U)}{3N_{EX}(D)}\left\langle C_{00}^{EX}(U)\right\rangle\frac{S}{5}\left[1-\frac{10\left\langle\alpha_{20}^{EX}(U)\right\rangle}{7\sqrt{5}}+\frac{\left\langle\alpha_{40}^{EX}(U)\right\rangle}{7}\right] \qquad [5.11]$$

Viewing the emission at 90° to the PUMP and DUMP propagation directions, the fluorescence observables are $I_Z(t)$ and $I_Y(t)$ (Chapter 2, section 2.5). As the altered excited state is no longer cylindrically symmetric about Z the fluorescence intensity and polarisation will now depend on the cylindrically asymmetric degree of alignment

written into the excited state by the DUMP pulse, the Z and Y components of the emission intensity after the application of the dump pulse are given by [5]

$$I_Z(D)=\frac{AN_{EX}(D)}{3}\left[1+\frac{2}{\sqrt{5}}\left\langle\alpha_{20}^{EX}(D)\right\rangle\right] \qquad [5.12]$$

$$I_Y(D)=\frac{AN_{EX}(D)}{3}\left[1-\frac{1}{\sqrt{5}}\left\langle\alpha_{20}^{EX}(D)\right\rangle-\left(\frac{3}{10}\right)^{\frac{1}{2}}\left\{\left\langle\alpha_{22}^{EX}(D)\right\rangle+\left\langle\alpha_{2-2}^{EX}(D)\right\rangle\right\}\right] \qquad [5.13]$$

where A is a constant of proportionality.

From equation 5.8 assuming a short PUMP-DUMP delay and an initial anisotropy of 4/7 the population remaining in the excited state is given by

$$F_R=1-\frac{S}{7} \qquad [5.14]$$

Comparison with parallel fields (Chapter 4, table 4.1) shows that the degree of population depletion is lower by a factor of five. In isotropic media this difference will become less marked as the excited state array relaxes.

The substitution of initial (undumped) degrees of K=2 and K=4 alignment of 4/7 and 8/21 respectively into equations 5.9-5.11 yields

$$\left\langle C_{00}^{ex}(D)\right\rangle=\frac{N_{ex}(U)}{3N_{ex}(D)}\left\langle C_{00}^{ex}(U)\right\rangle 3\left[\left(1-\frac{S}{7}\right)\right] \qquad [5.15]$$

$$\frac{\left\langle C_{20}^{ex}(D)\right\rangle}{\sqrt{5}}=\frac{N_{ex}(U)}{3N_{ex}(D)}\left\langle C_{00}^{ex}(U)\right\rangle\frac{4}{7}\left[\left(3-\frac{S}{4}\right)\right] \qquad [5.16]$$

$$\frac{\left\{\left\langle C_{22}^{ex}(D)\right\rangle+\left\langle C_{2-2}^{ex}(D)\right\rangle\right\}}{\sqrt{30}}=-\frac{N_{ex}(U)}{3N_{ex}(D)}\left\langle C_{00}^{ex}(U)\right\rangle\frac{S}{21} \qquad [5.17]$$

Recalling from Chapter 2 that in a medium with cylindrical asymmetry the measurement of the fluorescence anisotropy, defined (in a collinear excitation-detection geometry) by the Z and X polarisation components of the emission, is given by

$$R(D)=\left[\frac{\left\langle C_{20}^{ex}(D)\right\rangle}{\sqrt{5}}-\frac{\left\{\left\langle C_{22}^{ex}(D)\right\rangle+\left\langle C_{2-2}^{ex}(D)\right\rangle\right\}}{\sqrt{30}}\right]\Bigg/\left[\left\langle C_{00}^{ex}(D)\right\rangle+2\frac{\left\{\left\langle C_{22}^{ex}(D)\right\rangle+\left\langle C_{2-2}^{ex}(D)\right\rangle\right\}}{\sqrt{30}}\right] \qquad [5.18]$$

Substitution of equations 5.15-5.17 into 5.18 yields

$$R(D) = \frac{4}{7}\left[\left(3 - \frac{S}{6}\right)\right] \Big/ \left[\left(3 - \frac{11}{21}S\right)\right] \qquad [5.19]$$

The negative cylindrically asymmetric alignment contribution created by the DUMP pulse will act to increase the altered anisotropy. This is illustrated in figure 5.3.

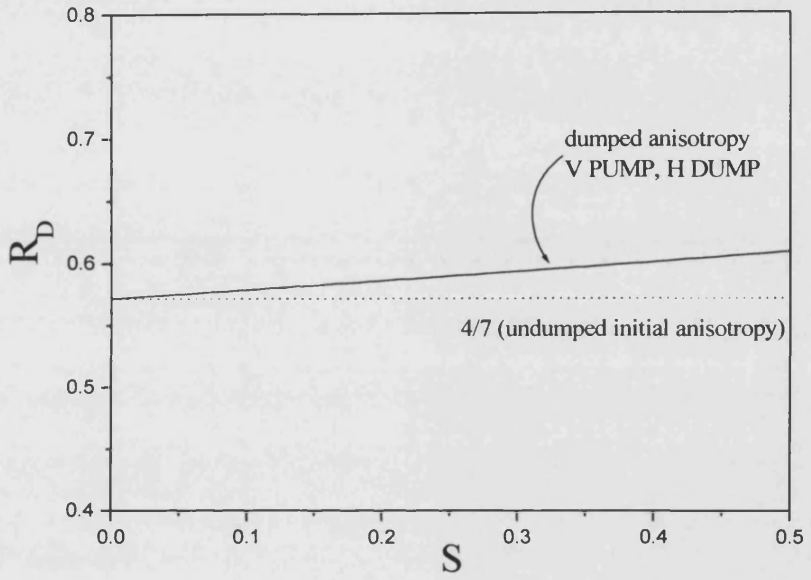

Figure 5.3: A plot of R_D for values of S from 0 to 0.5 for a DUMP polarisation orthogonal to the (Z polarised) PUMP shows that re-polarisation of the excited state can exceed the maximum fluorescence anisotropy achievable with two-photon excitation.

Lakowicz and co-workers have demonstrated that fluorescence anisotropy can be controlled (decreased *and* increased) using STED from single photon excited states [6,7]. Figure 5.3 shows that, in principle, re-polarisation of two-photon fluorescence anisotropy above the maximum value of 4/7 should be possible provided the DUMP pulse is applied before there is significant orientational relaxation of the excited state population. As will be seen, an increase in R_D over the undumped anisotropy of at least 10% is possible in Rhodamine 6G yielding an initial fluorescence anisotropy in excess of the two-photon limit.

5.3 Experimental procedure I

5.3.1 Experimental Setup

Polarised STED experiments were carried out using the regenerative amplifier and optical parametric amplifier described in Chapters 3 and 4. A schematic representation of the experimental arrangement is shown in figure 5.4.

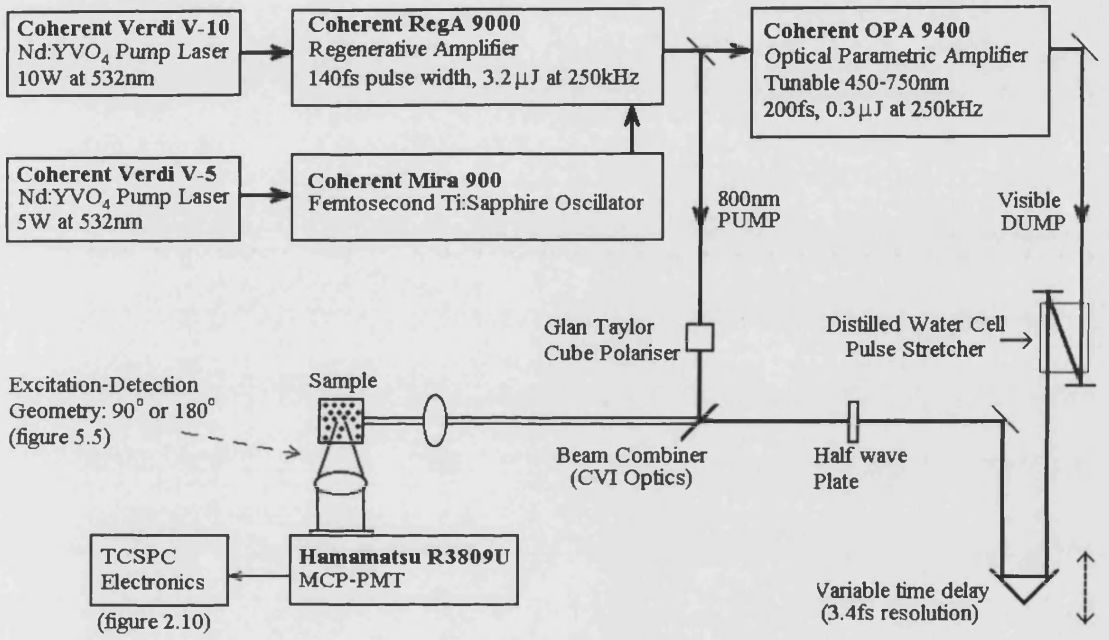

Figure 5.4: Experimental setup for the polarised stimulated emission depletion studies described in this chapter. The detection system for the experiments was the TCSPC apparatus introduced in Chapter 2; the excitation-detection geometry was set either to 90° or 180°, depending upon whether the excited state was being de-polarised or re-polarised.

The principal changes to the apparatus for these studies were the introduction of independent polarisation control of the PUMP and DUMP pulses via linear polarisers and half wave plates together with the use of polarised time resolved single photon counting (Chapter 2, section 2.6) to measure R(t) (and in particular R_U and R_D) as a function of PUMP-DUMP delay.

The excitation-detection geometries used for STED de-polarisation and re-polarisation experiments are shown in figure 5.5. A Z (vertical) PUMP polarisation was maintained in both layouts. Excited state de-polarisation employed an orthogonal PUMP-DUMP geometry identical to that used for population depletion measurements in Chapter 4.

Scattered laser light was blocked using an interference filter (Corion LS600) and glass cut-off filters (Schott BG39). This geometry is illustrated in figure 5.5A.

Excited state re-polarisation via STED employed a collinear PUMP-DUMP excitation-detection geometry. This required more aggressive filtering of the PUMP and DUMP pulses (16nJ at 800nm and 12.5nJ at 614nm respectively). To this end, glass cut-off filters (Schott BG39), several short pass interference filters (Corion LS550, 2 Coherent Short-Pass filters (50% transmission at 580nm) and 2 Coherent Short-pass filters (50% transmission at 540nm) were used in conjunction with a beam block to avoid laser breakthrough. This geometry is illustrated in figure 5.5B.

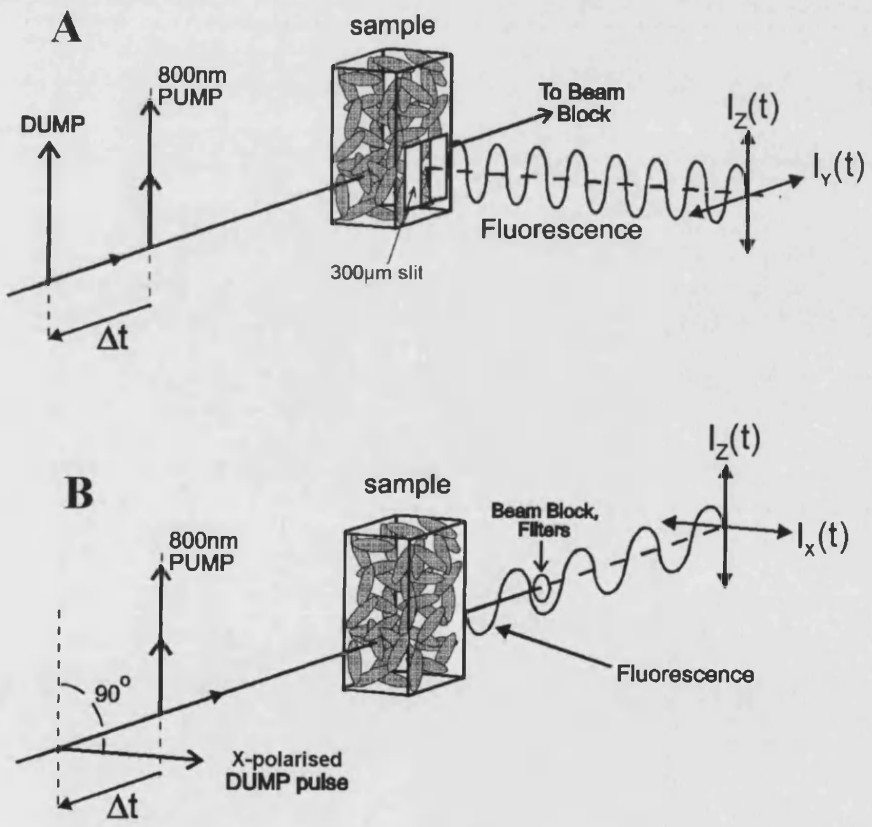

Figure 5.5: A) TCSPC measurements of excited state de-polarisation and the evolution of $\langle \alpha_{40}^{ex}(t) \rangle$ utilised a 90° excitation-detection geometry. A 300µm slit was used to isolate the 800 nm beam waist within the 1cm^2 cuvette. B) Re-polarisation of the excited state using a "V-H" beam configuration was carried out using a collinear excitation-detection geometry.

5.4 Results I – Excited State Alignment Control

STED has been used to modify the alignment of a two-photon excited state population of Rhodamine 6G in Ethylene Glycol in a series of demonstration experiments. Figure 5.6 shows a reduction of 0.23 in the fluorescence anisotropy 1ns after two-photon excitation using parallel PUMP and DUMP beams; on-sample PUMP and DUMP powers for this demonstration were 16nJ at 800nm (200fs pulsewidth) and 17nJ at 622nm (1ns pulsewidth) respectively.

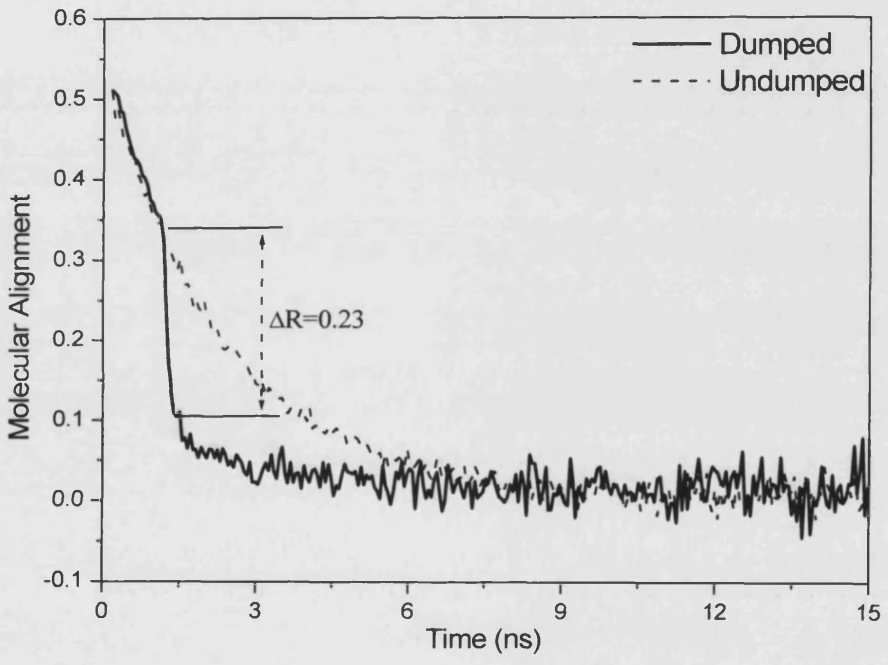

Figure 5.6: De-polarisation of Rhodamine 6G using STED. With parallel PUMP and DUMP polarisations, alignment reductions are maximised (ΔR=0.23)

Figure 5.7 shows re-polarisation of the excited state alignment of Rhodamine 6G in Ethylene Glycol 667ps after two-photon excitation using perpendicular PUMP and DUMP beams, with on-sample powers of 16nJ and 11.2nJ respectively.

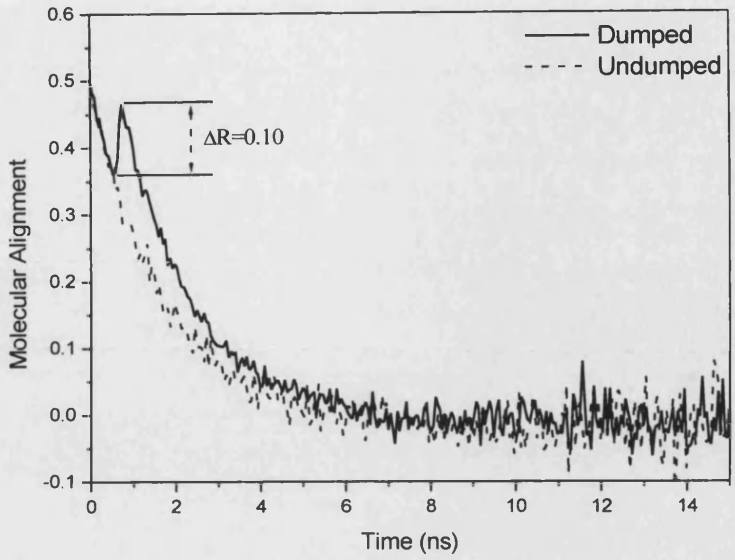

Figure 5.7: Re-polarisation of Rhodamine 6G in Ethylene Glycol using perpendicular PUMP and DUMP fields. The arrival of a horizontally polarised DUMP 667ps after excitation raises the fluorescence anisotropy by approx. 0.10.

The effect of the horizontally polarised DUMP pulse in figure 5.7 is to increase the fluorescence anisotropy by 0.10 to within 3% of the initial alignment prepared by two-photon excitation by the PUMP. By employing a short PUMP-DUMP delay it may be possible to negate the effects of excited state alignment relaxation (K=2 and K=4) due to rotational diffusion (τ_{20}=1.74ns) and modify the excited state alignment to exceed the limit of 0.571 achievable by two-photon excitation.

Figure 5.8 shows the modification in excited state alignment of Rhodamine 6G in Ethylene Glycol from a horizontally polarized DUMP pulse using an approximate PUMP-DUMP delay of 6ps. This (short) delay was estimated by adjusting the DUMP path length using the delay line such that the DUMP was shifted 6ps from the mid-point of depletion onset (figure 4.14). Two-photon excitation (undumped) in Rhodamine 6G yields an initial fluorescence anisotropy of 0.508. This differs from the predicted value of 0.571 by a factor (Ā, Chapter 2) of 0.89; this is similar to the deviation measured for single photon excitation relative to the theoretical limit of 2/5 (equation 2.49). Application of the DUMP pulse yields an initial anisotropy of 0.615, an increase of 10% and well above the 0.571 limit. With Ā=1, the modified anisotropy would be close to 0.7, and in excess of the three-photon limit of 0.667, as shown in table 5.1 [8].

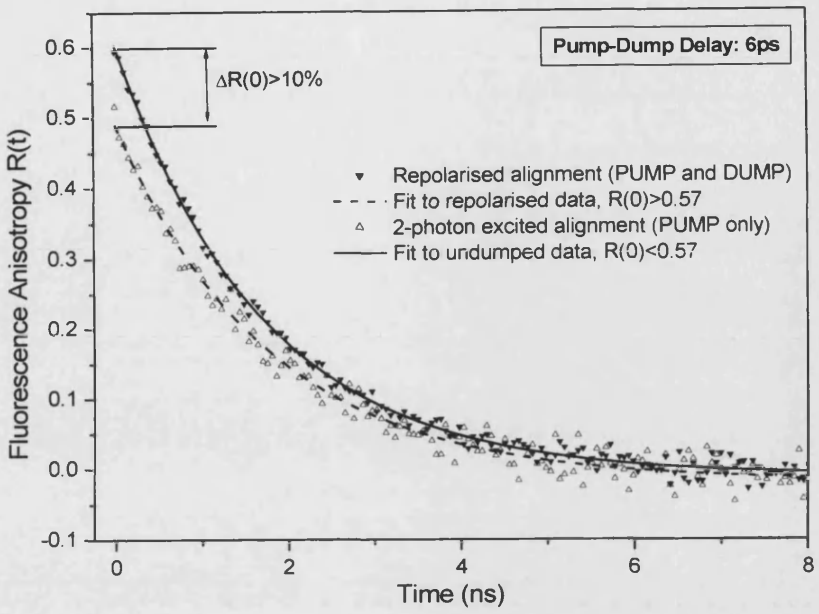

Figure 5.8: Excitation and re-polarisation of the Rhodamine 6G molecular alignment by perpendicular PUMP and DUMP fields. Introduction of a horizontally polarised DUMP field 6ps after excitation modifies the excited state alignment to a value above the two-photon limit.

Alignment	$R(0)_{uncorrected}$	$\bar{A}$	$R(0)_{corrected}$	*2 photon limit=0.571*
Unmodified	0.508	0.889	0.571	*3 photon limit=0.667*
Modified	0.615	0.889	0.692	*4 photon limit=0.727*

Table 5.1: Values of the initial (time zero) fluorescence anisotropy obtained for two-photon excitation of Rhodamine 6G with and without the presence of a strong horizontally polarised DUMP pulse delayed from two-photon excitation by 6ps. A further correction of the anisotropy (due to experimental and/or molecular factors) indicates that under ideal conditions an initial anisotropy value of 0.692 would be obtained, which lies between the three- and four-photon excitation limits.

It has been shown that STED following two-photon excitation is capable of both de-polarising and re-polarising an excited state population. The measurable changes induced by STED are reflected in an alteration of the excited state alignment moments. STED will also affect the K=4 moments of the excited state distribution; due to the constraints of spontaneous emission (equation 2.7), these changes are not observable. However, the measurement of R_D and R_U in STED de-polarisation together with knowledge of S for the DUMP transition can, as discussed in section 5.6, yield $\langle \alpha^{ex}_{40U} \rangle$. The measurement of K=4 dynamics via time-delayed PUMP-DUMP fluorescence anisotropy and intensity measurements is outlined below.

5.5 Excited State K=4 Dynamics

5.5.1 Introduction

The measurement of excited state hexadecapole (K=4) alignment is not a trivial undertaking. PUMP-DUMP delay measurements combined with picosecond TCSPC intensity and polarisation data and a well defined DUMP transition (S) are required. Nonetheless, the measurement of excited state K=4 parameters and their evolution would represent a significant advance yielding new information on excited state order and dynamics in both isotropic and ordered molecular systems. The information afforded by K=4 probe measurements in both isotropic and ordered environments is discussed in more detail below.

5.5.2 Isotropic Media

In an isotropic fluid medium, diffusive orientational dynamics are well described by the diffusion equation:

$$\frac{dP(\theta,\varphi,t)}{dt} = \nabla^2 P(\theta,\varphi,t) \qquad [5.20]$$

As shown in Chapter 1 (section 1.9) the moments of P(θ,φ,t) are given by:

$$\langle C_{KQ}(t)\rangle = \langle C_{KQ}(0)\rangle \exp[-DK(K+1)t] \qquad [5.21]$$

with $\gamma_{10}=\gamma_{1\pm1}=2D$

$\gamma_{20}=\gamma_{2\pm2}=\gamma_{2\pm1}=6D$

$\gamma_{30}=\gamma_{3\pm3}=\gamma_{3\pm2}=\gamma_{3\pm1}=12D$

$\gamma_{40}=\gamma_{4Q}$ $=20D$ etc. [5.22]

Knowledge of one orientational correlation function (e.g. $\langle \alpha_{20}(t)\rangle$) is sufficient to describe the orientational behaviour of all the moments of the distribution. In isotropic media where probe molecule motion exhibits inertial (free rotation) or co-operative

behaviour, this simple picture of orientational relaxation does not hold. NMR [9-11] and Optical Kerr Effect [12,13] measurements of γ_{20} in water and acetonitrile do not agree with the corresponding measurements of γ_{10} obtained from microwave and terahertz measurements of the complex index of refraction [14-17]. In an effort to reconcile these discrepancies, direct (time domain) pump-probe measurements of γ_{10} in these two liquids were recently made using terahertz-field-induced second-harmonic generation (TFISH) [18]. TFISH measurements of $(\gamma_{10})^{-1}$ in water and acetonitrile yield values which do not agree with the (diffusive) predictions of γ_{20} data [9-13]. It is clear that outside the diffusive regime the measurement of more than one order parameter is essential.

Measurements of K>2 dynamics are not allowed by conventional pump-probe techniques such as polarisation spectroscopy [19] or the Optical Kerr Effect [12,13] which are based on the third order nonlinear response of the molecular system. Pump-probe experiments involving higher order (six-wave) mixing have been shown to yield information on γ_{10} and γ_{30} [20]. Polarised STED with the subsequent (fast) measurement of the altered emission anisotropy affords an equivalent degree of higher order correlation in fluorescence.

5.5.3 Ordered Molecular Environments

Probe molecule motion in an ordered system such as an aligned nematic liquid crystal (Chapter 2) is significantly slower than that obtained for small molecules. The rotational motion, whilst clearly exponential in nature, does not obey the predictions of equation 5.22 in that γ_{KQ} is strongly Q-dependent. In the nematic phase of 5CB $\gamma_{22}>\gamma_{20}$ with γ_{22} showing an anti-Arrenhius temperature dependence [21]. Given that θ motion is highly constrained and φ diffusion is unrestricted (i.e. 0-2π), it would be extremely interesting to compare $\langle \alpha_{20} \rangle$ and $\langle \alpha_{40} \rangle$ probe dynamics. In addition to the measurement of orientational relaxation data, the knowledge of equilibrium (steady state) excited state moments is crucial in determining the probe orientational distribution function. Figure 5.9 shows the fluorescence anisotropy decay for Oxazine 4 in 5CB at 25°; in this system R(t, β=0°) decays to a constant value in the region of 0.4 [22]. This corresponds to the initial anisotropy prepared by single photon excitation in an isotropic medium and in the absence of additional excited state order would point to a $\cos^2\theta$ distribution of Oxazine

4 transition dipole moments with respect to the nematic director. However, as initial R(0,β) measurements have shown, the ground state is characterised by a similar value for $\langle\alpha_{20}(ss)\rangle$ but a large negative $\langle\alpha_{40}\rangle$ moment that gives rise to an orientational distribution peaked at 38° to the director [23]. Measurements of solely $\langle\alpha_{20}(ss)\rangle$ would indicate a parallel alignment to $\hat{n}$, an error of 38° and a wholly misleading picture of probe order in the nematic phase. It is therefore highly desirable to measure both $\langle\alpha_{20}\rangle$ and $\langle\alpha_{40}\rangle$ equilibrium order parameters in excited state molecular populations.

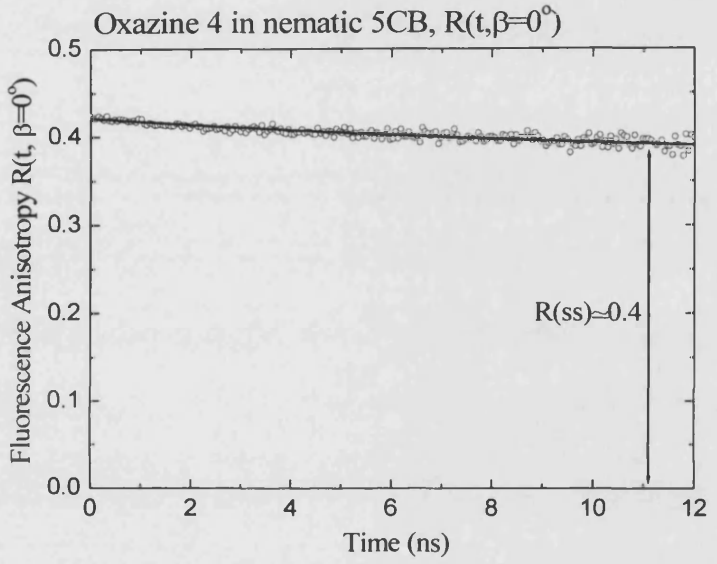

Figure 5.9: Fluorescence anisotropy measurements of Oxazine 4 in 5CB yield a steady state alignment of ~0.40. This value corresponds to the initial anisotropy that would be prepared by single photon excitation in an isotropic medium and in the absence of additional excited state order, and without the knowledge of higher order moments an unrealistic picture of probe order would be obtained {original data from [22]}

In Chapter 3 it was seen that the measurement of K=2 and K=4 degrees of cylindrically symmetric alignment was sufficient to determine the ground state orientational distribution function. Predictions for the K=6 moment of the probe distribution function were found to be in good agreement with experimental measurements using two-photon excitation. The crucial step in determining the distribution function is the measurement of both the K=2 and K=4 moments.

5.6 Simulation of Excited State K=4 Dynamics using STED

The weak depletion analysis introduced in section 5.2 predicts that the K=4 hexadecapole excited state moment $\langle \alpha_{40}^{EX}{}_U \rangle$ immediately prior to the arrival of the DUMP pulse can be determined using STED. Re-arranging equation 5.2 in terms of $\langle \alpha_{40}^{EX}{}_U \rangle$ gives

$$\langle \alpha_{40}^{EX}{}_U \rangle = \frac{35}{12S}\left\{\left(3-\frac{11}{7}S\right)R_U + [(1+2R_U)S-3]R_D - \frac{2}{5}S\right\} \qquad [5.23]$$

In the weak depletion limit S can be determined from measurements of the fractional remaining excited state population (F_R) as shown in equation 5.1. Since the fluorescence anisotropy prior to and following the onset of STED can also be measured experimentally, it is possible to obtain a value for $\langle \alpha_{40}^{EX}{}_U \rangle$. By making a series of measurements of R_U, R_D and F_R for different PUMP-DUMP delays, the temporal evolution of the hexadecapole excited state moment (i.e. $\langle \alpha_{40}^{EX}(t) \rangle$) can be determined.

5.6.1 Saturation Effects and Finite Ground State Relaxation.

The expression for the magnitude of the undumped K=4 alignment term $\langle \alpha_{40}^{EX}{}_U \rangle$ given in equation 5.23 assumes both weak saturation and fast relaxation of the ground state vibrational levels. In this case, the Saturation parameter S can be determined from the fluorescence observables F_R and R_U by equation 4.19 (Chapter 4, section 4.4). It was shown in the Chapter 4 that for low values of τ_P/τ_R, the measured values of 1-F_R begin to deviate significantly from those predicted by this analysis as S approaches unity. The rate equation analysis given later in section 4.5, however, continues to predict this parameter for larger values of S. Before attempting an experimental measurement of the excited state K=4 alignment dynamics it would be prudent to know how well the other fluorescence observable (R_D) used in equation 5.23 is predicted by the weak depletion analysis of Chapter 4 for large S.

Figure 5.10 shows a numerical simulation of R_D as a function of S for a number of values of τ_P/τ_R. These curves where calculated from equation 4.25, using Mathematica in an analogous manner to those for $1\text{-}F_R$ in Chapter 4.

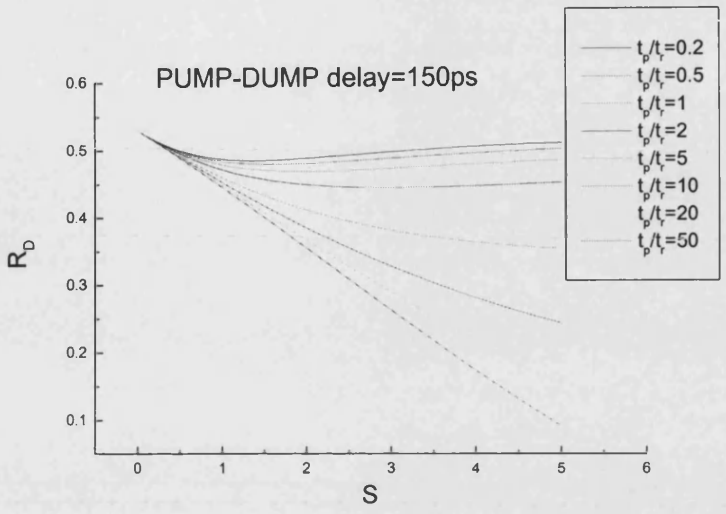

Figure 5.10: Plot of the variation in R_D for increasing S predicted using rate equation analysis. Unless the dump pulsewidth is very long in comparison to the ground state relaxation time, there is substantial deviation from the linear behaviour of equation 4.19 for large S.

It can be seen from figure 5.10 that the discrepancies between the numerical solutions for R_D from equation 4.25 and the weak depletion analysis results (see figure 5.2) are more pronounced than for $1\text{-}F_R$. As S passes unity, equation 5.4 breaks down completely for shorter dump pulsewidths and R_D begins to increase again for large S.

5.6.2 Simulation of $\left\langle \alpha_{40}^{EX} \right\rangle$ Measurements.

The numerical simulations of the fluorescence observables after dumping (presented in this and the previous chapter) show that the approximations underpinning equation 5.23 break down unless S<<1. Such low levels of depletion cause experimental difficulties however, as it becomes difficult to distinguish the dumped fluorescence observables from the undumped observables due to the noise in the measurements. This problem is exacerbated by the relatively low repetition rate of the femtosecond laser system. Furthermore, the change in fluorescence anisotropy due to STED is comparable to (or less than) the change due to orientational relaxation on the timescale of the instrument response function. These effects tend to lead to large relative errors in the measurement of the relevant quantities unless the collection time is very long.

All these factors mitigate against using a low value of S while those in section 5.6.1 prevent the use of strong saturation. It would be extremely advantageous, therefore, to quantify the discrepancy of equation 5.23 from the true value of $\langle \alpha_{40}^{EX}{}_U \rangle$ as a function of S as this would allow a compromise value to be chosen for the experiment. To achieve this, the Mathematica programme was used to calculate values of the dumped fluorescence observables (1-F_R, R_D) for a specific initial excited state alignment and value of S using equations 4.23-4.26. These were then used to construct an effective saturation parameter S_{eff} using the relation

$$S_{eff} = \frac{3(1-F_R)}{1+2R_U} \qquad [5.24]$$

as S can no longer be determined directly from F_R using equation 4.19 due to saturation. S_{eff} is substituted into equation 5.23 along with the calculated value of R_D to obtain a value of $\langle \alpha_{40}^{EX}{}_U \rangle$. The results of these predictions are shown in figure 5.11 as a function of PUMP-DUMP delay for several values of S. The undumped excited state distribution used in these calculations is given by

$$P_U(\theta,\varphi) = \frac{1}{\sqrt{4\pi}}\left[Y_{00}(\theta,\varphi) + \frac{4\sqrt{5}}{7} Y_{20}(\theta,\varphi)\exp\left[-\frac{t_{PD}}{\tau_{20}}\right] + \frac{8}{21} Y_{40}(\theta,\varphi)\exp\left[-\frac{3t_{PD}}{10\tau_{20}}\right]\right] \qquad [5.25]$$

where t_{PD} is the delay between PUMP and DUMP pulses. This distribution is equivalent to a two-photon excited state where equation 5.22 holds.

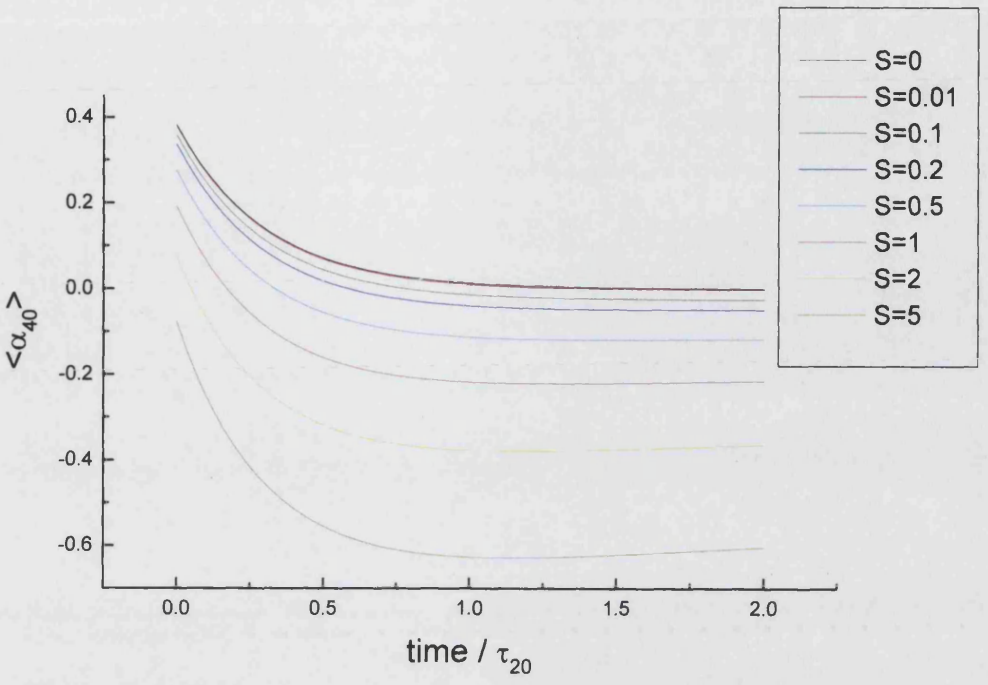

Figure 5.11: Simulations of the measured decay of the $\langle \alpha_{40} \rangle$ moment given by equation 5.23 and the affect on the $\langle \alpha_{40} \rangle$ moment by saturation of the DUMP transition for a two-photon prepared state. In these simulations τ_P/τ_R =2.1.

As expected, the results of the simulations indicate that only for very small values of S (S<0.1) do the values of the K=4 moment given by equation 5.23 closely match the initial values. However, to a good first order approximation, the effect of saturation causes a vertical displacment of the observed decay curves with only minimal distortion of the decay behaviour until very high (S>2) saturation is reached.

To quantify these differences, the simulated data for each value of the saturation parameter was fitted to a single exponential decay of the form

$$\left\langle \alpha_{40\ U}^{EX} \right\rangle = A \exp\left[-t/\tau_{40} \right] + y_0 \qquad [5.26]$$

The parameters obtained from these fits are summarised in table 5.3 along with the percentage deviation from the expected result.

S	0	0.01	0.1	0.2	0.5	1	2	5
y_0	0.000	-0.002	-0.026	-0.051	-0.121	-0.222	-0.377	-0.625
A	0.381	0.381	0.385	0.388	0.400	0.420	0.459	0.559
τ_{40}/τ_{20}	0.300	0.299	0.295	0.290	0.277	0.262	0.247	0.243
χ^2/1E-7	0	0.001	1.34	5.39	33.6	100	400	900
$\Delta A/\%$	0	0.0	1.0	1.8	5.0	10.2	20.5	46.7
$\Delta\tau_{40}/\%$	0	0.3	1.7	3.3	7.7	12.7	17.7	19.0

Table 5.2: Summary of the parameters obtained by fitting the simulated <P4> decays and the discrepancies from the expected results as saturation increases. The quality of the reduced square fits χ^2 is also shown, indicating that the decay remains exponential until strong saturation (S>2) is reached.

5.6.3 Choice of Saturation Parameter

Table 5.3 showed that low values of S yield the lowest distortions in τ_{40} from the weak depletion limit predictions in section 5.2. However, it is necessary to deplete the excited state such that the change in anisotropy due to STED is resolvable from the anisotropy change due to orientational averaging of the excited state population. To this end, a maximum value of S (S_{MAX}) of 1.5 was chosen as a compromise between the validity of the predicted τ_{40} and the feasibility of measuring small changes in anisotropy using detection apparatus with a experimental response of approx. 100ps [24]. Using the stimulated emission cross-sections measured for Rhodamine 6G and Fluorescein in the previous chapter and the identity $S=\sigma E/h\nu A$, it is possible to calculate the maximum DUMP energy (E_{MAX}) allowed in the determination of τ_{40} for these probes.

For the example of Fluorescein, using the results obtained in Chapter 4 (a 1.45ps DUMP pulse at 580nm, a stimulated emission cross-section of $3.55\text{x}10^{-16}\text{cm}^2$ and $A=1.77\text{x}10^{-6}\text{cm}^2$), an S of 1.5 corresponds to a maximum DUMP energy of 2.6nJ.

5.7 Experimental Realisation

In order to verify the feasibility of this application of STED (i.e. the determination of moments "hidden" from conventional spectroscopic techniques) a measurement of the lifetime of the $\langle \alpha_{40}^{EX}(t) \rangle$ moment (τ_{40}) was carried out in systems obeying small step isotropic fluid diffusive orientational dynamics. The validity of this approach was tested by measurement of the relaxation dynamics of $\langle \alpha_{40}^{ex}(t) \rangle$ created by two-photon excitation of Rhodamine 6G in Ethylene Glycol and Fluorescein in Ethylene Glycol. Here orientational relaxation dynamics are well described by small step rotational diffusion [5] in which the alignment relaxation rates (γ_{KQ}) are given by equation 5.22. The relationship between the directly measurable fluorescence anisotropy decay time (τ_{20}) and that for τ_{40} is therefore (from equation 5.22)

$$\tau_{40} = 0.3\tau_{20} \qquad [5.27]$$

Figure 5.12 shows fluorescence anisotropy decays for Rhodamine 6G and Fluorescein in Ethylene Glycol; best fits to experimental data yield re-orientational lifetimes (τ_{20}) of 1.74ns and 2.15ns respectively. For small step rotational diffusive systems, the corresponding values of τ_{40} are 522ps and 645ps respectively (equation 5.27).

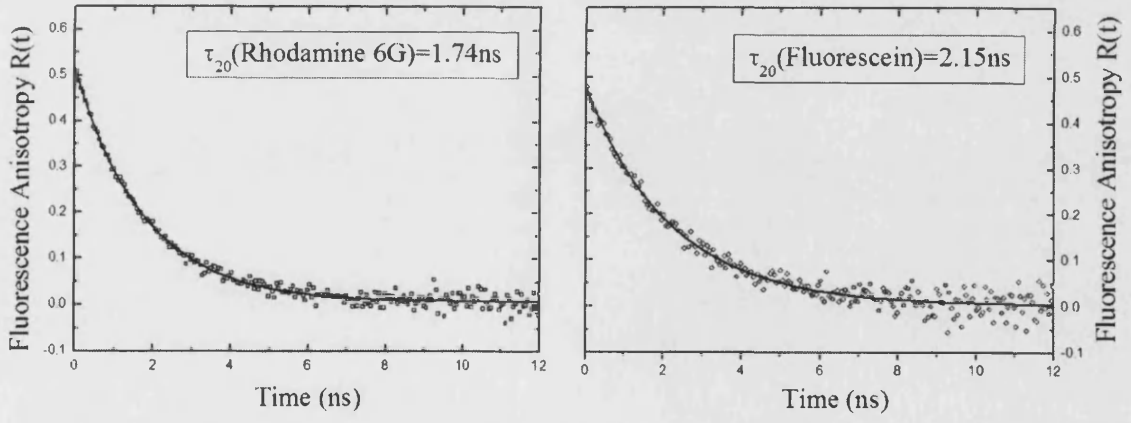

Figure 5.12: "undumped" anisotropy decays for Rhodamine 6G and Fluorescein in Ethylene Glycol yield τ_{20} values of 1.74ns and 2.15ns respectively. From equation 5.27, the predicted values for τ_{40} in these (small step diffusive) systems are 522ps and 645ps respectively.

5.8 Experimental Procedure II

The experimental setup and optical layout for the measurement of τ_{40} was identical to the STED excited state de-polarisation demonstration experiment described in section 5.3. The samples investigated were Fluorescein in Ethylene Glycol (E.G.) and Rhodamine 6G in E.G. (approx. $5x10^{-4}M$). The experimental parameters used in the investigations are summarised in table 5.4.

Experimental Parameter	Fluorescein in E.G.	Rhodamine 6G in E.G.
PUMP energy / wavelength	28nJ at 800nm	14.4nJ at 800nm
DUMP energy	2nJ	3nJ
DUMP wavelength	580nm	640nm
DUMP pulsewidth	1.4ps	1.0ps
PUMP-DUMP delay	150ps-1500ps	100ps-1200ps

Table 5.3: Summary of the experimental parameters used in the measurement of τ_{40} for Fluorescein in Ethylene Glycol and Rhodamine 6G in Ethylene Glycol.

With the DUMP path blocked, an initial "undumped" fluorescence anisotropy measurement was made to establish the τ_{20} re-orientational lifetime and to provide a prediction for τ_{40} in the sample (section 5.7)

Polarised fluorescence intensity measurements were made for constant PUMP and DUMP powers at several different PUMP-DUMP delays. The fluorescence anisotropy decays were constructed from equation 1.30. Figure 5.13 and 5.14 show the fluorescence intensity and anisotropy decays obtained at several PUMP-DUMP delays in Fluorescein.

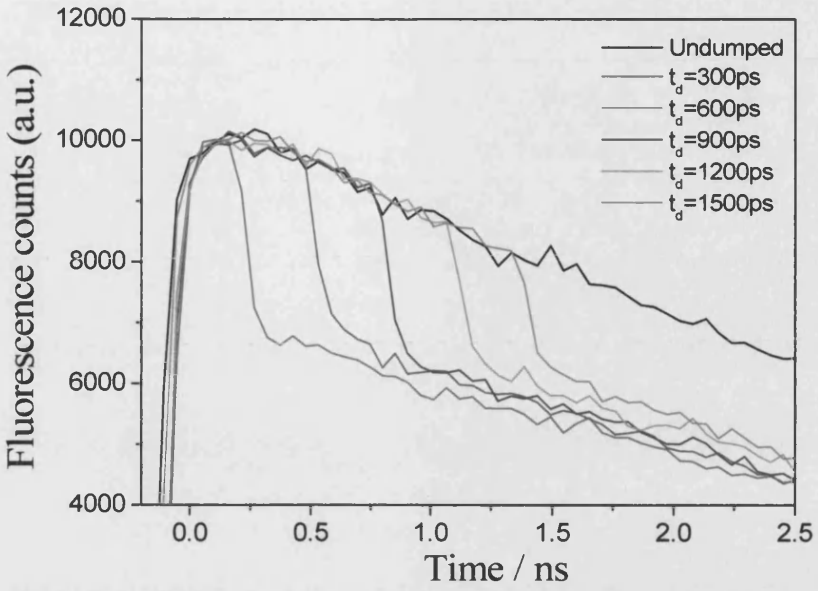

Figure 5.13: Fluorescence depletion at five PUMP-DUMP delays for Fluorescein in Ethylene Glycol. The undumped fluorescence is shown for comparison.

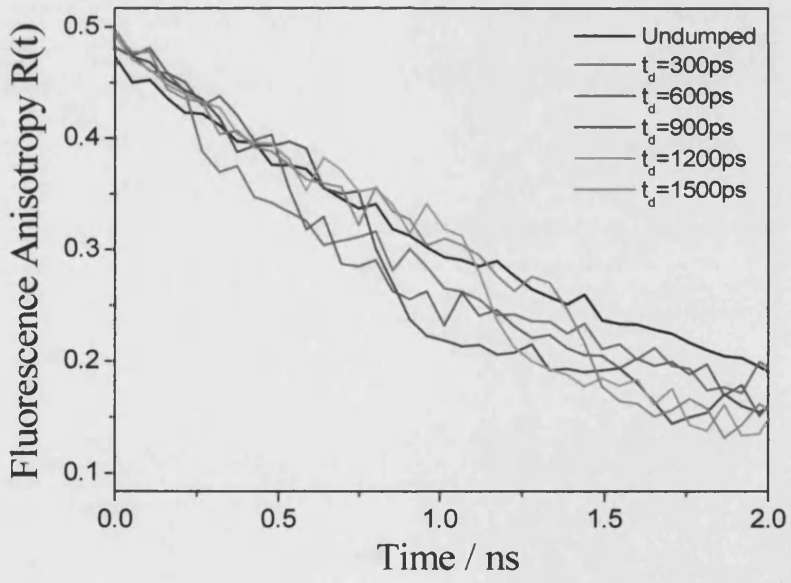

Figure 5.14: Undumped and dumped fluorescence anisotropy measurements at five PUMP-DUMP delays for Fluorescein in Ethylene Glycol.

Values of R_U, R_D and F_R were obtained from the dumped fluorescence anisotropy measurements for each PUMP-DUMP delay; with this information, it was possible to establish a value for $\langle \alpha_{40}^{EX} \rangle$ at each interval. τ_{40} was obtained by fitting the $\langle \alpha_{40}^{EX} \rangle$ values to a single exponential.

5.9 Results II

The evolution of $\langle \alpha_{40}^{EX}(t) \rangle$ for Fluorescein in Ethylene Glycol and Rhodamine 6G in Ethylene Glycol is shown in figure 5.15; simulated data using the procedure outlined in section 5.6 is included for comparison for both probes.

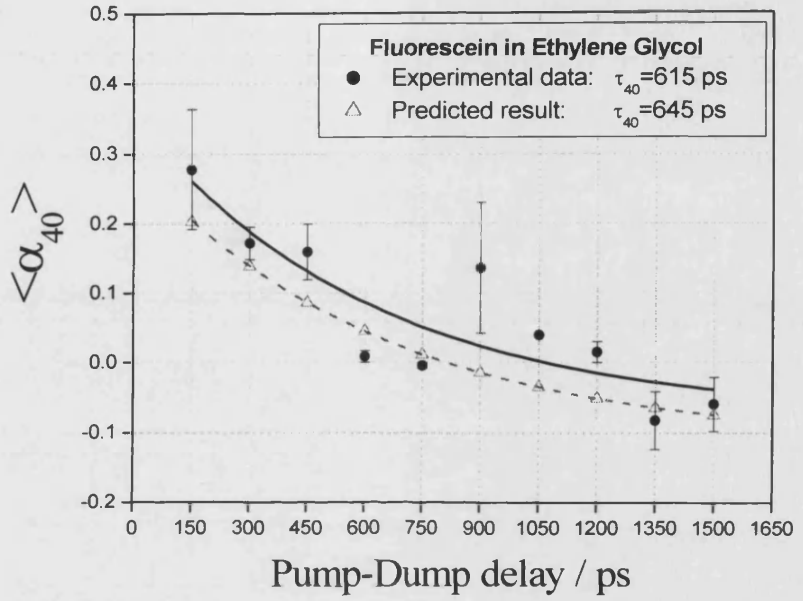

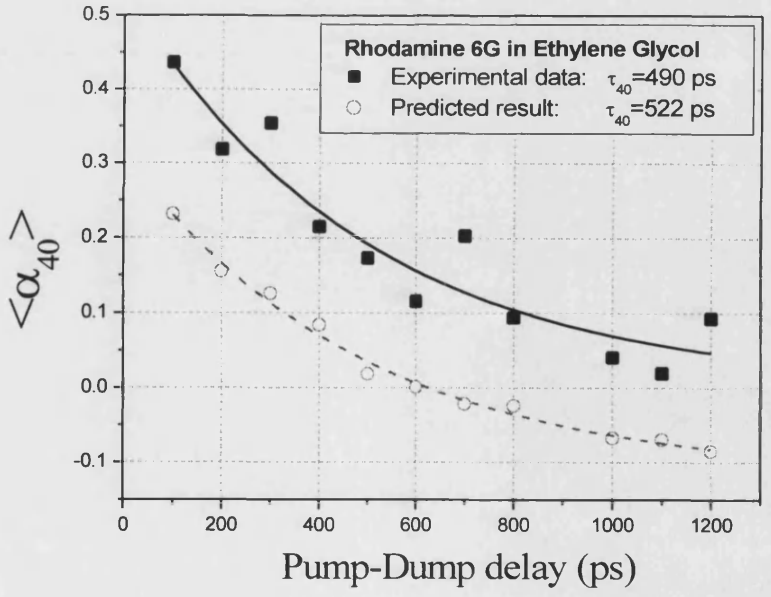

Figure 5.15: Plots of the evolution of the K=4 (hexadecapole) excited state moment for Fluorescein in Ethylene Glycol and Rhodamine 6G in Ethylene Glycol. Exponential fits to the measured data yielding τ_{40}(Fluorescein)=615ps and τ_{40}(Rhodamine 6G)=490ps compare favourably with the theoretical values of 645ps and 522ps respectively.

Single exponential fits to both sets of experimental data yielded values of τ_{40} in good agreement with predictions from the simulated data and the small step diffusive model. The rate equation analysis presented in section 5.6 suggests that moderate saturation of the DUMP transition would not significantly distort the magnitude and relaxation rate of the measured $\langle \alpha_{40}^{EX} \rangle$ moment; this is supported by both sets of experimental results.

The simulations also predict an offset in the absolute value of the $\langle \alpha_{40}^{EX} \rangle$ moment. This is observed in both Fluorescein and Rhodamine 6G. In the former, a good agreement between the predicted offset and that obtained by experiment is seen. In the case of Rhodamine 6G however, there is a significant discrepancy between predicted and measured offsets. This may be due to small amounts of DUMP induced fluorescence (Chapter 4, section 4.6.3.4) in the experiment. Exciting molecules from lower vibrational levels of the ground state to S_1 will modify the excited state alignment and population during the DUMP pulse, distorting the fluorescence observables immediately after STED. Additionally, the modification in excited state alignment may alter the saturation behaviour.

Preliminary investigations by members of the group [25] into modelling the effects of DUMP induced (single and two-photon) fluorescence suggest that its principal effect upon the measured K=4 moment is to cause a positive offset in the τ_{40} decay. This may partially explain the discrepancy in the offset observed between theoretical predictions and experimental measurements for Rhodamine 6G.

5.10 Discussion

From the results shown in section 5.9 it is clear that the form of $\langle \alpha_{40}^{ex}(t) \rangle$ given by equation 5.23 is relatively insensitive to saturation, with noticeable deviations from exponential decay only when S≥2. With optimal DUMP conditions, this corresponds to over 50% depletion of the excited state population. For the experiments performed in this chapter, S was kept below 1.5. The difference between true and measured values of $\langle \alpha_{40}^{ex}(t) \rangle$ is seen to be (to first order) a constant that is independent of PUMP-DUMP delay. With the provision that S<2, the distortion to the measured decay rate is minimal,

Although the offset in the measured K=4 moments increases rapidly with saturation, this level can be predicted provided that S can be determined accurately, and that there is no contamination of the fluorescence signal by excitation from the lower vibrational levels of S_0 by the DUMP. Even if this is not the case, it should still be possible to determine the shift in $\langle \alpha_{40}^{ex}(t) \rangle$ for an isotropic system as the steady state value (i.e. at long PUMP-DUMP delays) must be zero. The other measured moments can then be corrected by simple linear correction.

For a system with intrinsic order a similar approach can be taken. It was shown in chapters 2 and 3 that the K=2,4,and 6 moments of the ground state distribution could be determined using (conventional) single and two-photon fluorescence anisotropy measurements. This data, combined with de-polarisation measurements with appropriate corrections [25] will permit determination of $\langle \alpha_{40}^{ex}(0) \rangle$ and provide the appropriate linear correction at time zero.

5.11 Conclusions

In addition to excited state population modification (Chapter 4), STED has been shown to bring about significant changes in excited state molecular alignment as measured by a reduction or increase in fluorescence anisotropy upon application of the DUMP pulse.

The creation of very highly ordered molecular arrays is now possible; re-polarisation experiments on Rhodamine 6G yield an initial (dumped) fluorescence anisotropy in excess of the limit predicted for three-photon excitation. STED is, therefore, clearly useful as a means of controlling excited state alignment and preparing initial degrees of molecular order that are otherwise unachievable using conventional single or two-photon excitation.

The interaction of polarised light with an ordered molecular array coupled with the measurement of fluorescence observables before and immediately after the DUMP process represents a higher order correlation measurement and, as such, is able to circumvent single photon selection rules. This allows the measurement of previously "hidden" excited state information. Variable PUMP-DUMP delay anisotropy and intensity experiments on Rhodamine 6G and Fluorescein have yielded the first (to our knowledge) measurements of hexadecapole alignment relaxation in an excited state.

References for Chapter 5

1. J R Lakowicz, *Principles of Fluorescence Spectroscopy* (2nd Ed.), Kluwer Academic, (1999)
2. B Valeur, *Molecular Fluorescence*, Wiley-VCH, Weinheim (2001)
3. L W Runnels and S F Scarlata, Biophys. J. **69** 1569 (1995)
4. A J Bain, R J Marsh and D A Armoogum, UK patent application 0211781.0. (2002)
5. A J Bain, P Chandna, and J Bryant, J. Chem. Phys. **112**, 10418 (2000)
6. J Kuśba, V Bogdanov, I Gryczynski and J R Lakowicz, Biophys. J. **67**, 2024 (1994)
7. I Gryczynski, Z Gryczynski and J R Lakowicz, Photochem. Photobiol. **67**(6), 641 (1998)
8. D A Armoogum, R J Marsh and A J Bain, Proc. SPIE **5222A** (2003)
9. D W G Smith and J G Powles, Mol. Phys. **10**, 451 (1966)
10. H J Böhm, R M Lynden-Bell, P A Madden and I R McDonald, Mol. Phys. **51**, 761 (1984)
11. T T Bopp, J. Chem. Phys. **47**, 3621 (1967)
12. D McMorrow and W T Lotshaw, J. Phys. Chem. **95**, 10395 (1991)
13. E W Castner Jr, Y J Chang, Y C Chu and G E Walrafen, J. Chem. Phys. **102**, 653 (1995)
14. J T Kindt and C A Schmuttenmaer, J. Phys. Chem. **100**, 10373 (1996)
15. C Rønne, L Thrane, P-O Åstrand, A Wallqvist, K V Mikkelsen and S R Keiding, J. Chem. Phys. **107**, 5319 (1997)
16. J Barthel, K Bachhuber, R Buchner and H Hetzenauer, Chem. Phys. Lett. **165**, 369 (1990)
17. D S Venables and C A Schmuttenmaer, J. Chem. Phys. **108**, 4935 (1990)
18. D J Cook, J X Chen, E A Morlino and R M Hochstrasser, Chem. Phys. Lett. **309**, 221 (1999)
19. M Lee, A J Bain, P J McCarthy, C H Han, J N Haseltine, A B Smith III and R M Hochstrasser, J. Chem. Phys. **85**(8), 4341 (1986)
20. S Lin, I D Hands, D L Andrews and S R Meech, J. Phys. Chem. A **103**, 3830 (1999)
21. J Bryant, Ph.D. Thesis, University of Essex (2000)
22. E M Monge, D A Armoogum and A J Bain, Proc. SPIE **4797**, 264 (2002)
23. E M Monge, Ph.D. Thesis, University of London (2003)
24. J Bryant, Ph.D. Thesis, University of Essex (2000)
25. R J Marsh, D A Armoogum and A J Bain (to be published)